Isopolytypic Growth of Nonpolar 4H-AlN on 4H-SiC and Its Device Applications

February 2009

Masahiro HORITA

Electronic Science and Engineering
Kyoto University

Abstract

AlN and high Al-content AlGaN with a nonpolar orientation have attracted much attention for applications in polarization-free deep-ultraviolet (UV) light-emitting devices. Since Al(Ga)N has a wurtzite structure (2H-polytype) as a thermally stable phase, most of the researches have focused on 2H-Al(Ga)N. On the other hand, the growth of 4H-polytype AlN on 4H-SiC ($11\bar{2}0$) substrates by molecular-beam epitaxy (MBE) was reported from Kyoto University in 2003. The 4H-AlN layer grown on 4H-SiC ($11\bar{2}0$) is expected to be another promising template for polarization-free light-emitting devices. Besides the optoelectronic devices, electrical properties of the isopolytypically grown 4H-AlN/4H-SiC interface are of great interest, due to the electrical neutrality of the interface in spite of the heterovalency between AlN and SiC. However, there is large room for improvement of the crystalline quality of 4H-AlN layers. For example, it has been revealed that there exist a number of stacking faults (SFs) in 4H-AlN layers as elucidated by high-resolution transmission electron microscopy (HRTEM).

In this study, high-quality isopolytypic growth of nonpolar 4H-AlN on 4H-SiC and its properties have been investigated. In addition, feasibility studies of optoelectronic and electronic devices have been carried out to demonstrate the potential of the nonpolar 4H-AlN. The contents of this thesis are as followings.

In Chapter 2, pretreatment of nonpolar SiC substrates is described. Pretreatment is important to realize isopolytypic growth of 4H-AlN with high crystalline perfection. The "*ex-situ* HCl gas etching" and "*in-situ* Ga deposition and desorption" are investigated. Formation of periodic step structures and reduction of surface oxygen are described.

In Chapter 3, reduction of SFs and threading dislocations (TDs) in 4H-AlN ($11\bar{2}0$) and ($1\bar{1}00$) nonpolar faces is presented. Since the surface roughening will initiate inclusion of 2H structure (SF), realization of a flat surface is focused to avoid the inclusion. In 4H-AlN ($11\bar{2}0$) growth, the optimization of Ⅲ/V supply ratio has been carried out to keep a flat surface during growth in addition to the realization of flat surface of nonpolar SiC substrates by HCl gas etching as mentioned in the last chapter. The density of extended defects in 4H-AlN has been characterized by using TEM observation as well as x-ray diffraction (XRD), which has revealed that the SF and TD densities are drastically reduced to 2×10^5 cm^{-1} and 8×10^7 cm^{-2}, respectively, compared with the 4H-AlN previously reported (SF: 5×10^6 cm^{-1}, TD: 4×10^{10} cm^{-2}). In 4H-AlN ($1\bar{1}00$) growth, stable

layer-by-layer growth has been realized by using SiC substrates with clear step-and-terrace structures. Cross-sectional TEM observation has revealed that SF generation during growth is suppressed effectively.

In Chapter 4, structure of extended defects in 4H-AlN and relationships between extended defects and the linewidth of XRD ω-scan are discussed. The structure of extended defects in 4H-AlN layers has been hardly identified. The SF structure and the Burgers vectors of TDs have been clarified from TEM observation in this study. The impacts of extended defects on the linewidth of XRD ω-scan are analyzed based on the defect structure determined above. In addition to the extended-defect structure, the lattice constant, the band structure and the phonon mode of 4H-AlN have been investigated. The in-plane and out-of-plane lattice constants of 4H-AlN are characterized by using high-resolution XRD (HRXRD), indicating the coherent growth of about 300-nm-thick 4H-AlN on 4H-SiC. From the spectra of optical reflectance (OR) and cathodoluminescence (CL) from 4H-AlN, the bandgap energy of 4H-AlN has been estimated to be about 0.2 eV smaller than that of 2H-AlN. In laser Raman scattering spectroscopy, several phonon peaks have been observed, which are determined to be the phonon modes of 4H-AlN which are different from those of 2H-AlN.

In Chapter 5, growth of 4H-AlN/4H-AlGaN multiple quantum well (MQW) structure has been demonstrated as a basis of optoelectronic device application. To control the composition of high Al-content AlGaN, Ga incorporation into AlN $(11\bar{2}0)$ and $(1\bar{1}00)$ has been investigated, where anomalous difference in Ga incorporation has been found. In the growth of AlGaN $(1\bar{1}00)$ layers, it has been revealed that the AlGaN has a 4H structure and the comparable crystalline quality to 4H-AlN $(1\bar{1}00)$. The MQW structures of 4H-polytype AlN/AlGaN $(1\bar{1}00)$ with 4-nm-thick well layers have been fabricated. Structural analyses by TEM observation indicate the realization of perfectly isopolytypic growth without generation of extended defects in the MQW structure. In CL measurements, a large intensity of the band edge emission from the MQW has been observed. The blue shift of the band edge emission has not been observed with increasing the excitation power density, which indicates that the MQW structure is free from the internal electric field.

In Chapter 6, fabrication of SiC metal-insulator-semiconductor field-effect transistors (MISFETs) with isopolytypically grown 4H-AlN as a gate dielectric has been presented as a basis of electronic device application. *N*-channel MISFETs have been fabricated by using 4H-AlN $(11\bar{2}0)$ heteroepitaxial layers grown on 4H-SiC $(11\bar{2}0)$. The MISFETs exhibit clear transistor operation for the first time. The MISFETs have shown normally-ON characteristics.

In Chapter 7, a summary of the present study is given, together with the remaining issues to be solved and suggestions for future work.

Acknowledgements

I would like to express my deepest gratitude to Professor Tsunenobu Kimoto for his supervision, continuous guidance, and kind encouragement through fruitful discussions.

I would like to thank Professor Susumu Noda for his providing the opportunity to accomplish this work and for his valuable suggestions. I acknowledge Professor Yoichi Kawakami for his helpful advice and stimulating comments on this dissertation.

I would like to express my hearty appreciation and gratitude to Associate Professor Jun Suda for his continuous guidance concerning experimental details, helpful suggestions, and constructive discussions throughout this work. I am also indebted to Research Associate Yusuke Nishi for his fruitful suggestions and his support in my daily work. I also thanks for Associate Professor Mitsuru Funato for assistance with transmission electron microscopy (TEM) as well as his valuable comments.

I am truly indebted to Emeritus Professor Hiroyuki Matsunami for his continuous guidance and encouragement throughout this work.

I would like to appreciate Dr. Norio Onojima for his introduction to research on growth of nonpolar AlN and his helpful suggestions. I wish to offer my gratitude to Dr. Robert Armitage for collaborating in nonpolar 4H-AlN growth and for careful reading of the manuscript and meaningful comments.

I wish to express gratitude to Dr. Yuki Negoro and Dr. Katsunori Danno for their kind encouragement to investigation and valuable suggestions. I would like to thank Dr. Shun-ichi Nakamura and Dr. Atsushi Koizumi for their careful instruction in SiC CVD growth and their helpful advice.

I would like to deeply appreciate to Mr. Masato Noborio for his helpful advice for study of AlN/SiC MIS devices as well as sharing life at university.

I am very much obliged to Mr. Shin-ichi Kamiya, Mr. Yuki Nakano, Mr. Koichi Amari, Mr. Hironori Okumura, and Mr. Hiroki Miyake for valuable discussion on MBE growth and device processes in nitride semiconductors.

I wish to acknowledge Mr. Junji Kaido, Mr. Yosuke Kanzaki, Mr. Hiroaki Kawano, Mr. Hironori Yoshioka, Mr. Katsuhiko Fukunaga, Mr. Ryota Suzuki, Mr. Kei Senga, Mr. Toru Hiyoshi, and Mr. Kazuki Yamaji for sharing meaningful time to discuss epitaxial growth, characterization and device processes in SiC as well as other semiconductor materials.

I wish to express gratitude to Dr. Giovanni Alfieri, Dr. Gan Feng, and
Dr. Kumaresan Ramanujam for their fruitful comments. I am also much obliged to Mr. Keiji Wada, Mr. Tsutomu Hori, Mr. Toshihiko Hayashi, Dr. Hiromi Kaneko, Mr. Hirokazu Fujiwara, Mr. Hiroaki Saito, Mr. Takeshi Tawara, and Dr. Kazuhiro Nishizono for their helpful suggestions.

I am grateful to Ms. Yoriko Ohnaka, Ms. Mizuki Yamada, and Ms. Noriko Matsumura for kindly supporting my daily work. Special thanks are also due to Mr. Kotaro Kawahara, Mr. Yuichiro Nanen, Mr. Naoki Watanabe and all the members of Semiconductor Science and Engineering Laboratory for their kindness and support.

I would like to thank Mr. Yoshimitsu Yoshioka, Dr. Shin Sasaki and
Mr. Hiroyuki Kinoshita from SiXON Ltd., Japan for supplying 4H-SiC $(11\bar{2}0)$ and $(1\bar{1}00)$ substrates.

This work was supported in part by Grant-in-Aid for Research Fellow from the Japan Society for the Promotion of Science (JSPS), Japan. This work was also financially supported in part by a Grand-in-Aid for the Scientific Research (No. 18206032/20360008) from JSPS, in part by a Grant for Industrial Technology Research (No. 04A48511d) from New Energy and Industrial Technology Development Organization, Japan, and in part by the 21st Century Center of Excellence Program (Grant No. 14213201) and the Global Center of Excellence Program (C09), the Ministry of Education, Culture, Sports, Science and Technology of Japan.

Finally, I really thank my parents, brother and all my friends for their understanding, continuing care, support and heartfelt encouragement.

February, 2009
Masahiro Horita

Contents

Chapter 1

Introduction

1.1 Background

Semiconductor devices have been growing in performance and increasing use by the technological innovation ever since the first transistor was invented in 1948. Semiconductor devices are currently spread among all areas of our lives. The devices include integrated circuits (ICs) (processing units, logic devices, analog devices and memories), power devices, radio-frequency (RF) devices and optoelectronic devices such as light-emitting diodes (LEDs) and laser diodes (LDs). The ICs are mounted in personal computers, home electronics and all electric devices and the power devices are used for power conversion systems from a power station to each electric device. The RF devices are utilized for wireless communication and the optoelectronic devices are employed for display equipments, optical data storage and high-speed wired communication. Although the ICs must have the largest marketplace among semiconductor devices, the markets of the power devices and the optoelectronic devices are large in next place after ICs and these devices support human living as well as ICs. Toward further convenience of our lives, each device is required to enhance the performance, that is, higher-speed processing units, large-capacity memories, higher-speed communication systems, higher-efficient light source and light emission at undeveloped wavelength and so on. On the other side of these performance advances, humankind faces the critical issues today, that is, the depletion of energy sources and global warming. Crude is expected to be exhausted in 40 years and other fossil fuels are also being depleted. And the large energy consumption is leading to the change the global climate. We have to research and develop ways to use energy efficiently for the future. Electric energy is the most controllable energy, which is used at any place in the world. Ultra low-loss and high-power electric devices can handle large amount of electric power with high efficiency, leading to reduction of conversion loss of the electric energy. And solid-state light-emitting devices are possible to be high-efficient, resulting in suppression of power consumption at terminal equipments. Development of semiconductor devices is anticipated from both aspects of new application and low energy loss.

Most of the present power devices are made of technologically-advanced Si due to the availability of high-quality and large-area wafers and excellent oxide (SiO_2). The RF devices and the optoelectronic devices are mainly formed of group-Ⅲ arsenide (GaAs, AlAs, InAs) and group-Ⅲ phosphide (GaP and InP) compound semiconductor and its alloys due to the higher electron mobility of GaAs than Si and the suitability of the band structure for light emission. However, these materials are approaching to the physical limits for enhancement of the performances. Si-based power devices are reaching to the limitation of energy-loss reduction and GaAs-based RF devices are being inadequate for high-frequency high-power use. High-efficient light-emitting devices operating at short visible or violet wavelength are physically irrealizable with group-Ⅲ arsenide or phosphide alloys. Group–Ⅲ nitride (Ⅲ–N) and Silicon Carbide (SiC) are the most promising semiconductor materials to fulfill these demands.

1.2 Group-Ⅲ Nitrides and SiC

1.2.1 Properties and current status of group-Ⅲ nitrides

Group-Ⅲ nitrides (InN, GaN and AlN) are Ⅲ-V compound semiconductors composed of tetrahedrally bonded cation and anion atoms in a closed-packed structure. All three binaries and their alloys crystallize in both wurtzite and zincblende structures, where the wurtzite structure is thermodynamically more stable [1]. Here, wurtzite and zinc-blende structures are also referred to as 2H and 3C structures in Ramsdell's notation [2], respectively. Since these compounds are direct-transition-type semiconductors[1], they have attracted much attention as the candidates for light-emitting devices [7]. In addition, excitons are capable of stable existence in GaN due to the large binding energy of 28 meV than the thermal energy of room temperature, also indicating the potential for high-efficient light-emitting devices [8]. These materials can cover continuously from 0.7 eV (the bandgap of wurtzite InN [9–11]) to 6.2 eV (the bandgap of wurtzite AlN [12]) by appropriate alloying (Fig. 1.1). The physical properties of GaN and AlN are listed in Table 1.1.

In the late 1980s, Amano *et al.* reported the important techniques for GaN related optoelectronic devices, that is, growth of high-quality GaN with low-temperature AlN buffer layers [13] and realization of *p*-GaN by low-energy electron beam irradiation [14]. In response to this, LEDs for the blue and green regions of the spectrum and LDs operating at the violet region of 405 nm were developed and commercialized in the 1990s [15–18]. On the other hand, recently, ultraviolet (UV) light-emitting devices operating at the wavelengths of 400–220 nm have been attracted much attention for high-density optical data storage, sterilization, chemical analysis and illumination lamps. The growth and fabrication technology for LEDs and LDs with emission in the wavelength range of 400–365 nm (the bandgap of

[1]Zinc-blende AlN is theoretically expected to have an indirect bandgap [3–6]. The indirect bandgap of zinc-blende AlN changes to direct structure with tensile strain [6].

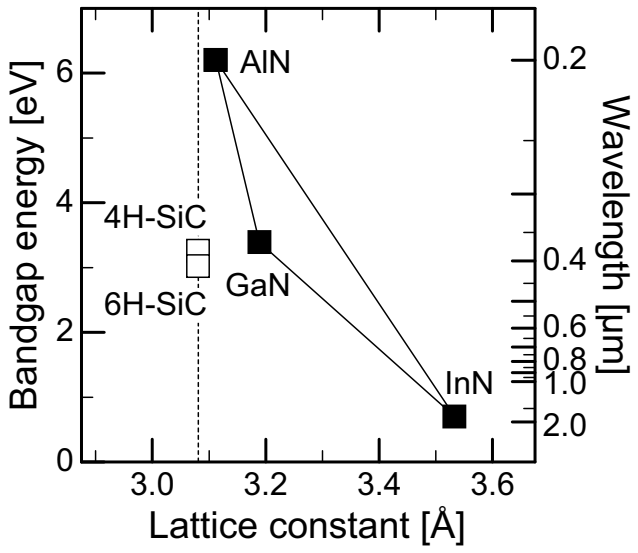

(a) a-axis

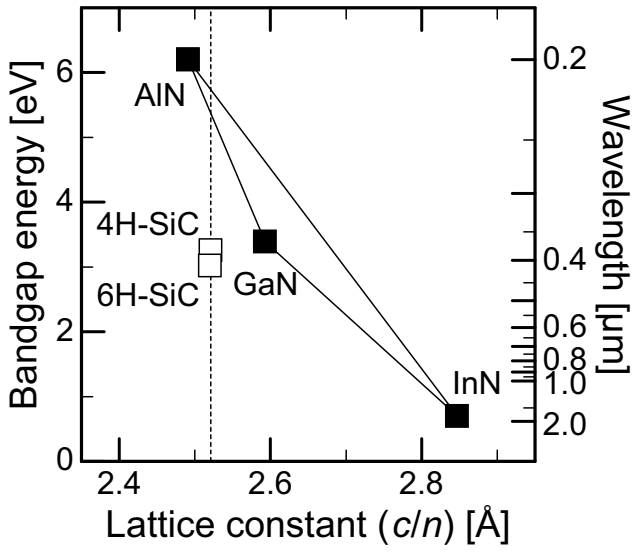

(b) c-axis

Figure 1.1: Relationships between bandgap and (a) a-axis / (b) c-axis lattice constant for hexagonal Ⅲ–Ns and SiC. The dashed lines show the lattice constants of 4H-SiC.

Table 1.1: Physical properties of GaN, AlN, SiC and most common other semiconductor materials.

Properties	GaN	AlN	SiC			Si	GaAs
			4H	6H	3C		
Crystal structure	WZ	WZ	4H	6H	ZB	Dia.	ZB
Lattice constant [Å]	3.189^a 5.186^c	3.112^a 4.982^c	3.081^a 10.05^c	3.081^a 15.12^c	4.36	5.43	5.65
Band structure	D.	D.	I.D.	I.D.	I.D.	I.D.	D.
Bandgap [eV]	3.42	6.2	3.26	3.02	2.3	1.12	1.42
Electron mobility [cm^2/Vs]	900	400	$1000^{\perp c}$ $1200^{/\!/c}$	$450^{\perp c}$ $100^{/\!/c}$	1000	1500	8500
Hole mobility [cm^2/Vs]	20	14	100	50	50	450	400
Electron saturation velocity [10^7 cm/s]	2.7	1.9	2.2	1.9	2.7	1	1
Breakdown field [MV/cm]	3.3	1.5	3	3	2	0.3	0.4
Thermal conductivity [W/cmK]	1.3	2.9	4.9	4.9	4.9	1.5	0.46
Relative dielectric constant	$9.5^{\perp c}$ $10.4^{/\!/c}$	8.5^*	$9.7^{\perp c}$ $10.2^{/\!/c}$	$9.7^{\perp c}$ $10.2^{/\!/c}$	10	11.9	12.8
Conductivity control	△	△	◯	◯	△	◯	◯
Thermal oxide	×	×	◯	◯	◯	◯	×
Conductive wafer	△ (SiC)	△ (SiC)	◯	◯	△ (Si)	◯	◯
Insulating wafer	△ (Sap.)	△ (Sap.)	◯	◯	×	△ (SOI)	△

WZ: Wurtzite ZB: Zincblende Dia.: Diamond
D.: Direct I.D.: Indirect
◯: Excellent △: Fair ×: Difficult
Sap.: Sapphire SOI: Silicon on insulator
*The data of anisotropy reported are uncertain.

GaN) is fairly mature due to the similarity in the recombination mechanisms and device design with the blue and green devices. In contrast, devices with emission wavelengths less than 365 nm require AlGaN active regions and high Al-content AlGaN is particularly needed for deep-UV light emitting devices operating at 220–300 nm. A lot of groups reported growth of AlGaN with high-Al-composition [19–21] and UV light-emitting devices operating at the wavelength less than 365 nm [22–24]. Taniyasu *et al.* reported the first AlN LEDs operating at 210 nm in 2006, which is the shortest wavelength among Ⅲ–Ns [25]. The growth of AlGaN has proved to be significantly more difficult compared with GaN because aluminum adatoms have a much larger sticking coefficient and much lower surface mobility than gallium adatoms. Consequently, devices based on the AlGaN active layers so far have not achieved the same efficiency as the InGaN-based devices. For instance, the external quantum efficiency (EQE) of LEDs operating at 285–240 nm is limited to 1% and the first AlN LED shows the EQE of 10^{-6}% [25].

Heteroepitaxy on foreign substrates is one of challenges for high-quality growth of Ⅲ–Ns. Most of defects such as threading dislocations (TDs) and grain boundaries are generated at the hetero interface due to the lattice and thermal mismatches. Although bulk GaN [26, 27] and AlN [28, 29] is available now, it will take a long time to achieve high-quality and large-area wafers at a reasonable cost. The recent GaN growth technique of epitaxial lateral overgrowth (ELO) [30, 31] is inadequate for AlGaN light-emitting devices, where the TD density of GaN has been reduced to 10^7–10^8 cm^{-2}. It was reported that the InGaN layers efficiently emit light due to the carrier localization originated from the indium molar fluctuation although the layers contain TDs at a large density [32]. To achieve high-efficient deep-UV light-emitting devices where the carrier localization effect by indium can not be employed, growth of higher-quality AlGaN layers is required compared with the case of InGaN layers. Among foreign substrates for heteroepitaxial growth, SiC is one of the candidates for high-quality AlN and AlGaN growth because of the relatively small lattice mismatch between AlN and SiC ($\Delta a \sim 0.9\%$ as shown in Fig. 1.1). In the previous study from our group, layer-by-layer growth of AlN from the initial stage of epitaxy is possible on SiC (0001) by plasma-assisted molecular beam epitaxy (PAMBE), indicating good wetting of AlN on SiC [33, 34].

1.2.2 Properties and current status of SiC

SiC is a group Ⅳ–Ⅳ compound semiconductor composed of silicon (Si) and carbon (C) atoms with the ratio of unity in tetrahedral bond configurations as the case of Ⅲ–Ns. Due to the strong bonding of Si–C, SiC has superior thermal and chemical stabilities, and has been widely used for polishing powders and heat-resistant coatings. SiC is also a famous material for taking numerous polytypes, which are different crystal structures based on the same chemical composition. Considering the Si–C pair (bilayer) as a sphere, there are three possible occupation sites denoted by A, B and C as shown in Fig. 1.2. For example, the

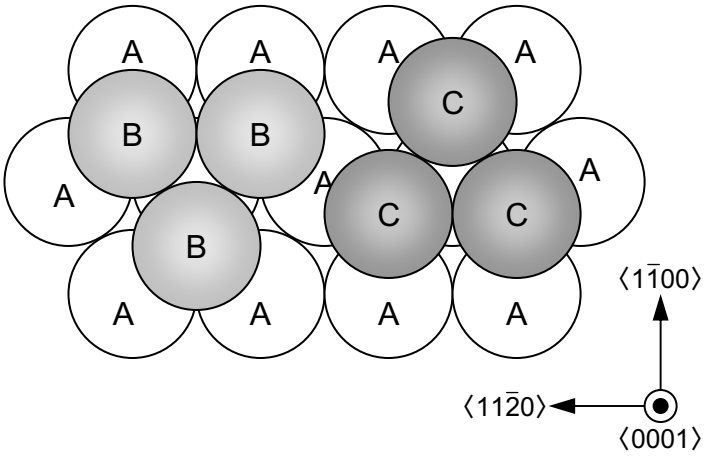

Figure 1.2: Hexagonal closed packing of Si–C or III–N pairs.

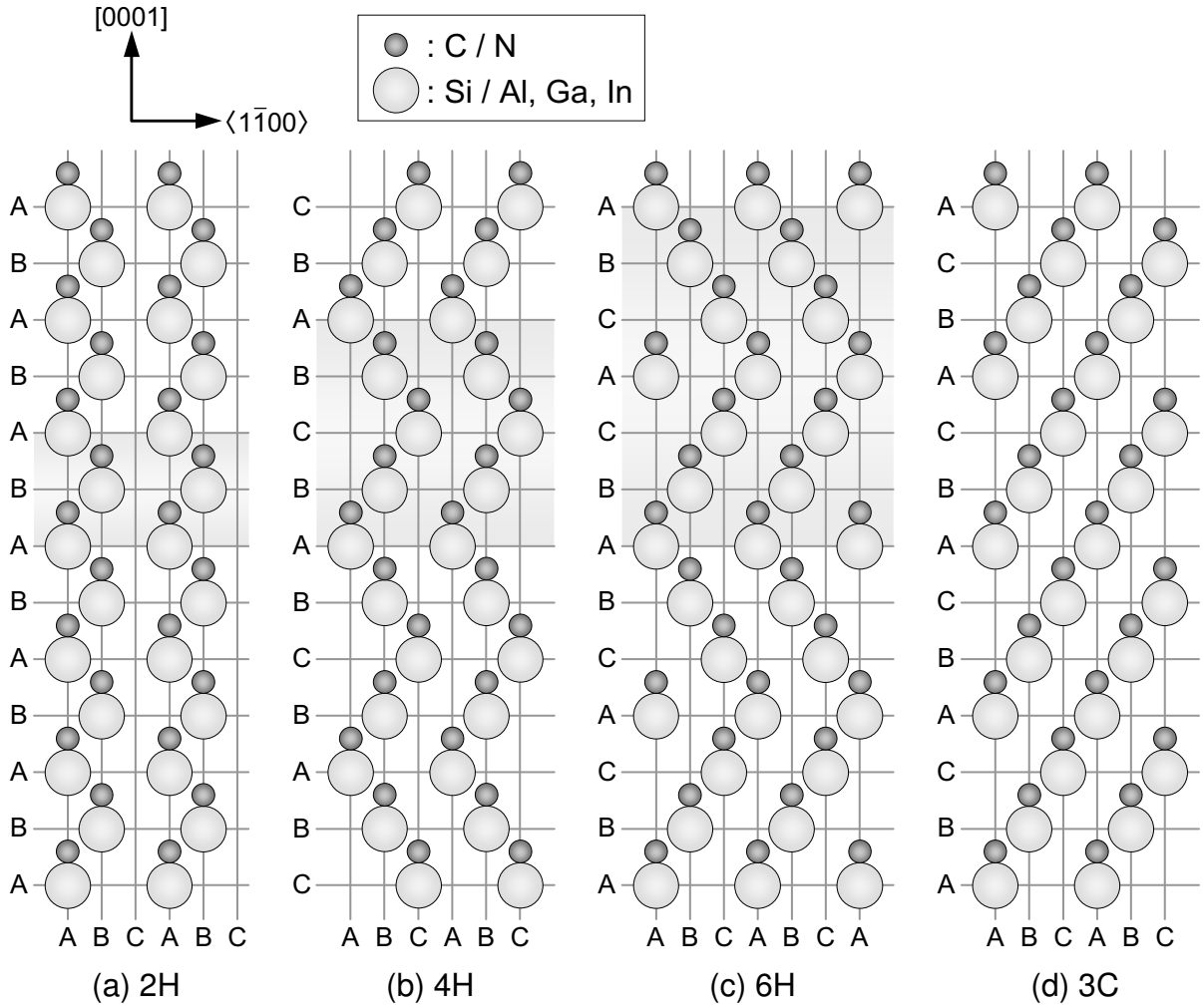

Figure 1.3: Stacking orders along [0001] (*c*-axis) for (a) 2H-, (b) 4H-, (c) 6H- and (d) 3C-structures of SiC or III–Ns.

B- or C-site bilayer can be placed on the A-site bilayer. Two simple stacking sequences are ABAB... (zincblende) and ABCABC... (wurtzite) structures, where Ⅲ–Ns crystallize as referred in Section 1.2.1. In the case of SiC, more than 200 polytypes have been found. The most popular and important polytypes for electronic device applications are 3C-, 4H-, and 6H-SiC. In Ramsdell's notation [2], polytypes are represented by the number of layers in the unit cell and the crystal structure (C for cubic, H for hexagonal, and R for rhombohedral). The structures of 3C-, 4H-, and 6H-SiC are shown in Fig. 1.3. The mechanical properties are almost invariant with the polytype, while the electrical and optical properties do drastically change with the polytype. Control of the polytype during crystal growth of SiC is a crucial issue, because inclusions of other polytypes severely deteriorate the performance of SiC or Ⅲ–N devices. With the stable characteristics of SiC physically and chemically, it has historically been difficult to obtain high-quality and large-area single crystals without any inclusions of other polytypes.

The physical properties of SiC are different for each polytype, as listed in Table 1.1. Both 4H- and 6H-SiC have wide bandgaps [35], suggesting that SiC devices can operate at high temperatures. The breakdown field of 3 MV/cm is one order of magnitude larger than for Si and GaAs [36]. This parameter is important to reduce the on-resistance in power devices. The high saturation drift velocity enables devices to operate at high frequencies [37–39]. Heat generated in devices by Joule heating can be easily transferred to a heat sink due to the high thermal conductivity of SiC [40, 41].

SiC substrates with the 3C-, 4H- and 6H-polytypes are commercially available. 3C-SiC is made by chemical vapor deposition (CVD) on Si (001) substrates [42] and its crystal quality is rather poor because of the large lattice mismatch (20%) between 3C-SiC and Si. On the other hand, bulk crystals of 4H-SiC and 6H-SiC are made by a physical vapor transport (seeded sublimation growth) technique known as the "modified-Lely method" [43]. High-quality bulk materials (TD density is $\leq 10^4$ cm^{-2}) are now commercially available with relatively large diameters, up to 75 mm [44]. Recently, ultra-low-dislocation density bulk SiC (TD density is $\leq 10^2$ cm^{-2}) has been reported [45]. Moreover, the conductivity of bulk SiC can be controlled, and *n*-type, *p*-type and semiinsulating substrates are available for both 4H- and 6H-polytypes. Therefore, 4H- and 6H-SiC can be used as high-quality substrates for Ⅲ–N devices, provided that challenges associated with heteroepitaxy are overcome.

Apart from substrate use for Ⅲ–Ns, SiC is promising material for electric power devices. Due to the breakthrough of "step-controlled epitaxy" [46, 47], high-quality epilayer without any inclusions can be available and both *n*-type and *p*-type doping can be controlled in a wide range (10^{14}–10^{19} cm^{-3}). The technique of selective conductivity control by ion implantation has been also mature. Now there have been many reports on SiC power devices. Intensive studies on fundamentals of SiC schottky barrier diodes (SBDs) [48–50] have led to commercial production of 4H-SiC SBDs. As for switching devices, metal-insulator-semiconductor field-effect transistors (MISFETs) are considered promising due to their high

switching frequency and have been investigated extensively. Since SiC is the only compound semiconductor to yield SiO_2 by thermal oxidation, metal-oxide-semiconductor (MOS) devices can be fabricated on SiC substrates. SiC power metal-oxide-semiconductor field-effect transistors (MOSFETs) are attractive power switching devices because of the possibility to realize high capacity with low loss and high switching speed. However, a high interface-state density, in particular for 4H-SiC (0001), has been found to cause large inversion channel resistivity [51, 52], limiting the performance of SiC MOSFETs. This is because that the SiO_2/SiC interface has one to two orders of magnitude higher interface state density than the SiO_2/Si interface. This renders the as-grown thermal oxide rather useless as dielectric for SiC-based MOS devices [53, 54]. Two principle reasons have been suggested for this behavior [55]. (1) Incomplete oxidation of carbon atoms in SiC leads to the formation of carbon clusters which are believed to contribute interface states on account of their graphitic and therefore semi-metallic nature. (2) The steep increase in interface states toward the conduction band edge, especially in 4H-SiC, is due to so-called near interface traps (NITs). Their microscopic origin is as yet unclear but it was suggested that they result from oxygen deficiency [54]. These states act as interface traps for electrons and cause the large channel resistivity in MOS devices. Therefore, many efforts have been made to reduce the channel resistivity at the SiO_2/SiC interface. Nitridation following thermal oxidation [56–59] and deposited SiO_2 with post-annealing in a nitrous oxide ambient [60–62] have been attempted to reduce interface states and enhance the channel mobility. Fabrication of MOS structures on other crystal faces like $(11\bar{2}0)$ [63, 64] and $(03\bar{3}8)$ [65] has been also attempted to improve SiC MOSFET performance.

1.3 Growth of Nonpolar Group-Ⅲ Nitrides on Nonpolar SiC Substrate

1.3.1 Nonpolar group-Ⅲ nitrides for light-emitting devices

Ⅲ–Ns with wurtzite structure have strong polarization along [0001] due to the large electron affinity of nitrogen. Quantum well (QW) structures based on Ⅲ–Ns grown on the (0001) face exhibit strong internal electric fields because of the discontinuities in piezoelectric and spontaneous polarization at the heterointerfaces. These internal fields result in lower internal quantum efficiency, which suppress the realization of high-efficiency LEDs. With the goal of avoiding this problem, much attention has recently been given to nonpolar growth orientation. The nonpolar faces, that is, $(11\bar{2}0)$ and $(1\bar{1}00)$ are the plane perpendicular to a (0001) polar face as shown in Fig. 1.4. The wave functions of electrons and holes spatially overlap each other in the QW on nonpolar faces while they separate on the polar face as shown in Fig. 1.5. This spatial overlap in nonpolar faces leads to high-efficient light emission.

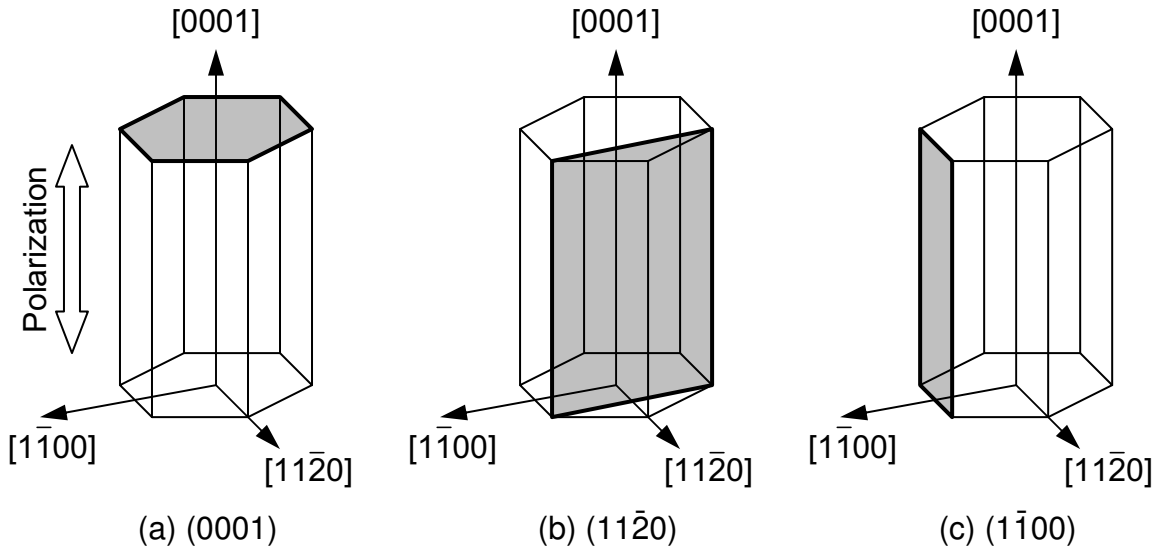

Figure 1.4: Schematic illustration of (a) (0001), (b) (11$\bar{2}$0) and (c) (1$\bar{1}$00) faces in III–N and SiC.

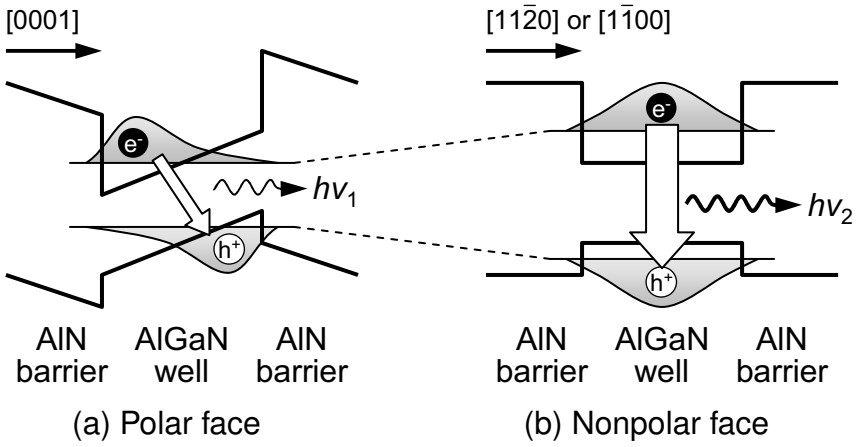

Figure 1.5: Band structures of an AlN/AlGaN/AlN quantum well formed on (a) polar faces and (b) nonpolar faces. Schematics of the electron/hole wave functions, recombination states and light emission are also shown.

Extensive studies on growth of GaN with nonpolar orientations have been carried out using various substrates and growth methods. In addition to SiC substrates, sapphire (Al_2O_3), lithium aluminate ($LiAlO_2$) and zinc oxide (ZnO) substrates are given for the nonpolar Ⅲ–N growth, listed in Table 1.2. Growth of GaN $(11\bar{2}0)$ on Al_2O_3 $(1\bar{1}02)$ by metal-organic vapor phase epitaxy (MOVPE) [66] and growth of GaN $(1\bar{1}00)$ on $LiAlO_2$ (100) by MBE [67] have been reported. Since ZnO has the same structure as GaN (wurtzite) and small lattice mismatches to GaN, growth of GaN on ZnO substrates in both $(11\bar{2}0)$ and $(1\bar{1}00)$ faces have been reported [68, 69]. In these heteroepitaxial growth systems, reduction of stacking faults (SFs) and TDs contained in Ⅲ–Ns layers is the key issue. It is particularly important to reduce SFs parallel to (0001), that is, basal plane SFs caused for in-plane anisotropy of lattice mismatches. Various methods for SF reduction have been reported. Haskell *et al.* have reported GaN $(11\bar{2}0)$ with a low SF density of 4×10^5 cm^{-1} grown on free-standing GaN $(11\bar{2}0)$ by MOVPE [70]. In addition, ELO growth technique is effective in GaN $(11\bar{2}0)$ growth as well as (0001) growth, resulting in SF reduction to the density of 3×10^3 cm^{-1} [71]. The chemical stability at the growth temperature is also important for growth substrates. In case of GaN growth on ZnO, room-temperature growth by pulse laser deposition is necessary to suppress the interface reaction [68, 69].

SiC substrates have the advantages of these substrates for nonpolar AlN growth from the viewpoints of the lattice mismatches for both $[11\bar{2}0]$ and [0001] (see Fig. 1.1, Table 1.2), the wafer size and the chemical stability. Stemmer *et al.* have reported the first growth of nonpolar AlN on nonpolar 6H-SiC by MBE [72], and nonpolar AlN growth on SiC substrates has been intensively investigated by Onojima *et al.* and Armitage *et al.* since 2002 [73–75]. In these reports, AlN $(11\bar{2}0)$ and $(1\bar{1}00)$ can be grown on SiC $(11\bar{2}0)$ and $(1\bar{1}00)$, respectively. The epitaxial relationship is AlN [0001] // SiC [0001] in both systems. However, the crystal qualities of AlN $(11\bar{2}0)$ layers grown on 6H-SiC $(11\bar{2}0)$ and 4H-SiC $(11\bar{2}0)$ are very different. The full-width at half-maximum (FWHM) of x-ray diffraction (XRD) with [0001] beam incidence is 3000 arcsec in the AlN grown on 6H-SiC while that is 90 arcsec in the AlN grown on 4H-SiC, indicating that the AlN grown on 4H-SiC has much higher quality than the AlN grown on 6H-SiC. One of the most important challenge to AlN growth on SiC is "polytype mismatch". As referred in Sections 1.2.1 and 1.2.2, Ⅲ–Ns forms wurtzite (2H) structure in the thermally stable state while SiC forms 4H or 6H structure. In case of nonpolar growth, the crystal structure of 2H-AlN is not matched to that of either 4H- or 6H-SiC at the interface because of the differences in the [0001] stacking sequences of 2H-AlN and 4H- or 6H-SiC as shown in Fig. 1.6 (a) and (b). This structural mismatch is corresponding to atomically-spaced high-density dislocations at the interface, resulting in extremely high-density TDs in 2H-AlN grown on 6H-SiC. Figure 1.7 shows high-resolution transmission electron microscopy (HRTEM) images of AlN $(11\bar{2}0)$ epilayers grown on 6H-SiC and 4H-SiC substrates. The TEM observation has elucidated that a number of defects exist at the interface and that defective 2H-AlN was grown on 6H-SiC as anticipated. On the other hand, it has been revealed that the AlN grown on 4H-SiC forms not 2H (wurtzite)

Table 1.2: Substrates for nonpolar-face AlN growth.

Substrate and its crystal face		Homoepitaxy		Heteroepitaxy			
		AlN	GaN	SiC	Al_2O_3	γ-$LiAlO_2$	ZnO
		$(11\bar{2}0)$/ $(1\bar{1}00)$	$(11\bar{2}0)$/ $(1\bar{1}00)$	$(11\bar{2}0)$/ $(1\bar{1}00)$	$(1\bar{1}02)$	(100)	$(11\bar{2}0)$/ $(1\bar{1}00)$
Crystal face of AlN layer		$(11\bar{2}0)$/ $(1\bar{1}00)$	$(11\bar{2}0)$/ $(1\bar{1}00)$	$(11\bar{2}0)$/ $(1\bar{1}00)$	$(11\bar{2}0)$	$(1\bar{1}00)$	$(11\bar{2}0)$/ $(1\bar{1}00)$
Crystal structure		Hex. (WZ)	Hex. (WZ)	Hex. (4H, 6H)	Tri.	Tetra.	Hex. (WZ)
Lattice mismatch	a-axis	—	−2.4%	+1.0%	+5.1%	−0.9%	−4.2%
	c-axis	—	−3.9%	−1.1%	−2.8%	−3.6%	−4.3%
Wafer size		×	×	◯	◯	◯	◯
Stability at AlN growth temperature		◯	◯	◯	◯	△	×
Conductivity		◯	◯	◯	×	×	◯

Hex.: Hexagonal Tri.: Trigonal Tetra.: Tetragonal
WZ: Wurtzite
◯: Excellent △: Fair ×: Poor

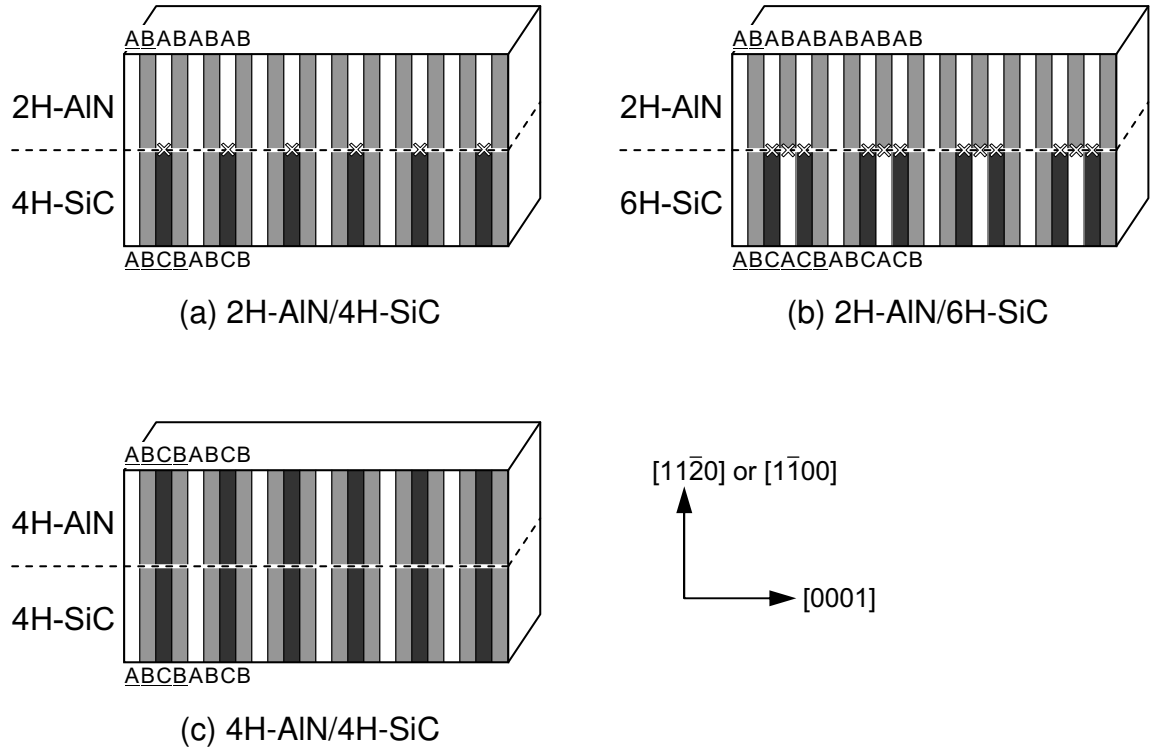

Figure 1.6: Schematic illustration of polytype mismatch between nonpolar (a) 2H-AlN/4H-SiC, (b) 2H-AlN/6H-SiC and (c) 4H-AlN/4H-SiC. The cross indices indicate partial dislocations extended perpendicularly to the page.

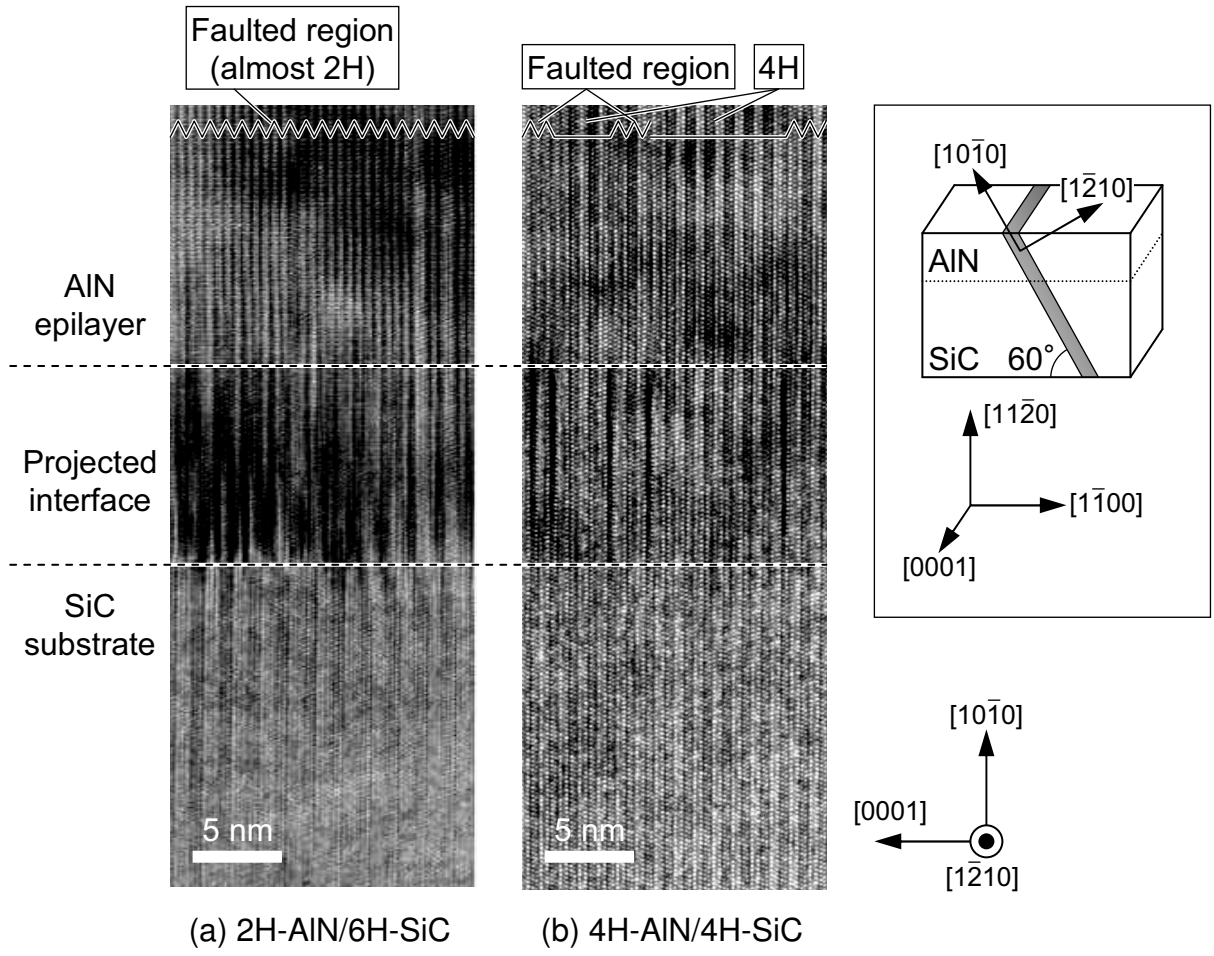

Figure 1.7: Cross-sectional high-resolution TEM images of (a) 2H-AlN/6H-SiC (11$\bar{2}$0) and (b) 4H-AlN/4H-SiC (11$\bar{2}$0) interfaces [74]. The inset shows the geometry of TEM specimens. In the upper of the TEM images, the regions of 4H structures and faulted region are shown by straight and notched lines, respectively.

structure but metastable 4H structure. This is the first report of "4H-polytype AlN" and then Robert *et al.*have reported that high-quality 4H-AlN ($1\bar{1}00$) can be also grown on 4H-SiC ($1\bar{1}00$). The availability of metastable 4H-AlN on nonpolar 4H-SiC suggests the possibility of AlN growth without polytype mismatch at the interface. It has been expected that the growth with polytype matched interface, that is, "isopolytypic growth" results in the high-quality AlN. However replication of the crystal structure from 4H-SiC substrates to AlN epilayers is not perfect and 2H inclusions and other defects have been observed at a high density as shown in Fig. 1.7 (b). To promote the isopolytypic growth and to achieve 4H-AlN in a whole area of nonpolar 4H-SiC are important for optoelectronic devices as well as electric power devices. In addition to the high-quality growth of 4H-AlN, the properties of the novel polytype structure of AlN should be investigated, which is assumed to be partly different from that of 2H-AlN (wurtzite) as well as the case of SiC.

1.3.2 AlN/SiC heterointerface with nonpolar face for metal-insulator-semiconductor devices

As referred in Section 1.2.2, enhancement of the inversion channel mobility at the MOS interface is the one of the key issues. Undoped AlN can be available for an alternative gate dielectric since it has the large bandgap energy of 6.2 eV. AlN is a suitable insulating material due to its high dielectric constant ($\epsilon_{\mathrm{AlN}} = 8.5$) compared to SiO_2 ($\epsilon_{\mathrm{SiO_2}} = 3.9$) [76–80]. There are a few reports on SiC MISFETs with AlN gate dielectrics grown by MBE on SiC (0001) off-axis faces [81, 82]. In these reports, the MISFETs suffer from large gate leakage current and small drain current. Since 2H-AlN is grown on 6H- or 4H-SiC (0001) off-axis substrates, the crystal structure does not match between substrates and epilayers, resulting in a high density of dislocations at the AlN/SiC interface. These dislocations must generate the interface states, leading to the low channel mobility, and also degrade the AlN crystal quality, resulting in large gate leakage current. The isopolytypic nonpolar 4H-AlN/4H-SiC expects to be one of the solution for this problem because no defects are formed at the interface as mentioned in Section 1.3.1. On the other hand, the heterovalency between AlN and SiC is another issue in AlN/SiC interfaces, that is, AlN is group Ⅲ-V semiconductor while SiC is group Ⅳ-Ⅳ. In the heterovalent structure of AlN/SiC, donorlike N–Si and acceptorlike Al–C bonds exist at a high density equivalent to in-plane atomic density. It is assumed that the balance of the number between N–Si and Al–C bonds dramatically affects interface properties. The ratio of N–Si and Al–C bonds can be settled into unity at the nonpolar interface while the ratio readily varies depending on the interface structure in the (0001) polar face.

From the viewpoints of both heteropolytype and heterovalency, utilization of the nonpolar AlN/SiC interface to MIS devices expects to improve the electric properties such as the interface state density and the channel mobility.

1.4 Outline of This Thesis

In this thesis, heteroepitaxial growth of high-quality nonpolar 4H-AlN on nonpolar 4H-SiC using MBE is studied toward optoelectronic device applications as well as electronic device applications. The surface structures of SiC substrates and AlN epilayers during growth are investigated in both $(11\bar{2}0)$ and $(1\bar{1}00)$ faces to obtain 4H-AlN epilayers with excellent crystalline quality. Since there are few reports on nonpolar orientations of 4H-AlN, the structure of defects contained in 4H-AlN is obscure. The defect structure in nonpolar 4H-AlN is intensively characterized by TEM and the relationship between the type of defect structure and the FWHM of XRD is studied. In addition to defect structure, the basic properties of 4H-AlN such as the band structure and the lattice vibration mode are characterized, which have not been experimentally reported. Feasibility of light-emitting devices and electronic power devices should be demonstrated once high-quality growth of 4H-AlN and isopolytypic 4H-AlN/4H-SiC interfaces are available. For optoelectronic devices, 4H-AlGaN growth is attempted applying the isopolytype growth technique and optical properties of 4H-AlGaN and AlN/AlGaN/AlN multiple quantum well (MQW) in 4H-polytype system are investigated. Toward electric power devices, the interface properties of isopolytypic AlN/SiC are studied by fabrication of AlN/SiC MIS devices.

In Chapter 2, the MBE growth system used in this study and pretreatment of nonpolar SiC substrates are described. Pretreatment is important to realize isopolytypic growth of 4H-AlN with high crystalline perfection. The "*ex-situ* HCl gas etching" and "*in-situ* Ga deposition and desorption" are investigated. Formation of periodic step structures and reduction of surface oxygen are described.

In Chapter 3, optimization of 4H-AlN growth condition is performed. Two-dimensional (2D) layer-by-layer growth at the initial stage is achieved in both $(11\bar{2}0)$ and $(1\bar{1}00)$ faces. Reduction of extended defects such as SFs and TDs contained in AlN layers is exhibited in both $(11\bar{2}0)$ and $(1\bar{1}00)$ compared with the past studies and 4H-AlN isopolytypically grown on 4H-SiC $(11\bar{2}0)$ is particularly achieved in a large area.

In Chapter 4, defect structure of SFs and TDs contained in 4H-AlN is investigated with TEM and XRD analyses. From the two methods of TEM observations, that is, imaging with two different diffraction beam and high-resolution lattice imaging, the defect structure contained in 4H-SiC is determined. The impact of SFs on XRD linewidth in nonpolar 4H-AlN $(11\bar{2}0)$ and $(1\bar{1}00)$ is discussed, which is different state from nonpolar 2H-GaN or 2H-AlN. In addition to the extended-defect structure, the lattice constant, the band structure and the phonon mode of 4H-AlN have been investigated.

In Chapter 5, growth of 4H-AlGaN and 4H-AlN/4H-AlGaN MQW structure have been studied as a basis of optoelectronic device application. Composition controllability of AlGaN layers with both nonpolar $[11\bar{2}0]$ and $[1\bar{1}00]$ orientations is presented for growth of AlN/AlGaN MQW structure. The crystal structure, crystalline quality and growth kinetics of AlGaN layers grown on 4H-SiC $(1\bar{1}00)$ are discussed compared with 4H-AlN layers.

In addition to AlGaN growth, growth of AlN/AlGaN MQW structure is investigated. The crystalline quality of MQW structure is examined by TEM observations. The cathodoluminescence (CL) from the AlGaN layers and the MQW structure are discussed.

In Chapter 6, the properties of 4H-AlN/4H-SiC isopolytypically matched interface are investigated. The band offsets at the 4H-AlN/4H-SiC interface and the dielectric properties of AlN epilayers are characterized. Fabrication of 4H-SiC MISFETs with heteroepitaxially grown 4H-AlN as a gate insulator and its definite FET operation is demonstrated.

In Chapter 7, conclusions and suggestions for future work are presented.

References

[1] H. Okumura, K. Ohta, G. Feuillet, K. Balakrishnan, S. Chichibu, H. Hamaguchi, P. Hacke, and S. Yoshida, J. Cryst. Growth **178**, 113 (1997).

[2] L. S. Ramsdell, Amer. Min. **32**, 64 (1947).

[3] F. Sökeland, M. Rohlfing, P. Krüger, and J. Pollmann, Phys. Rev. B **68**, 075203 (2003).

[4] H. Hernández-Cocoletzi, D. A. Contreras-Solorio, and J. Arriaga, Appl. Phys. A **81**, 1029 (2005).

[5] M. B. Kanoun, S. Goumri-Said, A. E. Merad, and H. Mariette, J. Appl. Phys. **98**, 063710 (2005).

[6] K. Kobayashi and S. Komatsu, J. Phys. Soc. Jpn. **77**, 084703 (2008).

[7] F. A. Ponce and D. P. Bour, Nature **386**, 351 (1997).

[8] B. Monemar, Phys. Rev. B **10**, 676 (1974).

[9] Y. Nanishi, Y. Saito, and T. Yamaguchi, Jpn. J. Appl. Phys. **42**, 2549 (2003).

[10] V. Yu. Davydov, A. A. Klochikhin, R. P. Seisyan, V. V. Emtsev, S. V. Ivanov, F. Bechstedt, J, Furthmuller, H. Harima, A. V. Mudryi, J. Aderhold, O. Semchinova, and J. Graul, phys. stat. sol. (b) **229**, R1 (2002).

[11] J. Wu, W. Walukiewicz, K. M. Yu, J. W. Age Ⅲ, E. E. Haller, H. Lu, W. J. Schaff, Y. Saito, and Y. Nanishi, Appl. Phys. Lett. **80**, 3967 (2002).

[12] Q. Gao and A. Yoshida, Jpn. J. Appl. Phys. **33**, 2453 (1994).

[13] H. Amano, N. Sawaki, I. Akasaki, and Y. Toyoda, Appl. Phys. Lett. **48**, 353 (1986).

[14] H. Amano, M. Kito, K. Hiramatu, and I. Akasaki, Jpn. J. Appl. Phys. **28**, L2112 (1989).

[15] S. Nakamura , T. Mukai, and M. Senoh, Appl. Phys. Lett. **64**, 1687 (1994).

[16] S. Nakamura, M. Senoh, N. Iwasa, and S. Nagahama, Jpn. J. Appl. Phys. **34**, L797 (1995).

[17] S. Nakamura, M. Senoh, S. Nagahama, N. Iwasa, T. Yamada, T, Matsushita, Y. Sugimoto, and H. Kiyoku, Appl. Phys. Lett. **70**, 1417 (1997).

[18] S. Nagahama, N. Iwasa, M. Senoh, T. Matsushita, Y. Sugimoto, H. Kiyoku, T. Kozaki, M. Sano, H. Matsumura, H. Umemoto, K. Chocho, and T. Mukai, Jpn. J. Appl. Phys. **39**, L647 (2000).

[19] Y. Kida, T. Shibata, H. Naoi, H. Miyake, K. Hiramatsu, and M. Tanaka, phys. stat. sol. (a) **194**, 498 (2002).

[20] S. Heikman, S. Keller, S. Newman, Y. Wu, C. Moe, B. Moran, M. Schmidt, U. K. Mishra, J. S. Speck, and S. P. DenBaars, Jpn. J. Appl. Phys. **44**, L405 (2005).

[21] M. Takeuchi, S. Ooishi, T. Ohtsuka, T. Maegawa, T. Koyama, S. F. Chichibu, and Y. Aoyagi, Appl. Phys. Express **1**, 021102 (2008).

[22] T. Takano, Y. Narita, A. Horiuchi, and H. Kawanishi, Appl. Phys. Lett. **84**, 3567 (2004).

[23] K. Iida, T, Kawashima, A. Miyazaki, H, Kasugai, S. Mishima, A. Honshio, Y. Miyake, M. Iwaya, S. Kamiyama, H. Amano, and I. Akasaki, Jpn. J. Appl. Phys. **43**, L499 (2004).

[24] H. Hirayama, T. Yatabe, N. Noguchi, T. Ohashi, and N. Kamata, Appl. Phys. Lett. **91**, 071901 (2007).

[25] Y. Taniyasu, M. Kasu, and T. Makimoto, Nature **441**, 325 (2006).

[26] A. Gassmann, T. Suski, N. Newman, C. Kisielowski, E. Jones, E. R. Weber, Z. L. Weber, M. D. Rubin, H. I. Helava, I. Grzegory, M. Beckowski, J. Jun, and S. Porowski, J. Appl. Phys. **80**, 2195 (1996).

[27] R. Held, G. Newak, B. E. Ishaug, S. M. Seutter, A. Parkhomovsky, A. M. Dabrian, P. I. Cohen, I. Grzegory, and S. Porowski, J. Appl. Phys. **85**, 7697 (1999).

[28] Y. Kumagai, T. Yamane, and A. Koukitsu, J. Cryst. Growth **281**, 62 (2005).

[29] R. T. Bondokov, S. G. Mueller, K. E. Morgan, G. A. Slack, S. Schujman, M. C. Wood, J. A. Smart, and L. J. Schowalter, J. Cryst. Growth **310**, 4020 (2008).

[30] A. Usui, H. Sunakawa, A. Sakai, and A. Yamaguchi, Jpn. J. Appl. Phys. **36**, L899 (1997).

[31] C. I. H. Ashby, C. C. Mitchell, J. Han, N. A. Missert, P. P. Provencio, D. M. Follstaedt, G. M. Peake, and L. Griego, Appl. Phys. Lett. **77**, 3233 (2000).

[32] Y. Narukawa, Y. Kawakami, M. Funato, Sz. Fujita, Sg. Fujita, and S. Nakamura, Appl. Phys. Lett. **70**, 981 (1997).

[33] N. Onojima, J. Suda, and H. Matsunami, Jpn. J. Appl. Phys. **42**, L445 (2003).

[34] J. Suda, N. Onojima, T. Kimoto, and H. Matsunami, Mater. Res. Soc. Symp. Proc. **798**, Y3.4 (2004).

[35] G. B. Dubrovskii and V. I. Shur, Sov. Phys. Semicond. **17**, 1847 (1975).

[36] W. V. Muench and I. Pfaffeneder, J. Appl. Phys. **48**, 4831 (1977).

[37] I. A. Khan and J. A. Cooper, Jr., Mater. Sci. Forum **338–342**, 204 (2000).

[38] I. A. Khan and J. A. Cooper, Jr., IEEE Trans. Electron Devices **47**, 269 (2000).

[39] W. V. Muench and E. Pettenpaul, J. Appl. Phys. **48**, 4823 (1977).

[40] D. Hobgood, M. Brady, M. Brixius, V. Tsvetkov, and C. H. Carter, Jr., Mater. Sci. Forum **338–342**, 3 (2000).

[41] G. A. Slack, J. Appl. Phys. **35**, 3460 (1964).

[42] H. Nagasawa, K. Yagi, and T. Kawahara, J. Cryst. Growth **237–239**, 1244 (2002).

[43] Yu. M. Tairov and V. F. Tsvetkov, J. Cryst. Growth **52**, 146 (1981).

[44] H. McD. Hobgood, M. F. Brady, M. R. Calus, J. R. Jenny, R. T. Leonard, D. P. Malta, St. G. Müller, A. R. Powell, V. F. Tsvetkov, R. C. Glass, and C. H. Carter, Jr., Mater. Sci. Forum **457–460**, 3 (2004).

[45] D. Nakamura, I. Gunjishima, S. Yamaguchi, T. Itoh, A. Okamoto, H. Kondo, S. Onda, and K. Takatori, Nature **430**, 1009 (2004).

[46] T. Kimoto, A. Itoh, and H. Matsunami, phys. stat. sol. (b) **202**, 247 (1997).

[47] H. Matsunami and T. Kimoto, Mater. Sci. & Eng. R **20**, 125 (1997).

[48] T. Kimoto, T. Urushidani, S. Kobayashi, and H. Matsunami, IEEE Electron Device Lett. **14**, 548 (1993).

[49] A. Itoh, T. Kimoto, and H. Matsunami, IEEE Electron Device Lett. **16**, 280 (1995).

[50] K. J. Schoen, J. M. Woodall, J. A. Cooper, Jr., and M. R. Melloch, IEEE Trans. Electron Devices **45**, 1595 (1998).

[51] H. Yano, T. Hirao, T. Kimoto, and H. Matsunami, Appl. Phys. Lett. **78**, 374 (2001).

[52] N. S. Saks, S. S. Mani, and A. K. Agarwal, Appl. Phys. Lett. **76**, 2250 (2000).

[53] J. N. Shenoy, M. K. Das, J. A. Cooper, Jr., M. R. Melloch, and J. W. Palmour, J. Appl. Phys. **79**, 3042 (1996).

[54] O. Kordina, C. Hallin, A. Henry, J. P. Bergmann, I. G. Ivanov, A. Ellison, N. T. Son, and E. Janzén, phys. stat. sol. (b) **202**, 321 (1997).

[55] K. Y. Gao, T. Seyller, L. Ley, F. Ciobanu, G. Pensl, A. Tadich, J. D. Riley, and R. G. Leckey, Appl. Phys. Lett. **83**, 1830 (2003).

[56] P. Jamet, S. Dimitrijev, and P. Tanner, J. Appl. Phys. **90**, 5058 (2001).

[57] G. Y. Chung, C. C. Tin, J. R. Williams, K. McDonald, R. K. Chanana, R. A. Weller, S. T. Pantelides, L. C. Feldman, O. W. Holland, M. K. Das, and J. W. Palmour, IEEE Electron Device Lett. **22**, 176 (2001).

[58] L. A. Lipkin, M. K. Das, and J. W. Palmour, Mater. Sci. Forum **389–393**, 985 (2002).

[59] T. Kimoto, Y. Kanzaki, M. Noborio, H. Kawano, and H. Matsunami, Jpn. J. Appl. Phys. **44**, 1213 (2005).

[60] G. Y. Chung, J. R. Williams, T. Isaacs-Smith, F. Ren, K. McDonald, and L. C. Feldman, Appl. Phys. Lett. **81**, 4266 (2000).

[61] H. Yano, T. Hatayama, Y. Uraoka, and T. Fuyuki, Mater. Sci. Forum **527–529**, 971 (2006).

[62] T. Kimoto, H. Kawano, M. Noborio, J. Suda, and H. Matsunami, Mater. Sci. Forum **527–529**, 987 (2006).

[63] H. Yano, T. Hirao, T. Kimoto, H. Matsunami, K. Asano, and Y. Sugawara, IEEE Electron Device Lett. **20**, 611 (1999).

[64] H. Yano, T. Kimoto, and H. Matsunami, Mater. Sci. Forum **353–3**, 627 (2000).

[65] T. Hirao, H. Yano, T. Kimoto, H. Matsunami, and H. Shiomi, Mater. Sci. Forum **389–393**, 1065 (2002).

[66] M. D. Craven, S. H. Lim, F. Wu, J. S. Speck, and S. P. DenBaars, Appl. Phys. Lett. **81**, 469 (2002).

[67] O. Brandt, Y. J. Sun, L. Däweritz, and K. H. Ploog, Physica E **23**, 339 (2004).

[68] A. Kobayashi, S. Kawano, Y. Kawaguchi, J. Ohta, and H. Fujioka, Appl. Phys. Lett. **90**, 041908 (2007).

[69] A. Kobayashi, S. Kawano, K. Ueno, J. Ohta, H. Fujioka, H. Amanai, S. Nagao, and H. Horie, Appl. Phys. Lett. **91**, 191905 (2007).

[70] B. A. Haskell, F. Wu, M. D. Creven, P. T. Fini, S. P. DenBaars, J. S. Speck, and S. Nakamura, Appl. Phys. Lett. **83**, 1554 (2003).

[71] B. A. Haskell, F. Wu, M. D. Craven, S. Matsuda, P. T. Fini, T. Fujii, K. Fujito, S. P. DenBaars, J. S. Speck, and S. Nakamura, Appl. Phys. Lett. **83**, 644 (2003).

[72] S. Stemmer, P. Pirouz, Y. Ikuhara, and R. F. Davis, Phys. Rev. Lett. **77**, 1797 (1996).

[73] N. Onojima, J. Suda, T. Kimoto, and H. Matsunami, Jpn. J. Appl. Phys. **41**, L1348 (2002).

[74] N. Onojima, J. Suda, T. Kimoto, and H. Matsunami, Appl. Phys. Lett. **83**, 5208 (2003).

[75] R. Armitage, J. Suda, and T. Kimoto, Appl. Phys. Lett. **88**, 011908 (2006).

[76] T. Adam, J. Kolodzey, C. P. Swann, M. W. Tsao, and J. F. Rabolt, Appl. Surf. Sci. **175–176**, 428 (2001).

[77] A. Samman, S. Gebremariam, L. Rimai, X. Zhang, and J. Hangas, J. Appl. Phys. **87**, 3101 (2000).

[78] C. -M. Zetterling, M. Östling, N. Nordell, O. Schön, and M. Deschler, Appl. Phys. Lett. **70**, 3549 (1997).

[79] C.-M. Zetterling, M. Östling, K. Wongchotigul, M. G. Spencer, X. Tang, C. I. Harris, N. Nordell, and S. S. Wong, J. Appl. Phys. **82**, 2990 (1997).

[80] T. Hashizume, E. Alekseev, D. Pavlidis, K. S. Boutros, and J. Redwing, J. Appl. Phys. **88**, 1983 (2000).

[81] N. Onojima, J. Kaido, J. Suda, T. Kimoto, and H. Matsunami, Mater. Sci. Forum **457–460**, 1569 (2004).

[82] N. Onojima, J. Kaido, J. Suda, and T. Kimoto, phys. stat. sol. (c) **2**, 2643 (2005).

Chapter 2

Experimental Details of Crystal Growth

2.1 Introduction

The 4H-AlN is the metastable phase of AlN. This indicates that the energy state of 4H-AlN is higher than that of 2H-AlN and 4H-AlN will be changed into 2H-AlN by overcoming an energy barrier, the value of which has still been unknown. When the growth is carried out at a higher temperature, the grown AlN will more progressively tend to have 2H structure. It is assumed that lower growth temperature is favorable for faultless 4H-AlN growth. In most cases, epitaxial growth of group–Ⅲ nitrides (Ⅲ–Ns) is accomplished via metal-organic vapor phase epitaxy (MOVPE) techniques [1–4]. However, the MOVPE growth generally requires a high temperature at the range of 1000–1200°C for AlN growth and the very high temperature of 1600°C has been reported for growth of AlN with low dislocation density [5]. In fact, Akasaka *et al.* have reported that AlN layers grown on both nonpolar 4H-SiC $(11\bar{2}0)$ and $(1\bar{1}00)$ by MOVPE have normal 2H structure [6].

In this study, molecular-beam epitaxy (MBE) is employed for isopolytypic growth of 4H-AlN on nonpolar 4H-SiC. By using an MBE growth system, thermal decomposition of source materials is unnecessary because of assisting of plasma, resulting in decrease of the AlN growth temperature to the range of 600–1000°C. Not only reduction of growth temperature but also control of growth kinetics is important for isopolytypic epitaxy of the metastable phase. Since there are few tools for the *in-situ* analysis of the growth mode and growth mechanism in MOVPE, the number of studies on growth behavior of Ⅲ–Ns has been very small. In the MBE growth, *in-situ* analysis of crystal growth kinetics and real-time monitoring of transitional surface structure are possible due to incorporated characterization tools in ultra-high vacuum (UHV) [1, 7–9]. From the viewpoint of availability of kinetics observation and control, MBE is an ideal growth method for achievement of isopolytypic high-quality growth of 4H-AlN.

In this chapter, configuration of the MBE system using in this study is presented. Sub-

strate pretreatments for MBE growth established in AlN growth on SiC (0001) are reviewed and the effects of the pretreatments for nonpolar 4H-SiC substrates is discussed.

2.2 Molecular-beam Epitaxy for Group-Ⅲ Nitrides Growth

2.2.1 Ultra-high vacuum system

The epitaxial growth of AlN described in this study is carried out using an MBE growth system shown schematically in Fig. 2.1 (EV-1000S, Eiko). The system consists of a growth chamber, a sample-transfer chamber and a sample-exchange chamber. The sample-transfer chamber and sample-exchange chamber separated by gate valves are installed to prevent air from coming directly into the growth chamber when loading and unloading samples. A schematic diagram of the pumping system is presented in Fig. 2.1 (a). The sample-exchange chamber is exhausted by a turbo-molecular pump connected to a rotary pump. The pressure reaches 1×10^{-5} Pa in 1 hour and the ultimate vacuum pressure is 3×10^{-6} Pa. The sample-exchange chamber is equipped with an infrared lump, where samples loaded can be heated to ∼200°C for degassing. The pressure in the sample-transfer chamber is normally lower than 7×10^{-7} Pa, achieved using a sputter ion pump. The growth chamber, shown in Fig. 2.1 (b), is pumped by a turbo-molecular pump connected to a scroll pump, which is accomplished to an oil-free system. The exhaust velocity of the turbo-molecular pump is 1300 l/s and the pressure reaches 4×10^{-8} Pa. The growth chamber is equipped with a liquid nitrogen cryo-shroud, cooled to liquid nitrogen temperature (77K) during growth for adsorption of residual gases. By using the cryo-shroud, the background pressure inside the chamber can be below 6×10^{-9} Pa. During epitaxial growth of AlN, the pressure is 10^{-3} Pa due to the inflow of nitrogen source gas. The growth chamber is equipped with a quadrupole mass spectroscopy (QMS) system, which can detect residual gases in UHV as well as impurity in nitrogen source gas.

2.2.2 Substrate heating and *in-situ* reflection high-energy electron diffraction systems

The SiC substrates used in this study are installed into a substrate holder. The substrate holder is made of molybdenum (Mo) and heated up to 1000°C by a tantalum (Ta) heater placed behind it. The substrates are secured to the holder using a retaining ring which is made of tungsten (W). A diffuser plate made of pyrolytic boron nitride (PBN) is used for improved heating uniformity. The substrate temperature (T_{sub}) is measured by a thermocouple located just behind the substrate. Although the actual substrate temperature may be lower than the thermocouple temperature, the measured temperature without any

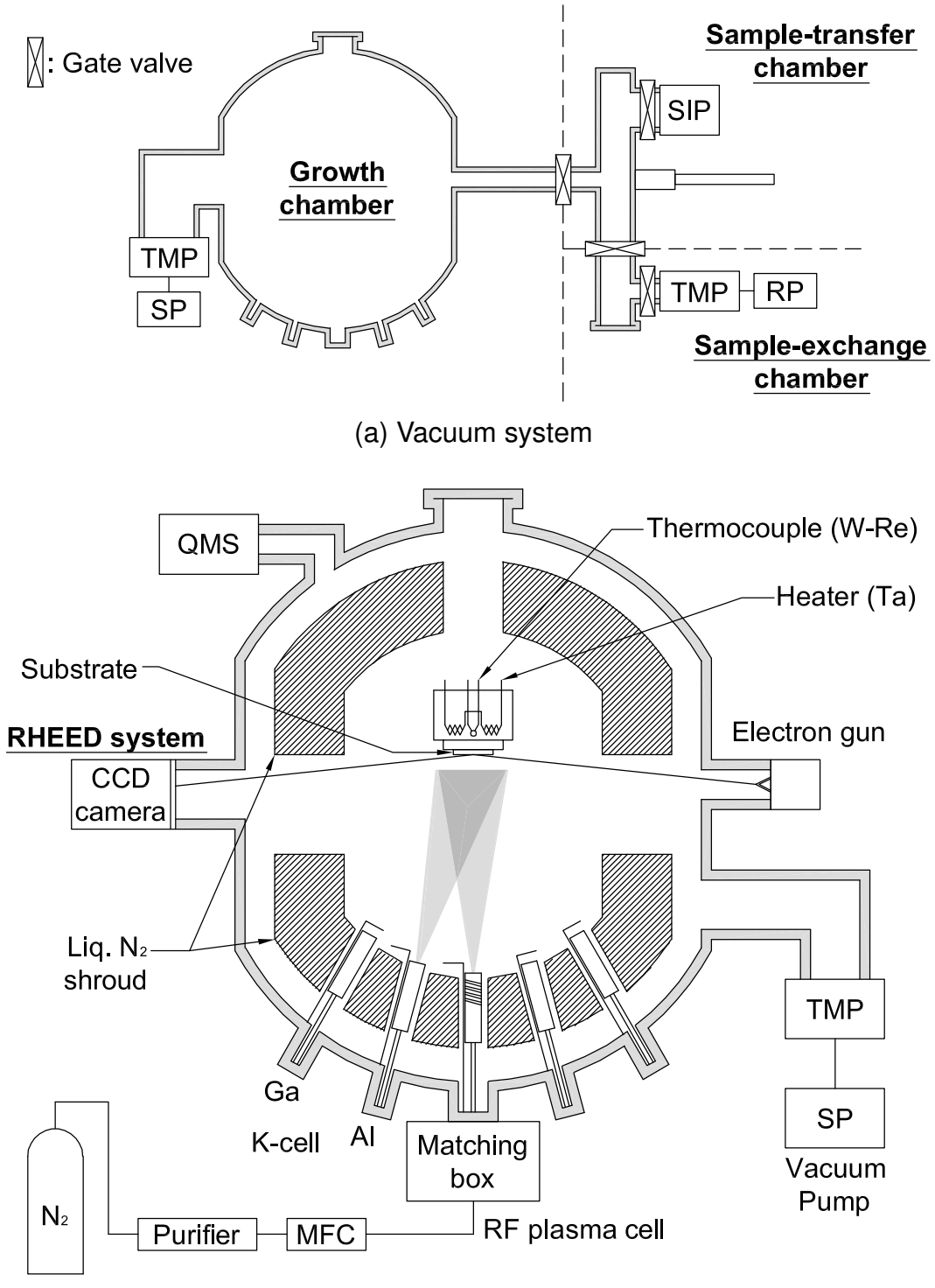

Figure 2.1: Schematic view of MBE (a) vacuum system and (b) growth chamber used in this study.

corrections is given as the substrate temperature in this study.

An MBE growth system which operates in UHV allows incorporation of several surface monitoring tools. Among the analytical tools available, reflection high-energy electron diffraction (RHEED) has contributed advances in epitaxial technology and improvements in the quality of epitaxial layers. The electron beam emitted from a sharpened filament is diffracted at the surface atoms of sample, and builds up a diffraction pattern on a fluorescent screen. In this study, an electron beam accelerated by 20 kV is applied for RHEED observation. RHEED monitoring is conducted for *in-situ* analyses of the kinetics in AlN growth, and observed patterns are recorded through a 16-bit gradient Charge Coupled Device (CCD) camera. The monitoring of diffracted intensities is carried out by using a real-time image processing system (kSA400 RHEED system, k-Space Associates).

2.2.3 Effusion cells and radio-frequency plasma source

The growth chamber is equipped with effusion cells for elemental aluminum (Al) and gallium (Ga) evaporation and a radio-frequency (RF) plasma cell for producing active nitrogen (N^*). Each cell has an individual shutter blade made of Ta. The RF plasma cell is mounted perpendicularly to substrates and Al and Ga effusion cells are installed with 35°-tilting to the perpendicular of substrates.

Elemental Al of 6N (99.9999%) purity (E&M cooperation) and Ga of 7N (99.99999%) purity (E&M cooperation) are evaporated from Knudsen effusion cells (Applied EPI). Al and Ga metals are held in 200g-SUMO^{TM} effusion cell crucibles made of PBN. The SUMO effusion cell is developed to offer increased charge capacity without sacrificing material quality or cell performance. The crucible is comprised of a cylindrical reservoir with a small tapered orifice, thereby combining large capacity with excellent flux uniformity. For the Al effusion cell, the crucible includes a wide lip extending into a thermally isolated cold zone to prevent Al creep which can damage the cell. The Al and Ga effusion cells have different heater configurations. For use with Al, a cold-lipped SUMO effusion cell, which is operated with the bottom filament only, is used. This cell is designed to prevent overflow caused by Al wetting of the PBN crucible under nitrogen atmosphere. The heat shielding and heater filament are carefully positioned to allow efficient heating of the crucible body while maintaining an intentional cold lip. For use with Ga, a hot-lipped SUMO cell with a dual filament configuration is employed since metallic Ga tends to recondense at the crucible orifice. The two independent heater filaments provide a more efficient heating configuration, which allows the cell to operate at a lower power while still ensuring optimal heating of the crucible orifice

Intensities of the Al and Ga beam fluxes on the substrate surface are measured by a nude ion gauge located just below the sample. The operating temperature for the Al and Ga effusion cells during growth ranged from 1080–1150°C and 900–950°C, respectively. Temperature dependence of the beam equivalent pressure (BEP) of Al and Ga effusion cells

measured with the ion gauge are shown in Fig. 2.2. Epitaxial growth of AlN in this study required precise control of the Al beam flux intensity. The operating temperature for the Al effusion cell is controlled by a PID temperature control system (EC5700, Ohkura) and the temperature is stabilized within ±0.3°C.

As for a source to produce active nitrogen, an RF plasma cell is employed. A microwave of 13.56 MHz is applied for nitrogen activation. The plasma unit (UNI-Bulb RF Plasma Source, Applied EPI) is fitted with an optical emission detector that gives a photo-current reading correlated with the active nitrogen flux intensity. Nitrogen gas of 6N (99.9999%) purity (Extra Grade, Sumitomo Seika Chemicals) first passed through a gettering-type purifier (PS10A-MC1-N, SAES Getters) and then on to the RF plasma cell. The flow rate of nitrogen gas is typically controlled to 0.75 sccm by a mass flow controller (MFC) and the applied RF power is set to 300 W in this study. As shown in Fig. 2.3, the emission spectrum from the RF plasma cell is dominated by atomic transition peaks at 745.2, 821.2 and 869.2 nm.

2.3 Characterization Method

Surface features, such as the step structure and surface roughness of SiC substrates and AlN epilayers, is characterized using a Tapping-Mode atomic force microscopy (AFM) (Dimension 3100/Dimention V, Veeco Instruments) with silicon tips with ∼100 Å end-tip diameter (Nanosensors PointProbe PPP-NCHR). Crystalline quality, lattice constants and structural defects in the epilayer are investigated by high-resolution x-ray diffraction (HRXRD) and high-resolution transmission electron microscopy (HRTEM). The XRD measurements are performed with a triple crystalline x-ray diffractometer (SLX-2000, Rigaku). A copper (Cu) $K_{\alpha 1}$ line ($\lambda = 1.540562$ Å) is selected using a channel-cut double crystal germanium (Ge) (220) monochromator. The plan-view and cross-sectional TEM observations are performed on a microscope with the field-emission electron beam accelerated at 200 kV (JEM-2100F, JEOL) and 300 keV (H-9000NAR, Hitachi High-Technologies). The high-resolution energy-dispersive x-ray spectroscopy (EDS) and the high-angle annular dark-field (HAADF) for composition analysis of AlN/AlGaN multiple quantum well (MQW) nanostructure are taken using a scanning TEM (STEM) system (HD-2700, Hitachi High-Technologies). The cathodoluminescence (CL) from AlN is obtained using a single monochromator system (MONOCL3+, Oxford Instruments) combined with scanning electron microscopy (SEM) (JSM-6500F, JEOL). The EDS for analysis of Ga composition in AlGaN is performed using an EDS system (JED-2200F, JEOL) combined with the SEM. The phonon mode of 4H-AlN is characterized by a triple monochromator micro Raman system (T64000, HORIBA) with an Ar^+ laser probe ($\lambda = 488$ nm). The interface properties of AlN/SiC are examined by current-voltage (I–V) and capacitance-voltage (C–V) characteristics using a source measurement unit (model 4200/4210) and a high-frequency CV analyzer (model 590), respec-

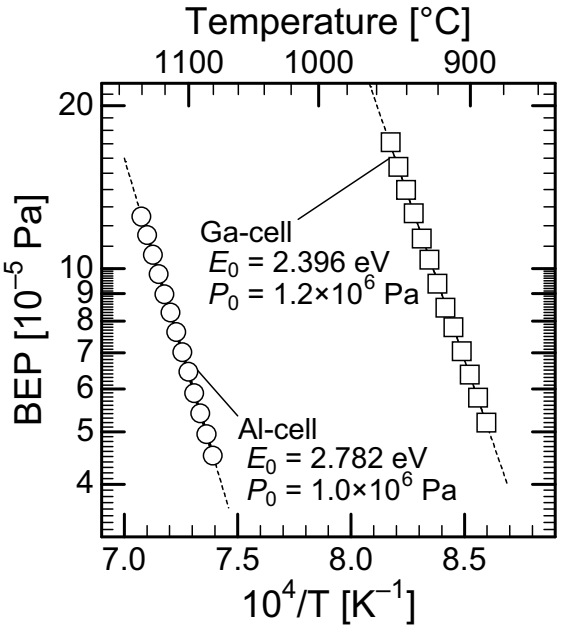

Figure 2.2: The beam equivalent pressure (BEP) of Al and Ga effusion cells in the Arrhenius plot. The BEP is fitted to the function of $P_{\mathrm{BEP}} = P_0 \exp(-E_0/kT)$.

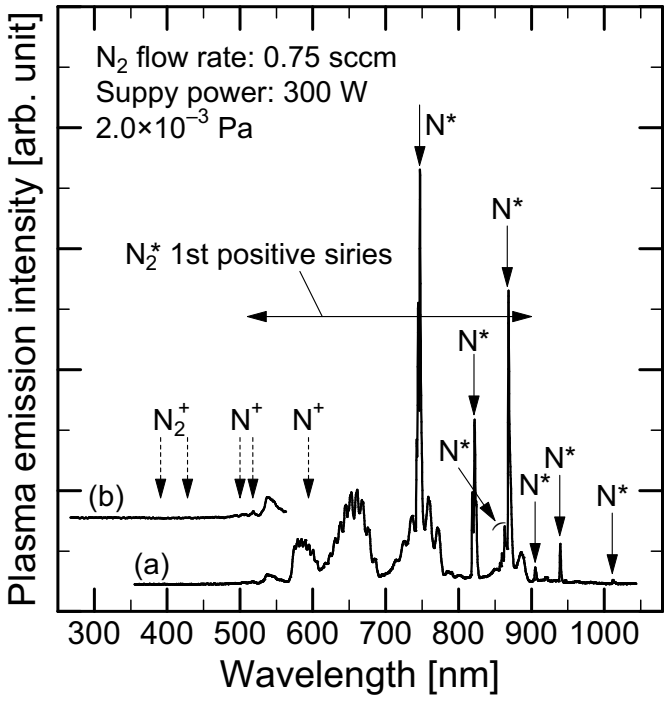

Figure 2.3: Typical emission spectra of nitrogen plasma activated by the RF cell. The main spectrum (a) was measured in the wavelength range of 350–1040 nm and the spectrum (b) was measured in the wavelength range of 200–870 nm with another spectrometer (partly shown). The arrows indicate the peak position where the dashed arrows mean absence.

tively, which are installed as a characterization system (4200-SCS, Keithley).

2.4 Preparation of nonpolar SiC Substrates

2.4.1 Chemical mechanical polishing and HCl-gas etching

Surface pretreatments are important techniques in epitaxial growth and device fabrication to realize high-performance devices. In the case of 6H- and 4H-SiC $(0001)_{\mathrm{Si}}$ faces, it has been reported that HCl-gas etching and chemical mechanical polishing (CMP) are effective surface pretreatments [10, 11]. Figure 2.4 shows the surface morphologies of 6H-SiC (0001) before and after treatments. A number of polishing scratches were observed in the mechanical-polished SiC wafers (Fig. 2.4 (a)). By CMP treatments for the mechanical-polished samples, step-and-terrace structures are obtained where steps with one Si–C bilayer height are observed [10]. When 6H- or 4H-SiC (0001)-vicinal substrates with the off-cut direction toward $\langle 1\bar{1}00\rangle$ are etched in an HCl/H_2 gas mixture, micro step bunching occurs and 6- or 4-bilayer-height steps are formed as shown in Fig. 2.4 (b) [11]. In this study, these treatments are applied to nonpolar 4H-SiC $(11\bar{2}0)$ and $(1\bar{1}00)$ surfaces.

The effect of CMP and HCl gas etching treatments for 4H-SiC nonpolar faces was investigated. For substrates with both $[11\bar{2}0]$ and $[1\bar{1}00]$ orientations, two sets of samples were prepared; one set was treated with only mechanical polishing (MP) (designated MP samples) and the other was treated with CMP following MP (designated CMP samples). The samples were put on a SiC-coated graphite susceptor and etched in an HCl/H_2 gas mixture in an induction-heated atmospheric-pressure horizontal cold-wall reactor (Fig. 2.5) at 1300°C for 10 min. The flow rates of HCl and H_2 were 3 sccm and 1 slm, respectively, where the density of HCl is 0.3%. The etching rates of SiC substrates were measured using SiO_2 masks. It was found that the etching rates for the $(11\bar{2}0)$ and $(1\bar{1}00)$ surfaces were almost equal, 13 ± 2 nm/min.

4H-SiC $(11\bar{2}0)$ substrates

Figure 2.6 (a) and (b) show the surface morphologies of 4H-SiC $(11\bar{2}0)$ MP samples before and after gas etching, respectively. A number of polishing scratches were observed in the MP samples before gas etching (Fig. 2.6 (a)), and the root-mean-square (RMS) roughness value before etching was 0.71 nm. The morphologies of the MP samples after gas etching (Fig. 2.6 (b)) were very wavy and some hollows were observed, although the polishing scratches with sharp edges faded out. The depth of the hollows is almost the same as that of the scratches ($1 \sim 2$ nm), suggesting that the wavy morphologies are caused by polishing scratches. The RMS value of the gas-etched MP samples was 1.12 nm. Surface morphologies became flat when the etching was employed for a much longer time (100 min as shown in the inset of Fig. 2.6 (b)). Figure 2.7 (a) shows the surface morphology of 4H-SiC $(11\bar{2}0)$ CMP samples before gas etching. The polishing scratches on the MP samples

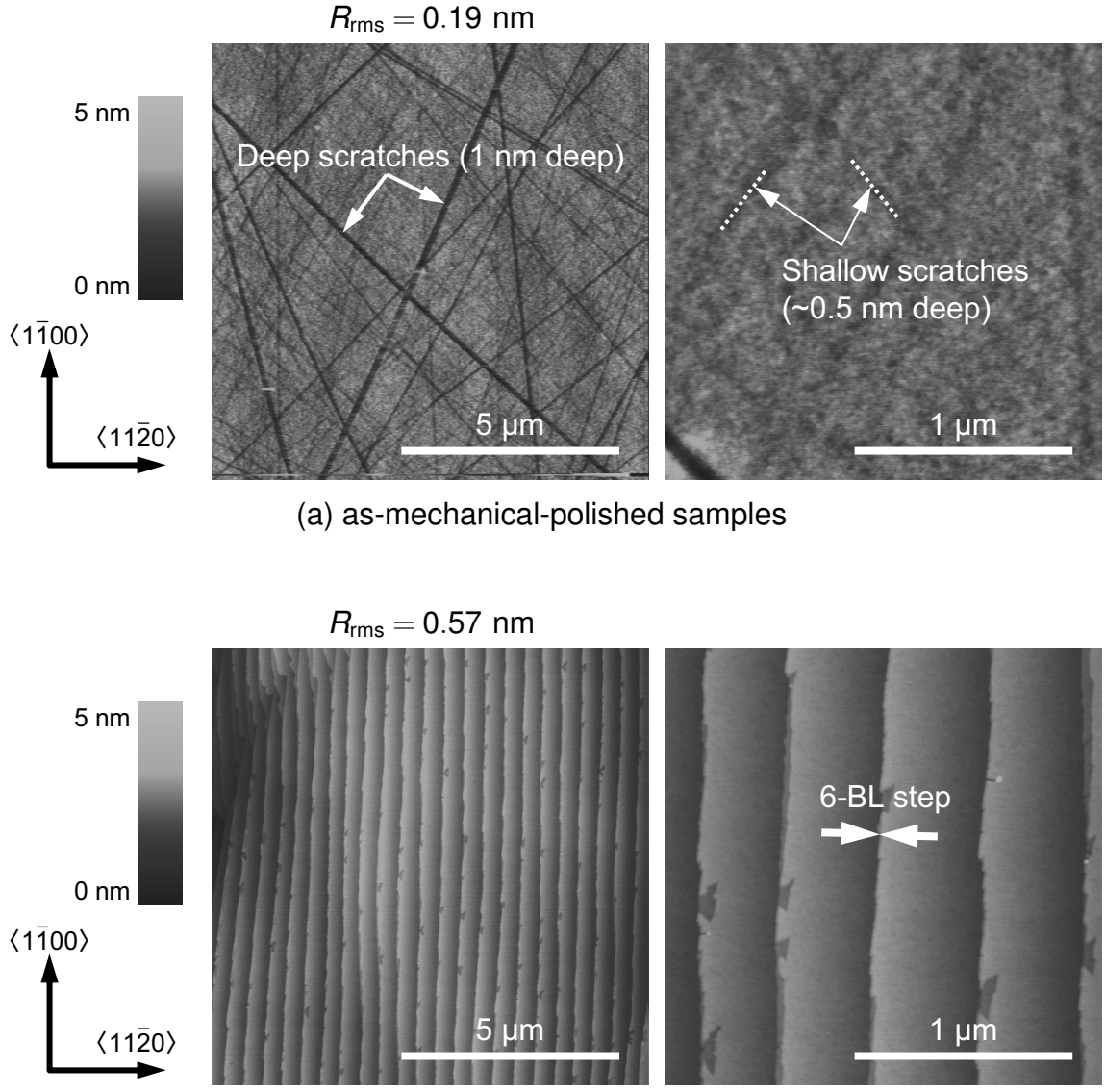

Figure 2.4: Surface morphologies of 6H-SiC $(0001)_{Si}$: (a) as-mechanical-polished samples and (b) HCl-gas-etched samples following CMP [10, 11]. Each of right figures shows a magnified image of the left one.

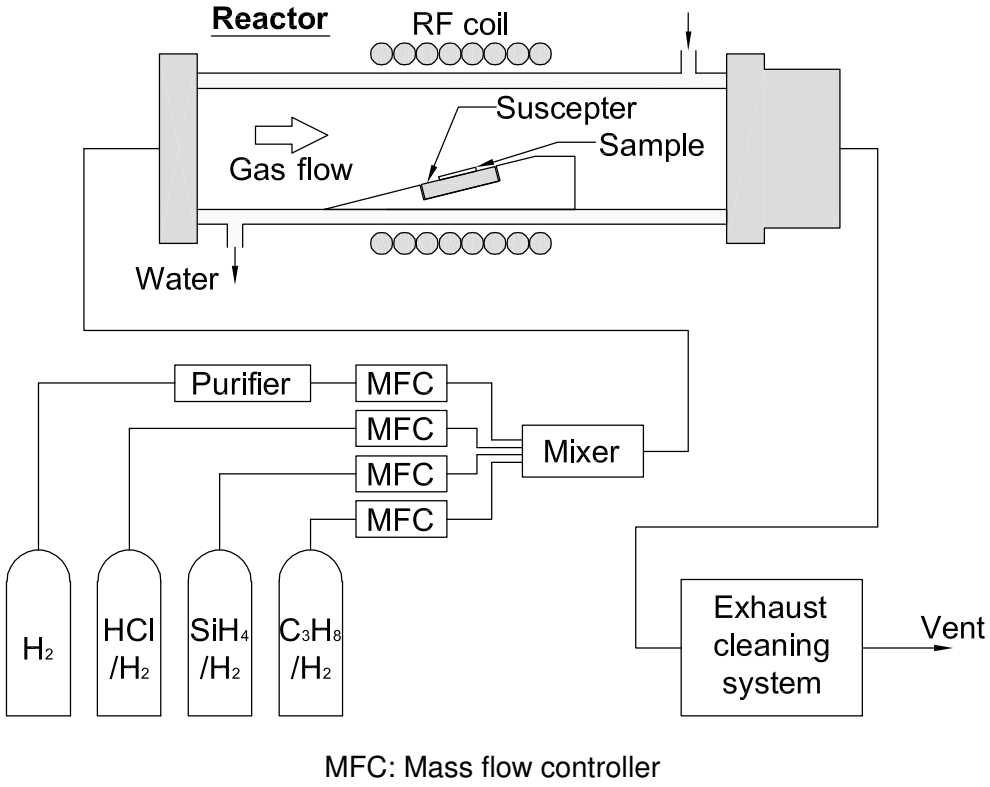

Figure 2.5: Schematic diagram of the cold-wall chemical vapor deposition (CVD) system for HCl gas etching and SiC epitaxial growth.

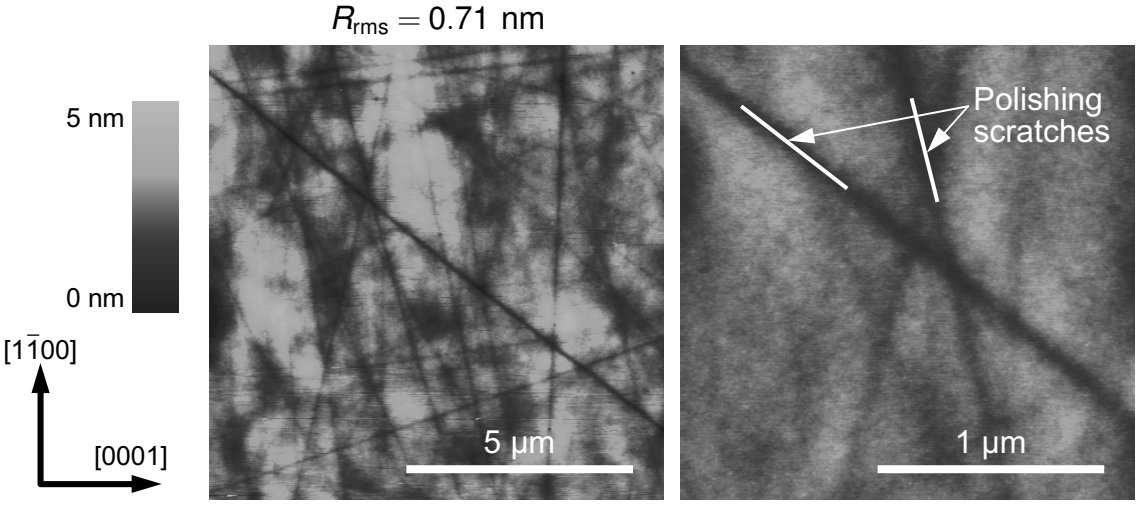

(a) as-received MP samples

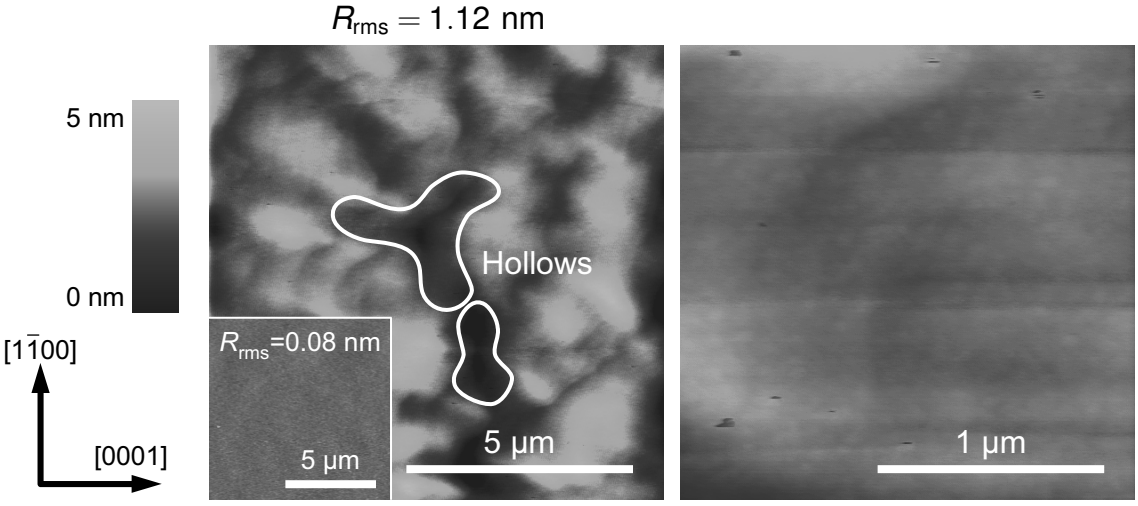

(b) gas-etched MP samples

Figure 2.6: Surface morphologies of 4H-SiC (11$\bar{2}$0): (a) as-received MP samples and (b) gas-etched MP samples. Each of right figures shows a magnified image of the left one. The inset in the left image of (b) shows the morphology of a MP sample etched for 100 min.

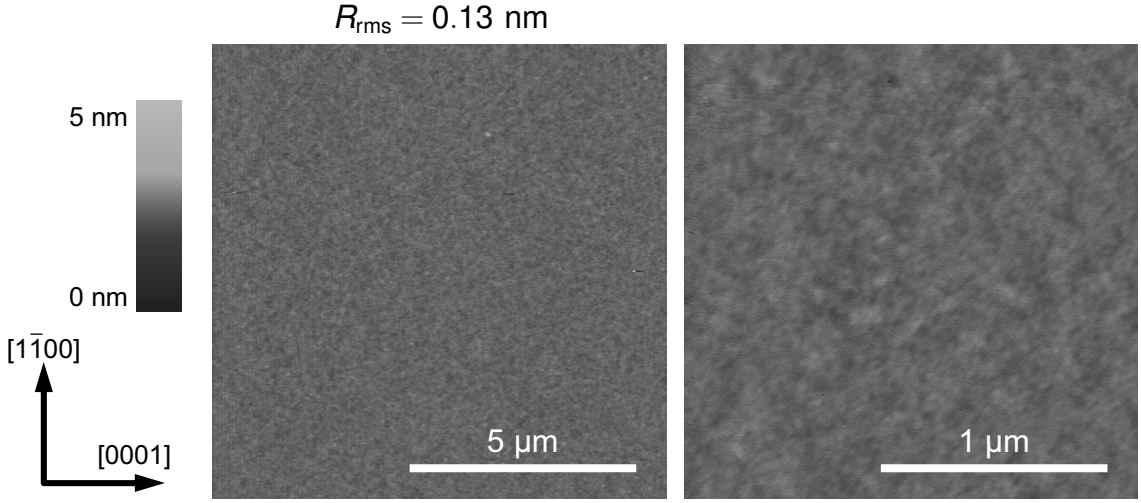

(a) as-received CMP samples

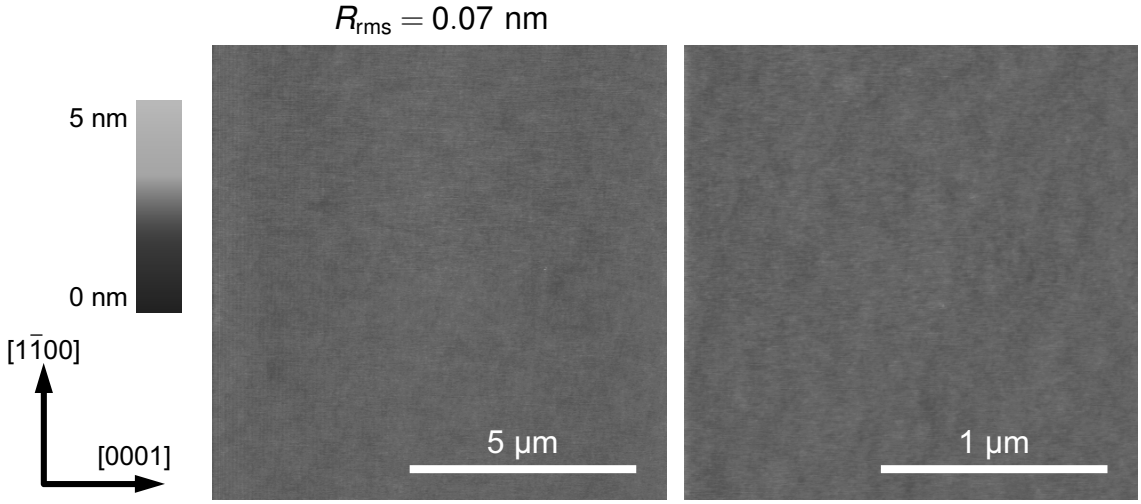

(b) gas-etched CMP samples

Figure 2.7: Surface morphologies of 4H-SiC (11$\bar{2}$0): (a) as-received CMP samples and (b) gas-etched CMP samples. Each of right figures shows a magnified image of the left one.

were removed by CMP treatments and the morphologies exhibited flat surfaces. The RMS roughness value of CMP samples before etching was 0.13 nm. Figure 2.7 (b) shows the surface morphology of gas-etched 4H-SiC $(11\bar{2}0)$ CMP samples. The RMS roughness value of the gas-etched CMP samples was 0.07 nm. The reduction of the RMS roughness values indicates that the gas etching effectively removes micro roughness which was formed by the CMP treatment. It should be noted that atomic steps were not observed in any of the $(11\bar{2}0)$ samples within AFM resolution limits.

4H-SiC $(1\bar{1}00)$ substrates

The surface morphology of 4H-SiC $(1\bar{1}00)$ MP samples before gas etching is shown in Fig. 2.8 (a), where a high density of polishing scratches was observed. Figure 2.8 (b) shows the surface morphology of 4H-SiC $(1\bar{1}00)$ MP samples after gas etching. Although the polishing scratches were effectively removed, a number of macro steps along the $[11\bar{2}0]$ direction were observed, the typical height of which was ∼2 nm. Atomic steps were observed between the macro steps, indicating that the etching process progressed in a step-flow mode and macro step bunching occurred toward the $\langle 0001 \rangle$ directions. On the other hand, the morphologies of as-polished $(1\bar{1}00)$ CMP samples exhibited very flat surfaces with blurred atomic steps as shown in Fig. 2.9 (a). Since the atomic steps were arranged unidirectionally and evenly spaced apart on the surface, these steps are related to an unintentional misorientation of the $(1\bar{1}00)$ substrates (∼0.1°). Figure 2.9 (b) shows the morphology of the gas-etched CMP sample processed from the sample shown in Fig. 2.9 (a). The gas-etched CMP samples have better-formed steps than the as-polished CMP samples, which have the same interval and in-plane direction of the steps. The height of the steps in the gas-etched CMP samples was 2.7 Å, which corresponds to the lattice spacing between 4H-SiC $(1\bar{1}00)$ planes $(=\frac{\sqrt{3}}{2}a = 2.66$ Å), indicating that step bunching does not occur. Given the complete absence of step bunching in the scratch-free CMP samples, the step bunching observed for the gas-etched MP samples is attributed to polishing scratches. The probable origin of step bunching in the MP samples is a higher etching rate of the $\{0001\}$ planes which comprise the scratch sidewalls (relative to $(11\bar{2}0)$), resulting in the appearance of $\{0001\}$ facets as macro steps.

Discussion

Atomic steps were clearly observed on the 4H-SiC $(1\bar{1}00)$ CMP samples as well as the MP samples, while not observed for any of the 4H-SiC $(11\bar{2}0)$ samples. The formation of a step-and-terrace structure is suggested that the plane forming the terraces is stable and surface atoms are removed from the step edges rather than the terraces, that is, the $(1\bar{1}00)$ plane is more stable in the gas-etching ambient than the $(11\bar{2}0)$ plane. On the other hand, no atomic steps were observed on the $(11\bar{2}0)$ surface by AFM although the CMP samples before and after gas etching exhibit flat surfaces. Since the noise amplitude of the AFM system is 0.6 Å, 4H-SiC $(11\bar{2}0)$ atomic steps (height $= \frac{1}{2}a = 1.54$ Å) should be detectable if

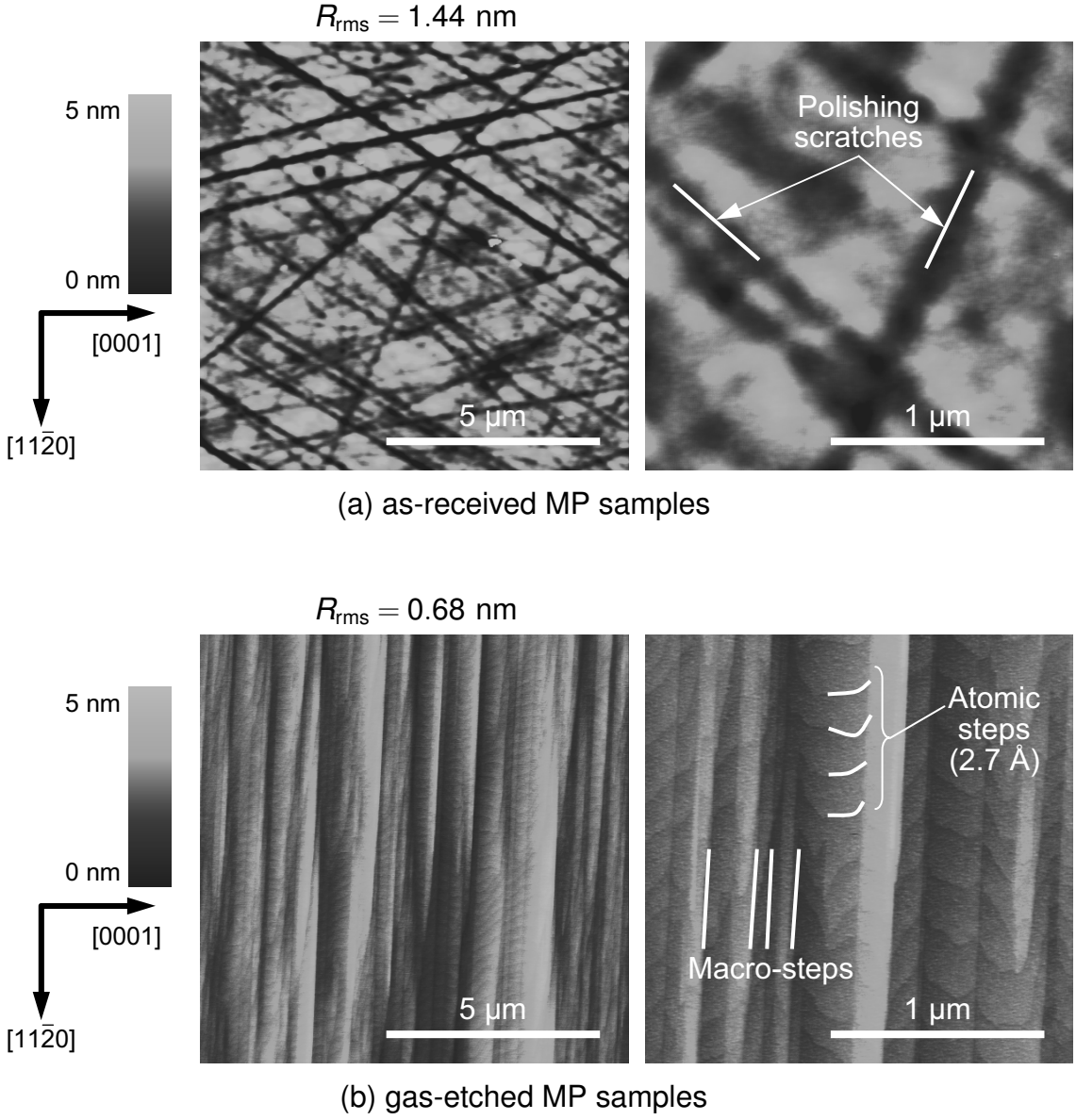

Figure 2.8: Surface morphologies of 4H-SiC ($1\bar{1}00$): (a) as-received MP samples and (b) gas-etched MP samples. Each of right figures shows a magnified image of the left one.

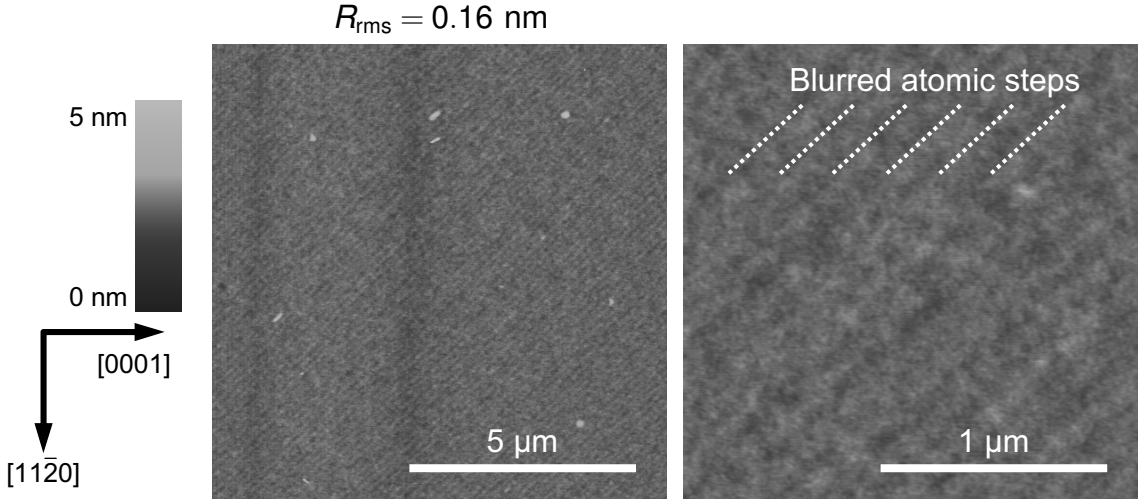

(a) as-received CMP samples

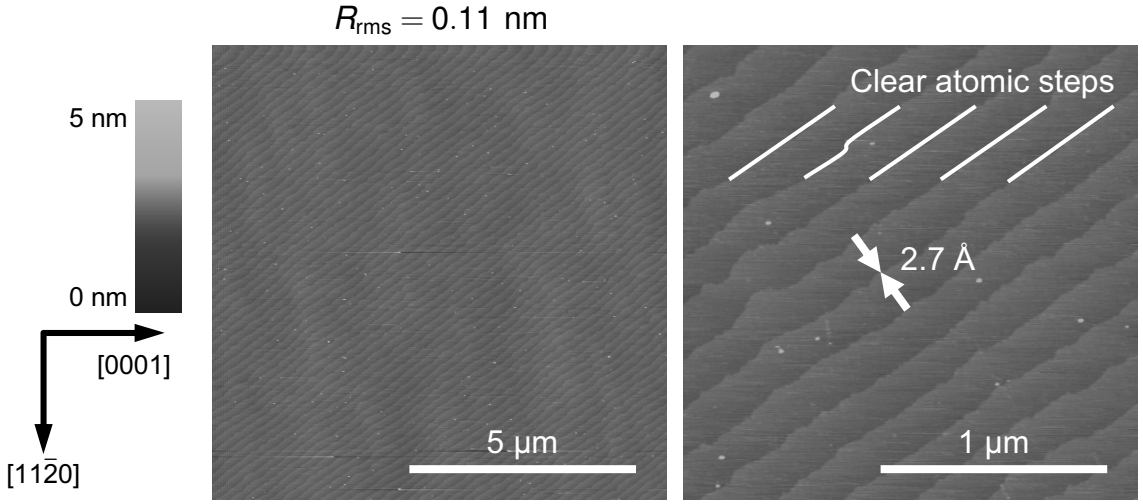

(b) gas-etched CMP samples

Figure 2.9: Surface morphologies of 4H-SiC ($1\bar{1}00$): (a) as-received CMP samples and (b) gas-etched CMP samples. Each of right figures shows a magnified image of the left one.

the interval between steps is larger than 10 nm (calculated from the size of the tip diameter and the step height). It has been reported that homoepitaxial layers grown on 4H-SiC $(11\bar{2}0)$ also exhibit smooth surfaces without observable steps [12, 13]. The surface of SiC $(11\bar{2}0)$ tends to be very flat for both gas etching and SiC homoepitaxial growth processes. One possible explanation for the smooth surfaces observed for 4H-SiC $(11\bar{2}0)$ is the formation of a high density of nanometer-scale facets or islands formed which are too small to resolve by AFM.

2.4.2 *In-situ* Ga deposition and desorption treatment

Growth kinetics at the initial stages is affected by not only the surface morphology of SiC substrates but also the chemical condition. In the case of AlN (0001) growth on SiC (0001), removal of residual oxygen and realization of a 1/3 monolayer (ML) silicon-adsorbed superstructure have been reported to be effective in realization of initial two-dimensional (2D) growth of AlN [14]. A chemically-stable silicate adlayer was formed after the HCl gas etching, which was characterized by *in-situ* x-ray photoelectron spectroscopy (XPS) analysis. Although the silicate adlayer is impossible to decompose at 1000°C in an UHV, *ex-situ* HF treatment could successfully remove it from the HCl-gas-etched surface. However, a few oxygen atoms still remained on the surface treated with HF due to the adsorption of oxygen atoms during transfer through the air. An additional treatment, *in-situ* Ga deposition and desorption process, was effective to eliminate those residual oxygen atoms [15, 16] and a multiple treatment was more valid in particular [14]. In this procedure, the following reaction process proceeds [16, 17];

$$SiO_2 + 2Ga \longrightarrow SiO \uparrow + Ga_2O \uparrow . \tag{2.1}$$

Figure 2.10 shows the *in-situ* XPS spectra obtained from the HCl-treated, HF-treated and Ga-treated surfaces of 6H-SiC $(0001)_{Si}$ substrates. Since the silicate adlayer was removed by HF treatment, the Si $2p_{3/2}$ peak tended to shift from SiO_2 to SiC. Although the silicate adlayer was removed, the O 1s peak was still observed due to the sticking of oxygen atoms to the surface. The residual oxygen was removed by Ga treatment, leading to the lowering of the O 1s peak intensity.

To examine the effect of these treatments for nonpolar 4H-SiC surfaces, *in-situ* XPS measurements were performed for 4H-SiC $(11\bar{2}0)$ and $(1\bar{1}00)$ treated with HCl gas etching, HF solution, and Ga deposition and desorption process. The results are shown in Fig. 2.11, and the integral intensity of the O 1s peaks and the position of the Si $2p_{3/2}$ peaks for the treatments on each surface were summarized in Fig. 2.12. For both $(11\bar{2}0)$ and $(1\bar{1}00)$ surfaces, the O 1s peak intensities were smaller than that on the (0001) surface, indicating that the residual oxygen atoms on nonpolar surfaces were less than those on the (0001) surface. In the HF treatment (compared with HCl-treated and HF-treated samples in Figs. 2.11 and 2.12), a shift of the Si $2p_{3/2}$ peak was observed on the $(1\bar{1}00)$ surface as

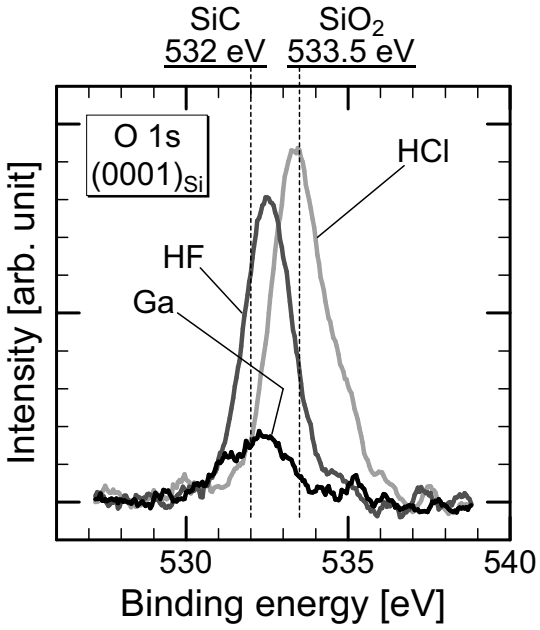

(a) O 1s from (0001)

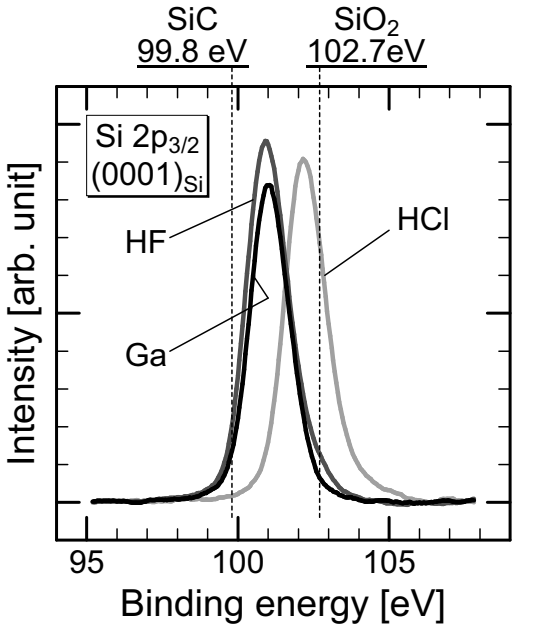

(b) Si $2p_{3/2}$ from (0001)

Figure 2.10: XPS spectra of (a) O 1s and (b) Si $2p_{3/2}$ peaks obtained from the HCl-treated (light gray line), HF-treated (dark gray line) and Ga-treated (black line) surfaces of 4H-SiC (0001).

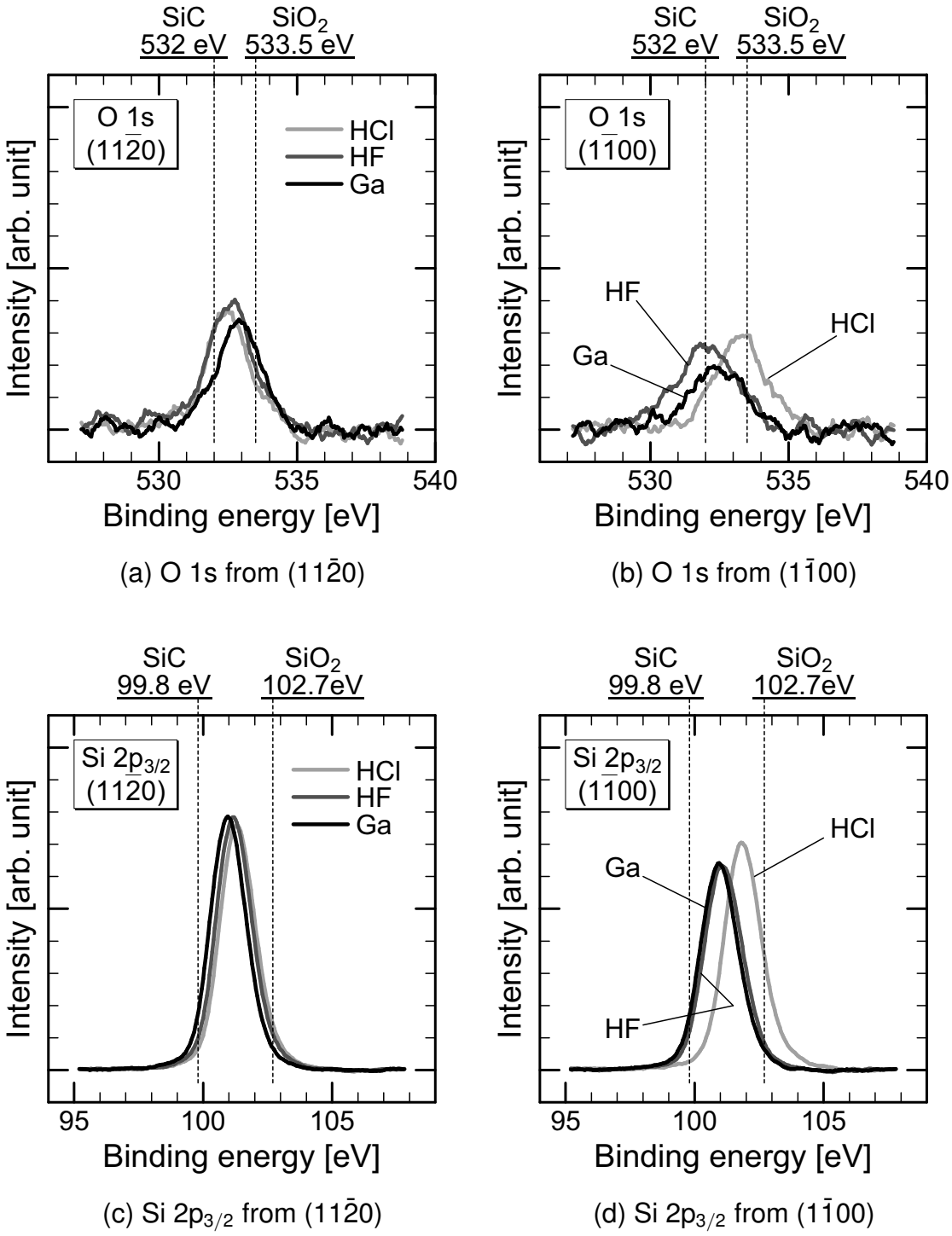

Figure 2.11: XPS spectra obtained from the HCl-treated (light gray line), HF-treated (dark gray line) and Ga-treated (black line) surfaces of 4H-SiC (11$\bar{2}$0) [(a), (c)] and (1$\bar{1}$00) [(b), (d)]. O 1s and Si $2p_{3/2}$ peaks are shown in (a), (b) and (c), (d), respectively. The scales of the intensity for O 1s [(a), (b)] and for Si $2p_{3/2}$ [(c), (d)] are the same as those shown in Fig. 2.10.

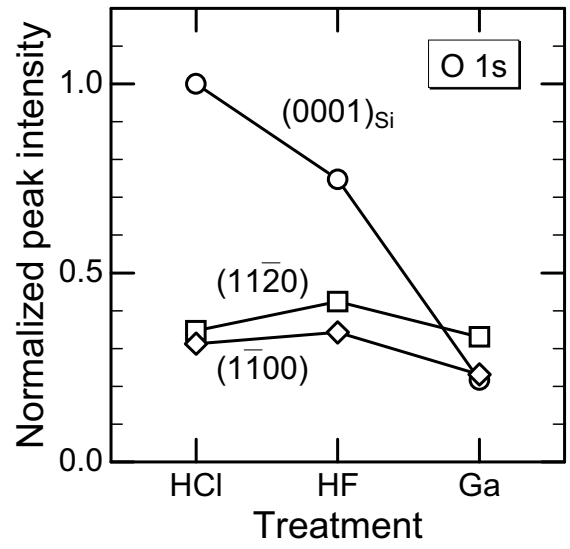

(a) O 1s peak intensity

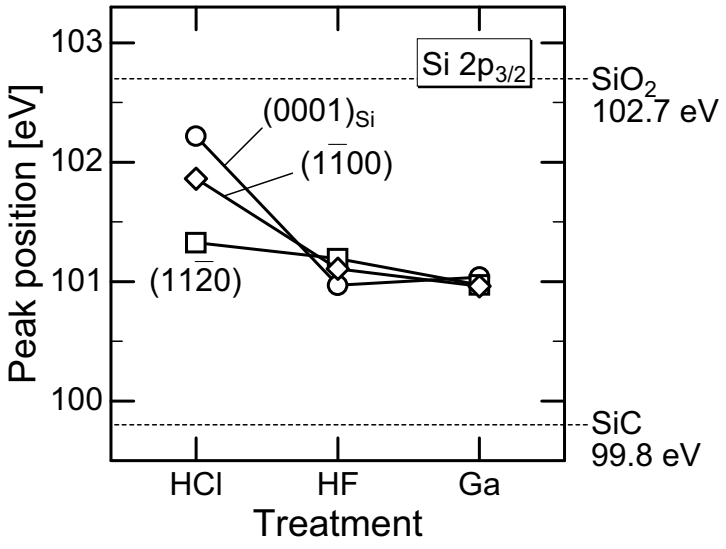

(b) Si $2p_{3/2}$ peak position

Figure 2.12: (a) the integral intensity of the O 1s peaks and (b) the position of the Si $2p_{3/2}$ peaks of XPS spectra taken from the HCl-treated, HF-treated and Ga-treated surfaces of 4H-SiC (0001) (circle), (11$\bar{2}$0) (square) and (1$\bar{1}$00) (rhombus). In (a), the peak intensities are normalized by that of HCl-treated (0001) surface.

the case of (0001), and a slight shift was seen on the $(11\bar{2}0)$ surface. In the Ga treatment (compared with HF-treated and Ga-treated samples in Figs. 2.11 and 2.12), a decrease of the O 1s peak was observed on the $(1\bar{1}00)$ surface, and a slight decrease was seen on the $(11\bar{2}0)$ surface. From these results, the effectivity of the treatments for clean surfaces of 4H-SiC is concluded; $(11\bar{2}0) < (1\bar{1}00) < (0001)$. In the observation of RHEED patterns before and after Ga treatment for $(11\bar{2}0)$ and $(1\bar{1}00)$ surfaces, the diffraction spot became bright, indicating that the Ga treatment is effective for a 4H-SiC nonpolar surface.

The difference in the treatment effectivity between $(11\bar{2}0)$ and $(1\bar{1}00)$ surfaces may be understood considering the configuration of Si and C atoms on 4H-SiC surfaces. Figure 2.13 shows a cross-sectional view of atomic arrangements for the most stable surface for hydrogen-terminated nonpolar 4H-SiC along [0001] direction, which are expected to form in HCl treatment [18]. The $(11\bar{2}0)$ surface is exactly normal to (0001). In contrast, the $(1\bar{1}00)$ surface consists of atomic facets tilted to [0001] and $[000\bar{1}]$. It is believed that the crystal faces tilted toward [0001] contribute bonding with oxygen atoms resulting in the formation of the silicate adlayer or adsorption of oxygen atoms. Further investigation such as low-energy electron diffraction (LEED) and scanning tunneling microscopy (STM) observations will reveal the structure of atomic bonding to oxygen.

2.4.3 Discussion and experimental procedures for growth

Gas-etching treatments are effective to remove polishing scratches and reduce surface roughness on SiC $(11\bar{2}0)$. For $(1\bar{1}00)$ surface, well-formed step-and-terrace structures are obtained after gas etching only if the substrate is first treated by CMP to remove scratches. *In-situ* Ga deposition and desorption process is effective to remove residual oxygen in both nonpolar $(11\bar{2}0)$ and $(1\bar{1}00)$ surfaces of SiC as the case for a (0001) surface.

In this study, based on the results described in Section 2.4, the growth of AlN and AlGaN is carried out in the procedures as follows. 4H-SiC $(11\bar{2}0)$ and $(1\bar{1}00)$ on-axis wafers manufactured at CREE Inc. and SiXON Inc. are used as substrates. The substrates are immersed in a H_2SO_4/H_2O_2 mixture at 80°C. Then the substrates are dipped in HCl, aqua regia and HF solutions, rinsed by deionized water and blown by dry nitrogen. These wet chemical processes are performed before HCl gas etching and MBE growth. The substrates are treated by HCl gas etching in the conditions as discussed in Section 2.4: the temperature 1300°C, atmospheric pressure, H_2 including 0.3% HCl, flow rate 1 slm and etching time 10 min.

For MBE growth, the substrates treated with HCl gas followed by the wet chemical processes are loaded into the sample-exchange chamber. After the chamber evacuated to 10^{-5} Pa, the substrate is outgassed and then transferred into the growth chamber via the sample-transfer chamber. Figure 2.14 represents a typical procedure for epitaxial growth of AlN. The substrate temperature is raised to 600°C at a ramp rate of 30°C/min. Ga metal is deposited to the substrate at 600°C and then the substrate temperature increases to

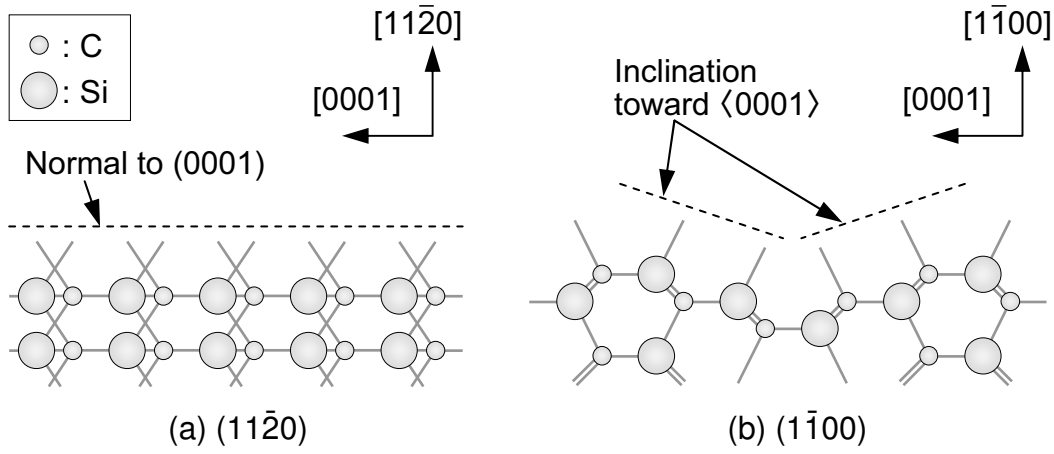

Figure 2.13: Atomic surface structures of 4H-SiC (a) (11$\bar{2}$0) and (b) (1$\bar{1}$00) plane.

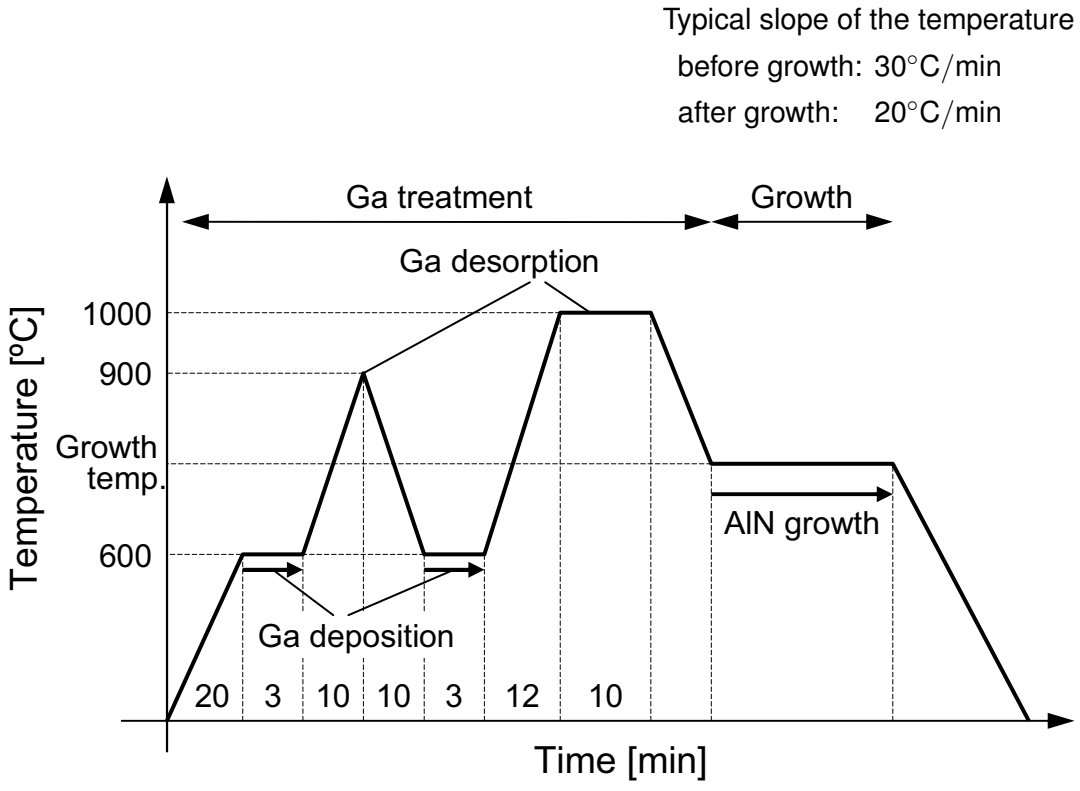

Figure 2.14: Typical procedure for epitaxial growth of AlN used in this study.

1000°C. This Ga deposition and desorption process is performed two times and the substrate temperature is maintained at 1000°C for 10 min after increasing for the second desorption process. Following the Ga treatment, the temperature is decreased to growth temperature. Active nitrogen is generated by the RF plasma cell and maintained for 10 min with the closed shutter to stabilize the gas flow and the growth chamber pressure. After the stabilization of nitrogen plasma, vaporized Al and active nitrogen are introduced simultaneously to the substrate surface. At the end of growth the shutters of the cells are closed simultaneously and then the substrate temperature is lowered to room temperature at a rate of −20°C/min.

2.5 Summary

In this chapter, experimental equipments and pretreatment of SiC surface were explained. The precise control of source material supply is possible in the MBE system for optimization of growth condition.

In SiC substrate preparation, *ex-situ* gas-etching treatments are effective to remove polishing scratches and to reduce surface roughness on SiC $(11\bar{2}0)$. For $(1\bar{1}00)$ surface, well-formed step-and-terrace structures are obtained after gas etching only if the substrate is first treated by CMP to remove scratches. *In-situ* Ga deposition and desorption process is effective to remove residual oxygen in both nonpolar $(11\bar{2}0)$ and $(1\bar{1}00)$ surfaces of SiC as the case for (0001) surface.

In the next chapter, AlN growth on SiC substrates with an atomically flat surface is performed in the MBE system. Impacts of SiC surface treatments and AlN growth conditions are discussed. An etching technique of the SiC surface using high-temperature HCl gas and a precise control of Ⅲ/V ratio in MBE growth are proposed as effective methods for growth of high-quality AlN.

References

[1] K. Balakrishnan, H. Okumura, and S. Yoshida, J. Cryst. Growth **189–190**, 244 (1998).

[2] H. Okumura, K. Balakrishnan, H. Hamahuchi, T. Kaizumi, S. Chichibu, H. Nakanishi, T. Nagatomo, and S. Yoshida, J. Cryst. Growth **189–190**, 364 (1998).

[3] C. D. Lee, V. Ramachandran, A. Sagar, R. M. Feenstra, D. W. Greve, W. L. Sarney, L. S. Riba, D. C. Lock, S. Bai, W. J. Choyke, and R. P. Devaty, J. Electron. Mater. **30**, 162 (2001).

[4] O. Brandt, R. Muralidharan, P. Waltereit, A. Thamm, A. Trampert, H. V. Kiedrowski, and K. H. Ploog, Appl. Phys. Lett. **75**, 4019 (1999).

[5] M. Imura, H. Sugimura, N. Okada, M. Iwaya, S. Kamiyama, H. Amano, and I. Akasaki, J. Cryst. Growth **310**, 2308 (2008).

[6] T. Akasaka, Y. Kobayashi, and T. Makimoto, Appl. Phys. Lett. **90**, 121919 (2007).

[7] M. H. Xie, S. M. Seutter, W. K. Zhu, L. X. Zheng, H. Wu, and S. Y. Tong, Phys. Rev. Lett. **82**, 2749 (1999).

[8] S. M. Seutter, M. H. Xie, W. K. Zhu, L. X. Zheng, H. S. Wu, and S. Y. Tong, Surf. Sci. Lett. **445**, L71 (2000).

[9] N. Fujita, M. Yoshizawa, K. Kushi, H. Sasamoto, A. Kikuchi, and K. Kishino, J. Cryst. Growth **189–190**, 385 (1998).

[10] L. Zhou, V. Audurier, and P. Pirouz, J. Electrochem. Soc. **144**, L161 (1997).

[11] S. Nakamura, T. Kimoto, and H. Matsunami, Appl. Phys. Lett. **76**, 3412 (2000).

[12] J. Takahashi and N. Ohtani, phys. stat. sol. (b) **202**, 163 (1997).

[13] Z. Y. Chen, T. Kimoto, and H. Matsunami, Jpn. J. Appl. Phys. **38**, L1375 (1999).

[14] N. Onojima, J. Suda, and H. Matsunami, Jpn. J. Appl. Phys. **42**, L445 (2003).

[15] R. Kaplan and T. M. Parrill, Surf. Sci. Lett. **165**, L45 (1986).

[16] S. Wright and H. Kromer, Appl. Phys. Lett. **36**, 210 (1980).

[17] U. Starke, phys. stat. sol. (b) **202**, 475 (1997).

[18] Th. Seyller, R. Graupner, N. Sieber, K. V. Emtsev, L. Ley, A. Tadich, J. D. Riley, and R. C. G. Leckey, Phys. Rev. B **71**, 245333 (2005).

Chapter 3

Isopolytypic Growth of Nonpolar 4H-AlN and Reducing Extended Defect Densities

3.1 Introduction

One of the most important challenges in AlN growth on SiC is "polytype mismatch". Group–Ⅲ nitrides (Ⅲ–Ns) form wurtzite (2H) structure in the thermally stable state while SiC forms 4H or 6H structure. Possibility of isopolytypic growth of 4H-AlN on 4H-SiC was demonstrated as a method to overcome the polytype mismatch between AlN and SiC [1]. However, transmission electron microscopy (TEM) studies revealed that the 4H-AlN layers still contain high densities of extended defects such as stacking faults (SFs) and threading dislocations (TDs). Further reduction of the densities of these defects is desirable to develop 4H-AlN grown on 4H-SiC $(11\bar{2}0)$ and $(1\bar{1}00)$ for device applications.

The extended defects originated from incomplete polytype replication from 4H-SiC to AlN. To further improve the AlN epilayer quality it is necessary to enhance the polytype replication process, that is, increase the fraction of AlN which is initially nucleated in the 4H-SiC structure. As clearly seen in the cross-sectional TEM images, SFs originate at the AlN/SiC interface, suggesting that control of the initial growth stage is absolutely crucial.

To enhance the polytype replication process, two key experimental procedures have been introduced. The first is to prepare an atomically flat, damage-free and clean 4H-SiC substrate surface, and the second is careful optimization of the Ⅲ/V ratio during AlN nucleation. Since AlN naturally prefers the 2H structure, lateral overgrowth along the $\langle 0001 \rangle$ direction may result in 2H inclusions as shown in Fig. 3.1, which is regarded as SFs in 4H material. To keep an AlN surface flat during growth prevents lateral growth and thereby leads to high phase purity. Furthermore, substrate surface cleaning is also essential since SiC surface contamination may prevent AlN adatoms from 'sensing' the substrate stacking sequence, resulting in poor polytype replication.

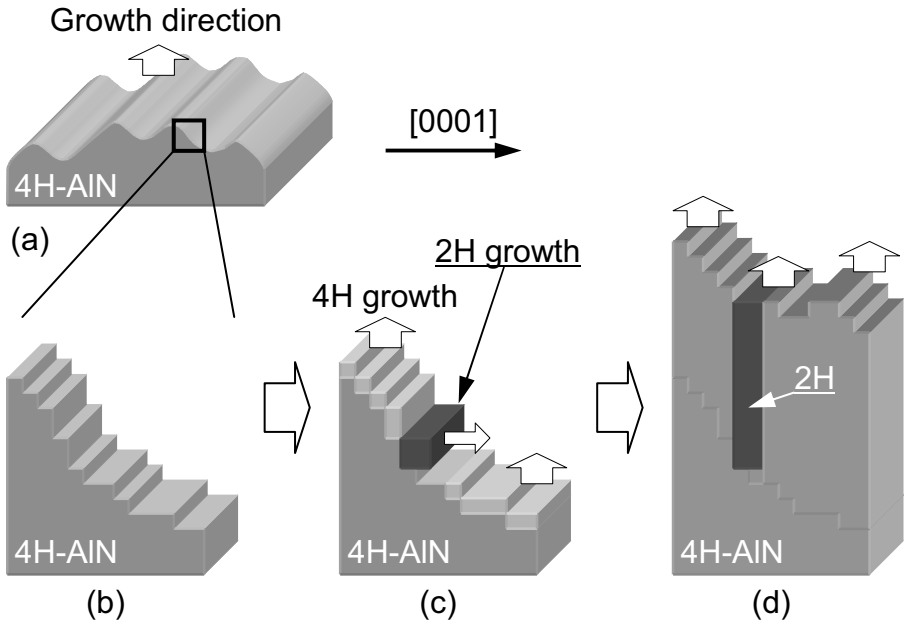

Figure 3.1: Schematics of 2H-inclusion formation in AlN growth on a ridged surface along the ⟨0001⟩ direction: (a) a ridged surface of 4H-AlN layers growing upward, (b) a magnified image of side walls (denoted by the square in (a)) where a side wall is formed with atomic steps, (c) growth of several atomic layers from (b) where 2H-AlN laterally grows in part, and (d) growth of a number of layers from (c) where a 2H inclusion is introduced.

In this chapter, reduction of extended defects contained in 4H-AlN both (11$\bar{2}$0) and (1$\bar{1}$00) nonpolar faces is presented. Impacts of Ⅲ/V ratio during AlN growth on the crystalline quality were investigated. Following the realization of the atomically flat SiC substrates, which is discussed in Section 2.4, and the optimization of Ⅲ/V ratio, growth of AlN (11$\bar{2}$0) and (1$\bar{1}$00) layers was performed under the optimal conditions. The densities of extended defects in 4H-AlN layers were examined by TEM observation.

3.2 4H-AlN (11$\bar{2}$0) Growth on 4H-SiC (11$\bar{2}$0)

3.2.1 Interpretation of reflection high-energy electron diffraction patterns

In-situ reflection high-energy electron diffraction (RHEED) observation is valuable for characterization of crystal structure and growth kinetics [2, 3]. In this section, the relationship between RHEED patterns and crystal structure on (11$\bar{2}$0) surfaces is described. Figure 3.2 shows the theoretical patterns of (11$\bar{2}$0) surfaces of 2H and 4H crystal observed with [1$\bar{1}$00] and [0001] beam incidences. 4H and 2H patterns are different in the intensity of 1$\bar{1}$00 group spots. Figure 3.3 (a) and (b) show RHEED patterns experimentally observed from 4H-SiC substrates. In the image of [0001] beam incidence, three bright streaks of 11$\bar{2}$0, 2$\bar{1}\bar{1}$0 and $\bar{1}$2$\bar{1}$0 and one-third-order dark streaks were observed. Since the one-third-order streaks originate from streaking of 1$\bar{1}$00 group spots as shown in Fig. 3.3 (c), the crystal structure is determined by the intensity of these streaks. In the image of [11$\bar{2}$0] beam incidence, streaks in the first-order Laue zone were observed in addition to those in the zeroth-order Laue zone. The streaks in the first-order Laue zone are equivalent to 1$\bar{1}$0l group and the stacking periodicity along [0001] appears in this line as shown in Fig. 3.3 (d). The streaks indicated by white arrows in Fig. 3.3 (b) show the 4H structure of SiC substrates. From the RHEED patterns and the interpretation, the crystal structure was determined as average information in the area of the electron beam spot (1-mm×5-mm-ellipse). In the RHEED patterns of AlN layers grown under Al-rich conditions shown in Fig. 3.3 (e) and (f), weak half-order reconstruction streaks along all azimuths at growth temperature of 750°C, which become strong with cooling. Since the reconstruction patterns disappeared with heating at 1000°C for 1 h, it is speculated that the reconstruction originate from the Al adatoms as the case of 4H-AlN (1$\bar{1}$00) [4].

3.2.2 Optimization of Ⅲ/V ratio

In epitaxial growth of compound semiconductors, the supply ratio of materials greatly affects the crystalline quality. In GaN (0001) growth, metal Ga bilayer is formed on a GaN surface under Ga-rich conditions and contributes migration enhancement of Ga atoms, leading to the realization of flat growth surfaces [5]. To obtain flat growth surfaces, opti-

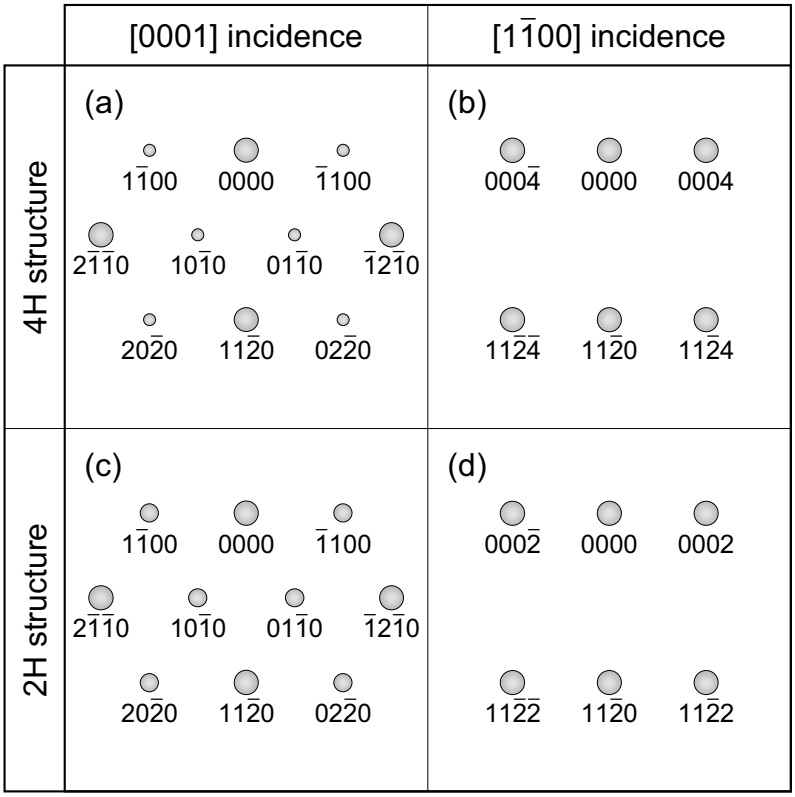

Figure 3.2: Theoretical RHEED patterns of (11$\bar{2}$0) surface of 4H crystal [(a), (b)] and 2H crystal [(c), (d)]. (a), (c) are observed in beam incident geometry parallel to [0001] direction, and (b), (d) parallel to [1$\bar{1}$00] direction.

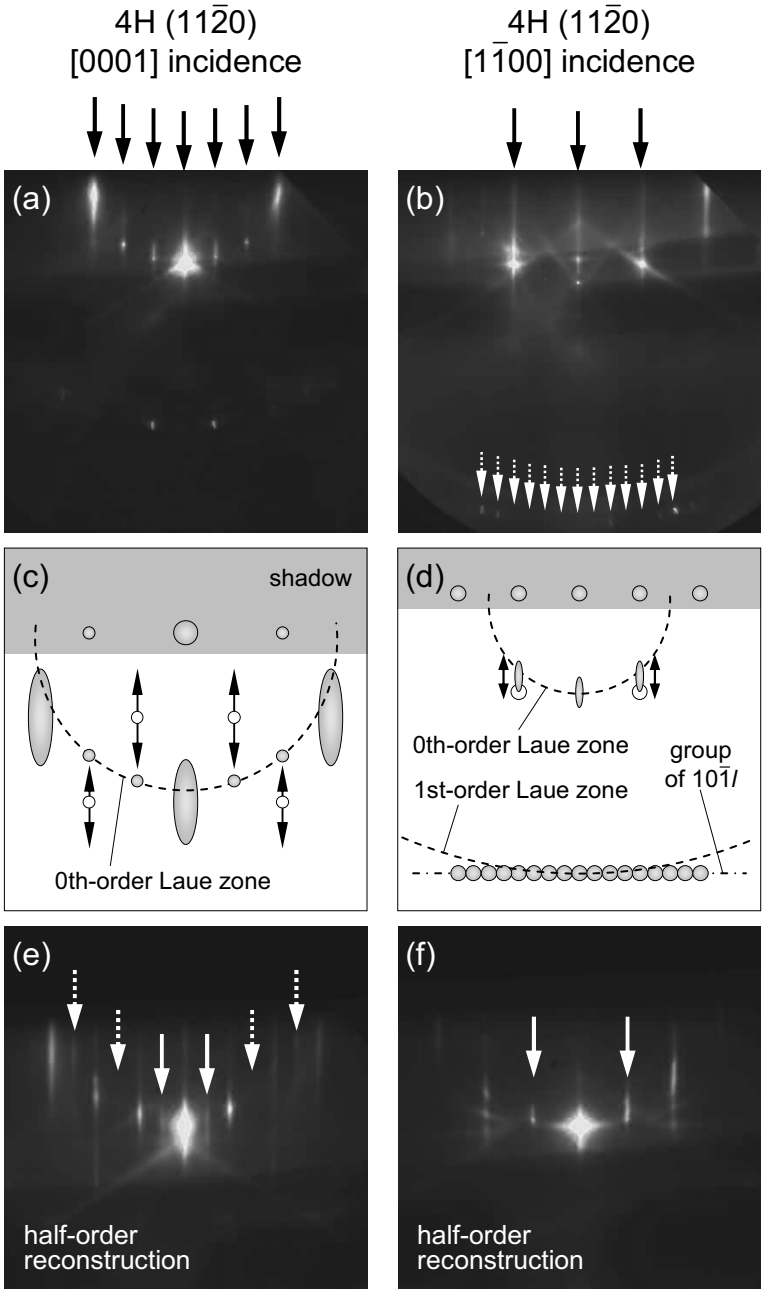

Figure 3.3: RHEED patterns experimentally observed on 4H-SiC (11$\bar{2}$0) [(a), (b)] and 4H-AlN (11$\bar{2}$0) with reconstructed surfaces [(e), (f)]. (a), (e) were observed in beam incidence geometry parallel to [0001] direction, and (b), (f) parallel to [1$\bar{1}$00] direction. The interpretation of the RHEED patterns for (a) and (b) is shown in (c) and (d), respectively. Original patterns in (a) and (b) and reconstruction patterns in (e) and (f) are denoted by the arrows where the dashed arrow indicates the small intensity.

mization of Ⅲ/V ratio was carried out to obtain high-quality AlN layers. The AlN growth was performed at 950°C under various Al beam equivalent pressure (BEP) values ranging $1.0 \sim 2.0 \times 10^{-7}$ Pa. A N_2 flow rate of 1.0 sccm and radio-frequency (RF)-plasma power of 400 W were used.

After *in-situ* cleaning, sharp and intense RHEED streaks from 4H-SiC $(11\bar{2}0)$ were observed as shown in Fig. 3.4 (a). Figure 3.4 (b)–(e) shows the RHEED patterns observed after the growth of AlN under various Al flux values. For Al-rich conditions, the RHEED pattern was unchanged from that of the 4H-SiC substrate, indicating that the AlN layer has the 4H polytype. The RHEED pattern of the very Al-rich sample (Fig. 3.4 (b)) became faint as growth proceeded, due to the coverage of the surface by metallic Al. The pattern for the slightly Al-rich sample (Fig. 3.4 (c)) remained unchanged throughout the growth. Contrary to this, for AlN grown under N-rich conditions, $01\bar{1}0$-group diffraction gradually appeared as shown in Fig. 3.4 (d) and (e). For AlN layers grown under slightly N-rich conditions (Fig. 3.4 (d)), intensity of $01\bar{1}0$-group diffraction was weaker than other of $\bar{1}2\bar{1}0$ diffraction. It suggests that the layer is mixture of 4H and 2H polytypes, that is, some portion is 4H and the rest is 2H (or 4H structure with high density SFs). The RHEED pattern of a very N-rich sample (Fig. 3.4 (e)) appeared nearly identical to the pattern expected for the ideal 2H polytype. From these results, it can be concluded that polytype replication from SiC substrates to AlN epilayers occurred only when AlN was grown under Al-rich conditions. With decreasing Ⅲ/V ratio during growth, the fraction of 2H inclusions increased. Observation of selected-area diffraction (SAD) patterns in cross-sectional TEM has led to the similar results. Figure 3.5 (a) shows a SAD pattern from 4H-SiC substrates, which shows 4H structure. For AlN layers grown under slightly Al-rich conditions, the SAD pattern showed the same pattern as SiC substrate, indicating the AlN layers have 4H structure. On the other hand, SAD patterns from AlN layers grown under very N-rich conditions indicated 2H structure. Observation of 2H structure in the SAD patterns implies that the structure of the AlN layers almost completely changed to 2H structure and that 4H structure was minor.

The crystalline quality of the AlN layer was assessed by x-ray diffraction (XRD) $(11\bar{2}0)$ measurements. Table 3.1 shows the full-width at half-maximum (FWHM) values of XRD $2\theta/\omega$- and ω-scans of AlN layers grown under various Ⅲ/V ratios. For measurement, $[1\bar{1}00]$ beam incidence was used and receiving slit (acceptance angle of 30 arcsec) was attached. Both the $2\theta/\omega$- and ω-scan FWHM values decreased with increasing Ⅲ/V ratio. Figure 3.6 indicates the ω-scan spectra of AlN layers grown under slightly Al-rich and slightly N-rich conditions measured each reflection with different beam incidence. In the measurement with [0001] beam incidence, SFs and interfacial dislocations are strongly affected the FWHM value compared with $[1\bar{1}00]$ beam incidences (the detail of the affection is discussed in Section 4.2). This indicates that the AlN layers grown under slightly N-rich conditions contain SFs and TDs at a high density.

Figure 3.7 (a)–(d) shows the surface morphologies of AlN with various Ⅲ/V ratios.

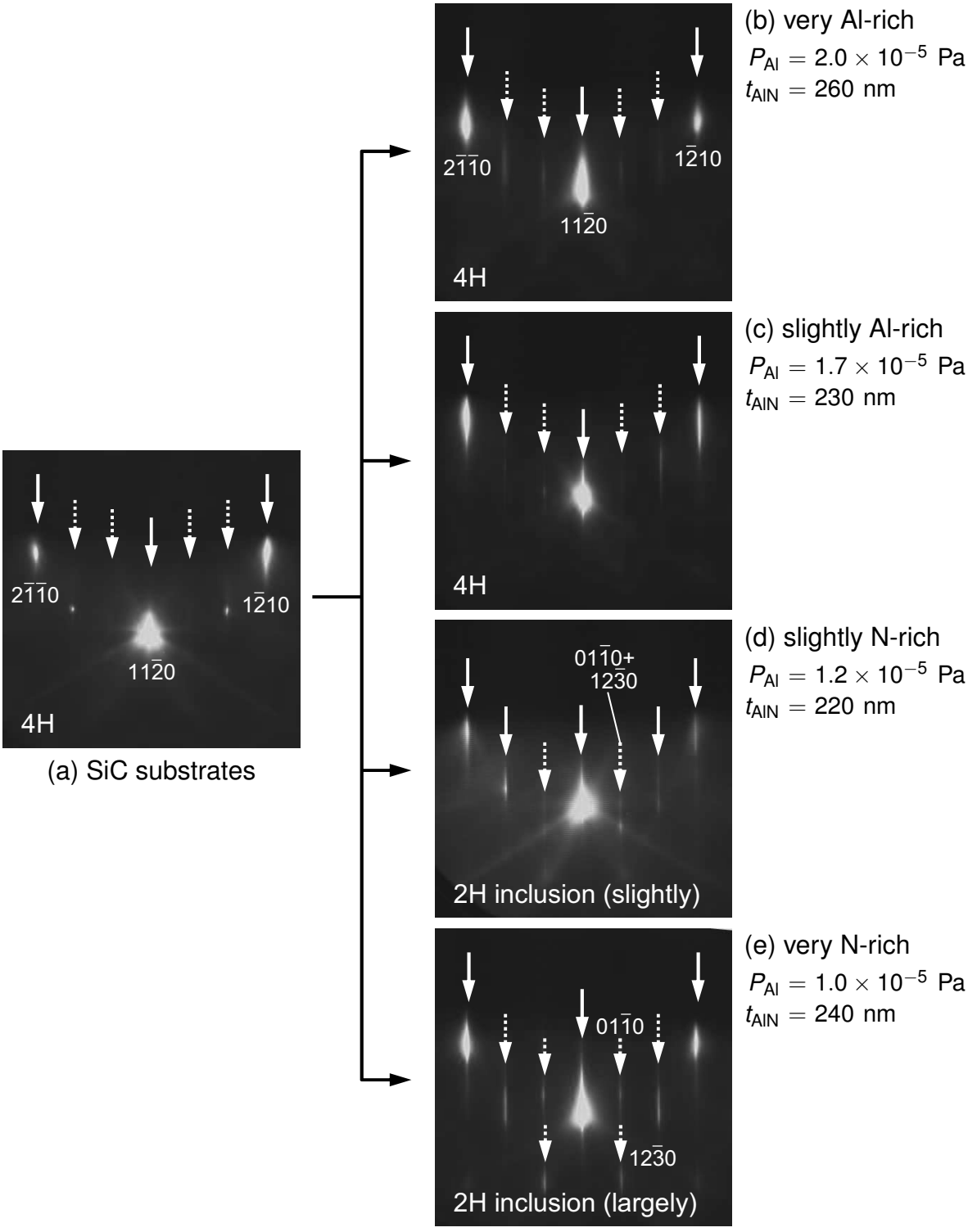

Figure 3.4: RHEED patterns of (a) SiC substrates and AlN layers grown for 30 min on 4H-SiC (11$\bar{2}$0) substrates under (b) very Al-rich, (c) slightly Al-rich, (d) slightly N-rich and (e) very N-rich conditions. The growth of AlN layers was performed under a constant condition of N* supply and varying the flux of Al vapor. The BEP of supply Al (P_{Al}) and the thickness of AlN layers (t_{AlN}) are shown.

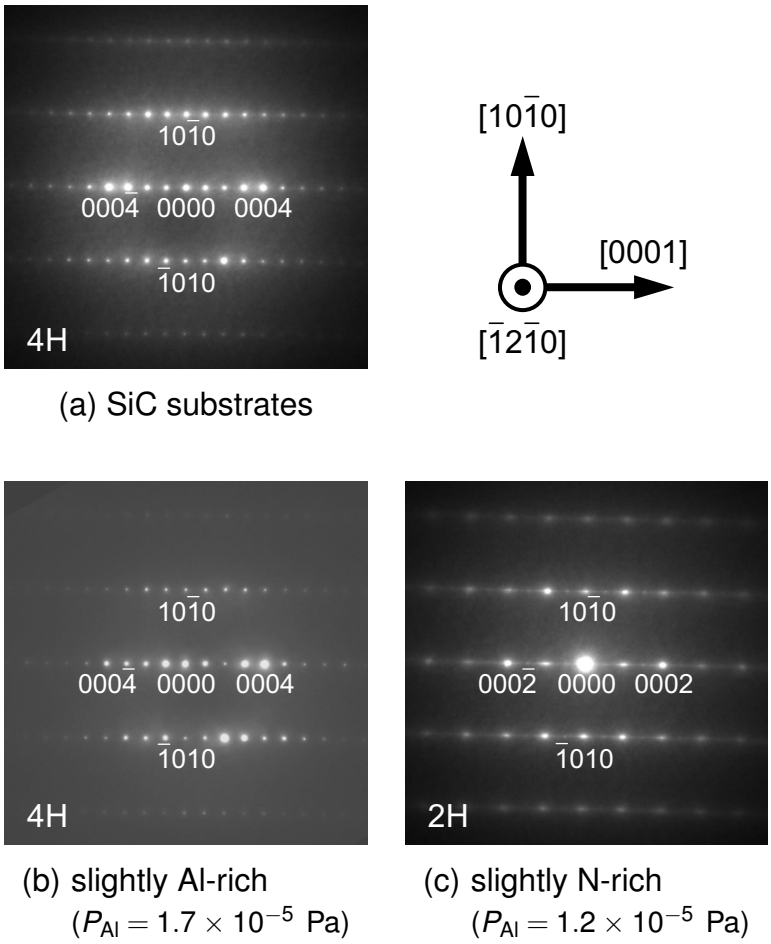

Figure 3.5: Selected-area diffraction patterns of cross-sectional TEM: (a) 4H-SiC $(11\bar{2}0)$ substrates, and about 500-nm-thick AlN $(11\bar{2}0)$ layers grown under slightly (b) Al-rich and (c) N-rich conditions. The electron beam incidence is $[\bar{1}2\bar{1}0]$. The BEP of supply Al (P_{Al}) during AlN growth is shown in parentheses.

Table 3.1: FWHM values of $2\theta/\omega$- and ω-scans for AlN grown on 4H-SiC $(11\bar{2}0)$ with various Ⅲ/V ratios.

Ⅲ/V ratio (Al BEP [Pa])	Very Al-rich (2.0×10^{-5})	Slightly Al-rich (1.7×10^{-5})	Slightly N-rich (1.2×10^{-5})	Very N-rich (1.0×10^{-5})
$2\theta/\omega$-scan	146	175	222	214
ω-scan	41	45	47	60

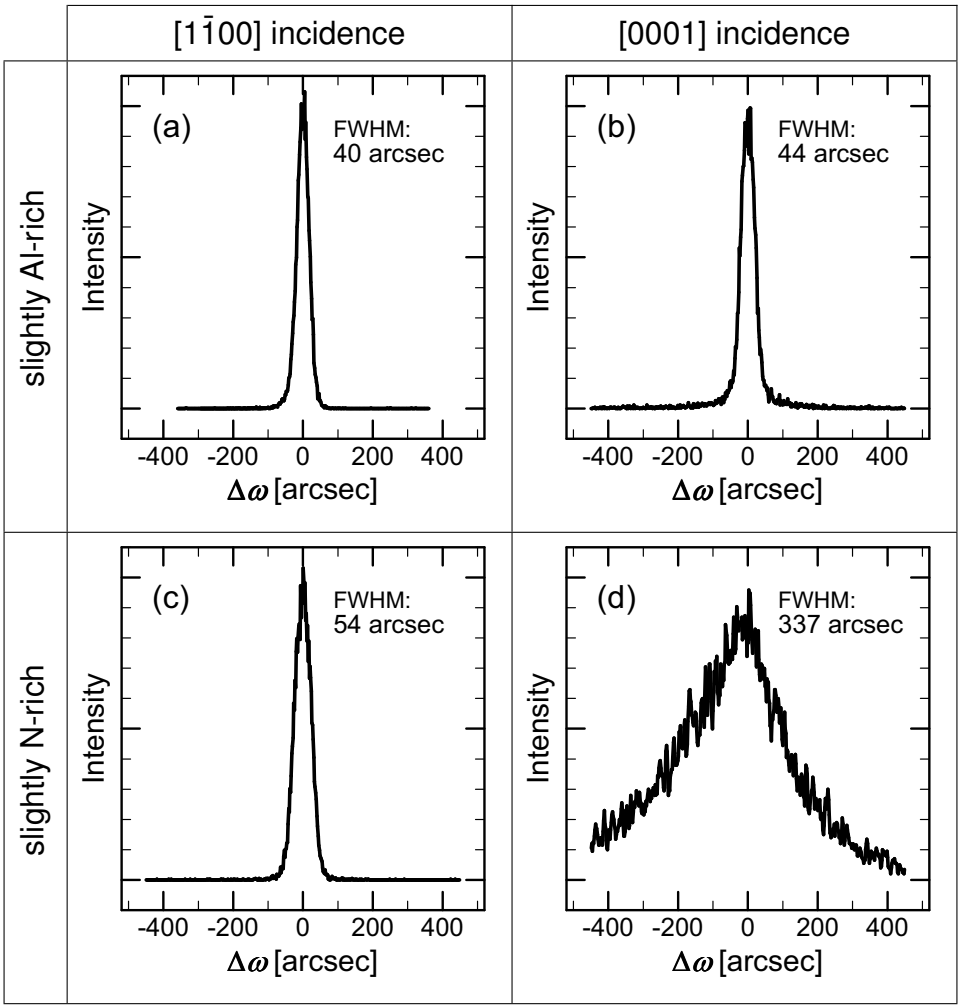

Figure 3.6: XRD ω-scans on (11$\bar{2}$0) diffraction for 470-nm-thick AlN layer grown under slightly Al-rich conditions ($P_{\mathrm{Al}} = 1.7 \times 10^{-5}$ Pa) [(a), (b)] and 220-nm-thick AlN layer grown under slightly N-rich conditions ($P_{\mathrm{Al}} = 1.2 \times 10^{-5}$ Pa) [(c), (d)]. (a), (c) were measured in x-ray incident geometry parallel to [1$\bar{1}$00] direction, and (b), (d) parallel to [0001] direction.

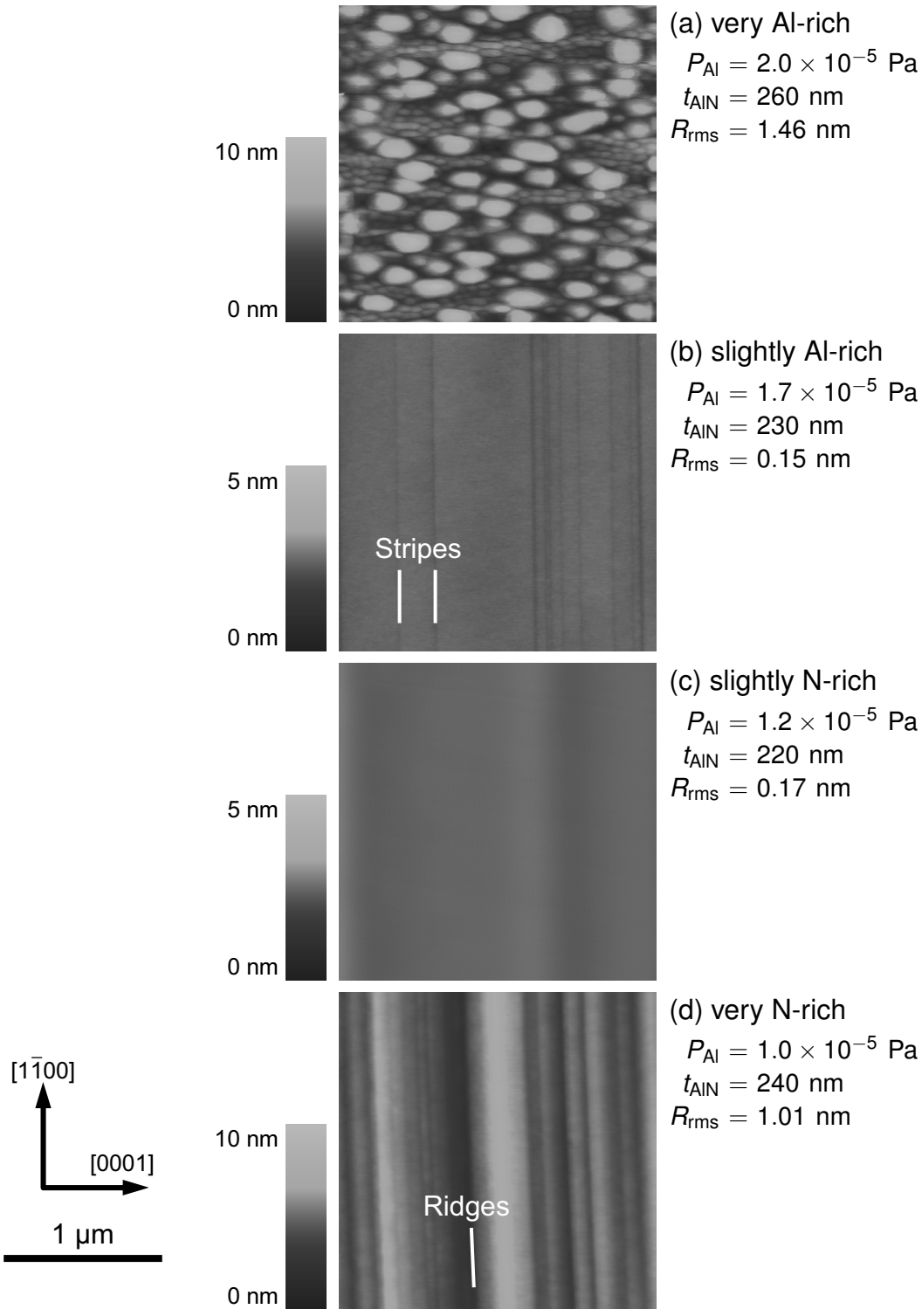

Figure 3.7: AFM images of AlN layers grown for 30 min on 4H-SiC (11$\bar{2}$0) under (a) very Al-rich, (b) slightly Al-rich, (c) slightly N-rich and (d) very N-rich conditions. The growth of AlN layers was performed under a constant condition of N^* supply and varying the flux of Al vapor. The BEP of supply Al (P_{Al}), the thickness of AlN layers (t_{AlN}) and the RMS roughness of surface morphologies (R_{rms}) are shown.

For slightly Al-rich and slightly N-rich conditions (Fig. 3.7 (b) and (c)), a considerably smooth AlN layer with an rms roughness of 0.15–0.17 nm was obtained. For slightly Al-rich conditions, several line depressions were observed in the image area (density 1×10^5 cm^{-1}). It appears that either slightly Al-rich or slightly N-rich growth conditions result in a smooth growth front. However, based on RHEED observations, slightly N-rich conditions should not be used due to the formation of 2H inclusions under such conditions (incomplete polytype replication). Considering both the XRD results and surface morphologies, it is concluded that the growth in slightly Al-rich conditions results in the highest quality 4H-AlN layers.

3.2.3 Growth mode

It has been found that the growth under slightly Al-rich conditions is important for high-quality growth as discussed in Section 3.2.2. Based on this result, AlN was grown under the optimized condition on 4H-SiC substrates with an atomically flat surface. The growth kinetics of epitaxial layers gives important information about the mechanism of extended-defect introduction. To evaluate the growth kinetics of 4H-AlN grown on 4H-SiC, RHEED intensity profiles were observed and the surface morphologies of the initial stage of AlN growth were measured. The AlN growth was performed on HCl-gas-etched 4H-SiC substrates in the temperature range of 600–950°C under slightly Al-rich conditions. A N_2 flow rate of 0.75 sccm and RF-plasma power of 300 W were used.

Figure 3.8 shows RHEED intensity profiles during AlN growth. Clear intensity oscillation of 11$\bar{2}$0 streak was observed during the initial growth independently of the growth temperature. The periods of the oscillation are 1.10, 1.03 and 1.03 at the growth temperatures of 600, 750 and 900°C, respectively. These periods corresponds to ∼1.6 Å of AlN growth, calculated from postgrowth thickness measurements assuming a constant growth rate. The equivalent thickness of the RHEED oscillation period (∼1.6 Å) is almost the same as the lattice spacing of AlN (11$\bar{2}$0) ($=\frac{1}{2}a \sim 1.56$ Å), indicating that the AlN layer grows mainly in a layer-by-layer mode during the initial growth.

On the other hand, the RHEED oscillation was damped with time, indicating that the growth mode changed to three-dimensional (3D)-like. Figure 3.9 shows the surface morphologies of samples before and after growth of a 1.6-nm-thick 4H-AlN (11$\bar{2}$0) epilayer. Undulation in nanometer-scale was observed in the thin AlN epilayer, implying that 3D-like nuclei were formed. The root-mean-square (RMS) roughness value of the thin AlN epilayer was larger than that of the SiC substrate.

In general, the durability of RHEED oscillation is depend on the growth temperature because of the correlation between the migration length (λ_s) and the spacing of steps (L_s) [6]. When the growth temperature is high, migration of adatoms is enhanced, leading to step advancing growth mode ($\lambda_s > L_s$) and RHEED oscillation is not observed. When the growth temperature is low, migration of adatoms is lowered, resulting in 3D growth mode ($\lambda_s \ll L_s$) and no oscillation is observed. When the growth temperature is moderate,

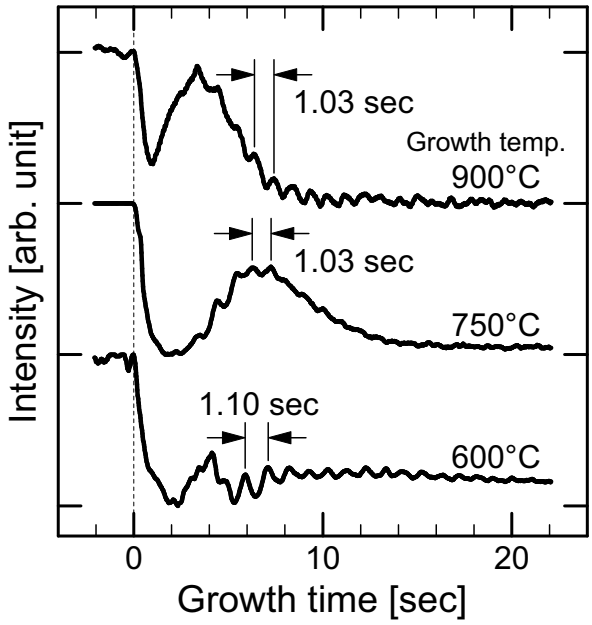

Figure 3.8: RHEED intensity profiles of a $11\bar{2}0$ streak observed during initial growth of 4H-AlN on 4H-SiC $(11\bar{2}0)$ at the temperatures of 600, 750 and 900°C.

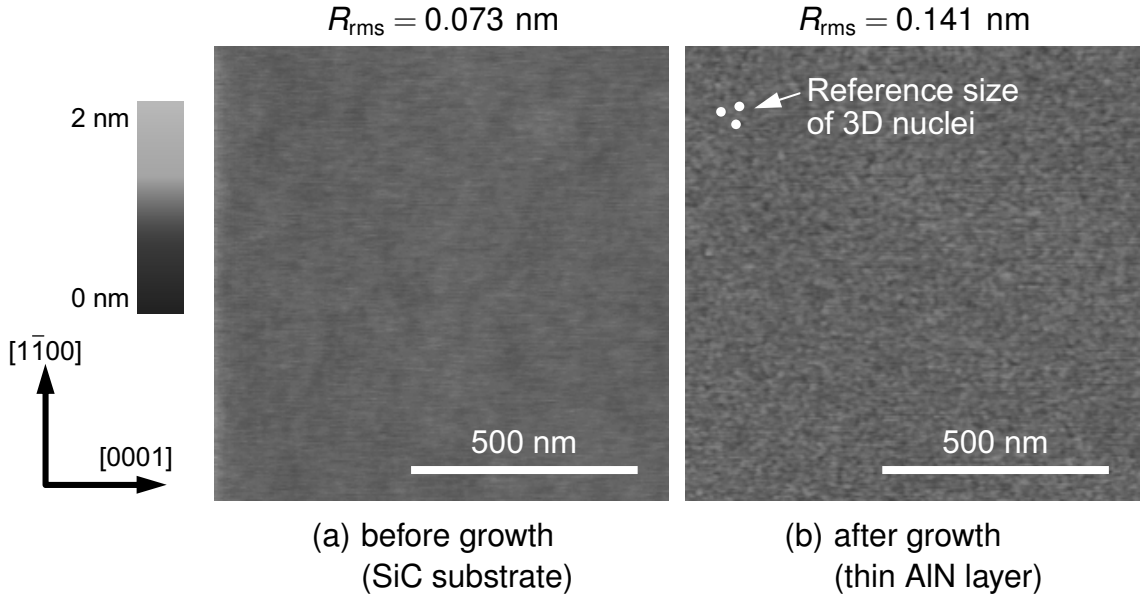

Figure 3.9: AFM images of (a) a 4H-SiC $(11\bar{2}0)$ substrate and (b) a 1.6-nm-(10-layer-)thick 4H-AlN $(11\bar{2}0)$ epilayer grown at 750°C. The closed white circles in (b) show the size of 3D nuclei identified in the image.

two-dimensional (2D) nucleation occur on the terrace in addition to step advanced growth, leading to layer-by-layer growth mode ($\lambda_s \lesssim L_s$) and oscillation is durable. In contrast, the RHEED oscillation was observed in the wide range of the growth temperature. The reason is now under investigation.

3.2.4 Characterization of extended defects

X-ray diffraction

For further evaluation of the crystal quality, a 470-nm-thick AlN layer grown under slightly Al-rich conditions was characterized by high-resolution XRD (HRXRD) examining the symmetrical (11$\bar{2}$0) reflection and the asymmetrical (11$\bar{2}$4) and (30$\bar{3}$0) reflections with [1$\bar{1}$00] x-ray incidence. Since the vectors of 11$\bar{2}$0, 11$\bar{2}$4 and 30$\bar{3}$0 in the reciprocal space are linearly independent of each other, dislocations of all Burgers vectors can be detected. The results are shown in Fig. 3.10. For all reflections, the ω-scan FWHM is less than 100 arcsec, indicating low TD density. For the (11$\bar{2}$0) diffraction, the minimum value observed is 40 arcsec. The minimum FWHM value is compared to that of the previously-reported non-optimized AlN layers. In the growth of the non-optimized AlN layers, substrates were as-polished 4H-SiC (11$\bar{2}$0), which were not treated by HCl gas etching, and the Ⅲ/V ratio of AlN growth was between slightly and very Al-rich conditions. The non-optimized 4H-AlN with a high density of SFs exhibited an ω-scan FWHM of 90 arcsec.

Transmission electron microscopy

To observe extended defects directly, 4H-AlN layers grown under optimized conditions were characterized by TEM. A cross-sectional TEM image of the AlN layer is shown in Fig. 3.11. Since sample cutting with a 30° inclination and a [$\bar{1}$2$\bar{1}$0] incident beam were used as shown in Fig. 1.7 for observation of the stacking structure discussed below, the interface was projected with a finite width. A number of stripes originate from the AlN/SiC interface was observed, the width of which broadened with tilting the TEM specimen to [0001]. This indicates that the stripes correspond to SFs and the SF density was 2×10^5 cm^{-1}. Figure 3.12 (a) and (b) show bright-field plan-view TEM images of a 4H-AlN epilayer with $\boldsymbol{g} = 1\bar{1}00$ and $\boldsymbol{g} = 0004$, respectively. Dark lines running along [1$\bar{1}$00] correspond to SFs in the TEM image under the $\boldsymbol{g} = 1\bar{1}00$ diffraction condition (Fig. 3.12 (a)), which was observed at the same density as the SFs in the cross-sectional TEM. A partial TD having Burgers vectors $\boldsymbol{b} = \frac{1}{3}\langle 1\bar{1}00\rangle$ exists at the end of the SF and the density of partial TDs is estimated to be about 7×10^7 cm^{-2} by examining a large area of 22 μm^2. A perfect TD was observed in the TEM image under the $\boldsymbol{g} = 0004$ diffraction condition (Fig. 3.12 (b)). The density of perfect TDs having Burgers vector of [0001] component is estimated to be about 1×10^7 cm^{-2} where two TDs were observed in an area of 22 μm. The geometry of SFs and TDs are summarized in Fig. 3.13 (a). Partial threading and interfacial dislocations exist at the end of the SF. Perfect threading dislocations are located at an irrelevant position to

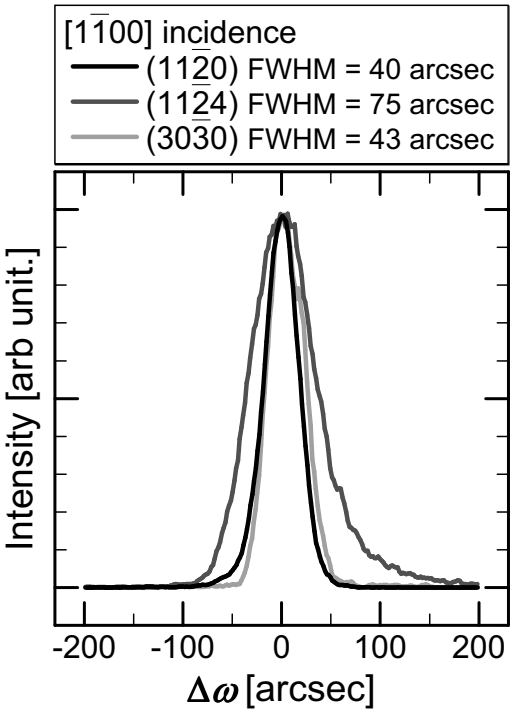

Figure 3.10: XRD ω-scan spectra for the optimized 4H-AlN layer grown on 4H-SiC (11$\bar{2}$0). Symmetrical (11$\bar{2}$0) and asymmetrical (11$\bar{2}$4) and (30$\bar{3}$0) reflections are shown. The x-ray incident geometry parallel to [1$\bar{1}$00] was used.

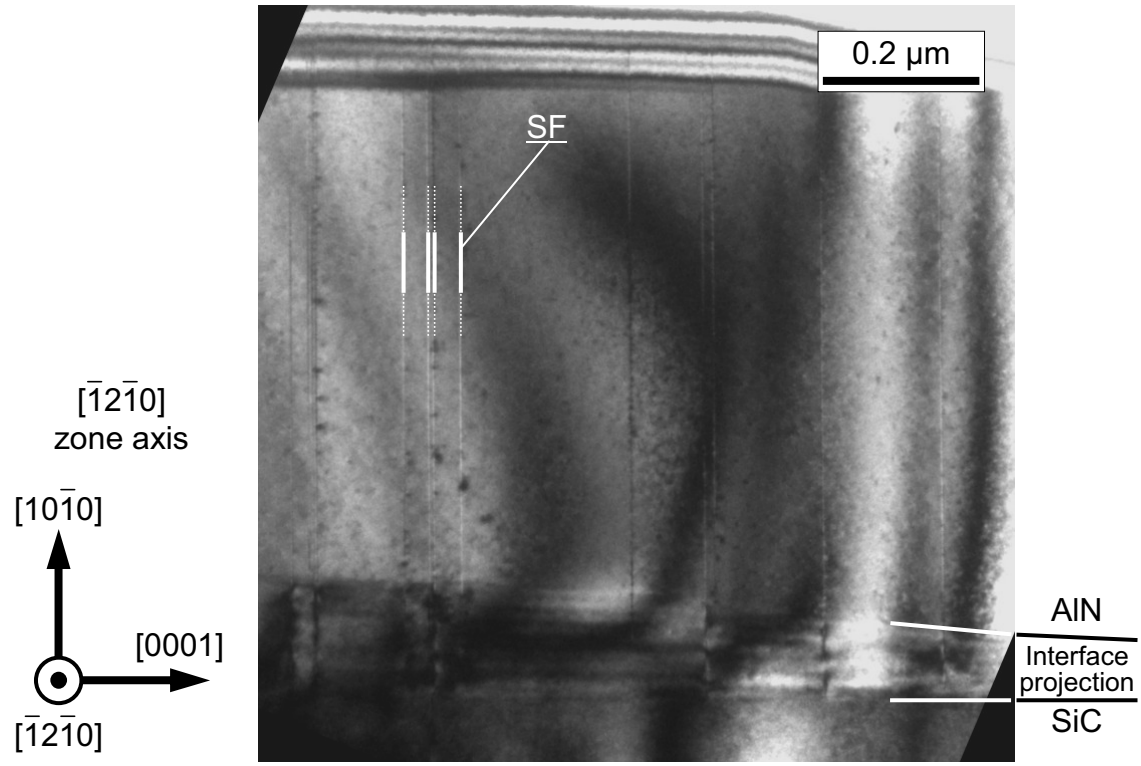

Figure 3.11: A cross-sectional bright-field TEM image of 4H-AlN grown on 4H-SiC (11$\bar{2}$0) under the optimized conditions. Sample cutting with a 30° inclination and a [$\bar{1}$2$\bar{1}$0] incident beam were used as shown in the inset of Fig. 1.7.

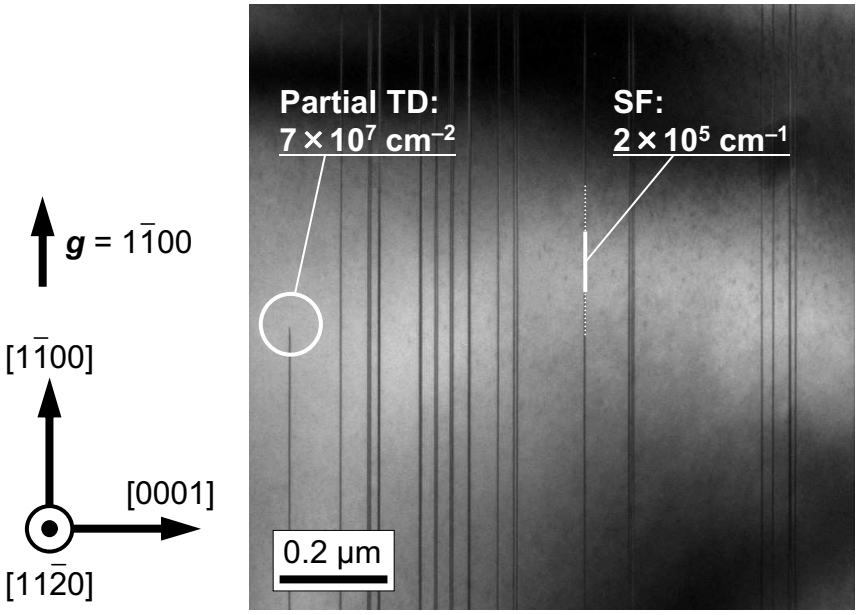

(a) $\boldsymbol{g} = 1\bar{1}00$

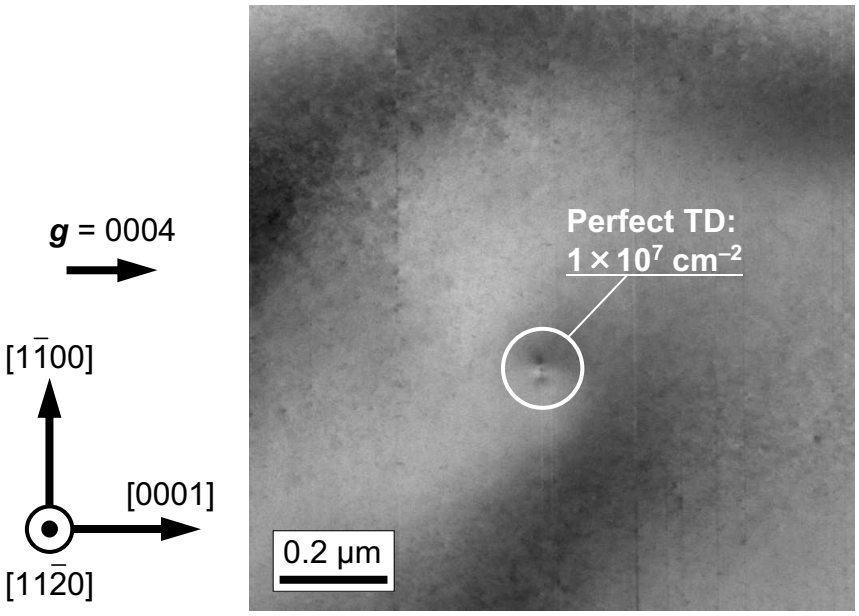

(b) $\boldsymbol{g} = 0004$

Figure 3.12: Plan-view TEM images of 4H-AlN grown on 4H-SiC (11$\bar{2}$0) under the optimized conditions observed under (a) $\boldsymbol{g} = 1\bar{1}00$ and (b) $\boldsymbol{g} = 0004$ two-beam conditions.

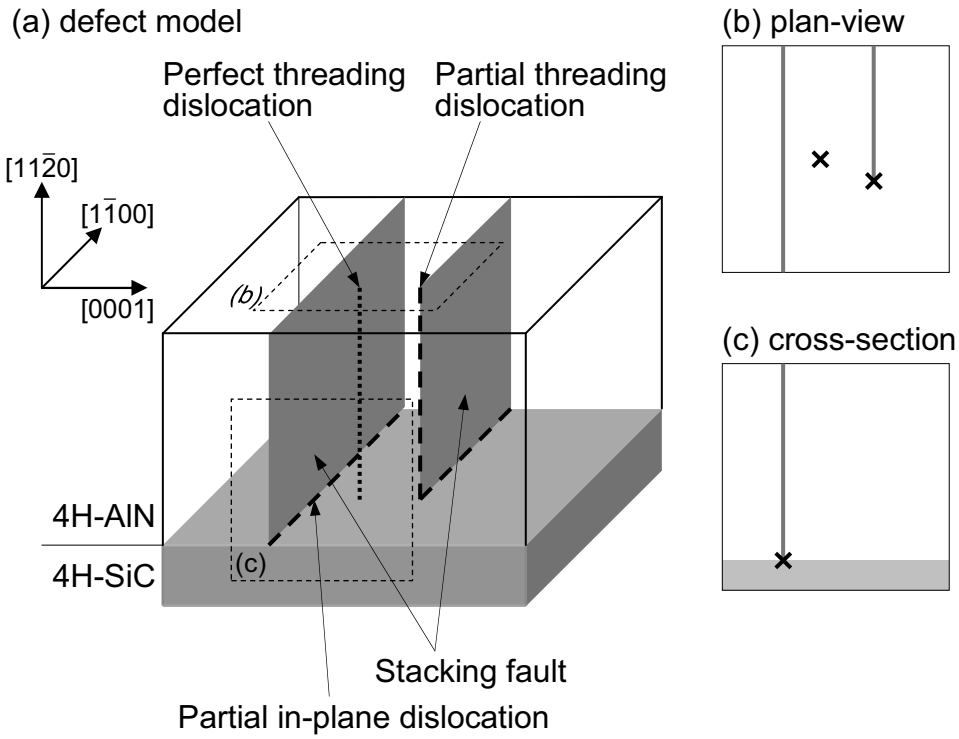

Figure 3.13: (a) Schematic illustration of extended defects in 4H-AlN. Schematic images of (b) plan-view and (c) cross-sectional TEM observed in the area denoted by dashed squares in (a). In (b) and (c), the gray lines and the cross indices show stacking faults and dislocations, respectively.

SFs. Figure 3.13 (b) and (c) indicate the schematic images of cross-sectional and plan-view TEM. The TDs cannot be detected in cross-sectional TEM because of the low density.

The 4H-AlN layer grown under optimized conditions are compared with the previously-reported 4H-AlN which were grown under non-optimized conditions. Figure 3.14 shows high-resolution TEM (HRTEM) images of the optimized and non-optimized 4H-AlN layers. In the TEM image of optimized AlN layer (Fig. 3.14 (a)), the periodic structure of the 4H polytype (ABCBABCB) with a c-axis lattice constant of 1.0 nm was clearly observed. It should be noted that there are no SFs within the observed area. On the other hand, the non-optimized AlN layer contained a number of 2H inclusions (Fig. 3.14 (b)) and the SF and TD densities were estimated to be 5×10^6 cm^{-1} and 4×10^{10} cm^{-2}, respectively.

3.2.5 Discussion

To reduce the extended defects, the growth was performed on SiC substrates with HCl gas etching treatment under optimized conditions. The FWHM value of XRD ω-scans from the AlN layer (40 arcsec) is smaller than that from the previously-reported AlN layer (90 arcsec). In the observation of extended defects by TEM, the SF density was 2×10^5 cm^{-1}, which was reduced in more than one order of magnitude from the previously-reported AlN layer. The densities of partial and perfect TDs were 7×10^7 cm^{-2} and 1×10^7 cm^{-2}, respectively. The total TD density of 8×10^7 cm^{-2} shows the reduction of two orders of magnitude from the previously-reported AlN layer. In the GaN $(11\bar{2}0)$ growth on sapphire $(1\bar{1}02)$ substrates without epitaxial lateral overgrowth (ELO) technique, the SF density of 4×10^5 cm^{-1} and the TD density of 3×10^{10} cm^{-2} have been reported [7]. The 4H-AlN $(11\bar{2}0)$ layers obtained in this study are as equivalent as the GaN layers in the SF density, and much superior in the TD density. The TD density is among the lowest ever reported for a thin heteroepitaxial nonpolar AlN layer on any substrate. The low TD density determined by TEM is consistent with the very sharp symmetrical and asymmetrical XRD ω-scan peaks.

In the 4H-AlN initial growth under optimized condition, 2D nuclei were not observed although RHEED oscillation was observed. Since it is speculated that the size of surface structure on 4H-SiC and 4H-AlN $(11\bar{2}0)$ is too small to resolve by atomic force microscopy (AFM), the observation of the surface in the atomic scale by scanning tunneling microscopy (STM) is required for a solution. The atomic surface structure may offer an explanation for the growth temperature dependence of RHEED intensity oscillation. If step-and-terrace structures on 4H-SiC $(11\bar{2}0)$ substrates can be realized, it may be another solution of growth kinetics of 4H-AlN $(11\bar{2}0)$. The feature of step-and-terrace structures on 4H-SiC $(11\bar{2}0)$ was observed by annealing at a high temperature of 1600°C in an Ar ambient as discussed in Section 6.2. The optimization of the annealing condition may lead to realization of step-and-terrace structures of SiC surfaces and a solution of growth kinetics of AlN.

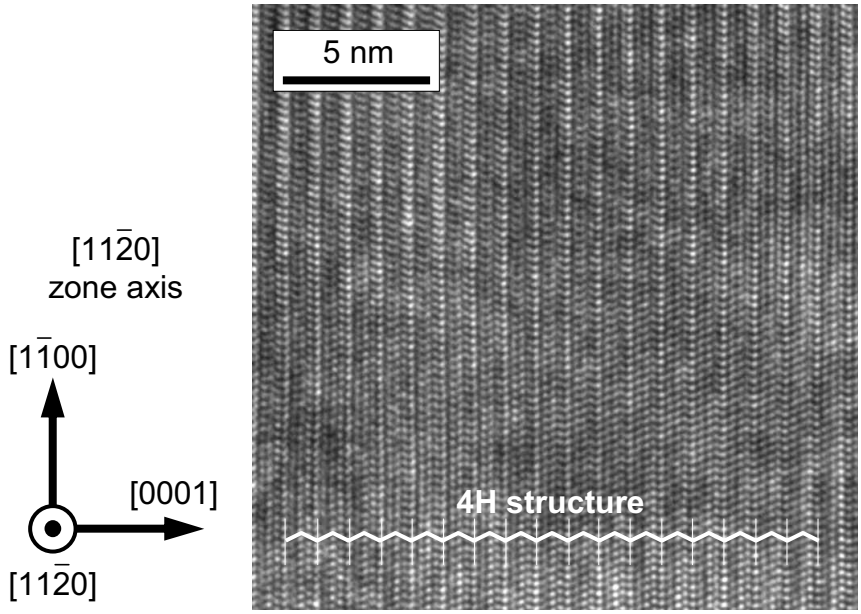

(a) AlN grown under optimized conditions

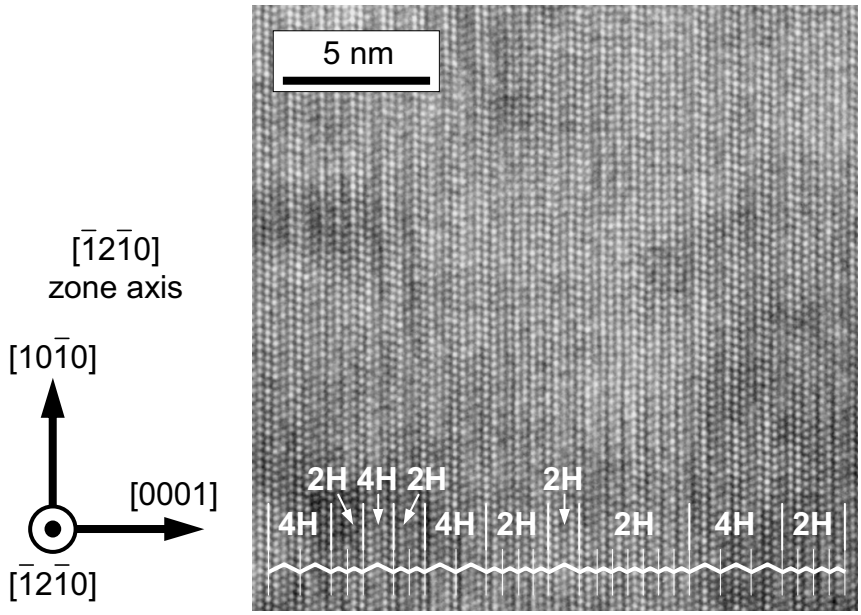

(b) AlN grown under non-optimized conditions

Figure 3.14: High-resolution TEM images of 4H-AlN grown on 4H-SiC (11$\bar{2}$0) under (a) optimized and (b) non-optimized conditions.

3.3 4H-AlN ($1\bar{1}00$) Growth on 4H-SiC ($1\bar{1}00$)

3.3.1 Interpretation of reflection high-energy electron diffraction patterns

As is the case for ($11\bar{2}0$), the relationship between RHEED patterns and crystal structure on ($1\bar{1}00$) surfaces is described in this section. Figure 3.15 shows the theoretical patterns of a ($1\bar{1}00$) surface of 2H and 4H crystal observed with [$11\bar{2}0$] and [0001] beam incidences. Since the stacking periodicity along [0001] appears in the pattern with the [$11\bar{2}0$] beam incidence, it can be distinguished between 4H and 2H structure. Figure 3.16 (a) and (b) show RHEED patterns experimentally observed from the 4H-SiC substrates with [0001] and [$11\bar{2}0$] incidence, respectively, and the interpretation of the patterns are shown in Fig. 3.16 (c) and (d), respectively. In the image of [$11\bar{2}0$] beam incidence, about ten streaks were observed. The interval of streaks corresponds to the period of stacking structure. When the crystal structure changes from 4H to 2H, the streaks of $1\bar{1}01$, $1\bar{1}03$ and so on ($1\bar{1}0l(l = 2n + 1$, n: integer)) disappear. From the RHEED patterns and this interpretation, the crystal structure can be determined. Figure 3.16 (e) and (f) show the RHEED patterns of AlN layers grown under Al-rich conditions. Weak half-order reconstruction streaks along all azimuths at growth temperature of 750°C, which become strong with cooling. It has been reported that the reconstruction is due to the Al adatoms [4].

3.3.2 Enhancement of layer-by-layer growth

It has been reported that isopolytypic 4H-AlN can be grown on 4H-SiC ($1\bar{1}00$) under slightly Al-rich conditions [4]. The RHEED oscillation has been also reported in the 4H-AlN ($1\bar{1}00$) growth under slightly Al-rich conditions, implying a possibility of layer-by-layer growth mode. However, the oscillation was observed for just ten cycles of initial growth. It is important for reduction of extended defects to realize stable layer-by-layer mode during growth.

AlN growth was performed on 4H-SiC substrates with well-formed step-and-terrace structures described in Section 2.4. Figure 3.17 shows the intensity of a RHEED streak as a function of the AlN growth time. The RHEED intensity oscillated for over 100 cycles from the start of growth. The period of the oscillation corresponds to ∼2.5 Å of AlN growth, calculated from postgrowth thickness measurements assuming a constant growth rate. The images shown in Fig. 3.18 (b) are the surface morphologies of a 4-nm-thick AlN epilayer. In the 4-nm-thick AlN layer, two kinds of steps were observed: one kind is steps formed from two-dimensional (2D) island edges (denoted by "1" in Fig. 3.18 (b)) and the other kind is vicinal surface steps with the same separation and direction as the substrate steps (denoted by "2" in Fig. 3.18 (b)). Both types of steps have height of 2.7 Å, corresponding to the lattice spacing of AlN ($1\bar{1}00$) ($=\frac{\sqrt{3}}{2}a = 2.66$ Å). The equivalent thickness

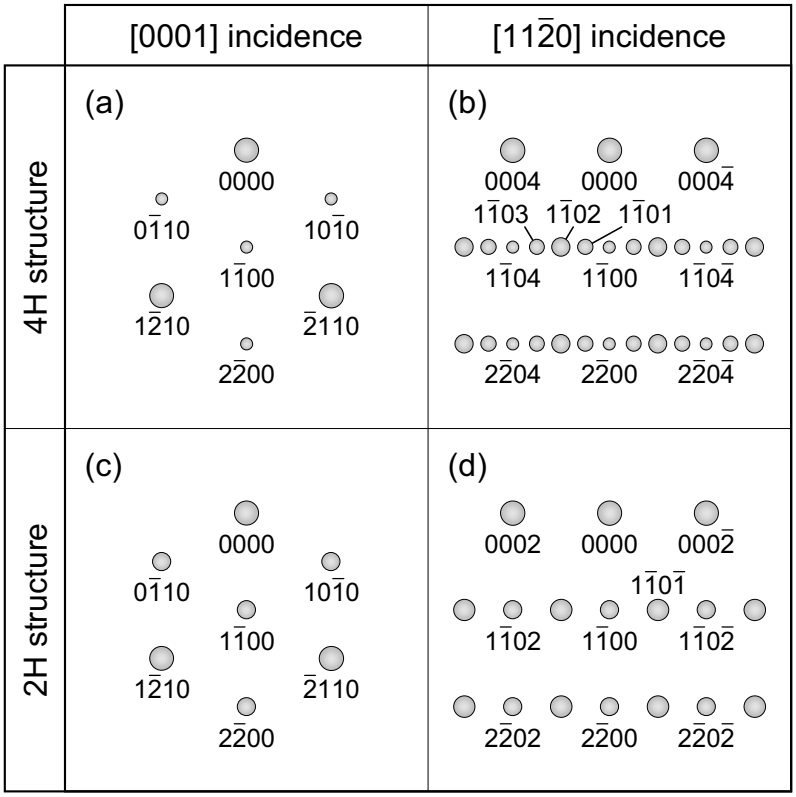

Figure 3.15: Theoretical RHEED patterns of (1$\bar{1}$00) surface of 4H crystal [(a), (b)] and 2H crystal [(c), (d)]. (a), (c) are observed in beam incident geometry parallel to [0001] direction, and (b), (d) parallel to [11$\bar{2}$0] direction.

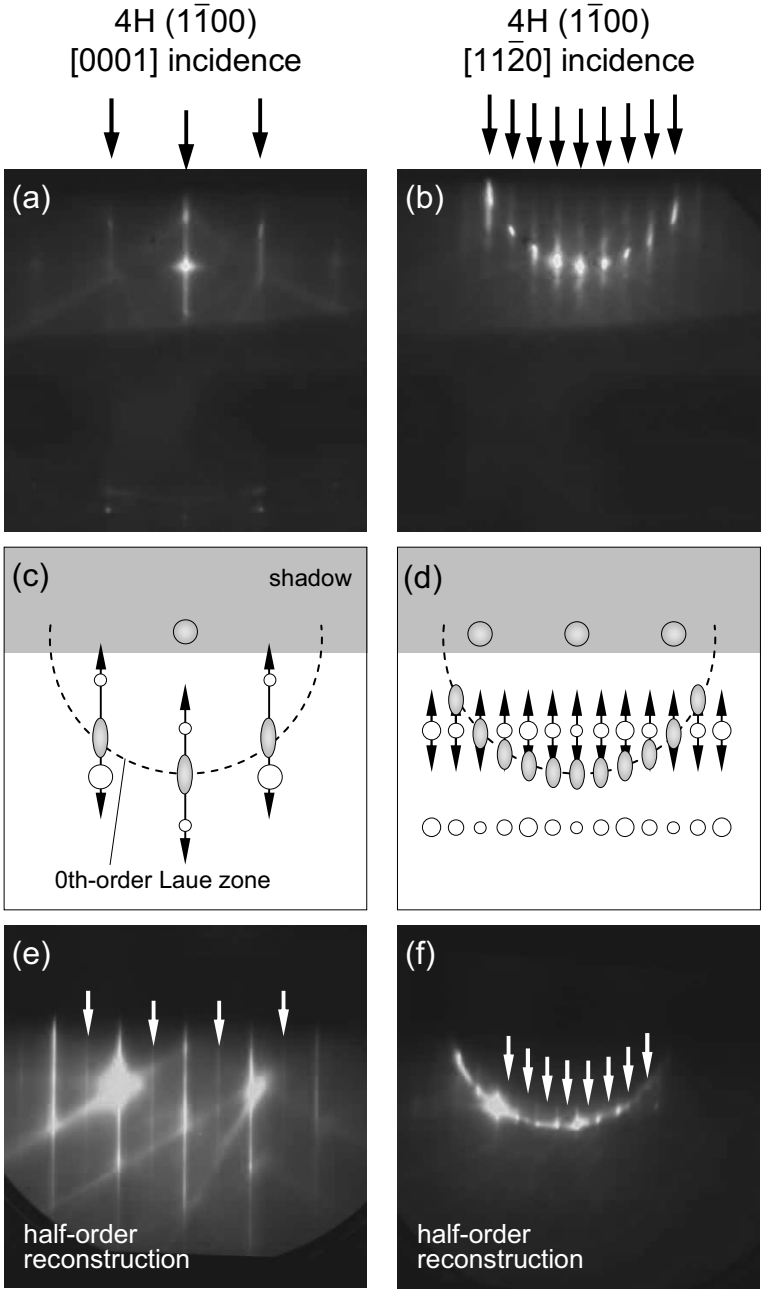

Figure 3.16: RHEED patterns experimentally observed on 4H-SiC (1$\bar{1}$00) [(a), (b)] and 4H-AlN (1$\bar{1}$00) with reconstructed surface [(e), (f)]. (a), (e) were observed in beam incidence geometry parallel to [0001] direction, and (b), (f) parallel to [11$\bar{2}$0] direction. The interpretation of the RHEED patterns for (a) and (b) is shown in (c) and (d), respectively. Original patterns in (a) and (b) and reconstruction patterns in (e) and (f) are denoted by the arrows.

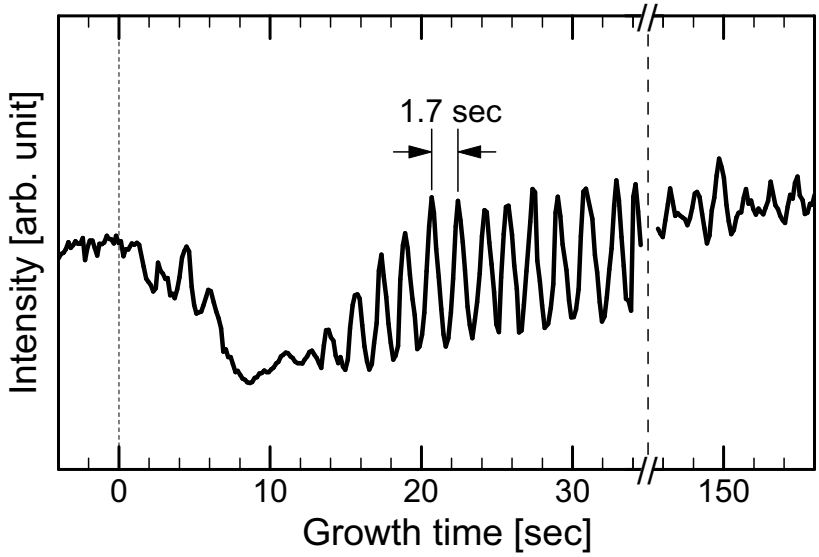

Figure 3.17: A RHEED intensity profile of a 1$\bar{1}$00 streak observed during initial growth of 4H-AlN on 4H-SiC (1$\bar{1}$00) at the growth temperature of 750°C. The profile is also shown in the growth time around 150 sec (∼90th cycle).

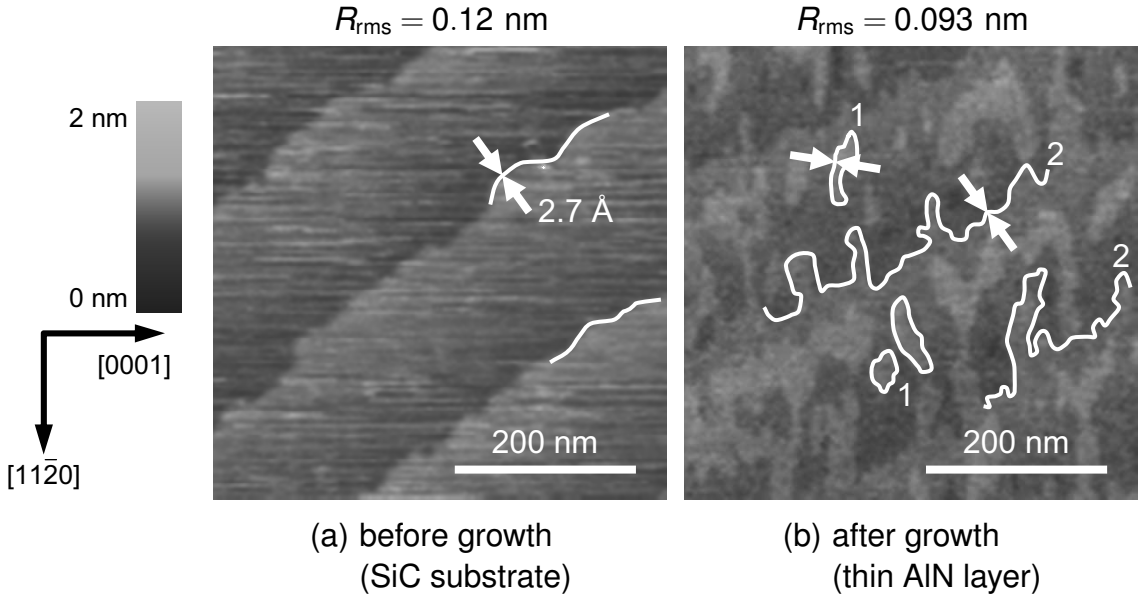

Figure 3.18: AFM images of (a) a 4H-SiC (1$\bar{1}$00) substrate and (b) a 4-nm-(16-layer-)thick 4H-AlN (1$\bar{1}$00) epilayer grown at 750°C. Pairs of arrows in both images show steps of 2.7-Å height. In (b), two-dimensional islands (denoted by "1") and steps originating from SiC substrate steps (denoted by "2") are visible.

of the RHEED oscillation period (∼2.5 Å) is almost the same as the lattice spacing of AlN $(1\bar{1}00)$ (2.7 Å). Thus the AlN layer grows mainly in a layer-by-layer mode. The 2D islands of AlN in Fig. 3.18 (b) have anisotropic shapes, elongated along $[11\bar{2}0]$, indicating that the velocity of step advance toward $[11\bar{2}0]$ is larger than that toward [0001].

3.3.3 Characterization of extended defects

X-ray diffraction

As is the case for 4H-AlN $(11\bar{2}0)$ growth, HRXRD measurements were performed for the symmetrical and asymmetrical reflections for 4H-AlN $(1\bar{1}00)$ epilayers. The ω-scan spectra for the symmetrical $(1\bar{1}00)$ and asymmetrical $(1\bar{1}02)$ and $(1\bar{2}10)$ reflections from 270-nm-thick AlN are shown in Fig. 3.19. Since the vectors of $1\bar{1}00$, $1\bar{1}02$ and $1\bar{2}10$ in the reciprocal space are linearly independent each other, dislocations of all Burgers vectors can be detected. The $(1\bar{2}10)$ reflection was obtained with [0001] x-ray incidence and the other reflections were taken with $[1\bar{1}00]$ x-ray incidence where the same incident x-ray can not be used in these reflections because of the limitation of incident geometry. For all reflections, the ω-scan FWHM is less than 100 arcsec, implying low TD density as is the case of high-quality 4H-AlN $(11\bar{2}0)$.

Transmission electron microscopy

To characterize SFs and dislocations, cross-sectional TEM observations were performed. Figure 3.20 (a) shows a bright-field TEM image of the 4H-AlN layer grown on a 4H-SiC $(1\bar{1}00)$ surface with well-formed step-and-terrace structures observed under the diffraction condition of $\boldsymbol{g} = 1\bar{1}00$. It is inferred that the dark lines correspond to SFs parallel to (0001) because the widths of the dark lines increase as the sample is tilted toward [0001]. Figure 3.20 (b) shows a dark-field TEM image of 4H-AlN layers reported in Ref. 4 observed under the diffraction condition of $\boldsymbol{g} = 1\bar{1}00$, which were grown on 4H-SiC substrates without step-and-terrace structures. SFs were observed as bright lines parallel to (0001). The SF density is estimated to be 1×10^6 cm^{-1} in the AlN layer grown on the surface with step-and-terrace structures (Fig. 3.20 (a)), which is reduced compared with that of the AlN on a substrate without step-and-terrace structures (5×10^6 cm^{-1}, shown in Fig. 3.20 (b)) [4]. It is notable that almost all the SFs originate from the AlN/SiC interface (denoted by dashed rectangles in Fig. 3.20 (a)). This is in contrast to the AlN on a substrate without step-and-terrace structures where SFs were found to have been generated not only at the interface (denoted by a dashed rectangle in Fig. 3.20 (b)), but also during growth of the AlN layer (denoted by dashed circles in Fig. 3.20 (b)).

To determine the detailed structure of the SFs, HRTEM observations were performed. Figure 3.21 shows a cross-sectional HRTEM image of the AlN/SiC interface where an AlN SF is included. Periodic patterns with 4-layer periods along the [0001] direction, which indicates 4H structure, were observed in the SiC substrate and the unfaulted AlN region.

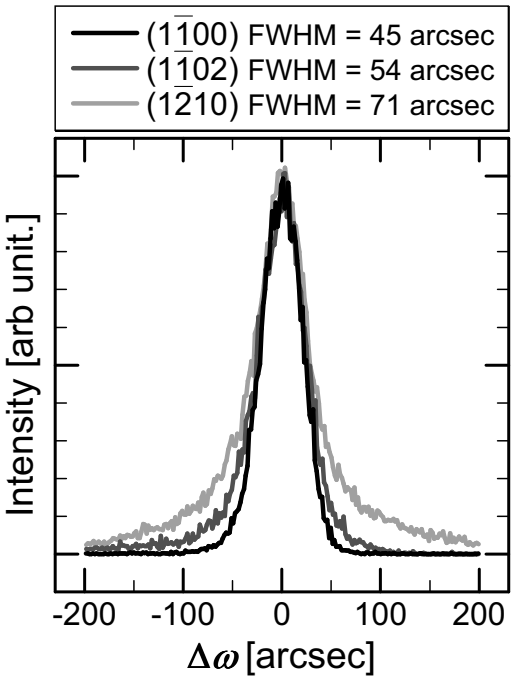

Figure 3.19: XRD ω-scan spectra for the optimized 4H-AlN layer grown on 4H-SiC (1$\bar{1}$00). Symmetrical (1$\bar{1}$00) and asymmetrical (10$\bar{1}$2) and (1$\bar{2}$10) reflections are shown. (1$\bar{1}$00) and (10$\bar{1}$2) reflections are obtained in x-ray incident geometry parallel to [11$\bar{2}$0] direction, and a (1$\bar{2}$10) reflection parallel to [0001] direction.

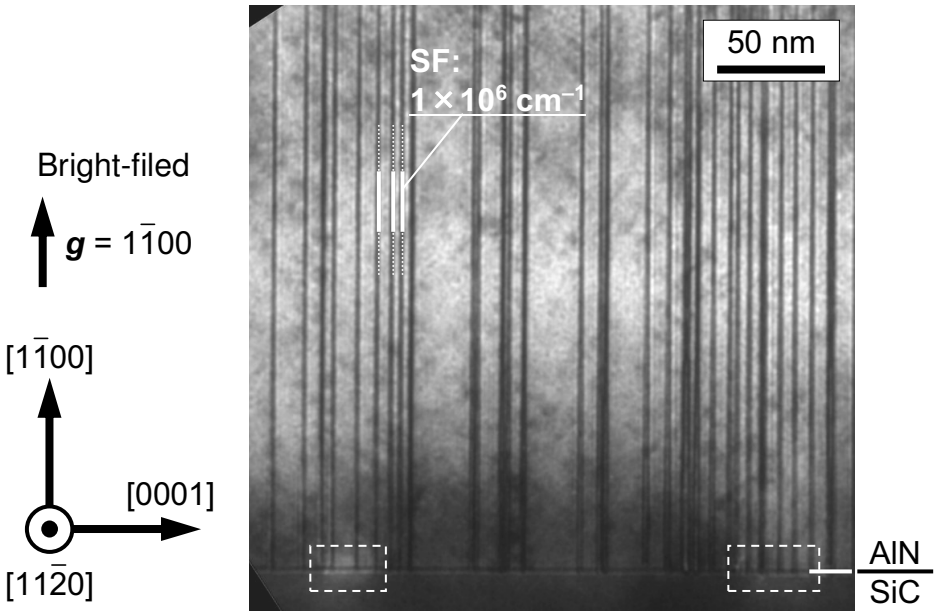

(a) on a substrate with well-formed step-and-terrace surface structures (bright-field image)

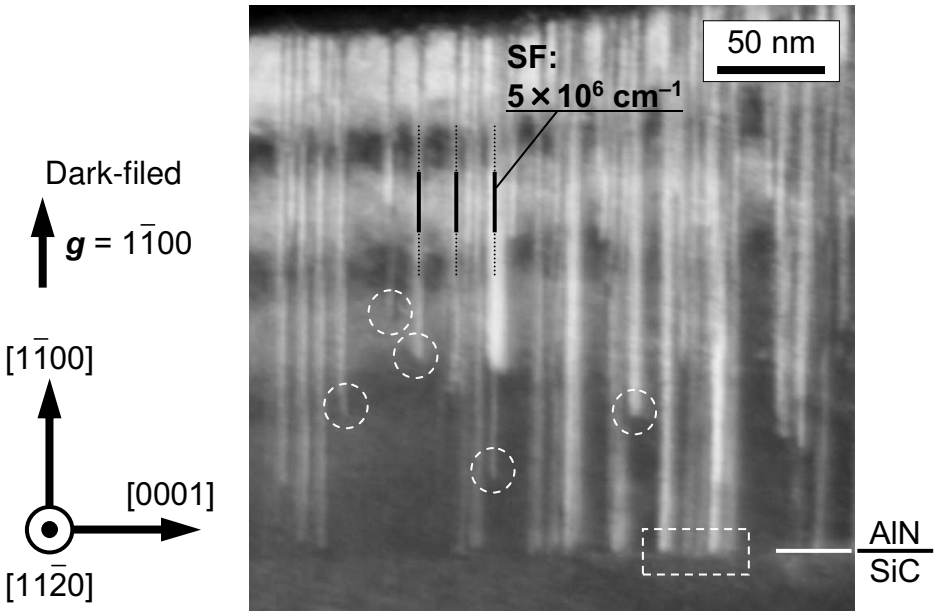

(b) on a substrate without step-and-terrace surface structures (dark-field image)

Figure 3.20: Cross-sectional TEM images of 4H-AlN layers grown on 4H-SiC (1$\bar{1}$00) substrates: (a) a bright-field TEM image of 4H-AlN layers grown on 4H-SiC substrate with well-formed step-and-terrace surface structures, and (b) a dark-field TEM image of 4H-AlN layers grown on 4H-SiC substrate without step-and-terrace surface structures. For several SFs, the originating points on the AlN/SiC interface and in the AlN layer are denoted by dashed rectangles and circles, respectively.

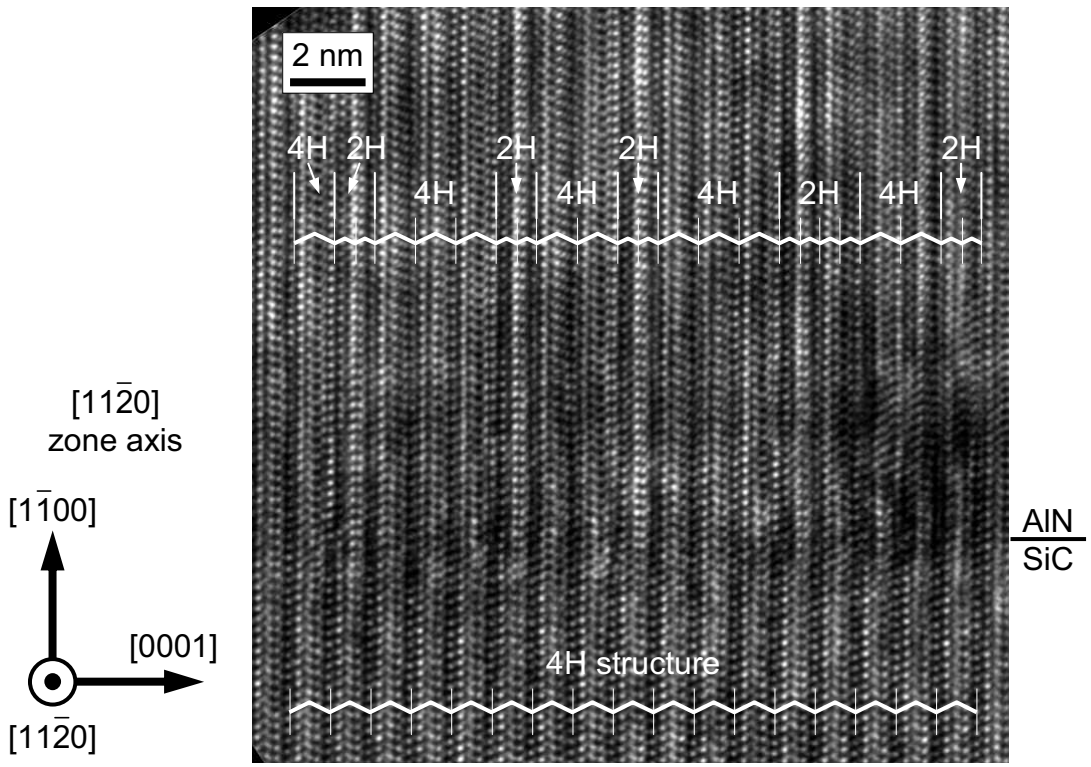

Figure 3.21: A high-resolution cross-sectional TEM image at 4H-AlN/4H-SiC (1$\bar{1}$00) interface. Stacking structure of the AlN layer and the SiC substrate is shown.

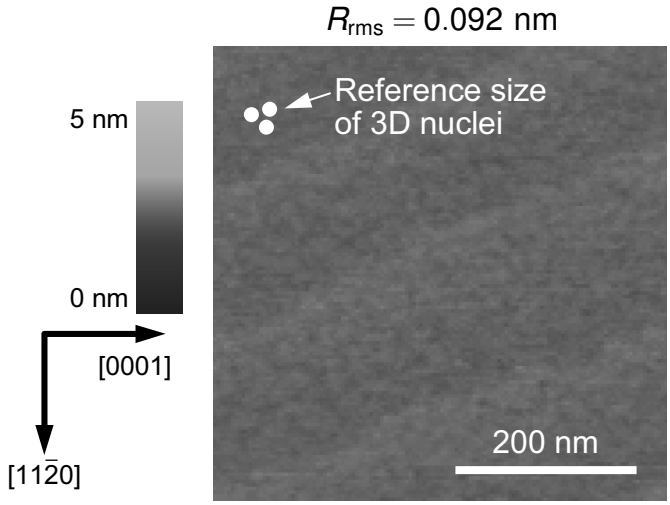

Figure 3.22: An AFM image of a 2-nm-(8-layer-)thick 4H-AlN (1$\bar{1}$00) epilayer grown at 750°C. The closed white circles show the size of 3D nuclei identified in the image.

Inside the AlN SFs, patterns with 2-layer periodicity were observed.

3.3.4 Discussion

Based on the RHEED oscillation and the surface morphologies with 2D islands, more stable layer-by-layer growth of 4H-AlN $(1\bar{1}00)$ was demonstrated on 4H-SiC substrates with step-and-terrace surface structures compared with the growth on substrates without step-and-terrace surface structures. It is speculated that layer-by-layer growth leads to better replication of the 4H structure from subsurface layers to the growing layers and inhibit the generation of SFs during AlN growth. Although the presently achieved SF density of 1×10^6 cm^{-1} is still rather large and may limit device applications, it is believed that there is a cause for optimism for possible further reductions in the SF density. The TEM observations reveal that almost all the SFs originate at the AlN/SiC interface, and the RHEED oscillations are very weak in the initial growth stage of $\sim$15 sec (about 10 cycles) as seen in Fig. 3.17. In the earliest stage of growth, AlN grew with 3D nuclei which were observed in surface morphologies of a 2-nm-(8-layer-)thick AlN layer shown in Fig. 3.22. These findings suggest that SF generation may be at least partly due to instability of the growth front at this initial stage of growth. If so, then precise control of the growth front at the initial stage (e.g. by modulating the Al and N source supplies) may lead to further reductions in SF density.

3.4 Summary

The growth of high crystalline quality AlN on 4H-SiC $(11\bar{2}0)$ and $(1\bar{1}00)$ substrates by using an atomically flat SiC surface and optimized Ⅲ/V ratio was investigated. In the AlN $(11\bar{2}0)$ layer grown on 4H-SiC $(11\bar{2}0)$, symmetric and asymmetric XRD ω-scans showed very sharp peaks with FWHMs of less than 100 arcsec. The AlN layer was found to be high-phase purity of 4H-AlN. Density of the basal plane SFs was estimated to be 2×10^5 cm^{-1}, and densities of partial and perfect TDs to be 7×10^7 cm^{-2} and 1×10^7 cm^{-2}, respectively. The SF and TD densities of 4H-AlN were reduced by two orders of magnitude, compared to that of the previously-reported 4H-AlN. In the AlN $(1\bar{1}00)$ growth on 4H-SiC $(1\bar{1}00)$ substrates, stable layer-by-layer growth was achieved by using SiC substrates with well-formed step-and-terrace surface structures. The layer-by-layer growth is confirmed by persistent RHEED oscillations over 100 cycles and the observation of 2D AlN islands by AFM. Moreover, layer-by-layer growth of AlN effectively suppresses SF generation during growth. In the next chapter, the properties examined for the 4H-AlN with a low defect density and the structure of defects in 4H-AlN are described, and in Chapters 5 and 6, basic applications of the high-quality 4H-AlN for light-emitting and electronic devices are demonstrated, respectively.

References

[1] N. Onojima, J. Suda, T. Kimoto, and H. Matsunami, Appl. Phys. Lett. **83**, 5208 (2003).

[2] J. M. van Hove, C. S. Lent, P. R. Pukite, and P. I. Cohen, J. Vac. Sci. Technol. B **1**, 741 (1983).

[3] J. H. Neave, B. A. Joyce, P. J. Dobson, and N. Norton, Appl. Phys. A **31**, 1 (1983).

[4] R. Armitage, J. Suda, and T. Kimoto, Appl. Phys. Lett. **88**, 011908 (2006).

[5] J. E. Northrup, J. Neugebauer, R. M. Feenstra, and A. R. Smith, Phys. Rev. B **61**, 9932 (2000).

[6] T. Sakamoto, Oyo Buturi **66**, 1298 (1997).

[7] B. A. Haskell, F. Wu, M. D. Creven, P. T. Fini, S. P. DenBaars, J. S. Speck, and S. Nakamura, Appl. Phys. Lett. **83**, 1554 (2003).

Chapter 4

Structural Properties and Extended Defects of Nonpolar 4H-AlN

4.1 Introduction

To understand the properties of 4H-AlN is important for device applications. Obtaining the lattice constant allows strain analyses in heterostructure where the strain field affects physical properties, leading to change the electrical and optical properties. Determination of the band structure enables to analyze the conduction mechanism and the luminescence mechanism. The lattice vibration mode has a close relationship with the crystal structure.

The properties of group–Ⅲ nitrides (Ⅲ–Ns) with 2H and 3C structure have been reported in large numbers. For example, the lattice constant [1, 2], the bandgap energy [3, 4], phonon energy [5, 6], elastic constant [7, 8] and so on have been reported (referred for each property of 2H- and 3C-AlN).

On the other hand, the 4H-polytype of AlN is metastable structure which can be grown only by polytype replication from 4H-SiC substrates. For this reason, there have been few reports about the properties of 4H-AlN and the structure of extended defects in 4H-AlN. The 4H-AlN has reported first by Onojima *et al.* [9] and reduction of extended defects has been achieved as discussed in Chapter 3. High-quality 4H-AlN layers with several-hundred-nm thickness have been available for characterization of properties.

For the structure of extended defects, there are a few reports about 2H-GaN $(11\bar{2}0)$ grown on sapphire $(1\bar{1}02)$ substrates [10, 11]. In these reports, the type of stacking faults (SFs) and the Burgers vectors of threading dislocations (TDs) have been discussed. SFs are classified into several groups from the viewpoint of the stacking order where each type of SFs expects to have a different effect to devices. The same holds true for the TDs. It has been found that SFs and TDs are contained in nonpolar 4H-AlN layers similarly to nonpolar 2H-GaN layers as discussed in Chapter 3. However, the growth of 4H-AlN on 4H-SiC is just developing and the structure of SFs and TDs has not been identified. In comparison with 2H-GaN $(11\bar{2}0)$, the 4H-AlN $(11\bar{2}0)$ may contain the same type of extended defects due to the same

growth orientations and may also contain different types of defects because of the difference of substrate or crystal structure.

In association with the extended-defect structure, x-ray diffraction (XRD) obtained from nonpolar 4H-AlN is studied. In nonpolar Ⅲ–Ns, the impact of extended defects on the full-width at half-maximum (FWHM) of XRD ω-scans is different from that in the case of Ⅲ–Ns (0001). In addition, the different influence is expected in between the nonpolar 4H-AlN and nonpolar 2H-GaN since the crystal structure is not the same.

In this chapter, the structure of extended defects included in 4H-AlN and the properties of 4H-AlN are presented. The extended-defect structure is investigated by transmission electron microscopy (TEM) observations. Based on the structure, the relationship between the densities of extended defects and the FWHM values of XRD measurement is discussed. The possible explanation for the incomprehensible relationship will be given. For the characterization of the properties of 4H-AlN, the lattice constant, the band structure and the lattice vibration mode are described. High-resolution XRD (HRXRD) measurements for the lattice constant, optical reflectance (OR) and cathodoluminescence (CL) measurements for the band structure, and laser Raman spectroscopy for the lattice vibration mode are performed. Dependence of these properties on the polytype are discussed using an index of "hexagonality".

Prior to discussion about the properties and the extended-defect structure, the concept of the hexagonality is explained [12]. The crystal structures of 3C, 4H, 2H and so on are just different in the stacking order, and are common in the constitute element and the application to the hexagonal structure. SiC has been reported more than 200 polytypes, where the polytype dependence has been progressively studied. In the study of polytypism, it is known that an index of hexagonality H is adaptable to indicate the polytype dependence. Considering closed-packed stacking, two types of stacking can be allowed due to the arbitrary property of atomic sites as shown in Fig. 4.1. From this viewpoint, the atoms in the hexagonal structure are sorted into hexagonal sites and cubic sites as shown in Fig. 4.2. The hexagonality is defined as the ratio of the number of hexagonal-sited atoms to the number of the total atoms.

4.2 Extended-Defect Structure

4.2.1 Classification of extended defects

Prior to the observation, the possible structure of extended defects is mentioned. SFs are sorted into intrinsic type I and extrinsic type E. The SFs of intrinsic type I are classified further into I_1, I_2 and I_3 types. In 4H-polytype crystal, an additional intrinsic type I_0 is possible to form. The structure of each type of SFs is listed in Fig. 4.3 and the characteristics are as follows.

- I_0: A single bilayer is removed without any shift of original crystal along the a-axis

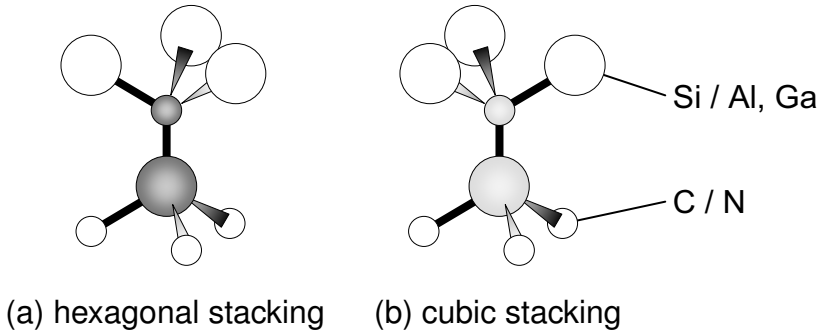

Figure 4.1: Schematic views of (a) hexagonal and (b) cubic stacking structures of SiC or Ⅲ–Ns. The bonds denoted by solid lines are on the same plane and those denoted by triangles are out-of-plane.

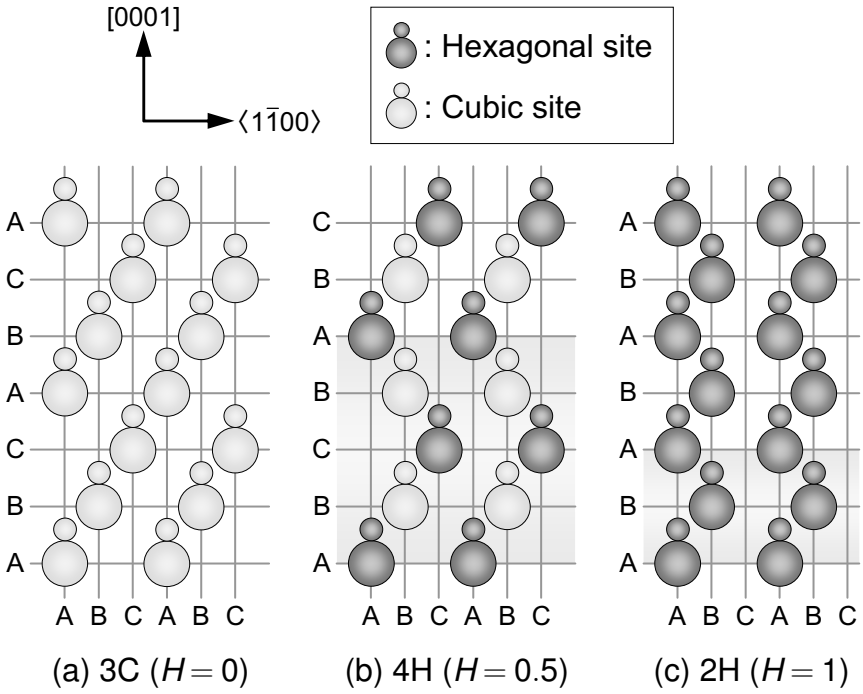

Figure 4.2: Schematics of crystal structure of (a) 3C, (b) 4H and (c) 2H. The atoms are classified into hexagonal sites (dark gray) and cubic sites (light gray). The hexagonality H of each structure is shown.

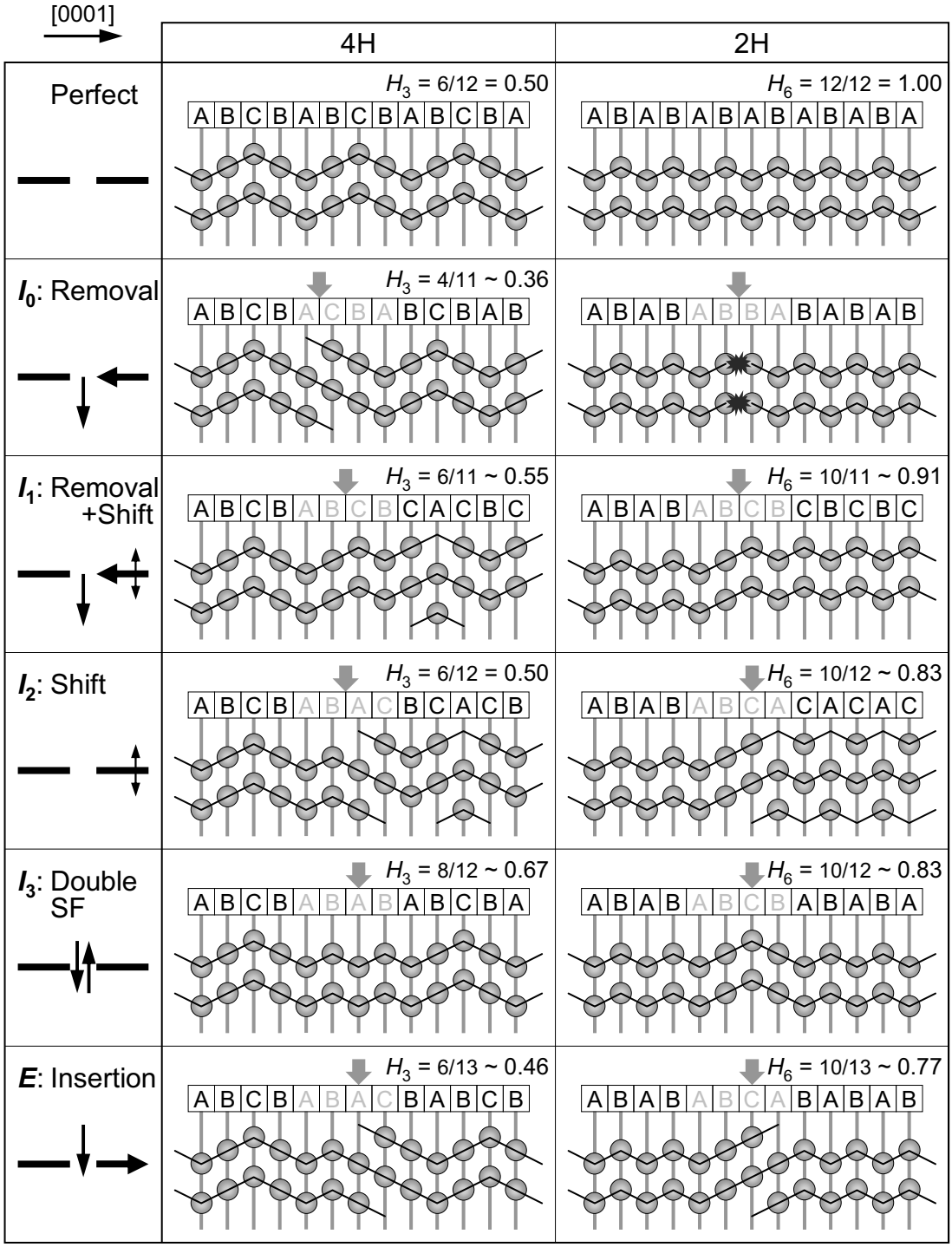

Figure 4.3: Schematics of SF structures in 4H- and 2H-polytype crystals. Partial hexagonality H_n in 3 units (4H) and 6 units (2H) along c-axis are shown.

direction. In 2H-polytype, this operation is impossible since the same bilayer appears alternately.

- I_1: A single bilayer is removed and the original crystal is shifted along the a- and c-axis directions.
- I_2: The original crystal is shifted along the a-axis direction.
- I_3: A single bilayer is shifted along the a-axis direction. This SF can be regarded as two of I_2-type SFs, so-called double SF.
- E: A single bilayer is inserted and the original crystal is shifted along the c-axis direction.

In 2H-GaN $(11\bar{2}0)$ grown on 4H-SiC $(11\bar{2}0)$, SFs of the I_1, I_2 and I_3 types have been reported where I_1-type SFs are mainly contained [11]. These SFs accompanies partial dislocations at the end. Figure 4.4 shows the location of a partial dislocation and its Burgers vectors[1] in I_2, E and I_3-type SFs. The SFs are also classified into Shockley type and Frank type from the component of the Burgers vector of partial dislocations.

- Shockley type: The partial dislocation does not include [0001] components as shown in Fig. 4.4 (a). This SF does not generate c-axis lattice relaxation.
- Frank type: The partial dislocation contains [0001] components as shown in Fig. 4.4 (b). This SF contributes c-axis lattice relaxation.

In I_3-type SFs shown in Fig. 4.4 (c), the Burgers vector of partial dislocations $\boldsymbol{b}$ is $\mathbf{0}$. It is assumed that two partial dislocations with the same magnitude and opposite sign each other are located with the atomic spacing. While dangling bonds are lined along the dislocation because of the existence of dislocations, the magnitude of the strain field around the dislocation is very small compared with partial dislocations of I_2- or E-type SFs. For each type of SFs, the Burgers vectors of partial dislocations and the type of Shockley/Frank are listed in Table 4.1.

[1] There are several modes for definition of the Burgers vectors. In this thesis, the Burgers vectors are defined by the 'FS/LH (Imperfect)' mode, that is, following process;

1. determine a left-hand (LH) circuit to the direction of the dislocation travel in a perfect crystal,
2. apply the circuit to the imperfect crystal resulting in opening the circuit,
3. set the Burgers vector $\boldsymbol{b}$ to the vector from finish point to start point (Finish to Start: FS) in the non-closed circuit.

If one of the parameters (FS/SF, LH/RH and Imperfect/Perfect) is changed, the sign of the Burgers vector is inverted.

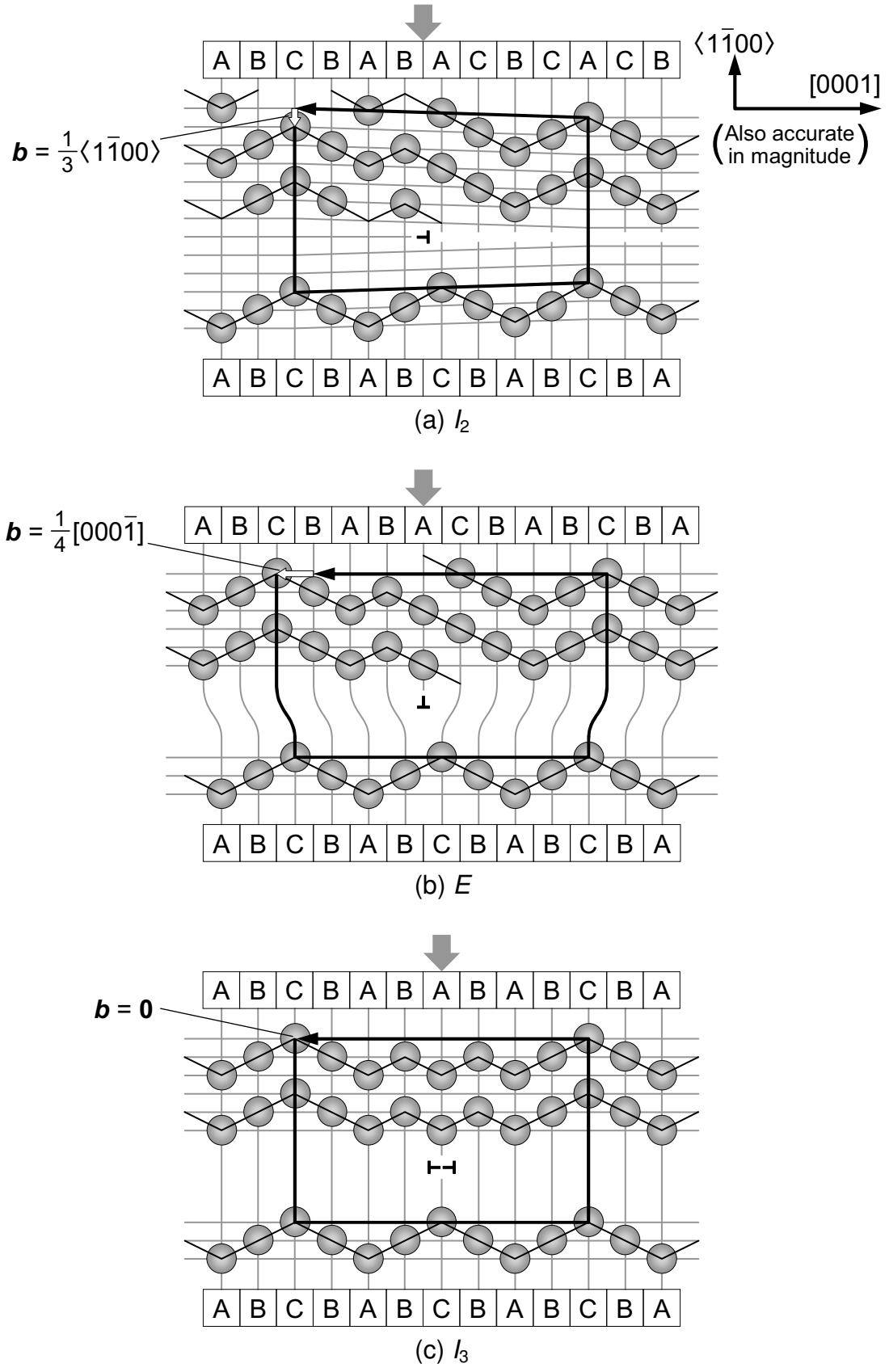

Figure 4.4: Structure schematics of (a) I_2- (b) E- (c) I_3-type SFs in 4H-polytype structure. For partial dislocations, the Burgers circuits (solid arrows) and the Burgers vectors (hollow arrows) are shown. The dislocations travel from the front side to the back side of the page.

Table 4.1: The Burgers vectors of partial dislocations and the type for each SF in 4H and 2H structures.

SF	$\boldsymbol{b}$ of partial dislocation		Type
	4H	2H	
I_0	$\frac{1}{4}[0001]$	$\frac{1}{2}[0001]$	Frank
I_1	$\frac{1}{3}\langle 1\bar{1}00\rangle + \frac{1}{4}[0001]$	$\frac{1}{3}\langle 1\bar{1}00\rangle + \frac{1}{2}[0001]$	Frank
I_2	$\frac{1}{3}\langle 1\bar{1}00\rangle$	$\frac{1}{3}\langle 1\bar{1}00\rangle$	Schockley
I_3	$\mathbf{0}$	$\mathbf{0}$	Schockley
E	$\frac{1}{4}[000\bar{1}]$	$\frac{1}{2}[000\bar{1}]$	Frank

4.2.2 Transmission electron microscopy analysis

Characterization of SFs and TDs has been partly performed in Sections 3.2.4 and 3.3.3. In addition to these, another observation was carried out to determine the defect structure certainly.

Figure 4.5 shows high-resolution TEM (HRTEM) of 4H-AlN $(11\bar{2}0)$ observed under the $\boldsymbol{g} = 0004$ condition of lattice imaging mode. In this mode, information of the $[10\bar{1}0]$ direction was lost and that of the [0001] direction was enhanced, resulting that the stacking structure was observed as the brightness. In the normal area, two bright stripes and two dark stripes were alternately observed. Compared with the 4H structure, it is expected that the atoms in hexagonal site are located between the bright strip and the dark strip. By applying this rule, the SF structure was determined to be ABCB<u>ABAB</u>ABCBA (I_3), which is the same result obtained in the previous chapter. The structure analysis was performed for more than 20 SFs, resulting that all of them have the same structure.

Figure 4.6 shows SFs in 4H-AlN grown on 4H-SiC $(11\bar{2}0)$ observed with different diffraction conditions. The SFs were visible under the diffraction condition of $\boldsymbol{g} = 10\bar{1}0$ while those were invisible under the diffraction condition of $\boldsymbol{g} = 0004$. In addition, two types of partial dislocations were observed at the AlN/SiC interface. One was high contrast (denoted by "1") and the other was low contrast (denoted by "2") under the diffraction condition of $\boldsymbol{g} = 10\bar{1}0$ (Fig. 4.6 (a)) while both of them were faint under the diffraction condition of $\boldsymbol{g} = 0004$ (Fig. 4.6 (b)). From the explanation of the I_3-type SF structure shown in Fig. 4.4 (c), the Burgers vector of partial dislocations accompanied with the I_3-type SFs is $\mathbf{0}$. This leads to the negligible small strain field and no contrast in low-magnification TEM images[2]. However, the interfacial dislocation denoted by "1" in Fig. 4.6 (a) was observed in high contrast under the diffraction condition of $\boldsymbol{g} = 10\bar{1}0$, indicating that the partial dislocation have the Burgers vector of $\boldsymbol{b} = \frac{1}{3}\langle 1\bar{1}00\rangle$. One possible explanation for these defects is that the SF consists of a set of two I_2-type SFs as shown in Fig. 4.7. A pair of partial dislocations of opposite sign exists in nanometer-scale interval and the stacking structure between the dislocations is the same as that of I_2-type SFs. In this structure, the SF has the same structure of I_3-type SFs and a certain degree of strain is generated around the dislocations.

4.2.3 Impact of extended defects on x-ray diffraction linewidth

Issue of x-ray diffraction characterization

XRD is one of the most useful methods for characterization of extended defects due to the non-destructivity and widely used in various materials including Ⅲ–Ns. In Ⅲ–Ns (0001), symmetrical ω-scan is used for the evaluation of screw TDs, so-called the tilt com-

[2]In Fig. 3.12 in Section 3.2.4, partial dislocations were just observed as the end of SFs and there is no contrast originates from strain fields.

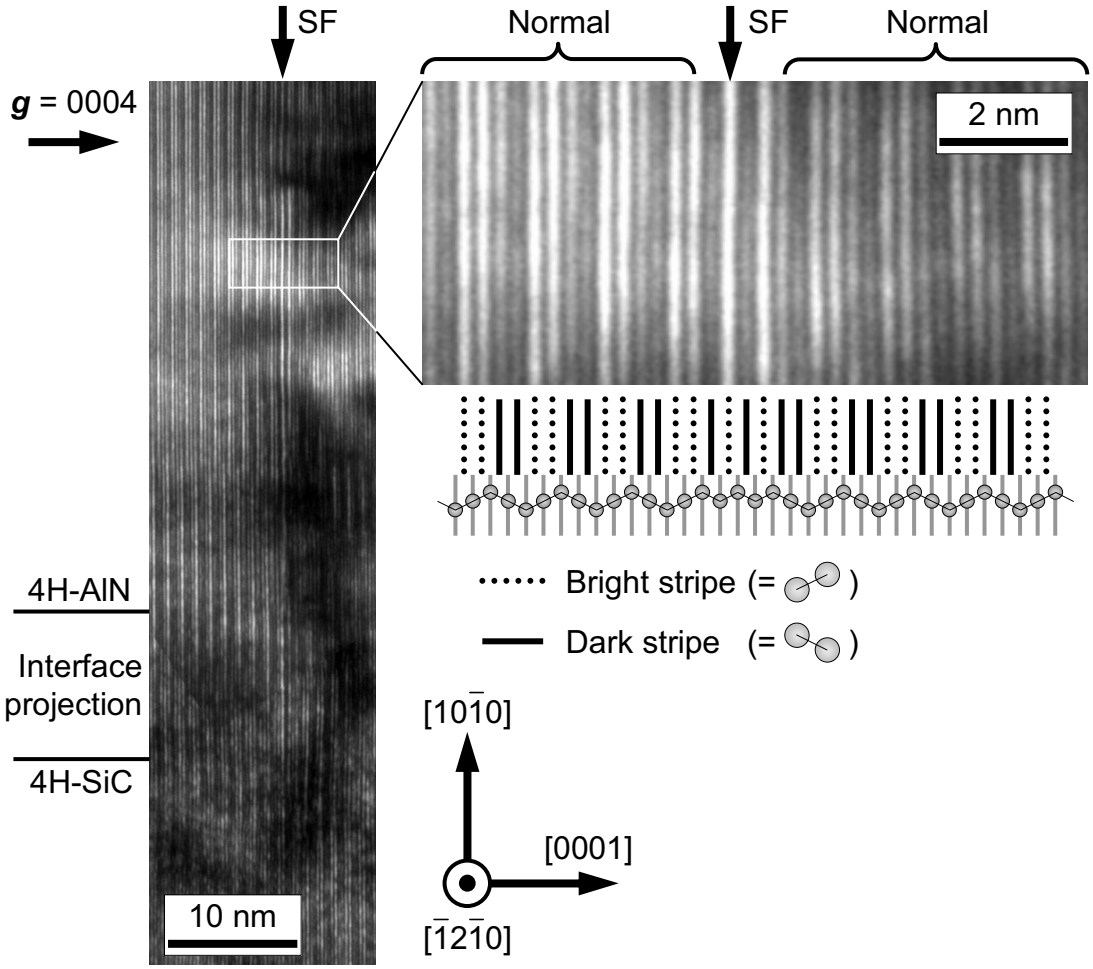

Figure 4.5: Cross-sectional HRTEM of 4H-AlN layers (11$\bar{2}$0) in a lattice imaging mode. Sample cutting with a 30° inclination and a [$\bar{1}$2$\bar{1}$0] incident beam were used as shown in the inset of Fig. 1.7. The area including a SF is magnified. Correspondence between the observed stripes and the crystal structure is shown.

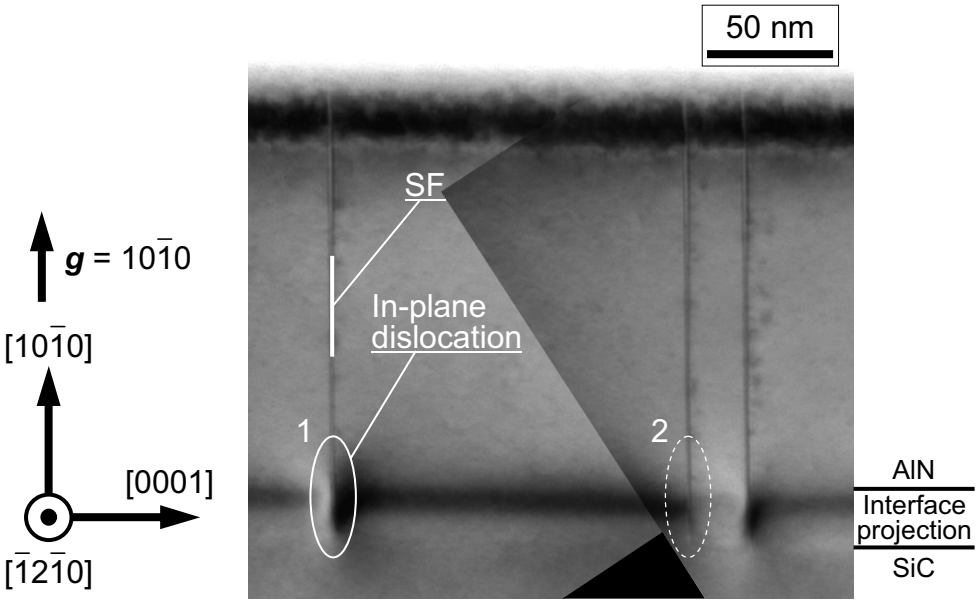

(a) $\boldsymbol{g} = 10\bar{1}0$

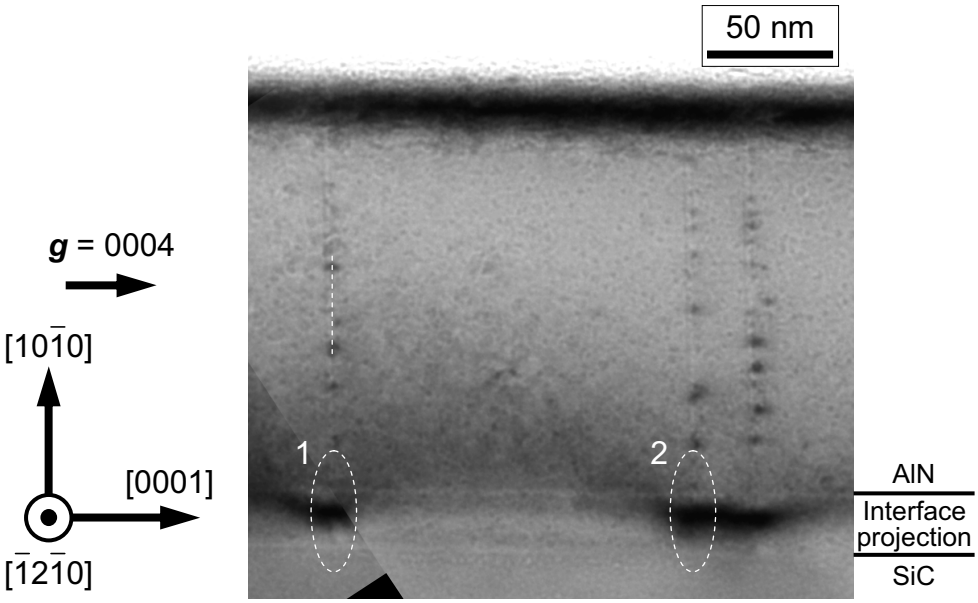

(b) $\boldsymbol{g} = 0004$

Figure 4.6: Cross-sectional TEM images of 4H-AlN layers grown on 4H-SiC (11$\bar{2}$0) observed in (a) $\boldsymbol{g} = 10\bar{1}0$ and (b) $\boldsymbol{g} = 0004$ diffraction conditions. Sample cutting with a 30° inclination and a [$\bar{1}$2$\bar{1}$0] incident beam were used as shown in the inset of Fig. 1.7. Faint contrasts of extended defects are shown by dashed lines. Interfacial dislocations with a fine contrast in (a) and a faint contrast in (b) (denoted by "1") and with a faint contrast in both conditions (denoted by "2") are visible.

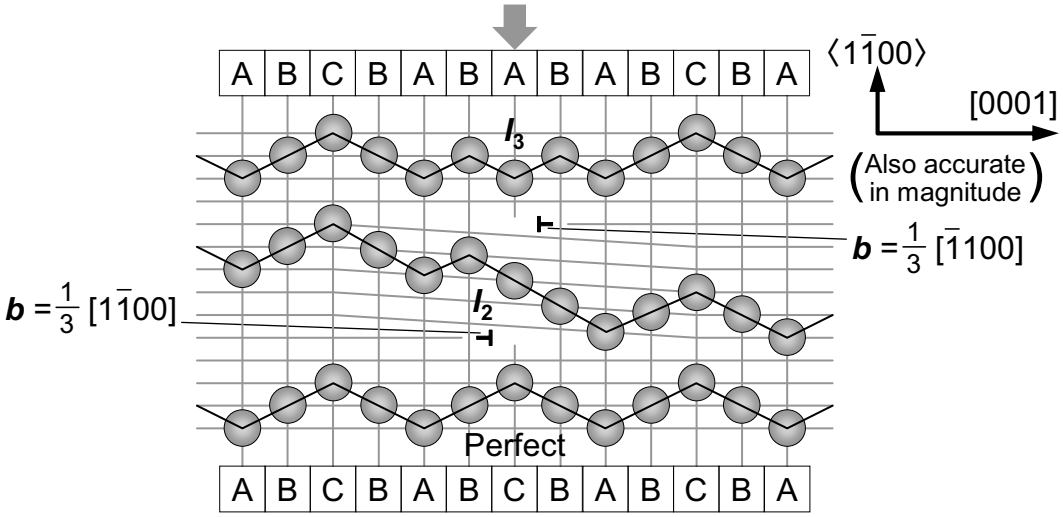

Figure 4.7: Structure schematics that two partial dislocations of the I_2 type form the same SF as the I_3 type in 4H-polytype structure. The dislocations travel from the front side to the back side of the page.

ponent, and asymmetrical ω-scan in the skew geometry or asymmetrical ϕ-scan is used for the characterization of edge TDs, so-called the twist component. In these measurements, the following characteristics are utilized: (1) the SF density is too low to affect, (2) the component difference of Burgers vectors ($[11\bar{2}0]/[0001]$) is correspond to the type of dislocations (screw/edge) and the effects are distinguished clearly, (3) the TD density is high compared with the interfacial dislocation, resulting in mainly contribution to broadening of the linewidth.

The situation is different in nonpolar Ⅲ–Ns including the 4H-AlN. In heteroepitaxially grown nonpolar Ⅲ–Ns, a number of basal plane SFs exist compared the case for Ⅲ–Ns (0001) [10]. Due to the high-density basal plane SFs and the accompanied partial dislocations, it has been reported that the FWHM value of ω-scans increase with the variation of x-ray incidence from $[1\bar{1}00]$ to [0001] [13]. In contrast to the reports, the different results were observed in nonpolar 4H-AlN grown on 4H-SiC. Figure 4.8 shows the XRD ω-scan spectra taken from 4H-AlN $(11\bar{2}0)$ and $(1\bar{1}00)$ with $[1\bar{1}00]/[11\bar{2}0]$ and [0001] x-ray incidence, where basal plane SFs are contained at the densities of 10^5–10^6 cm^{-1} as discussed in the previous chapter. The FWHM values are $\sim$50 arcsec independently to the beam incidence in both nonpolar faces, which are inconsistent results with the SF densities. In this section, the relationship between the SF density and the FWHM values of XRD ω-scans are described with theoretical analyses.

Calculation model

It is expected that broadening of the linewidth of XRD ω-scan peaks originates from the limitation of coherence length L_c. When the L_c along the beam incident direction is limited in a perfect crystal, the FWHM value δ is expressed in the following equation, so-called Scherrer's equation[3];

$$\delta = \frac{0.89\lambda}{L_\mathrm{c}\cos\theta_\mathrm{B}} \tag{4.1}$$

where the θ_B is the Bragg angle of a reflection plane and the λ is the wavelength of x-ray (=1.540562 Å). If the coherence length limited by every SFs, $L_\mathrm{c} = 1/\rho_\mathrm{SF}$ is given where the ρ_SF is the SF density. From the SF density of 4H-AlN, δ of ω-scan with [0001] x-ray incidence is estimated to be $300 \sim 3000$ arcsec.

The difference between the experimental results and the estimation of the FWHM value from Eq. 4.1 indicates that the coherence length does not limited by SFs. It is speculated that the limitation of the coherence length depends on the SF type. In order to understand the dependency, theoretical calculation was performed. Figure 4.9 shows the state of interference of two x-ray beams from the crystals separated by a SF. If the x-ray beams are in the same phase after the reflection, it shows that the SF does not limit the coherence

[3]The value of 0.89 is an approximate solution of the equation: $\mathrm{sinc}\left(\frac{\pi}{2}x\right) = \frac{1}{\sqrt{2}}$.

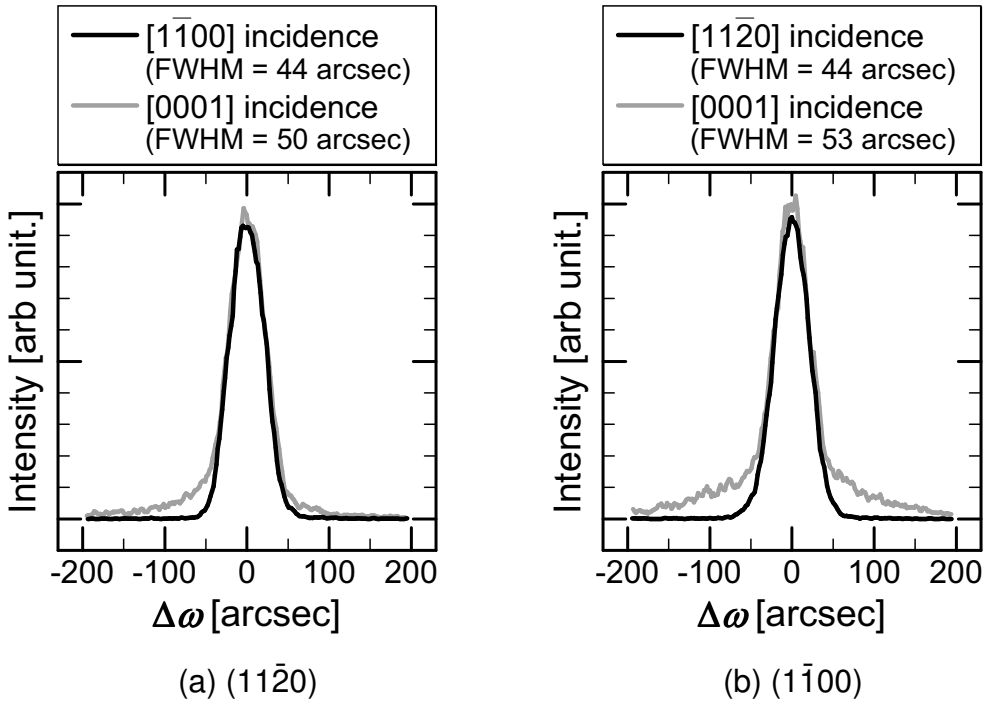

Figure 4.8: XRD ω-scan spectra of 4H-AlN (a) (11$\bar{2}$0) and (b) (1$\bar{1}$00) measured with the different x-ray incidence.

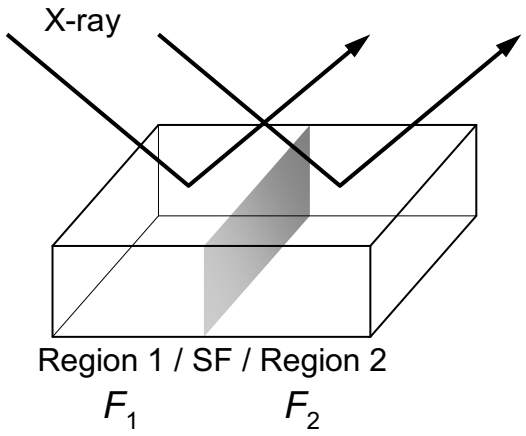

Figure 4.9: Schematics of x-ray interference from the crystals of the both sides of a SF.

length. The coherency of two x-ray beams were distinguished by the phase agreement of the crystal structure factor F;

$$F(\boldsymbol{g}) = \sum_{M=\mathrm{Al,N}} \sum_{j=1}^{4} f_j^M(\boldsymbol{g}) \exp\left(-2\pi \mathrm{i} \boldsymbol{g} \cdot \boldsymbol{r}_j^M\right) \tag{4.2}$$

where

$$\boldsymbol{g} = h\boldsymbol{a}_1^* + k\boldsymbol{a}_2^* + l\boldsymbol{c}^*, \tag{4.3}$$

$$\boldsymbol{r}_j^M = s_j^M \boldsymbol{a}_1 + t_j^M \boldsymbol{a}_2 + u_j^M \boldsymbol{c}. \tag{4.4}$$

The f_j^M, $\boldsymbol{g}$ and $\boldsymbol{r}_j^M$ show the atomic scattering factor, the diffraction vector and the position vector of atomic site, respectively. $\boldsymbol{a}_1$, $\boldsymbol{a}_2$ and $\boldsymbol{c}$ are the lattice translation vectors and $\boldsymbol{a}_1^*$, $\boldsymbol{a}_2^*$ and $\boldsymbol{c}^*$ are the reciprocal lattice vectors. The $\boldsymbol{g}$ is determined by the diffraction plane of XRD ($hk{\cdot}l$). The set of $\boldsymbol{r}_j^M$ ($M = \mathrm{Al}$, N, $j = 1, 2, 3, 4$) is determined by the crystal structures. The crystal structures for each SF type are listed in Table 4.2.

Relationships between x-ray diffraction linewidth and stacking fault type

The results are shown in Figure 4.10. For $\{11\bar{2}0\}$ reflections (symmetrical reflection on AlN $(11\bar{2}0)$ or asymmetrical $(1\bar{2}10)$ reflection on AlN $(11\bar{2}0)$ and $(1\bar{1}00)$), any types of SFs are not affect ω-scan spectra in both 4H and 2H structures. This result is consistent with the experimental results in 4H-AlN grown on 4H-SiC $(11\bar{2}0)$. On the other hand, it has been reported that the ω-scan linewidth in 2H-GaN $(11\bar{2}0)$ with the [0001] beam incidence is larger than that with the $[1\bar{1}00]$ beam incidence [13]. It is believed that the linewidth broadening originates from in-plane dislocations, which travel to in-plane directions and do not thread epilayers.

For $\{1\bar{1}00\}$ reflections (symmetrical reflection on AlN $(1\bar{1}00)$ or asymmetrical $(10\bar{1}0)$ reflection on AlN $(11\bar{2}0)$ and $(1\bar{1}00)$), the ω-scan linewidth is influenced by the I_1- and I_2-type SFs. This result is also consistent with the experimental results in 4H-AlN grown on 4H-SiC $(11\bar{2}0)$. If $\{3\bar{3}00\}$ reflections are used instead of $\{1\bar{1}00\}$, the ω-scan linewidth become insensitive to all types of SFs. For the detection of I_0- or E-type SFs, the $\{1\bar{1}02\}$ reflections are required. It should be noted that I_3-type SFs can not be detected in any diffraction planes.

4.2.4 Discussion

From the TEM observation, the major type of SFs contained in the 4H-AlN $(11\bar{2}0)$ and $(1\bar{1}00)$ layers is I_3 and the Burgers vector of partial dislocations is $\mathbf{0}$, which is the sum of the vectors of $\frac{1}{3}\langle 1\bar{1}00\rangle$ with the opposite sign. These results suggest that neither the SFs nor partial dislocations contained in nonpolar 4H-AlN affect the linewidth of XRD ω-scans. The situation in nonpolar 4H-AlN is different from that in nonpolar 2H-GaN. In the

Table 4.2: The relationships between the SF type and the stacking sequence of crystals in both side of the SF.

(a) 4H structure

Region 1	SF	Region 2
ABCB	I_1, I_2	CABC, ABAC, BACA, ACAB BCAC, CACB, ACBC, CBCA
ABCB	I_3	ABCB
ABCB	I_0, E	BCBA, CBAB, BABC

(b) 2H structure

Region 1	SF	Region 2
AB	I_1, I_2	BC, CA, CB, AC
AB	I_3	AB
AB	E	BA

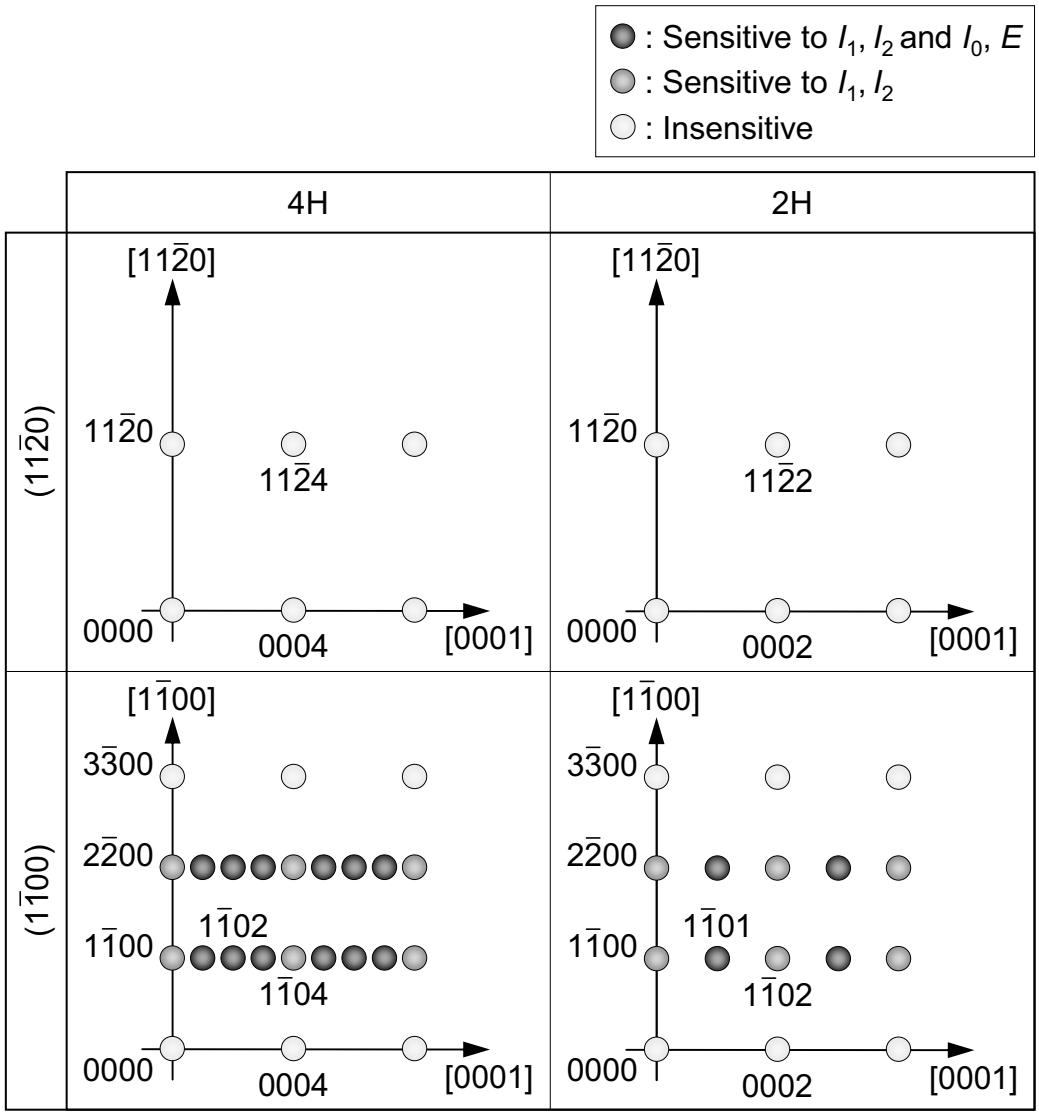

Figure 4.10: Dependence of sensitivity for XRD on the SF type and on the diffraction planes for 4H and 2H structure with $[11\bar{2}0]$ and $[1\bar{1}00]$ growth directions displayed in the reciprocal space.

nonpolar 2H-GaN, the major type of SFs is I_1 and the Burgers vector of partial dislocations is $\frac{1}{3}\langle 1\bar{1}00\rangle + \frac{1}{2}[0001]$. These SFs and partial dislocations contribute broadening of the ω-scan linewidth.

It is believed that the difference of extended-defect type between the 4H-AlN and 2H-GaN originates from the stability of the crystal phase and the magnitude of the lattice mismatch. Since the stacking order is changed in the SF region, the local hexagonality is varied. Due to the most stable structure of 2H (wurtzite), the closer value to 1 is more favorable for the hexagonality of Ⅲ–Ns. The local hexagonality H_n of SF structures is shown in Fig. 4.3, which is defined by the hexagonality of n units along c-axis including one SF. The I_3-type SF is the most stable for 4H structure while the I_1-type SF is the most for 2H structure. In 2H-GaN growth on sapphire or SiC substrates, a number of Frank-type SFs are required to relax the large lattice mismatch, resulting that the I_1-type SFs with the highest hexagonality are introduced. On the other hand, in nonpolar 4H-AlN growth on 4H-SiC, the polytype replication from substrates to epilayers effectively worked and a very few I_3-type SFs with the highest hexagonality are generated. Therefore, it is conclude that the narrow linewidth of XRD ω-scans is typical phenomena in isopolytypic 4H-AlN growth on 4H-SiC $(11\bar{2}0)$ and $(1\bar{1}00)$.

4.3 Lattice Constant

4.3.1 Measurement method and accuracy

The lattice constant of 4H-AlN is described. In contrast with Ⅲ–Ns (0001) (Fig. 4.11 (a)), it is expected that the 4H-AlN suffers from an anisotropic strain resulting that the sixfold symmetry along c-axis is violated as shown in Fig. 4.11 (b) and (c). In the orthorhombic crystal which results from the distortion of a hexagonal structure, the lattice constants of a, b and c are used for definition of the crystal structure. In order to express the lattice constant along the perpendicular direction to a-axis and the distortion of the crystal, parameters of m and γ are used, respectively, which are shown in Fig. 4.11 and defined as the following equations;

$$m = \sqrt{b^2 - \left(\frac{a}{2}\right)^2}, \tag{4.5}$$

$$\gamma = \cos^{-1}\left(-\frac{a}{2b}\right) \left(\frac{\pi}{2} < \gamma < \pi\right). \tag{4.6}$$

The lattice constants of m and c are in-plane directions for $(11\bar{2}0)$ growth and those of a and c are for $(1\bar{1}00)$ growth.

The three lattice constants of a, m and c are experimentally measured by three independent diffraction planes of HRXRD. To improve the accuracy and cancel the misalignment of diffractometer axes, a channel-cut double crystal Ge (220) analyzer was positioned in

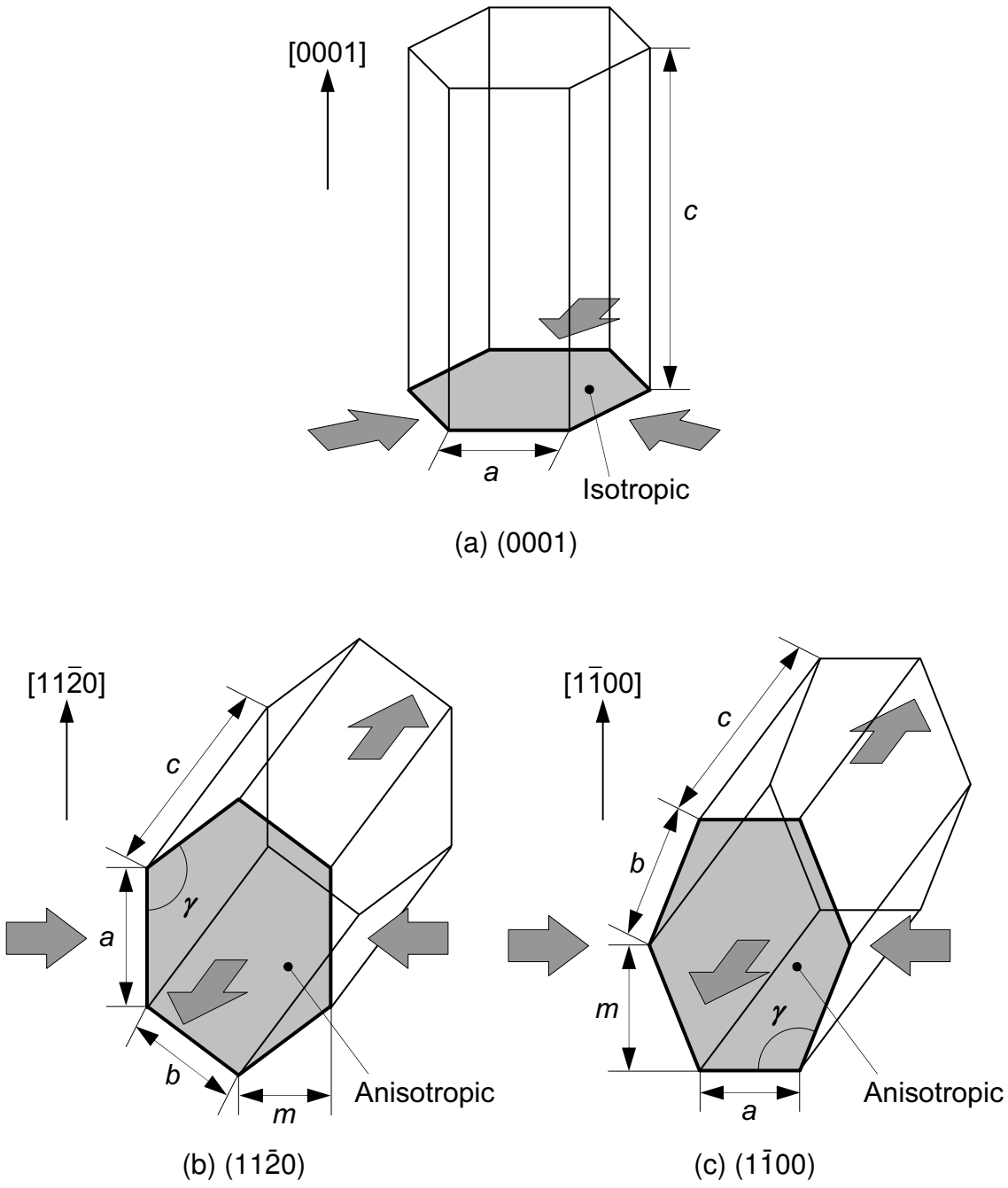

Figure 4.11: Schematics of distorted lattices with (a) [0001], (b) [11$\bar{2}$0] and (c)[1$\bar{1}$00] growth directions. The length of the lattice constants (a, b, c, m and γ) are shown.

front of a detector. The spacing of the planes d are calculated from the Bragg's equation;

$$d = \frac{\lambda}{2\sin\theta}. \tag{4.7}$$

From the differential form of Eq. 4.7, the relative error $\Delta\bar{d}$ of d is obtained;

$$\Delta\bar{d} = \frac{\Delta\theta}{\tan\theta} \tag{4.8}$$

where the θ and $\Delta\theta$ is the Bragg angle and its absolute error, respectively. This indicates that the higher-order diffraction gives the plane spacing with the smaller error. The lattice constants are calculated from the plane spacing by the operations of the constant product, the inverse and the Pythagoras's theorem in reciprocal space. The relative error is not changed by the operation of the constant product and the inverse, and the variations of the relative errors ($\Delta\bar{r}$, $\Delta\bar{x}$ and $\Delta\bar{y}$) by the operation using the Pythagoras's theorem are shown;

$$r = \sqrt{x^2 + y^2} \Rightarrow \Delta\bar{r} = \Delta\bar{x}\cos^2\alpha + \Delta\bar{y}\sin^2\alpha \tag{4.9}$$

$$y = \sqrt{r^2 - x^2} \Rightarrow \Delta\bar{y} = \frac{\Delta\bar{r}}{\sin^2\alpha} + \frac{\Delta\bar{x}}{\tan^2\alpha} \tag{4.10}$$

where the α is defined by $\tan\alpha = y/x$. It should be noted that diffraction planes should be selected to be enlarged the α to avoid magnification of an error when Eq. 4.10 is used. The absolute error of θ is estimated from the FWHM value of $2\theta/\omega$-scan, and the relative errors of the lattice constants are calculated using Eqs. 4.8–4.10.

4.3.2 Lattice constant measurement

The lattice constants of 270-nm-thick 4H-AlN $(11\bar{2}0)$ and $(1\bar{1}00)$ layers were measured as well as the 4H-SiC substrates. Considering the usage of high-order diffraction and the large angle of α for reduction of errors, the $(11\bar{2}0)$, $(11\bar{2}4)$ and $(1\bar{2}10)$ reflections were used for the $(11\bar{2}0)$ measurement, and the $(3\bar{3}00)$, $(2\bar{2}06)$ and $(30\bar{3}0)$ reflections were used for the $(1\bar{1}00)$ measurement. The results were shown in Table 4.3.

In both nonpolar faces, the in-plane lattice constants of 4H-AlN were the same as that of 4H-SiC, where the lattice mismatches in the in-plane directions is less than 0.02%. The angle γ of 4H-AlN is 0.2° larger or smaller than the undistorted value of 120°, suggesting that the lattice of 4H-AlN layers is distorted from the hexagonal structure. From the lattice constants measurements, the 4H-AlN layers are grown almost coherently on 4H-SiC substrates in both $(11\bar{2}0)$ and $(1\bar{1}00)$ growth.

4.3.3 Discussion

It has been revealed that the nonpolar 4H-AlN is coherently grown on 4H-SiC. This result is consistent with the TEM observations where I_3-type SFs are mainly contained and can

Table 4.3: The lattice constants of 4H-AlN layers grown on 4H-SiC (a) $(11\bar{2}0)$ and (b) $(1\bar{1}00)$. The lattice constants of 4H-SiC substrates and the lattice mismatches between the epilayer and the substrate are shown.

(a) 4H-AlN $(11\bar{2}0)$ / 4H-SiC $(11\bar{2}0)$

Parameter		4H-SiC substrate	4H-AlN epilayer	Difference
In-plane	c [Å]	10.0852 ± 0.0005	10.0853 ± 0.0018	<0.03%
	m [Å]	2.66772 ± 0.00003	2.66763 ± 0.00008	<0.005%
Out-of-plane	a [Å]	3.08020 ± 0.00002	3.10562 ± 0.00009	+0.83%
Distortion	γ [°]	119.9982 ± 0.0005	120.204 ± 0.002	+0.204°

(b) 4H-AlN $(1\bar{1}00)$ / 4H-SiC $(1\bar{1}00)$

Parameter		4H-SiC substrate	4H-AlN epilayer	Difference
In-plane	c [Å]	10.0860 ± 0.0005	10.0867 ± 0.0010	<0.02%
	a [Å]	3.08135 ± 0.00006	3.08064 ± 0.00013	−0.02%
Out-of-plane	m [Å]	2.66817 ± 0.00003	2.69096 ± 0.00007	+0.85%
Distortion	γ [°]	120.0033 ± 0.0011	119.788 ± 0.003	−0.212°

not generate lattice relaxation. On the other hand, the growth thickness of 270 nm is much larger than the critical thickness of AlN/SiC, which has been reported to be ∼5 nm [8, 14, 15]. One possible explanation for the coherent growth is that the lattice constants of 4H-AlN are varied from those of 2H-AlN. Figure 4.12 shows the relationship of the lattice constants among 2H-AlN, 3C-AlN and 4H-SiC. It is assumed that the lattice constants of 4H-AlN is between 2H and 3C. The c-axis lattice constant of AlN crosses over that of 4H-SiC between 2H- and 3C-AlN, and the a-axis lattice constant of AlN approach to that of 4H-SiC with varying from 2H- to 3C-AlN. Therefore, the lattice mismatches between 4H-AlN and 4H-SiC are smaller than those between 2H-AlN and 4H-SiC. The lattice constants of bulk 4H-AlN are unable to be calculated since the 4H-AlN epilayers suffer from a large biaxial strain. A relaxed thick 4H-AlN layer with no 2H inclusions is needed for estimation of the lattice constants of bulk 4H-AlN. Nevertheless measurements of XRD and TEM suggest the variation of the lattice constants from 2H-AlN to 4H-AlN.

4.4 Bandgap Energy

4.4.1 Prediction from SiC polytypism and theoretical calculation

The polytypism of the bandgap energy has been reported in SiC as shown in Fig. 4.13 [16]. 2H structure has the highest bandgap energy in the polytype structures of SiC. It is briefly expected that the bandgap energy of 4H-AlN is smaller than that of 2H-AlN.

The transition types are important as well as the bandgap energies. In first-principle studies, it is reported that 3C-AlN is the indirect transition type while 2H-AlN is the direct transition type [17–20]. Since the 4H is intermediate structure between 2H and 3C, the transition type of 4H-AlN can not be readily determined. Table 4.4 (a) shows the reported values of the bandgap energy (E_{g}) and transition type for AlN [20]. The calculation was also performed in this study, which is shown in Table 4.4 (b). It should be noted that both the calculations were based on the local density approximation (LDA) in density functional theory (DFT) where the values of the bandgap energy were underestimated. Both the calculations suggest that 4H-AlN has the indirect band structure and that the bandgap energy of 4H-AlN is smaller than that of 2H-AlN. On the other hand, Kobayashi *et al.* have reported that the transition type of 3C-AlN is changed to direct by a large tensile strain (−31.5 GPa). Therefore, it is expected that the 4H-AlN is similarly changed to be direct with a smaller strain because of the smaller difference between the bandgap energy and the energy for direct transition ($E_{\mathrm{d}} - E_{\mathrm{g}}$). Indeed, the 4H-AlN layers suffer from a large biaxial strain from SiC substrates.

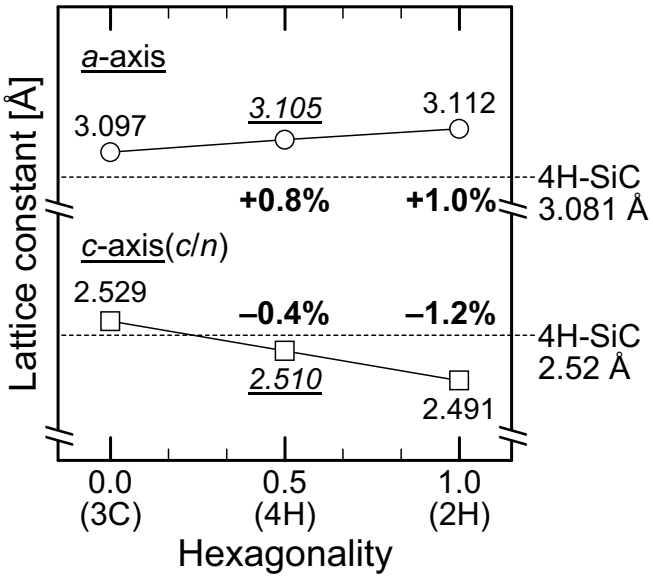

Figure 4.12: The lattice constants of 2H-AlN and 3C-AlN compared with that of 4H-SiC. The lattice constants of 4H-AlN are estimated from those of 2H- and 3C-AlN with linear approximation. The lattice mismatches between 2H-AlN and 4H-SiC and between 4H-AlN and 4H-SiC are shown.

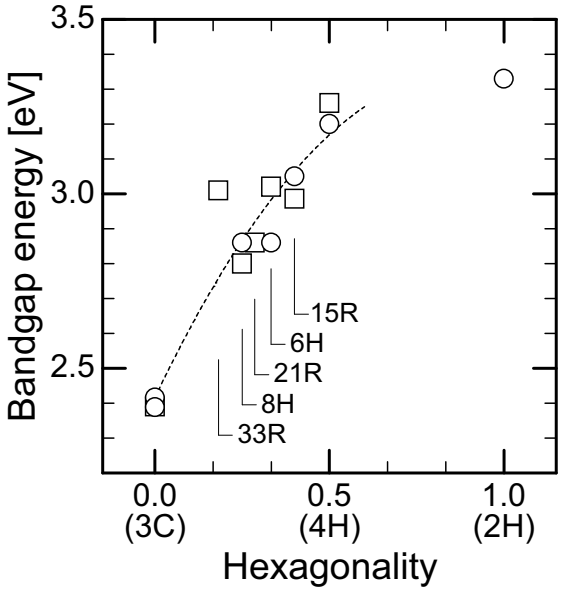

Figure 4.13: Dependence of the bandgap energy of SiC on the polytype [16]. The variation of the guide to the eye is shown by the dashed line.

Table 4.4: Calculated band parameters for AlN polytypes; (a) reported in Ref. 20 and (b) obtained in this study. Both the calculations are based on the DFT-LDA where the values of the bandgap energy were underestimated.

(a) Report in Ref. 20

Strcuture	Transition type	E_g[eV]	E_d[eV]	$E_d - E_g$[eV]	VBM–CBM
3C	Indirect	3.24	4.29 (Γ)	1.05	Γ–X
6H	Indirect	3.74	4.27 (M)	0.53	Γ–M
4H	Indirect	3.95	4.30 (Γ)	0.35	Γ–M
2H	Direct	4.31	4.31 (Γ)	0.00	Γ–Γ

(b) This study

Strcuture	Transition type	E_g[eV]	E_d[eV]	$E_d - E_g$[eV]	VBM–CBM
3C	Indirect	3.37	4.16 (Γ)	0.79	Γ–X
6H	Indirect	3.92	4.22 (Γ)	0.30	Γ–M
4H	Indirect	4.15	4.24 (Γ)	0.09	Γ–M
2H	Direct	4.31	4.31 (Γ)	0.00	Γ–Γ

E_g: Bandgap energy
E_d: Energy for direct transition
VBM: Valence band maximum
CBM: Conduction band minimum

4.4.2 Optical reflectance and cathodoluminescence

In order to obtain the bandgap energy of 4H-AlN experimentally, optical reflectance (OR) and cathodoluminescence (CL) measurements were performed. Figure 4.14 shows the OR and CL spectra taken from the 4H-AlN grown on 4H-SiC ($11\bar{2}0$) and 2H-AlN grown on 6H-SiC (0001). In the CL spectra, the band edge emission was observed at 5.82 and 5.99 eV for 4H-AlN and 2H-AlN, respectively. Since the AlN has an exciton binding energy of $50 \sim 80$ meV [21, 22], excitons can stably exist at room temperature. Therefore, the luminescence peaks from AlN originate from excitons. The luminescence peak of 5.99 eV in 2H-AlN at room temperature is reported to be bound exciton [23, 24]. In the OR spectra, the absorption edge was observed around 5.9 and 6.1 eV for 4H-AlN and 2H-AlN, respectively. Compared with several reports [24, 25], the absorption edge of the E_{A} exciton was determined at 6.11 eV for 2H-AlN. Although the shape of OR spectra for 4H-AlN was different from that for 2H-AlN, the absorption edge of the E_{A} exciton was determined at 5.88 eV for 4H-AlN. From these observations, it is determined that the bandgap energy of 4H-AlN is $\sim$0.2 eV smaller than that of 2H-AlN.

In CL spectra, the intensity of bound exciton peaks for 4H-AlN was comparable to that for 2H-AlN. In general, the intensity of the near band edge emissions for indirect transition semiconductor is several orders of magnitude lower than that for direct transition semiconductor. Consequently, it is believed that the 4H-AlN is direct transition type.

4.4.3 Discussion

The bandgap energy of 4H-AlN is $\sim$0.2 eV smaller than that of 2H-AlN. The calculation agreed with the experimental data in the tendency of variation from 2H- to 4H-AlN while it was not supported in the magnitude of the variation. Kobayashi *et al.* have reported that the variation of the bandgap energy from 2H- to 4H-AlN is 0.36 eV and the calculation in this study suggests that the variation is 0.07 eV. In addition, it is believed that the transition type of 4H-AlN is direct from the CL measurement while the calculations give a result of the indirect transition.

To make a solution for the inconsistence, it will be required to reconsider from the both sides of the calculation accuracy and the experimental condition. In the experimental, the CL and OR measurements were just carried out at room temperature. The measurements at a low temperature of liquid helium are essential to obtain the sharp peaks without phonon interaction. In OR measurement, a thick AlN layer (several microns) or an AlN layer with antireflection coating will be effective to avoid the interference and to obtain a precise value of luminescence peaks. The theoretical calculations imply that the transition type of the band structure is changed by the strain. The dependence of OR spectra on the strain field will provide the experimental evidence of the transition type switching.

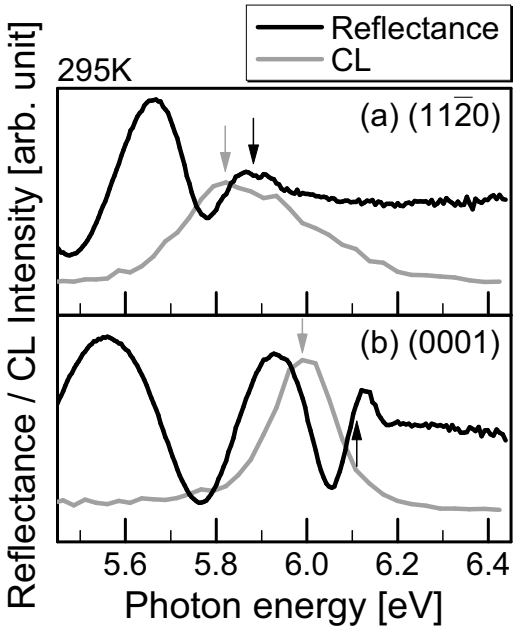

Figure 4.14: Spectra of optical reflectance (black) and cathodoluminescence (CL) (gray) from (a) 4H-AlN (11$\bar{2}$0) and (b) 2H-AlN (0001). The black arrows show the absorption edges of E_{A} and the gray arrows show the CL peaks from bound excitons.

4.5 Lattice Vibration Mode

4.5.1 Measurement of lattice vibration mode

Crystal has natural lattice vibration, which closely relates to the crystal structure. To know the lattice vibration mode of 4H-AlN results in elucidation of the physical properties of AlN. In this study, microscopic Raman scattering measurements were carried out for the 4H-AlN $(11\bar{2}0)$ to obtain the phonon mode at Γ point.

The measurements were performed with two different geometries, $x(y,-)\bar{x}$ and $x(z,-)\bar{x}$ as shown in Fig. 4.15. Here, Porto's notation is used [26]: x and $\bar{x}$ are the laser incident and scattered directions ($[11\bar{2}0]$), and y or z is the polarization direction of incident light, where y and z are the directions along $[1\bar{1}00]$ and [0001], respectively. From the Raman selection rules, the observable phonon modes are A_1(TO), E_1(TO) and E_2 in backscattering configurations of hexagonal nitrides, which are listed in Table 4.5 [26]. The typical phonon frequencies observed at 300K for 2H-AlN reported by Davydov *et al.* are shown in Table 4.6 [27].

Figure 4.16 shows Raman spectra of 0.5-μm-thick 4H-AlN and 1.0-μm-thick 2H-AlN grown under Al-rich and N-rich conditions, respectively. One peak (A_1(LA)) from the SiC substrate and three peaks (A_1(TO), ${E_2}^{\mathrm{H}}$, E_1(TO)) from the AlN layers were observed in the range of $600 \sim 700$ cm^{-1}. The observed peaks were assigned by considering their frequencies and Raman selection rules shown in Tables 4.5 and 4.6. Reported phonon frequencies of bulk 2H-AlN crystal are shown in Fig. 4.16 (dashed line). The peak positions of 4H-AlN were very different from those of bulk AlN, especially the A_1(TO) peak, while those of 2H-AlN were almost the same. Shifts of the A_1(TO), ${E_2}^{\mathrm{H}}$ and E_1(TO) peaks from bulk 2H-AlN were estimated to be +25.0, −2.6 and −6.4 cm^{-1} for 4H-AlN and +7.9, +0.6 and +0.3 cm^{-1} for 2H-AlN, respectively.

4.5.2 Discussion

The Raman shift values were estimated from the strain and the phonon deformation potential to compare the values experimentally obtained. The Raman shift $\Delta\omega_\lambda$ was expressed with the triaxial strain ϵ_{xx}, ϵ_{yy}, ϵ_{zz} and the deformation potentials a_λ, b_λ [28, 29];

$$\Delta\omega_\lambda = a_\lambda \left(\epsilon_{xx} + \epsilon_{yy}\right) + b_\lambda \epsilon_{zz}. \tag{4.11}$$

where the x-axis, y-axis and z-axis are parallel to $[11\bar{2}0]$, $[\bar{1}100]$ and [0001], respectively. The deformation potentials are listed in Table 4.7. The triaxial strain was estimated from the strain along the in-plane directions and the elastic constants;

$$\epsilon_{xx} = -\frac{C_{12}\epsilon_{yy} + C_{13}\epsilon_{zz}}{C_{11}}, \tag{4.12}$$

assumed the stress along growth direction $\sigma_{xx} = 0$. The elastic constants of $C_{11} = 345$ GPa, $C_{12} = 125$ GPa and $C_{13} = 120$ GPa were used [7] where the variation from 2H-AlN to

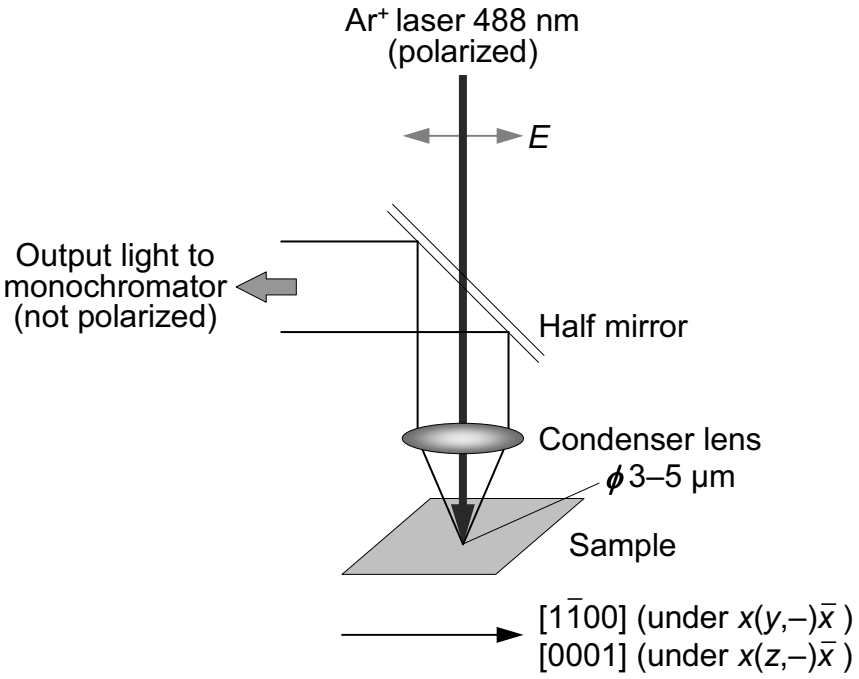

Figure 4.15: Schematics of the geometry of incident light and samples in the Raman spectroscopy system.

Table 4.5: Obsevable configurations of phonon modes in hexagonal Ⅲ-Ns.

Mode	$x(y,-)\bar{x}$		$x(z,-)\bar{x}$	
	$x(y,y)\bar{x}$	$x(y,z)\bar{x}$	$x(z,y)\bar{x}$	$x(z,z)\bar{x}$
A_1(TO)	+	−	−	+
E_1(TO)	−	+	+	−
E_2	+	−	−	−

Table 4.6: Typical phonon frequencies observed at 300K for (a) 2H-AlN and (b) 3C-AlN [27].

(a) 2H-AlN

Phonon mode	Frequency
$E_2{}^{\mathrm{L}}$	248.6
A_1(TO)	611
E_1(TO)	670.8
$E_2{}^{\mathrm{H}}$	657.4
A_1(LO)	890
E_1(LO)	912

(b) 3C-AlN

Phonon mode	Frequency
TO	655
LO	902

[unit: cm^{-1}]

Table 4.7: Phonon deformation potentials a_λ and b_λ for 2H-AlN [28].

	A_1(TO)	E_1(TO)	$E_2{}^{\mathrm{H}}$
a_λ	-784	-832	-877
b_λ	-390	-746	-911

[unit: cm^{-1}]

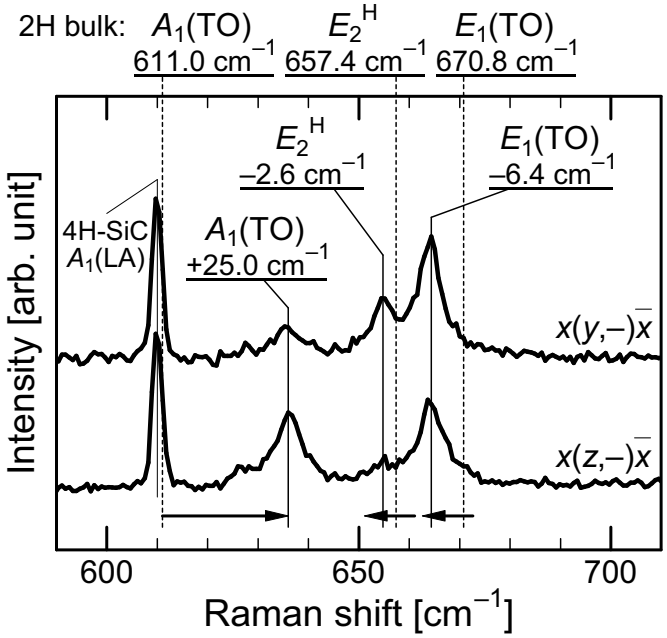

(a) 4H-AlN grown under Al-rich conditions

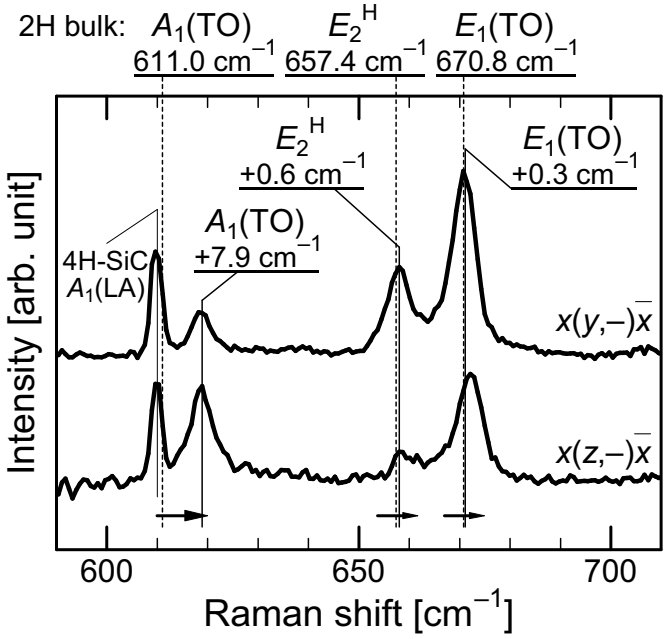

(b) 2H-AlN grown under N-rich conditions

Figure 4.16: Raman spectra taken from AlN layers under the $x(y,-)\bar{x}$ and $x(z,-)\bar{x}$ conditions; (a) 4H-AlN layers grown under Al-rich conditions and (b) 2H-AlN layers grown under N-rich conditions. The peak positions of 2H-AlN bulk reported and the peak shifts from the bulk are shown.

4H-AlN is ignored. The strain along the in-plane directions were assumed for the situations of (1) fully relaxed, (2) m-axis uniaxial coherent, (3) c-axis uniaxial coherent and (4) biaxial coherent. The results of the Raman shift estimation are shown in Table 4.8.

From the estimation, the Raman shift of AlN grown on 4H-SiC was in the range from -5.0 to $+7.0$ cm^{-1}. Compared with this, the shift of 4H-AlN experimentally obtained was out of the estimation while that of 2H-AlN was almost in the expected range. In particular, the shift of the A_1(TO) peak of 4H-AlN ($+25$ cm^{-1}) is too large to be explained by residual strain alone.

Since material properties depend on the crystal polytype in general, it does not make sense to attempt to evaluate the strain in the 4H-AlN epilayer by direct comparison with Raman data for bulk 2H-AlN. The dependence of phonon frequencies was also successfully explained by the concept of hexagonality [30]. This concept was applied to AlN. Since the hexagonality of the 4H structure is 0.5, in a first-order approximation the physical constants of 4H-AlN should lie in between those of 2H-AlN and 3C-AlN. As to the phonon frequencies, LO and TO modes of 3C-AlN split into A_1 and E_1 modes as shown in Fig. 4.17. Figure 4.18 shows the experimental Raman spectra of 4H-AlN compared with calculated 4H-AlN frequencies from the first-order approximation. The experimentally observed peaks agree well with the estimated frequencies. This agreement was confirmed by measurements of several other 4H-AlN layers. Although the calculation of phonon frequencies of bulk 4H-AlN has some error, good agreement between observed peaks and calculated peaks indicates successful observation of phonon mode of 4H-AlN.

4.6 Summary

Structure of extended defects in 4H-AlN and the relationship between extended defects and the linewidth of XRD have been discussed. TEM observation reveals that the stacking faults have the I_3 type structure (stacking sequence of ABCB<u>ABAB</u>ABCB), which are classified in Shockley type. The Burgers vector of the partial dislocations is determined to be $\mathbf{0}$, which is the sum of the vectors of $\frac{1}{3}\langle 1\bar{1}00\rangle$ with the opposite sign. The theoretical analysis revealed that the I_3-type SFs mainly contained in 4H-AlN can not be detected by XRD leading to the narrow linewidth of XRD ω-scans.

In addition to extended-defect structure, the lattice constant, the bandgap energy and the phonon mode of 4H-AlN have been investigated to understand the properties of 4H-AlN. HRXRD measurement reveals that the in-plane lattice constants of 4H-AlN are the same as those of 4H-SiC substrates, indicating that the 4H-AlN is coherently grown on 4H-SiC. From the OR and CL spectra from 4H-AlN, the bandgap energy of 4H-AlN is estimated to be about 0.2 eV smaller than that of 2H-AlN. In laser Raman scattering spectroscopy, the phonon peaks of A_1(TO), E_1(TO) and ${E_2}^{\mathrm{H}}$ are observed. These peaks are determined to be the phonon modes of 4H-AlN, which are different from those of 2H-AlN.

Table 4.8: The baiaxial strain under ideal coherent situations in 2H-AlN on 4H-SiC and the Raman shift estimated using the strains and the deformation potenstial.

		Relaxed	Uniaxially coherent		Biaxially coherent
			m-axis	c-axis	
Strain	ϵ_{xx}	0.00%	−0.36%	+0.40%	+0.04%
	ϵ_{yy}	0.00%	+1.01%	0.00%	+1.01%
	ϵ_{zz}	0.00%	0.00%	−1.15%	−1.15%
Raman shift [cm^{-1}]	A_1(TO)	0.0	−5.0	+1.3	−3.7
	E_1(TO)	0.0	−5.3	+5.3	−0.1
	$E_2{}^{\mathrm{H}}$	0.0	−5.6	+7.0	+1.3

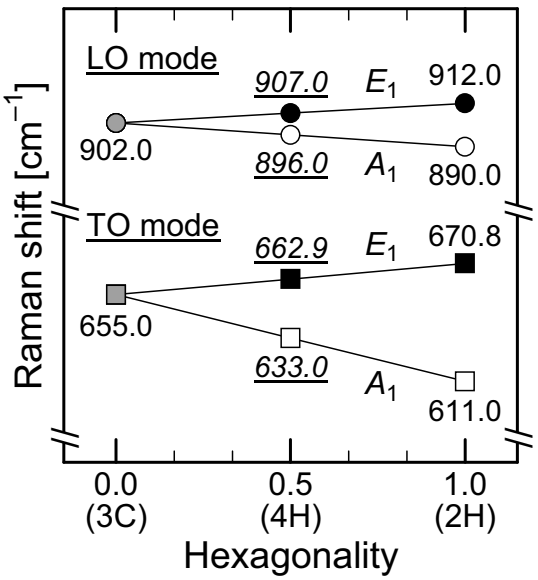

Figure 4.17: Splitting of phonon peaks of TO and LO modes from 3C- to 2H-AlN.

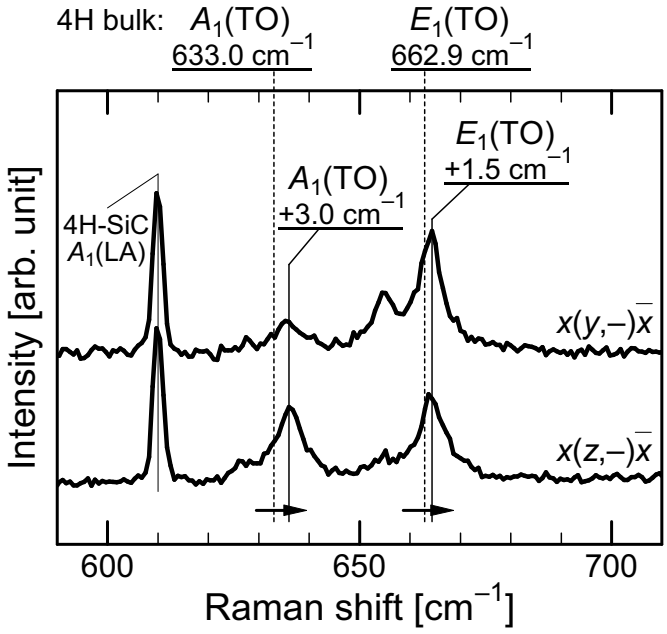

Figure 4.18: Raman spectra obtained from 4H-AlN layers grown under Al-rich (the same as the spectra shown in Fig. 4.16 (a)). The peak positions of 4H-AlN bulk estimated and the peak shifts from the bulk are shown.

References

[1] W. Yim, E. Stofko, P. Zanzucchi, J. Pankove, M. Ettenberg, and S. Gilbert, J. Appl. Phys. **44**, 292 (1973).

[2] I. Petrov, E. Mojab, R. C. Powell, J. E. Greene, L. Hultman, and J. E. Sundgren, Appl. Phys. Lett. **60**, 2491 (1992).

[3] Q. Gao and A. Yoshida, Jpn. J. Appl. Phys. **33**, 2453 (1994).

[4] W. R. L. Lambrecht and B. Segall, Phys. Rev. B **43**, 7070 (1991).

[5] M. F. MacMillan, R. P. Devaty, and W. J. Choyke, Appl. Phys. Lett. **62**, 750 (1993).

[6] H. Harima, T. Inoue, S. Nakashima, H. Okumura, Y. Ishida, S. Yoshida, T. Koizumi, H. Grille, and F. Bechstedt, Appl. Phys. Lett. **74**, 191 (1999).

[7] K. Tsubouchi and T. Mikoshiba, IEEE Trans. Sonics Ultrason. **32**, 634 (1985).

[8] M. E. Sherwin and T. J. Drummond, J. Appl. Phys. **69**, 8423 (1991).

[9] N. Onojima, J. Suda, T. Kimoto, and H. Matsunami, Appl. Phys. Lett. **83**, 5208 (2003).

[10] B. A. Haskell, F. Wu, M. D. Creven, P. T. Fini, S. P. DenBaars, J. S. Speck, and S. Nakamura, Appl. Phys. Lett. **83**, 1554 (2003).

[11] D. N. Zakharov, Z. Liliental-Weber, B. Wagner, Z. J. Reitmeier, E. A. Preble, and R. F. Davis, Phys. Rev. B **71**, 235334 (2005).

[12] F. Bechstedt, P. Käckell, A. Zywietz, K. Karch, B. Adolph, K. Tenelsen, and J. Furthmüller, phys. stat. sol. (b) **202**, 35 (1997).

[13] H. Wang, C. Chen, Z. Gong, J. Zhang, M. Gaevski, M. Su, J. Yang, and M. A. Khan, Appl. Phys. Lett. **84**, 499 (2004).

[14] S. Tanaka, R. S. Kern, R. F. Davis, and J. Bentley, Jpn. J. Appl. Phys. **35**, 1641 (1996).

[15] J. W. Matthews and A. E. Blaskeslee, J. Cryst. Growth **27**, 118 (1974).

[16] W. van Haeringen, P. A. Bobbert, and W. H. Backes, phys. stat. sol. (b) **202**, 63 (1997).

[17] F. Sökeland, M. Rohlfing, P. Krüger, and J. Pollmann, Phys. Rev. B **68**, 075203 (2003).

[18] H. Hernández-Cocoletzi, D. A. Contreras-Solorio, and J. Arriaga, Appl. Phys. A **81**, 1029 (2005).

[19] M. B. Kanoun, S. Goumri-Said, A. E. Merad, and H. Mariette, J. Appl. Phys. **98**, 063710 (2005).

[20] K. Kobayashi and S. Komatsu, J. Phys. Soc. Jpn. **77**, 084703 (2008).

[21] K. B. Nam, J. Li, M. L. Nakarmi, J. Y. Lin, and H. X. Jiang, Appl. Phys. Lett. **82**, 1694 (2003).

[22] E. Silveira, J. A. Freitas, Jr., M. Kneissl, D. W. Treat, N. M. Johnson, G. A. Slack, and L. J. Schowalter, Appl. Phys. Lett. **84**, 3501 (2004).

[23] K. Jeganathan, T. Kitamura, M. Shimizu, and H. Okumura, Jpn. J. Appl. Phys. **41**, L28 (2002).

[24] T. Onuma, S. F. Chichibu, T. Sota, K. Asai, S. Sumiya, T. Shibata, and M. Tanaka, Appl. Phys. Lett. **81**, 652 (2002).

[25] Y. Yamada, K. Choi, S. Shin, H. Murotani, T. Taguchi, N. Okada, and H. Amano, Appl. Phys. Lett. **92**, 131912 (2008).

[26] H. Harima, J. Phys.: Condens. Matter **14**, R967 (2002).

[27] V. Yu. Davydov, Yu. E. Kitaev, I. N. Goncharuk, A. N. Smirnov, J. Graul, O. Semchinova, D. Uffmann, M. B. Smirnov, A. P. Mirgorodsky, and R. A. Evarestov, Phys. Rev. B **58**, 12899 (1998).

[28] J.-M. Wagner and F. Bechstedt, Appl. Phys. Lett. **77**, 346 (2000).

[29] J. Gleize, M. A. Renucci, J. Frandona, E. Bellet-amalric, and B. Daudin, J. Appl. Phys. **93**, 2065 (2003).

[30] S. Nakashima and H. Harima, phys. stat. sol. (a) **162**, 39 (1997).

Chapter 5

Growth of Nonpolar 4H-polytype AlN/AlGaN Quantum Well Structure and Characterization of Optical Properties

5.1 Introduction

In order to achieve high efficient deep-ultraviolet (UV) light-emitting devices with AlN-based group–Ⅲ nitrides (Ⅲ–Ns), high-quality growth of quantum well (QW) structure with a nonpolar orientation is essential. Here the high-quality nonpolar 4H-AlN layers have been achieved on 4H-SiC $(11\bar{2}0)$ and $(1\bar{1}00)$ as presented in Chapter 3 and it has been found the possibility of the direct transition for the band structure of 4H-AlN in Section 4.4, which is indispensable for light-emitting devices. Growth of high Al-content AlGaN and realization of AlN/AlGaN QW structures should be the next step for optoelectronic device applications.

For AlGaN growth on nonpolar faces, it is important to understand the controllability of the composition. In the InGaN growth for visible light emission, there are a few reports discussed the difference of the In composition of InGaN in the crystal face of growth substrates, where the lower In composition of InGaN layers on planer GaN $(1\bar{1}00)$ substrates has been reported compared with (0001) [1]. It has also been reported that the misorientation of substrates toward $[11\bar{2}0]$ affect reduction of the In composition in InGaN (0001) growth [2]. However, difference of the Al or Ga composition in the crystal face for the nonpolar AlGaN growth has not been reported yet. In addition, there have been few reports on comparative studies between $(11\bar{2}0)$ and $(1\bar{1}00)$ in not only AlGaN growth but also InGaN growth. The relationships between the supply ratio of Al/Ga and the AlGaN composition should be investigated. Besides the controllability, the quality and the property of AlGaN layers are also important because AlGaN layers are used for well layers of QW structures.

Nonpolar AlGaN layers should be prevented from including extended-defects for high efficient light-emitting devices, where realization of 4H-polytype AlGaN expects to be effective as the case of 4H-AlN growth on 4H-SiC.

In addition to AlGaN growth, abrupt AlN/AlGaN interface without extended-defect generation is necessary for the QW structure [3]. Since the several-nanometer-thick active layers are required to exert the quantum confinement effect in QW structure, atomic mixing must be controlled at the AlN/AlGaN interface. Moreover, generation of extended defects must be also suppressed. The lattice mismatches between GaN and SiC are larger than those between AlN and SiC, suggesting that extended defects can be introduced. To suppress the atomic mixing and extended defects is needed for QW structures.

In this chapter, the growth of AlGaN layers and AlN/AlGaN multiple quantum well (MQW) structures on nonpolar 4H-SiC are described. First of all, the influence of the crystal faces of nonpolar $(11\bar{2}0)$ and $(1\bar{1}00)$ on the Ga composition of AlGaN layers is investigated. The relationships between the ratio of Al/Ga source supplied and the AlGaN composition are presented. Then high-quality growth of 4H-polytype AlGaN and its optical properties are displayed compared for the case of 4H-AlN. Using the 4H-AlGaN layers, MQW structure is realized. The structural and optical properties of MQW structures are characterized by transmission electron microscopy (TEM) and cathodoluminescence (CL), respectively.

5.2 Composition Control of High Al-Content Nonpolar AlGaN

5.2.1 Experimental detail

The relationships between the ratio of Al/Ga source supplied and the AlGaN composition in molecular-beam epitaxy (MBE) growth were studied. 4H-SiC $(11\bar{2}0)$ and $(1\bar{1}00)$ substrates were used for AlGaN growth. AlGaN was directly grown on SiC substrates at 750 and 600°C under slightly group-Ⅲ-metal-rich conditions: Beam equivalent pressure (BEP) of Al 2–8 $\times 10^{-5}$ Pa, BEP of Ga 0–26 $\times 10^{-5}$ Pa, N_2 flow rate 0.75 sccm and RF-plasma power 300–380 W. The Ga BEP ratio is defined as $P_{\mathrm{Ga}}/(P_{\mathrm{Al}} + P_{\mathrm{Ga}})$ where the P_{Al} and the P_{Ga} show the BEP of Al and Ga, respectively. To determine the Ga composition of AlGaN layers, energy-dispersive x-ray spectroscopy (EDS) analysis was used as well as x-ray diffraction (XRD) measurement. CL measurement was carried out to obtain luminescence spectra of AlGaN layers. The thickness of AlGaN layers was the range of 250–350 nm. All AlGaN layers discussed in this section showed 4H-polytype in reflection high-energy electron diffraction (RHEED) observation.

5.2.2 Difference of Ga incorporation between $(11\bar{2}0)$ and $(1\bar{1}00)$

The Ga composition x of $Al_{1-x}Ga_xN$ grown on 4H-SiC $(11\bar{2}0)$ and $(1\bar{1}00)$ under the same conditions was estimated by EDS, XRD and CL. The growth was performed under the Ga BEP ratio of 0.66 and the substrate temperature of 750°C.

Energy-dispersive x-ray spectroscopy

The EDS analysis revealed that the Ga composition of the AlGaN layers on $(1\bar{1}00)$ was 0.12. In contrast, epilayers grown on $(11\bar{2}0)$ contain negligible amount of Ga ($x < 0.01$). To trace the existence of Ga, EDS mapping was performed for the Al(Ga)N $(11\bar{2}0)$ layer, which did not include Ga in spite of Ga supply. In optical microscope observation, a number of metal droplets were observed on the AlGaN layer, which were also found in the scanning electron microscopy (SEM) image (Fig. 5.1 (a)). The EDS intensity mapping of N, Al and Ga in the same area of the SEM image are shown in Fig. 5.1 (b)–(d). From the SEM and EDS images, it was revealed that the metal droplets consisted of only Ga and that Ga were not incorporated into the AlN layer. It is expected that the Ga metal supplied was partly evaporated from the substrate and the rest of it was precipitated on the substrate without incorporating to AlN.

X-ray diffraction

In addition to the EDS analysis, XRD measurement was also performed to determine the Ga composition. In the estimation of Ga composition of nonpolar AlGaN layers from XRD measurement, the strain analysis should be applied since the AlGaN layer suffers from a large anisotropic strain as discussed in Section 4.3. However the AlGaN layer grown on 4H-SiC by MBE was determined 4H-polytype structure by an analysis of RHEED patterns, indicating that the general strain analysis cannot be applied because of the indefinite lattice constants of 4H-AlN bulk. Therefore, the simple estimation was carried out applying Vegard's law between strained 4H-AlN and relaxed 2H-GaN to the a-axis lattice constant of AlGaN layers measured from symmetrical XRD. The a-axis lattice constants of 3.106 and 3.107 Å were used for strained 4H-AlN on $(11\bar{2}0)$ and $(1\bar{1}00)$, respectively, which were experimentally obtained in XRD measurement, and that of 3.189 Å was used for relaxed GaN. The lattice constant of the AlGaN layers on $(11\bar{2}0)$ shows 3.106 Å, which is the same value of 4H-AlN $(11\bar{2}0)$, and the lattice constant of AlGaN layers on $(1\bar{1}00)$ shows 3.116 Å, corresponding to the Ga composition of $x = 0.11$. The results of EDS and XRD analyses indicate that the amount of Ga incorporation in the AlGaN $(1\bar{1}00)$ layer is much larger than that in the AlGaN $(11\bar{2}0)$.

Cathodoluminescence

Figure 5.2 shows the CL spectra taken from the AlGaN $(1\bar{1}00)$ and Al(Ga)N $(11\bar{2}0)$ layers, where the luminescent peaks from the near band edge emission of the AlGaN $(1\bar{1}00)$

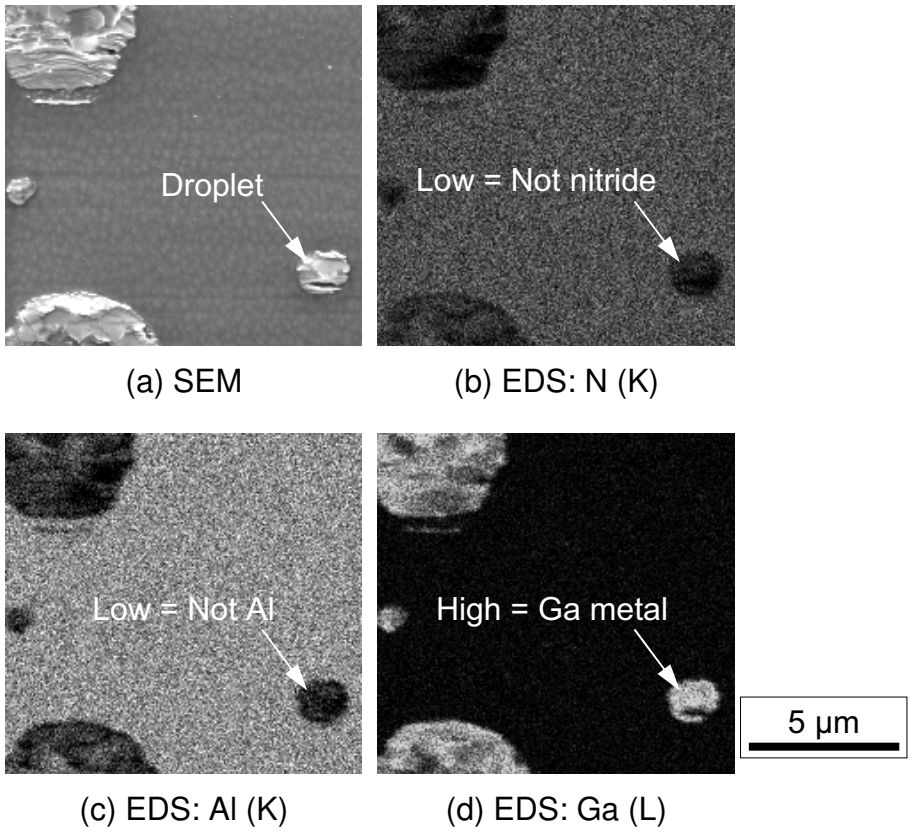

Figure 5.1: (a) an SEM image and EDS mapping images of (b) N (K-line), (c) Al (K-line) and (d) Ga (L-line) taken from Al(Ga)N ($11\bar{2}0$) layers grown at 750°C under the Ga BEP ratio of 0.66. In the EDS mapping images, the brightness displays the weight ratio.

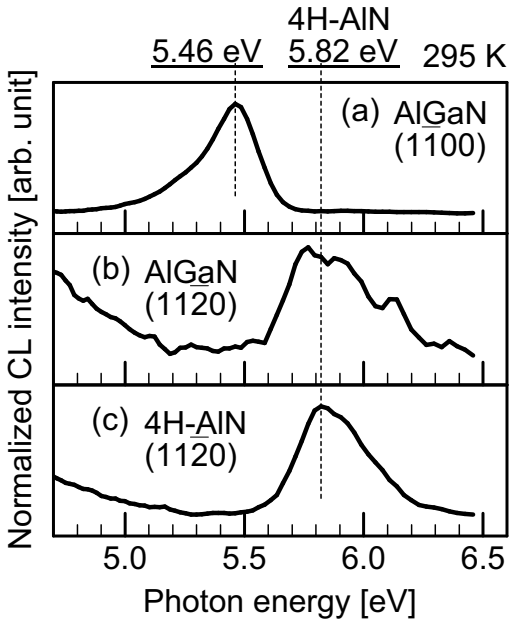

Figure 5.2: CL spectra of (a) AlGaN ($1\bar{1}00$), (b) Al(Ga)N ($11\bar{2}0$) and (c) 4H-AlN ($11\bar{2}0$) layers in the range of the band edge emission measured at room temperature (295K).

and Al(Ga)N ($11\bar{2}0$) layers were observed at 5.46 and 5.82 eV, respectively. The CL spectrum obtained from 4H-AlN is shown in Fig. 5.2 (c) as a reference. The energy of the band edge emission from 4H-AlN is ∼0.2 eV lower than that from 2H-AlN (5.99 eV at room temperature) as discussed in Section 4.4. The peak energy of the band edge emission from the AlGaN ($1\bar{1}00$) layers was lower than that of 4H-AlN while the peak of the band edge emission from the AlGaN ($11\bar{2}0$) layer was the same position as that of 4H-AlN. The emission peak from the AlGaN ($1\bar{1}00$) layers was observed at the 15%-position from the 4H-AlN (5.82 eV) to the wurtzite GaN (3.39 eV) at room temperature. The luminescence spectra indicate that Ga was certainly incorporated into the AlGaN ($1\bar{1}00$) layers at a composition of $x \sim 0.1$, while the Al(Ga)N ($11\bar{2}0$) layers contain negligible amount of Ga.

5.2.3 Dependence of Al/Ga flux ratio on AlGaN composition

The relationships between the Ga composition and the Ga BEP ratio in Al(Ga)N ($11\bar{2}0$) and AlGaN ($1\bar{1}00$) growth at the growth temperature of 750°C are shown in Fig. 5.3. In the growth of AlGaN ($1\bar{1}00$), Ga was incorporated at a Ga BEP ratio of more than 0.5 and $Al_{0.85}Ga_{0.15}N$ can be obtained at the Ga BEP ratio of 0.7. On the other hand, Al(Ga)N ($11\bar{2}0$) layers do not contain Ga up to the Ga BEP ratio of 0.75. To obtain Ga-contained AlGaN ($11\bar{2}0$) layers, growth at a reduced temperature of 600°C was performed, the results of which are also shown in Fig. 5.3. Although the temperature reduction is expected to lower the equilibrium pressure of Ga and to lead to increase the Ga incorporation, the Ga composition of AlGaN ($11\bar{2}0$) layers was not increased in the Ga BEP ratio range of 0.13–0.62. With increasing Ga BEP ratio to 0.9 at the growth temperature of 600°C, the Ga composition indicated increasing tendency although the AlGaN layers presented a rough and porous surface (not plotted in Fig. 5.3). One speculates that the 4H-polytype of AlGaN ($11\bar{2}0$) may cause to the very small incorporation of Ga and that it may not be observed in the 2H-AlGaN. Then, the growth of AlGaN ($11\bar{2}0$) on 6H-SiC substrates was also performed, where Onojima *et al.* have reported that not 4H- but 2H-AlN ($11\bar{2}0$) layers is grown [4]. The Ga composition of the wurtzite AlGaN ($11\bar{2}0$) layers on 6H-SiC, the structure of which determined by RHEED patterns, was as small as that of 4H-Al(Ga)N ($11\bar{2}0$) layers.

5.2.4 Discussion

From the EDS, XRD and CL measurements, Ga was incorporated into the AlGaN ($1\bar{1}00$) layers at a composition of $x \sim 0.1$ under the Ga BEP ratio of 0.66 while the Al(Ga)N ($11\bar{2}0$) layers contain negligible amount of Ga. Since Ga was not incorporated into the 2H-Al(Ga)N ($11\bar{2}0$) layers, it is believed that the low Ga incorporation for ($11\bar{2}0$) is general phenomena for high Al-content AlGaN in MBE growth. The surface morphologies were degraded with increasing the Ga flux for Al(Ga)N ($11\bar{2}0$) growth, and the band edge emission from the

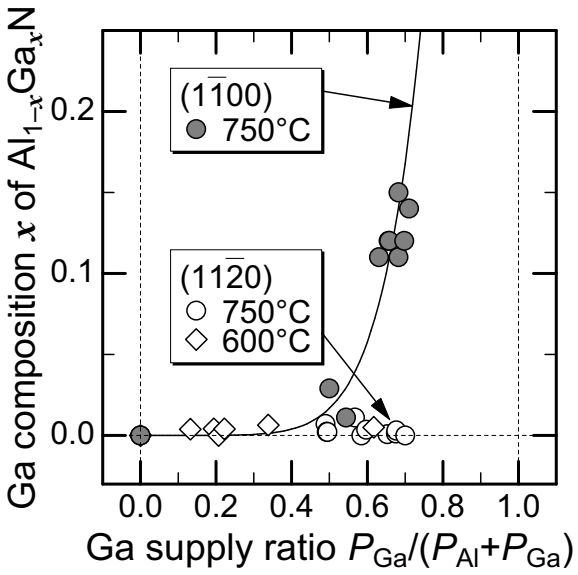

Figure 5.3: The dependence of Ga composition x of $Al_{1-x}Ga_xN$ on the beam equivalent pressure (BEP) ratio ($P_{Ga}/(P_{Al} + P_{Ga})$) in MBE growth under metal-rich conditions. The data are shown for 4H-AlGaN ($1\bar{1}00$) grown at 750°C (closed circle), 4H-AlGaN ($11\bar{2}0$) grown at 750°C (open circle) and 4H-AlGaN ($11\bar{2}0$) grown at 600°C (open square).

Al(Ga)N $(11\bar{2}0)$ layers was one fifth intensity of the emission from 4H-AlN $(11\bar{2}0)$. At the present time, it is concluded that the $(1\bar{1}00)$ is more favorable for AlGaN growth than the $(11\bar{2}0)$ from the viewpoint of the composition controllability.

It is considered the possible origin of the differences in Ga composition of AlGaN between on $(11\bar{2}0)$ and $(1\bar{1}00)$. The Al(Ga)N layers were grown under metal-rich conditions. In the 2H-GaN (0001) growth, it has been reported that several pseudomorphic Ga monolayer exists on the growth surface as adatoms, which enhances the migration of adatoms and contributes to improve the surface flatness in MBE growth [5]. It is believed that the growth surface of nonpolar AlN is in a similar situation. The atomic bond configuration is the most different things between $(11\bar{2}0)$ and $(1\bar{1}00)$, and it is resemblant between 2H $(11\bar{2}0)$ and 4H $(11\bar{2}0)$. Therefore two explanations may be speculated as follows:

- Ga atoms can not be incorporated into Al adatoms because of the limitation determined by the size of Ga and Al atoms and the interval of dangling bonds.
- Although Ga atoms exist in the adatom layer, Al atoms selectively crystallize into AlN from the adatom layer due to the difference of atomic bond configuration.

Although the difference of In incorporation has been reported in the InGaN growth [1, 2, 6], the reason for the difference is not determined. It is important for clarification of the origin to be carefully performed further experiments as well as theoretical calculations.

5.3 Growth of Nonpolar 4H-AlGaN $(1\bar{1}00)$ and Its Properties

5.3.1 Growth of nonpolar 4H-AlGaN

It has been found that growth of AlGaN with a flat surface is possible on $(1\bar{1}00)$ faces. In this section, the growth and properties of AlGaN layers are described compared with the case for 4H-AlN $(1\bar{1}00)$. High Al-content AlGaN layers were grown directly on 4H-SiC $(1\bar{1}00)$ substrates with the step-and-terrace structure discussed in Section 2.4.

Figure 5.4 (a) shows the RHEED patterns obtained from 4H-SiC substrates, where the 4H structure was observed (the detail is discussed in Section 3.3). The RHEED patterns were not changed after the $Al_{0.85}Ga_{0.15}N$ growth for 30 min ($\sim$290 nm) as shown in Fig. 5.4 (b). Observation of RHEED patterns revealed that the AlGaN has 4H-polytype structure as the case of 4H-AlN.

The growth kinetics was characterized by the RHEED intensity profiles which are shown in Fig. 5.5. As the case for 4H-AlN $(1\bar{1}00)$ growth, RHEED oscillations were observed during the initial stage of growth. The period of the oscillation corresponds to $\sim$2.7 Å of AlGaN growth, calculated from postgrowth thickness measurements assuming a constant growth rate. Since the component of step flow growth is not observed as RHEED intensity

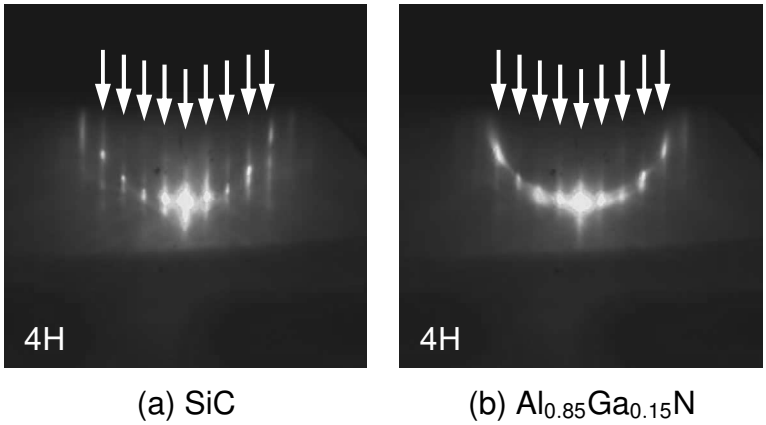

Figure 5.4: RHEED patterns from (a) SiC substrates and (b) $Al_{0.85}Ga_{0.15}N$ layers. The arrows show the streak position, the spacing of which indicates 4H structure.

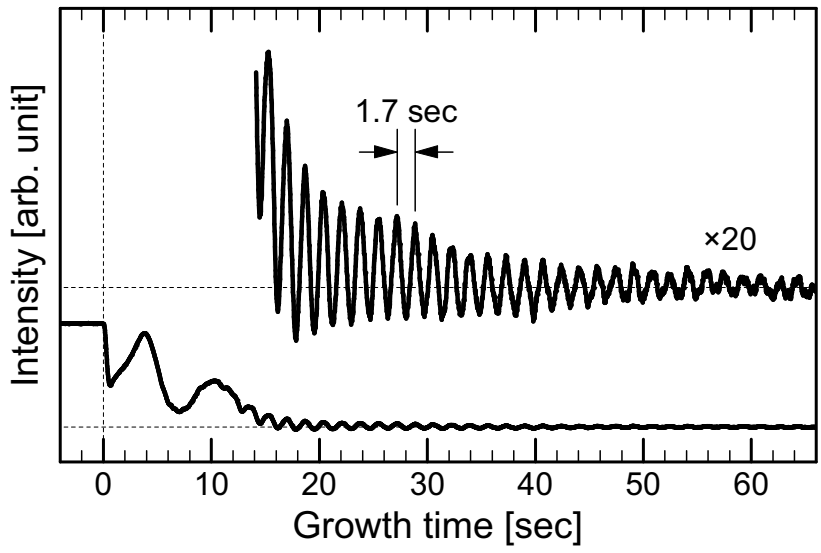

Figure 5.5: RHEED intensity profiles during the initial stage of AlGaN growth. The profiles are shown in the whole amplitude and the magnified amplitude.

oscillations, the thickness calculated from the oscillation period should be more than the thickness of two-dimensional (2D) islands. The estimated value of 2.7 Å is nearly equal to the spacing of AlGaN ($1\bar{1}00$) (∼2.702 Å, assuming $Al_{0.9}Ga_{0.1}N$), suggesting that the origin of the oscillation is layer-by-layer growth. This indicates that layer-by-layer growth can be realized in not only 4H-AlN but also 4H-AlGaN growth on 4H-SiC ($1\bar{1}00$) substrates. Since the layer-by-layer growth is effective for reduction of stacking faults (SFs) as discussed in Section 3.3, it is expected that generation of SFs is suppressed during AlGaN growth.

5.3.2 Structural properties

The crystalline quality and the lattice constants of 4H-AlGaN ($1\bar{1}00$) layers were characterized by high-resolution XRD (HRXRD). The Ga composition x of the $Al_{1-x}Ga_xN$ layer investigated was determined to be 0.90 by EDS and XRD, and the thickness was 290 nm.

Crystalline quality

The ω-scan spectra for the symmetrical ($1\bar{1}00$) and asymmetrical ($1\bar{1}02$) and ($1\bar{2}10$) reflections obtained from the AlGaN layer are shown in Fig. 5.6 to detect dislocations with every Burgers vector (the detail is discussed in Section 3.3). For all reflections, the ω-scan full-width at half-maximum (FWHM) value is less than 100 arcsec, implying low threading dislocation (TD) density as the case of high-quality 4H-AlN ($1\bar{1}00$).

Lattice constant

To confirm the coherency between 4H-AlGaN and 4H-SiC, the lattice constants of epilayers and substrates were measured by XRD (the detail of the method is presented in Section 4.3). The results are summarized in Table 5.1. The in-plane lattice constants of 4H-AlGaN were the same as that of 4H-SiC, where the lattice mismatches in the in-plane directions is less that 0.03%. The angle γ of 4H-AlGaN is 0.3° smaller than the undistorted value of 120° and slightly smaller than the γ of 4H-AlN (−0.2°), suggesting that the lattice of 4H-AlGaN layers is further distorted compared with the 4H-AlN grown on 4H-SiC. From the lattice constant measurements, coherent growth is possible for not only 4H-AlN but also 4H-AlGaN layers on 4H-SiC ($1\bar{1}00$) substrates.

5.3.3 Optical properties

To characterize the optical properties of AlGaN layers, CL measurement was performed. Figure 5.7 shows the CL spectra of 4H-$Al_{0.90}Ga_{0.10}N$ ($1\bar{1}00$) layers. The band edge luminescence of AlGaN was observed at the photon energy of 5.28 eV in a large intensity compared with the 4H-AlN. The luminescence from deep levels, so-called violet luminescence (VL) was observed for AlGaN around the energy of 3.37 eV. The VL peak was also observed for AlN around the energy of 3.60 eV. It is expected that these VL peaks originates from

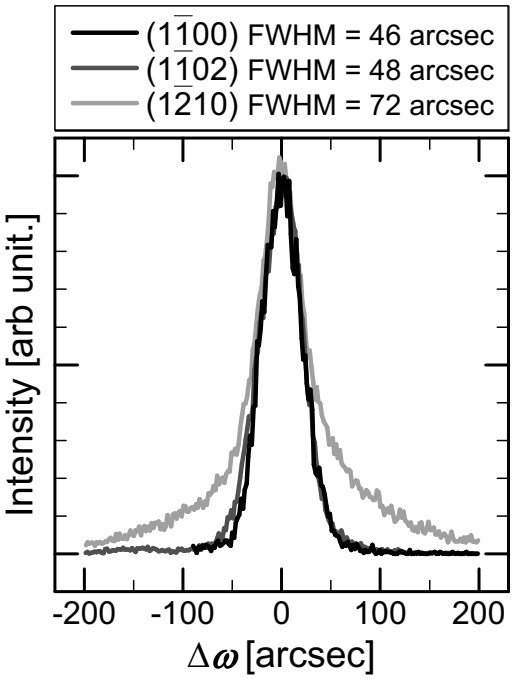

Figure 5.6: XRD ω-scan spectra of 4H-$Al_{0.9}Ga_{0.1}N$ (1$\bar{1}$00) grown on 4H-SiC (1$\bar{1}$00). Symmetrical (1$\bar{1}$00) and asymmetrical (10$\bar{1}$2) and (1$\bar{2}$10) reflections are shown. (1$\bar{1}$00) and (10$\bar{1}$2) reflections are obtained in x-ray incident geometry parallel to the [11$\bar{2}$0] direction, and a (1$\bar{2}$10) reflection parallel to the [0001] direction.

Table 5.1: The lattice constants of 4H-AlGaN layers grown on 4H-SiC (1$\bar{1}$00). The lattice constants of 4H-SiC substrates and the lattice mismatches between the epilayer and the substrate are shown.

4H-$Al_{0.9}Ga_{0.1}N$ (1$\bar{1}$00) / 4H-SiC (1$\bar{1}$00)

Parameter		4H-SiC substrate	4H-AlGaN epilayer	Difference
In-plane	c [Å]	10.0835 $\pm$ 0.0006	10.0820 $\pm$ 0.0009	<0.02%
	a [Å]	3.08108 $\pm$ 0.00008	3.08018 $\pm$ 0.00012	$-$0.03%
Out-of-plane	m [Å]	2.66816 $\pm$ 0.00003	2.70224 $\pm$ 0.00008	+1.28%
Distortion	γ [°]	120.0012 $\pm$ 0.0013	119.682 $\pm$ 0.003	$-$0.318°

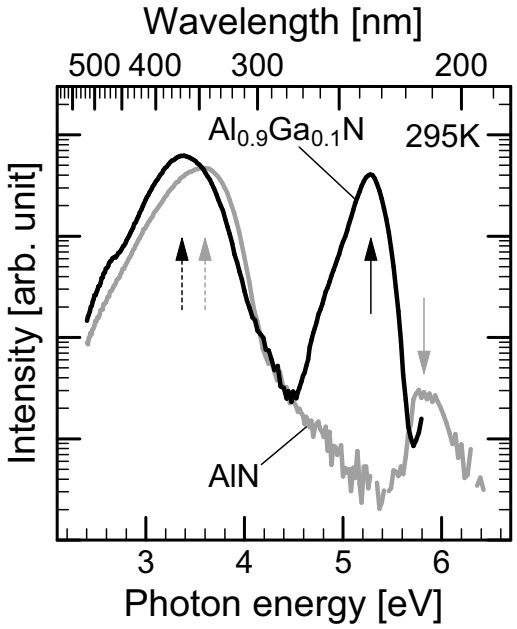

Figure 5.7: A CL spectrum taken from 4H-AlGaN ($1\bar{1}00$) (black line) in the wide range of the photon energy at room temperature (295K). A CL spectrum obtained from 4H-AlN ($1\bar{1}00$) (gray line) is shown as a reference. The solid and dashed arrows indicate the peak position of the band edge emission and the VL, respectively. The black and gray arrows indicate the peak from AlGaN and AlN, respectively.

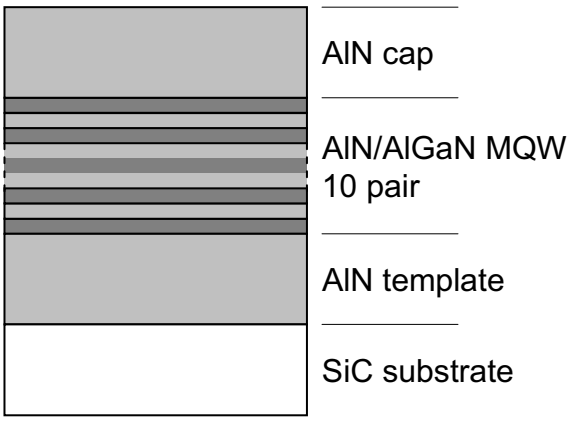

Figure 5.8: Schematics of MQW structure investigated in this study.

the same origin since the red shift of the VL peak was observed with increase of the Ga composition of AlGaN. Nepal *et al.* have reported that the origin of the VL peak observed at 3.4 eV in AlN is $(V_{III})^{3-}$ [7]. It is believed that the observed VL peak is the same as the reported one although the peak energy was slightly different.

5.3.4 Discussion

In the growth of AlGaN $(1\bar{1}00)$, the layer-by-layer growth was observed as the case for 4H-AlN growth. In addition, the 4H-$Al_{0.90}Ga_{0.10}N$ layers indicated the low TD density and the coherent growth on 4H-SiC substrates in XRD characterization, where the situation is similar to the 4H-AlN. TEM observation is required for determination of SF and TD densities. Nevertheless it is expected that the SF and TD densities of the AlGaN $(1\bar{1}00)$ layers are the same order of magnitude as those of 4H-AlN $(1\bar{1}00)$ layers.

In the CL measurement, a large intensity of the band edge emission was observed, indicating the application potentiality of 4H-polytype AlGaN for light-emitting devices. Further characterization such as the low-temperature spectra and the emission lifetime of luminescence peaks will give the luminescence process of 4H-AlGaN layers. Since the efficiency of the grating is abruptly lowered at the wavelength of 240 nm, the large intensity of the band edge emission from the 4H-AlGaN layer leads to the expectation that the intensity of the band edge emission from the 4H-AlN layer is larger than that practically observed.

5.4 Growth of 4H-AlN/4H-AlGaN Multiple Quantum Well Structure and Its Properties

5.4.1 Growth of MQW structure

It has been revealed that high Al-content 4H-AlGaN can be grown on 4H-SiC $(1\bar{1}00)$ with a comparable quality to 4H-AlN $(1\bar{1}00)$. Using the 4H-polytype AlN and AlGaN, realization of AlN/AlGaN MQW structure has been attempted as a basic application for light-emitting devices. Figure 5.8 shows the structure of MQW samples. The MQW structure consisted of an AlN template layer, 10 pairs of AlN /$Al_{0.90}Ga_{0.10}N$ MQW layers, and an AlN cap layer in order of growth. The typical values of the layer thickness are as follows: AlN template 50 nm, AlN barrier 15 nm, AlGaN well 4 nm, AlN cap 130 nm, where the thickness was optimized by Monte Carlo simulation (CASINO) [8] for CL observation with a 5-keV-accelerated electron beam probe.

In the MQW growth, it is important to prevent atomic mixing at the AlN/AlGaN interface. On the other hand, it has been reported that several Ga monolayers exist on the surface under the Ga-rich conditions during GaN growth in MBE, and that the adlayer contribute migration enhancement of Ga atoms, leading to realization of flat surfaces [5,

9, 10]. The adlayer has been reported for nonpolar GaN growth [11] and it has been believed that a similar phenomenon occurs during AlN growth including nonpolar faces. If MQW structure is continuously grown under metal-rich conditions without interruption of source supply, surface metal adlayer will give rise to the atomic mixing at the AlN/AlGaN interface, resulting in a gradual interface. In order to avoid this, an interruption of growth was introduced at the switching point of source supply. Figure 5.9 shows the sequence of source supply during the MQW growth.

Growth of the MQW structure was performed. The RHEED patterns were not changed during growth of the template layer, the MQW layers and the cap layer. Figure 5.10 shows the RHEED intensity profiles during growth of the MQW layers. RHEED oscillation was observed in the initial stage of every AlN growth and in the whole periods of AlGaN growth. It was found that layer-by-layer growth was realized in the whole of MQW layers. The periods of the oscillation during AlGaN and AlN growth were the same since the AlN and AlGaN layers were grown under the same condition of N^*.

The amplitude of the oscillation during AlGaN growth is smaller than that during AlN growth. There are two possible explanations for the phenomenon:

- Supply of Ga enhances the migration of adatoms and the growth kinetics shifts to step advancing mode. In general, the migration length of Ga atoms is lager than that of Al atoms.

- Supply of Ga lowers the migration of adatoms and the growth kinetics shifts to three-dimensional (3D) growth mode. Since the metal effusion cells for AlGaN growth were different from that for AlN growth, the growth conditions between AlGaN and AlN layers were slightly different. If the condition for AlGaN growth is more N-rich than that for AlN growth, the migration of adatoms will be reduced.

Dependence of the growth temperature and the Ⅲ/V ratio can be reveal the origin of the variation of the amplitude.

5.4.2 Structural properties

To confirm the MQW structure, XRD $2\theta/\omega$-scan was performed. Since MQW layers have periodical structure of QWs along the growth direction, satellite peaks can be observed around the main peak in XRD $2\theta/\omega$-scan. Figure 5.11 shows an XRD $2\theta/\omega$-scan of an AlN/AlGaN MQW sample with barrier and well thickness of 23 and 16 nm, respectively. $\pm$1st-order satellite peaks were observed, indicating that abrupt AlN/AlGaN interfaces was formed and that Ga was certainly contained in AlGaN layers. The QW period was calculated to be 39.2 nm from the positions of the satellite peaks, which agrees with the thickness expected from the growth rate (39.5 nm). For a 15-nm-thick AlN/4-nm-thick AlGaN MQW sample, satellite peaks were not observed. It is expected that the roughness of AlGaN layers leads to the low intensity of satellite peaks as well as the very small

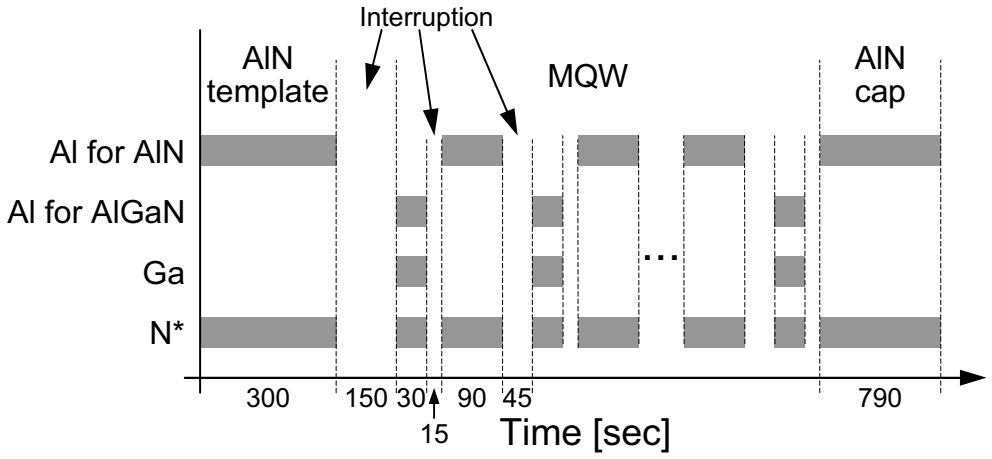

Figure 5.9: Supply sequence of Al, Ga and N* during growth for 15-nm-thick AlN/4-nm-thick AlGaN MQW structures.

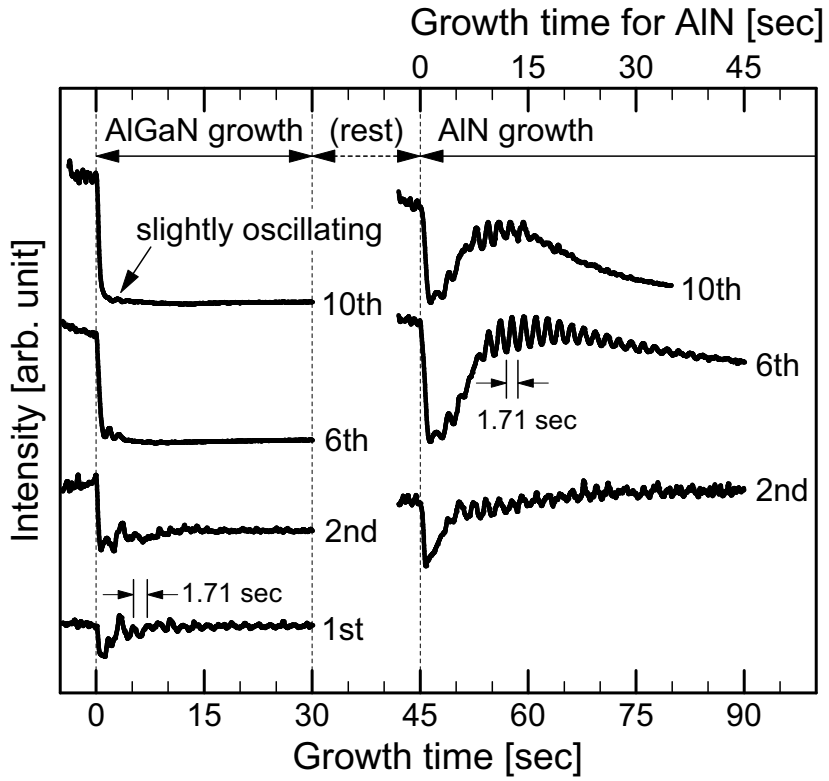

Figure 5.10: RHEED intensity profiles during each initial growth stage of MQW layers. The profiles of first AlGaN growth and AlN growth following the first AlGaN growth are numbered as "1st". A profile of the 1st AlN layer was missed but oscillating.

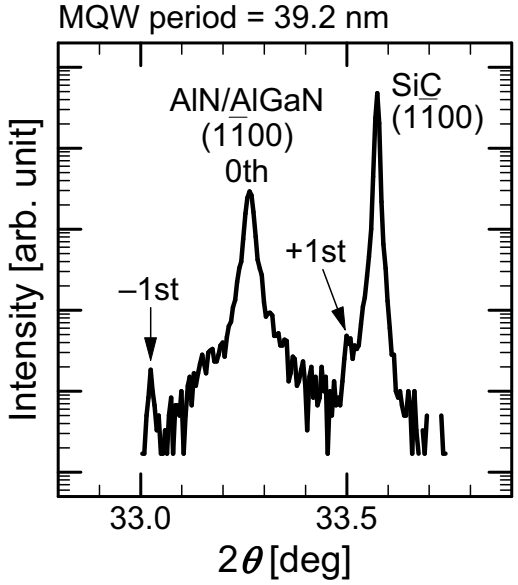

Figure 5.11: An XRD $2\theta/\omega$-scan spectrum of $(1\bar{1}00)$ reflections obtained from 23-nm-thick AlN/16-nm-thick AlGaN MQW structure grown on 4H-SiC $(1\bar{1}00)$. The period of MQW structure is estimated from the interval of the satellite peaks.

thickness (4 nm) and the low Ga composition (∼0.1) of AlGaN layers. The root-mean-square (RMS) roughness of the surface morphologies of the MQW samples was 0.6 nm, which is not negligible for the QW period of 19 nm in XRD.

To investigate the structural properties, TEM observations were performed. Figure 5.12 (a) shows the cross-sectional bright-field TEM image of a 15-nm-thick AlN/4-nm-thick AlGaN MQW sample observed under near the two-beam conditions. The MQW structure with abrupt interfaces was clearly observed. A number of SFs were observed, which originated from the AlN/SiC interface, as discussed in Section 3.3. It should be noted that generation of SFs were not observed at the AlN/AlGaN interfaces of MQW structures (the numbers of arrows in the interface and the upper layer are the same). Figure 5.12 (b) shows the high-resolution TEM images of an AlGaN layer containing a SF. The 4H structure was observed in the AlGaN layer and upper and lower AlN layers, indicating that no extended defects were generated at both the AlN/AlGaN and AlGaN/AlN interfaces. The SF was extended thorough the AlGaN layer without changing its structure. It is believed that very high-quality MQW will be realized if SFs originating from the AlN/SiC interface is suppressed by optimization of the initial stage of AlN growth.

In order to estimate the Ga composition, high-angle annular dark-field (HAADF) and EDS observations in scanning TEM (STEM) mode were carried out. Since the atomic weight (Z) contrast can be obtained in HAADF observation, existence of Ga atoms can be detected as brightness. Figure 5.13 (a) shows a cross-sectional HAADF STEM image of 23-nm-thick AlN/16-nm-thick AlGaN MQW samples. AlN/AlGaN stacking structure with abrupt interfaces was clearly observed. In the AlGaN layers, several bright stripes along $[1\bar{1}00]$ were observed, indicating higher Ga composition compared with the peripheral part. It is expected that SFs relates to the high Ga composition from the shape of high composition parts. However, a part of the bright stripes did not thread from the first layer (AlN/SiC interface side) to the last layer (surface side). For example, in Fig. 5.13 (a), 6 bright stripes were observed in the 7th AlGaN layer while 13 strips were observed in the 10th AlGaN layer. Figure 5.13 (b) shows a cross-sectional bright-field TEM image observed in exactly the same area as the HAADF image. Compared with the lateral ([0001] directional) position of SFs, the position of the bright stripes corresponds to that of SFs. The density of SFs was larger than that of bright stripes, indicating that the bright stripes were observed at not all of SFs. These results indicate that the high Ga-content SFs are formed in AlGaN layers and that generation of high Ga-content SFs results from not only existence of SFs but also other factor such as the surface roughness.

In between the high Ga-content SFs of AlGaN layers (denoted by the dashed box in Fig. 5.13 (a)), bright and dark contrasts were observed. This indicates the fluctuation of the Ga composition in AlGaN layers. From the EDS point analysis, difference of the Ga composition x of $Al_{1-x}Ga_xN$ was observed between the bright areas ($x = 0.07$) and dark areas ($x = 0.03$).

Figure 5.14 shows a cross-sectional HAADF STEM image of 15-nm-thick

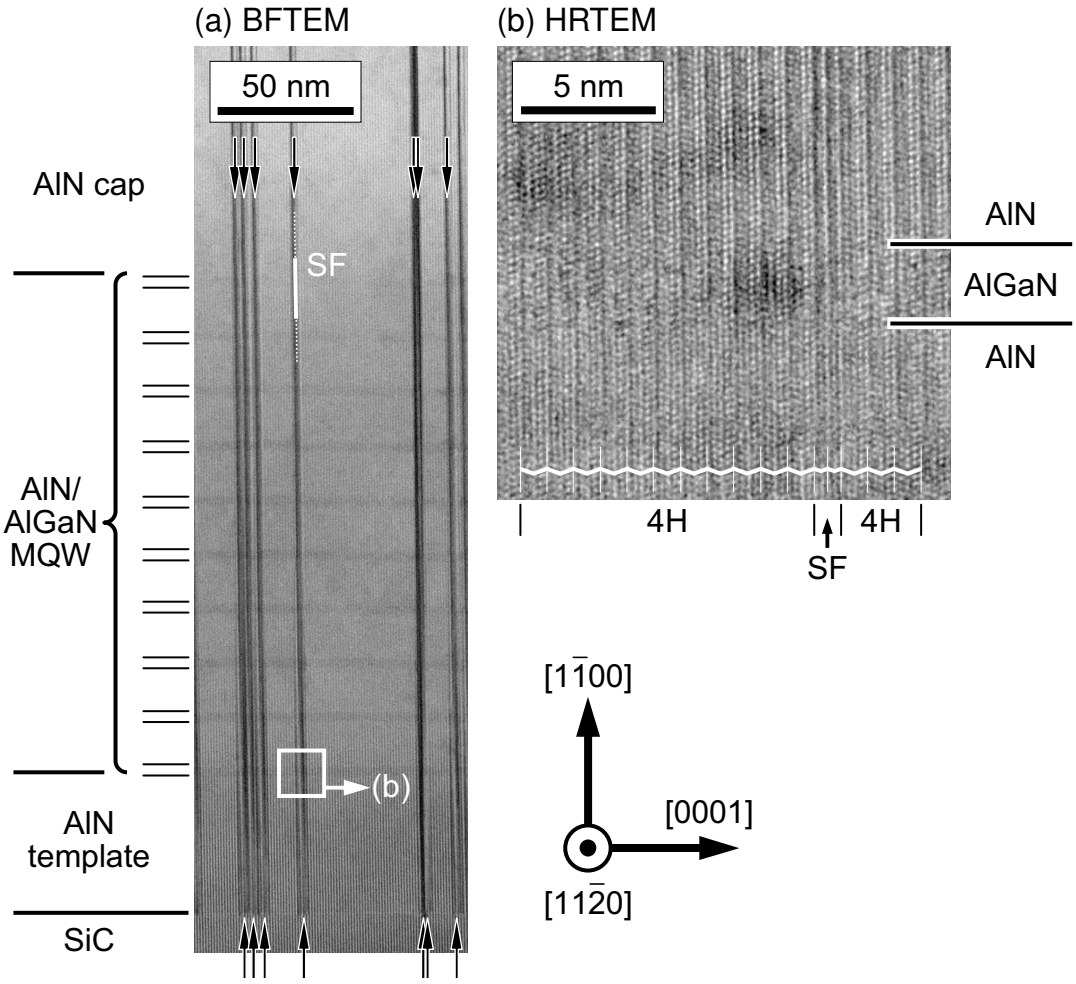

Figure 5.12: Cross-sectional TEM images of 15-nm-thick AlN/4-nm-thick AlGaN MQW structures; (a) low-magnification bright-field TEM observed under near the two-beam conditions of $\boldsymbol{g} = 1\bar{1}00$, (b) high-resolution TEM observed at an AlGaN layer with a SF (denoted by square in (a)). In (a), the arrows indicate generation of SFs at the AlN/SiC interface and extension of SFs toward the AlN cap layer.

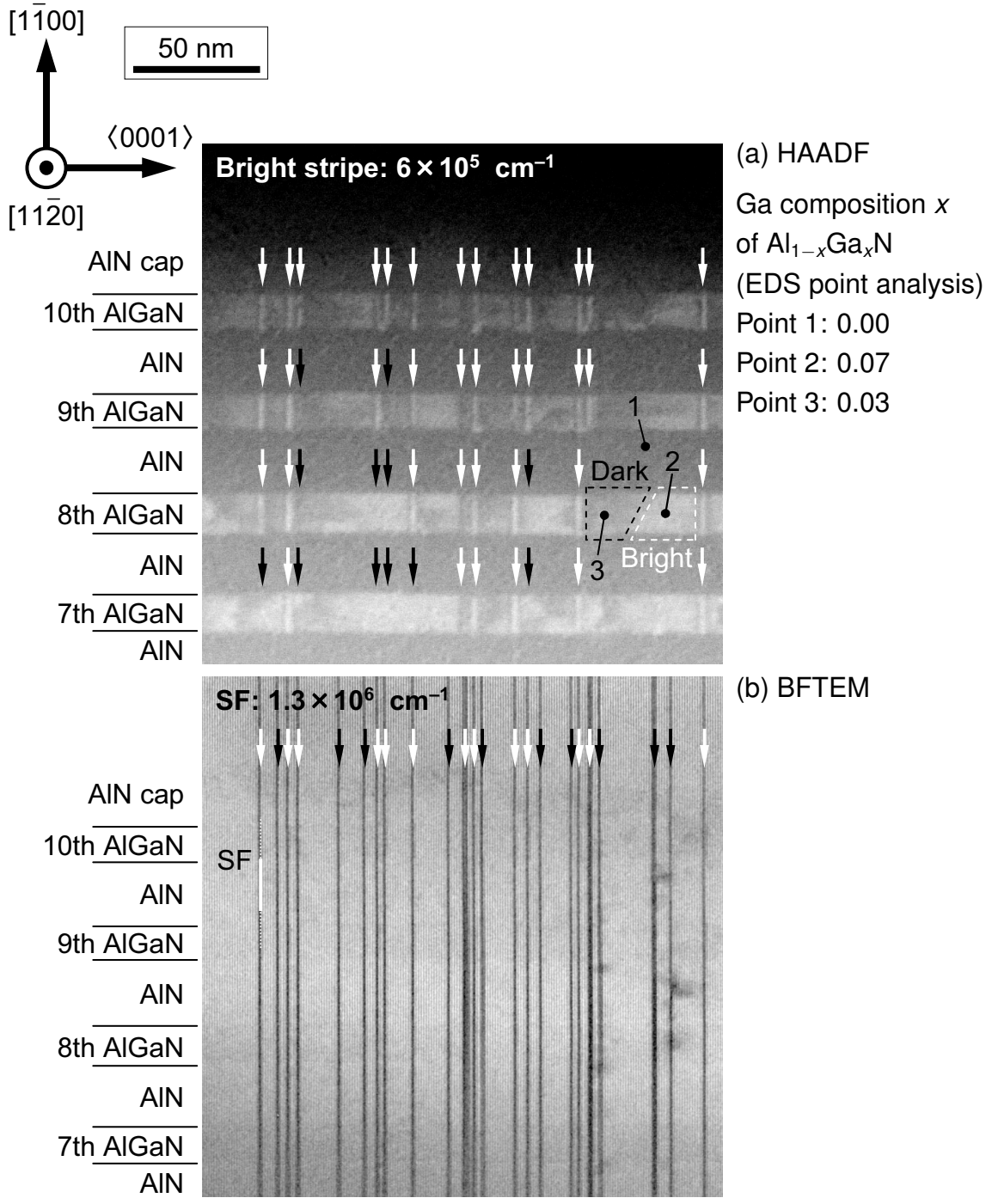

Figure 5.13: (a) A Z (atomic weight) contrast image observed in HAADF STEM and (b) a bright field TEM (BFTEM) image of 23-nm-thick AlN/16-nm-thick AlGaN MQW structures. The images are obtained from exactly the same area in the same sample. In (a), the white arrows show the bright stripes observed and the black arrows show no observation of stripes in each AlGaN layer. A dark contrast and a bright contrast were observed between the bright stripes in AlGaN layers in (a), which denoted by black and white dashed boxes, respectively. Measurement points of the EDS analysis are shown and the analysis results of the Ga composition x of $Al_{1-x}Ga_xN$ are summarized. In (b), the white and black arrows show the SFs where the bright stripes are and are not observed in (a), respectively.

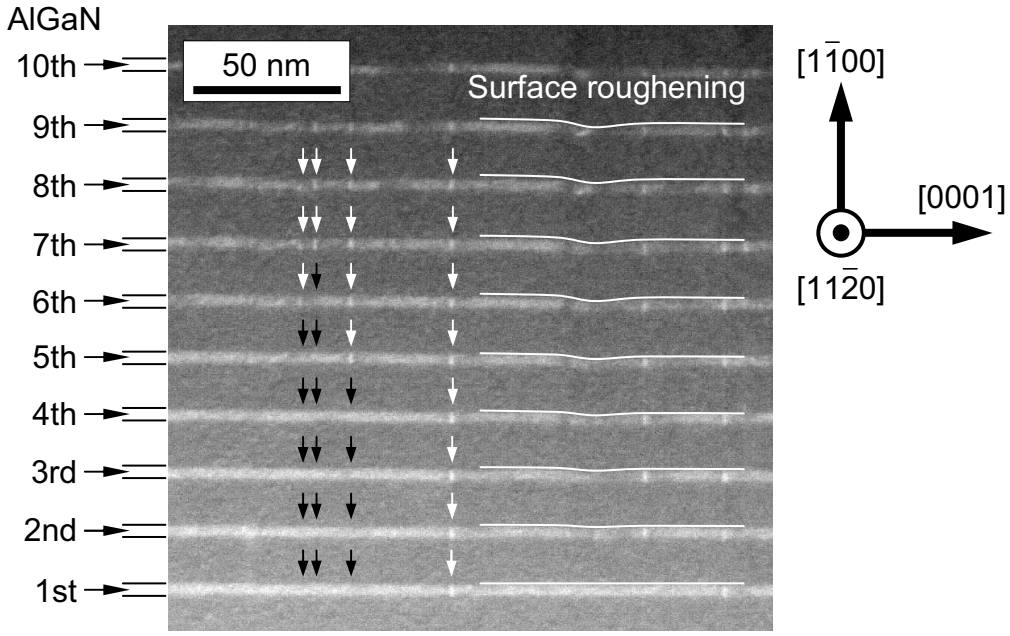

Figure 5.14: A Z (atomic weight) contrast image observed in HAADF STEM of 15-nm-thick AlN/4-nm-thick AlGaN MQW structures. The white arrows show the bright stripes observed and the black arrows show no observation of stripes in each AlGaN layer. The shapes of AlN/AlGaN interfaces are shown by the solid lines.

AlN/4-nm-thick AlGaN MQW samples. AlN/AlGaN stacking structure with abrupt interfaces was clearly observed in the 15 nm/4 nm MQW sample. The flatness of AlGaN layers degraded with advancing growth, leading to the very low intensity of satellite peaks in the XRD measurement. The bright stripes were observed in AlGaN layer as the case for 23-nm-thick AlN/16-nm-thick AlGaN MQW samples.

5.4.3 Optical properties

In order to characterize the optical properties, CL measurement was performed. Figure 5.15 (a) shows CL spectra of 15-nm-thick AlN/4-nm-thick AlGaN MQW samples as well as AlN and $Al_{0.90}Ga_{0.10}N$ $(1\bar{1}00)$ layers. The band edge emission peak of MQW layers was observed at 5.35 eV, which was slightly shifted from the band edge emission of AlGaN (5.28 eV). The peak position of the MQW band edge emission can be roughly estimated from the QW thickness and the Ga composition of AlGaN layers. The Ga composition of AlGaN layers in MQW samples was 0.93, which was 0.03 larger than the single $Al_{0.90}Ga_{0.10}N$ layer due to the difference of source supply conditions. The increase of the bandgap energy is estimated to be 0.07 eV from $Al_{0.90}Ga_{0.10}N$ to $Al_{0.93}Ga_{0.07}N$. In addition, the energy state is quantized by the formation of QW structure, leading to the bandgap energy is increased. The increase of the bandgap energy was roughly estimated to be $\sim$0.1 eV by assuming the AlGaN well thickness of 4 nm. From this estimation, the band edge emission peak should be shift for 0.17 eV toward the high energy. The peak shift from single AlGaN layers to MQW samples observed in the CL measurement (0.07 eV) was smaller than that estimated (0.17 eV).

Violet luminescence (VL) peaks from the MQW samples observed at 3.67 eV, which is higher energy compared with the AlN and AlGaN VL peaks. It is expected that the origin of the VL peak from the MQW sample is different from that of single AlN and AlGaN layers.

Figure 5.15 (b) shows the dependence of the excitation power density on the CL spectra of the band edge emission of 15-nm-thick AlN/4-nm-thick AlGaN MQW samples. A large intensity of band edge emission was observed compared with VL peaks in low temperature measurement. The blue shift of the band edge emission was not observed in more than two orders of magnitude variation of the excitation power densities.

5.4.4 Discussion

Growth of AlN/AlGaN MQW structure was performed and its structural and optical properties were characterized. The RHEED intensity oscillation indicates that layer-by-layer growth was achieved in the whole periods of AlGaN growth. From the TEM observation, it was found that generation of additional SFs did not occur at the AlN/AlGaN interfaces of MQW structures and that 4H-polytype AlN/AlGaN MQW structure was realized,

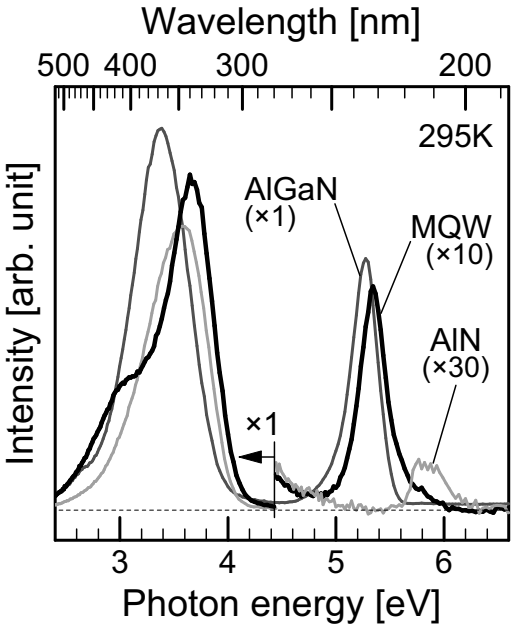

(a) CL spectra from MQW, AlGaN and AlN layers (RT)

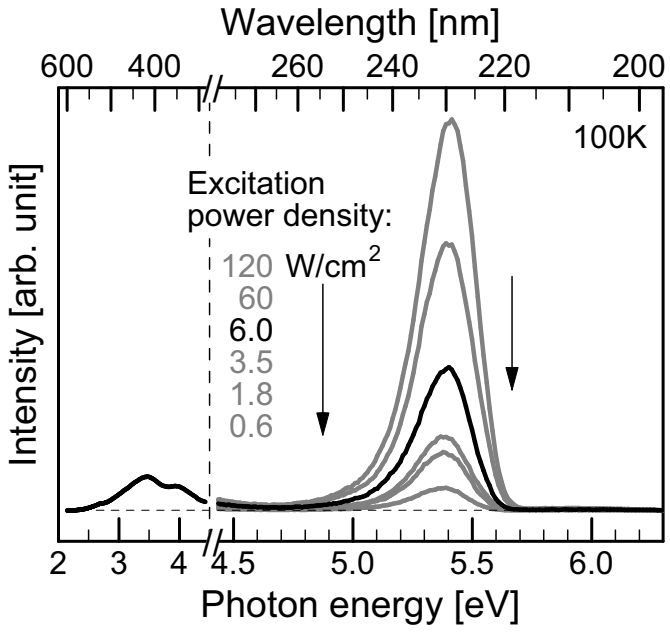

(b) Dependence of the excitation power density (LT)

Figure 5.15: (a) CL spectra obtained from 15-nm-thick AlN/4-nm-thick AlGaN MQW samples (black line), $Al_{0.90}Ga_{0.10}N$ layers (dark gray line) and AlN layers (light gray line). (b) Dependence of the excitation power density on CL spectra of the band edge emission of 15-nm-thick AlN/4-nm-thick MQW samples. In (a), the amplitude of the band edge emission peaks is magnified individually. In (b), a CL spectrum for the excitation power density of 6.0 W/cm^2 is displayed in the wide range of the photon energy. The measurement was performed at room temperature (RT) for (a) and a low temperature (LT) of 100K for (b).

which is consistent with XRD measurements. It is believed that the layer-by-layer growth contributes to suppress generation of extended defects at the AlN/AlGaN interfaces.

In the HAADF and EDS measurements, fluctuation of the Ga composition and high Ga-content SFs were observed. These may be explained by the surface dangling bond configuration. Figure 5.16 (a) shows the surface dangling bond configuration of a flat surface on 4H-AlN $(1\bar{1}00)$. The different configurations of $(3\bar{3}04)$ and $(3\bar{3}0\bar{4})$ are alternately located along [0001] with atomic spacing in this structure. In the initial stage of growth, the situation is close to Fig. 5.16 (a). The surface roughness increases with advancing growth, resulting that the surface structure shown in Fig. 5.16 (b) is growing. In this structure, the configuration sets of $(3\bar{3}04)$, $(3\bar{3}08)$ and $(3\bar{3}0\bar{4})$, $(3\bar{3}0\bar{8})$ appear along [0001] with more than atomic spacing. On each configuration set, the dangling bonds are only from Al or N atoms, indicating that the Ga incorporation is very different in these faces as the case for the (0001) and $(000\bar{1})$ growth. Since the dark contrasts, which partly denoted by the black dashed box in Fig. 5.13 (a), were observed at the right side of high Ga-content SFs, the situation as shown in Fig. 5.16 occurred between the high Ga-content SFs. The origin of high Ga-content SFs is now focused. The migration of adatoms is also different between the configuration sets of $(3\bar{3}04)$, $(3\bar{3}08)$ and $(3\bar{3}0\bar{4})$, $(3\bar{3}0\bar{8})$. In addition to this, the dangling bond configuration on the SFs is different from that on the 4H-AlN surface as shown in Fig. 5.16 (c). These may result in the formation of the high Ga-content SF in AlGaN layers. Theoretical calculations will give the origin of these phenomena as well as further experiments.

In the CL measurements, the band edge emission from MQW structure was observed at a lower energy than the estimated energy. One possible explanation for the lower peak position is the variation of Ga composition. Although the source supply conditions except for the supply time are the same in the 15-nm-thick/4-nm-thick and 23-nm-thick/16-nm-thick AlN/AlGaN MQW samples, it is speculated that the Ga compositions of AlGaN layers in both the types of MQW samples are different due to the difference of the AlGaN layer thickness. The other explanation for the lower peak position is the quantum wire emission from the high Ga-content SFs. The high Ga-content SFs can be work as the quantum wire extended toward the $[11\bar{2}0]$ direction with a height (the $[1\bar{1}00]$ direction) of AlGaN w ell thickness and a width (the [0001] direction) of two or four bilayers of AlGaN due to the high Ga composition. The quantum well or wire emission will be determined by observations of CL mapping combined with an SEM system with a low-energy accelerated electron beam probe or a TEM system.

From the VL peak observations, it is speculated that the origin of the VL from the MQW samples is different from that of single AlN or AlGaN layers. This may results from the interruption of growth at the AlN/AlGaN interfaces since the growth interruption under the non-optimized conditions leads to incorporation of impurities such as oxygen. It should be required to be investigated the origin to reduce the VL peaks.

A large intensity of the band edge emission was observed compared with the VL peaks

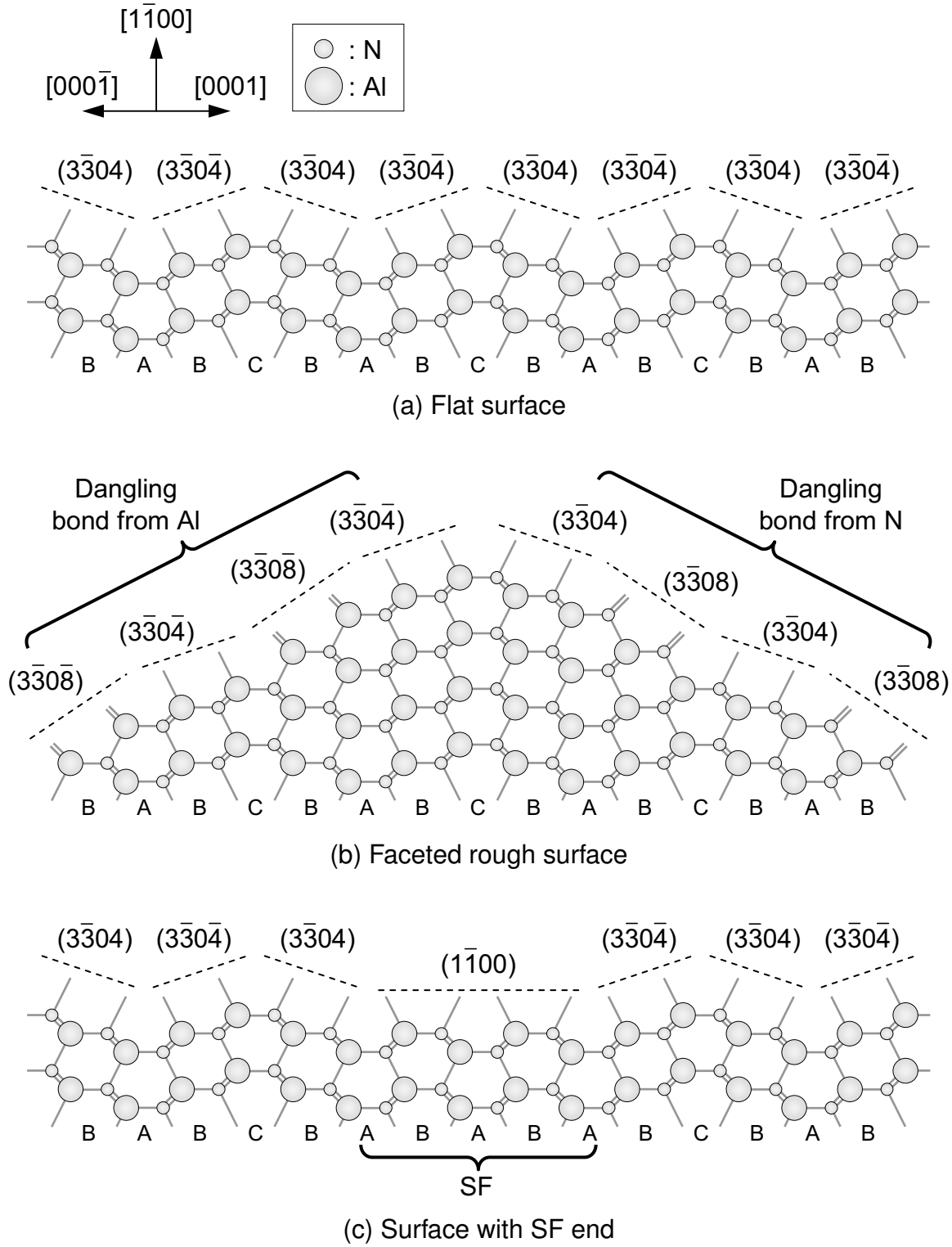

Figure 5.16: Schematics of the dangling bond configuration on (a) a flat surface, (b) a faceted rough surface and (c) a surface with a SF end of 4H-AlN (1$\bar{1}$00).

at a low temperature measurement. In addition, the blue shift of the band edge emission peak was not observed in the dependence of the excitation power density. These indicate the effectivity of nonpolar 4H-polytype AlN/AlGaN MQW structure.

5.5 Summary

Growth of AlGaN and AlN/AlGaN MQW structure with nonpolar orientations were performed toward the light-emitting device applications. In the AlGaN growth, it has been revealed that the Ga incorporation in $(1\bar{1}00)$ growth is much higher than that in $(11\bar{2}0)$ growth. The 4H-polytype AlGaN can be grown on 4H-SiC $(1\bar{1}00)$ and its crystalline quality is comparable to that of 4H-AlN $(1\bar{1}00)$. On the other hand, further innovation will be required for high-quality growth of AlGaN $(11\bar{2}0)$.

Using the 4H-polytype AlN and AlGaN $(1\bar{1}00)$, AlN/AlGaN MQW structure has been achieved. In the structure analysis of MQW structures, generation of additional extended defects was not observed and the 4H-polytype was achieved in the whole of MQW layers. In the compositional analysis of AlGaN layers, fluctuation of the Ga composition and high Ga-content SFs were observed. These phenomena should be suppressed for ideal MQW structure. Nevertheless, the formation of high Ga-content SFs has a possibility of quantum wires for new applications.

In the CL measurements, a large intensity of the band edge emission was observed. In addition, the blue shift of the band edge emission peak was not observed in the dependence of the excitation power density. These indicate the effectivity of nonpolar 4H-polytype AlN/AlGaN MQW structure.

References

[1] H. Yamada, K. Iso, S. Saito, K. Fujito, S. P. DenBaars, J. S. Speck, and S. Nakamura, Jpn. J. Appl. Phys. **46**, L1117 (2007).

[2] M. Kryśko, G. Franssen, T. Suski, M. Albrecht, B. Łucznik, I. Grzegory, S. Krukowski, R. Czernecki, S. Grzanka, I. Makarowa, M. Leszczyński, and P. Perlin, Appl. Phys. Lett. **91**, 211904 (2007).

[3] M. Koike, S. Yamasaki, S. Nagai, N. Koide, S. Asami, H. Amano, and I. Akasaki, Appl. Phys. Lett. **68**, 1403 (1996).

[4] N. Onojima, J. Suda, T. Kimoto, and H. Matsunami, Jpn. J. Appl. Phys. **41**, L1348 (2002).

[5] J. E. Northrup, J. Neugebauer, R. M. Feenstra, and A. R. Smith, Phys. Rev. B **61**, 9932 (2000).

[6] H. Yamada, K. Iso, M. Saito, H. Masui, K. Fujito, S. P. DenBaars, and S. Nakamura, Appl. Phys. Express **1**, 041101 (2008).

[7] N. Nepal, M. L. Nakarmi, J. Y. Lin, and H. X. Jiang, Appl. Phys. Lett. **89**, 092107 (2006).

[8] D. Drouin, A. R. Couture, D. Joly, X. Tastet, V. Aimez, and R. Gauvin, Scanning **29**, 92 (2007).

[9] G. Koblmüller, J. Brown, R. Averbeck, H. Riechert, P. Pongratz, and J. S. Speck, Jpn. J. Appl. Phys. **44**, L906 (2005).

[10] G. Koblmüller, R. Averbeck, H. Riechert, and P. Pongratz, Phys. Rev. B **69**, 035325 (2004).

[11] G. Koblmüller, S. Fernández-Garrido, E. Calleja, and J. S. Speck, Appl. Phys. Lett. **91**, 161904 (2007).

Chapter 6

Fabrication of 4H-AlN/4H-SiC (11$\bar{2}$0) Metal-Insulator-Semiconductor Field-Effect Transistors

6.1 Introduction

SiC metal-oxide-semiconductor field-effect transistors (MOSFETs) are the promising devices for low loss and high power electric switches as described in Chapter 1. Toward the MOS device applications, enhancement of channel mobility in the inversion layers is the key issue. Undoped AlN can be available for an alternative gate dielectric because of its large bandgap energy of 6.2 eV and a high dielectric constant of 8.5. Although there are a few reports on SiC metal-insulator-semiconductor FETs (MISFETs) with AlN gate dielectrics grown by molecular-beam epitaxy (MBE) on off-axis SiC (0001) faces [1–4], the MISFETs suffer from the large gate leakage current and the small drain current. Since the thermally stable structure of AlN is 2H, 2H-AlN grows on 4H-SiC (0001). Due to the polytype mismatch, a high density of partial dislocations is introduced at the 2H-AlN/4H-SiC interface as shown in Fig. 6.1 (a). The partial dislocations must generate the interface states, leading to the low channel mobility, and also degrade the AlN crystal quality, resulting in a large gate leakage current. In Chapter 3, it has demonstrated that metastable 4H-AlN can be grown on 4H-SiC (11$\bar{2}$0) face. In the case of 4H-AlN grown on 4H-SiC, few partial dislocation exists at the isopolytypic interface as shown in Fig. 6.1 (b), and crystalline quality of AlN is dramatically improved compared with the 2H-AlN grown on 4H-SiC (0001).

In addition to the polytype matching, the charge balance at the AlN/SiC interface should be considered due to the heterovalency between AlN and SiC [5, 6]. Figure 6.2 (a) shows the atomic bond configuration of the AlN/SiC interface, where AlN is grown on Si-terminated SiC (0001). In this structure, the N–Si bond rich interface is formed and one electron is donated per one N–Si bond, resulting that a large number of electrons and fixed charges are generated. It is expected that electrons laterally transported are highly scattered, leading

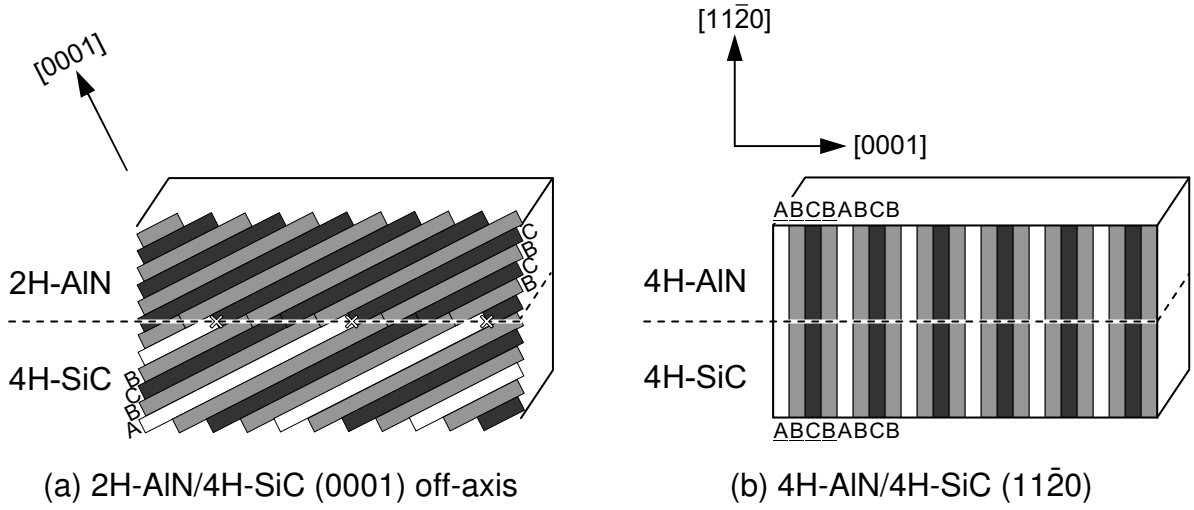

Figure 6.1: Schematic illustration of interfaces between (a) 2H-AlN grown on 4H-SiC (0001) off-axis substrates and (b) 4H-AlN grown on 4H-SiC (11$\bar{2}$0) substrates. The cross indices in (a) indicate atomic mismatches between AlN and SiC.

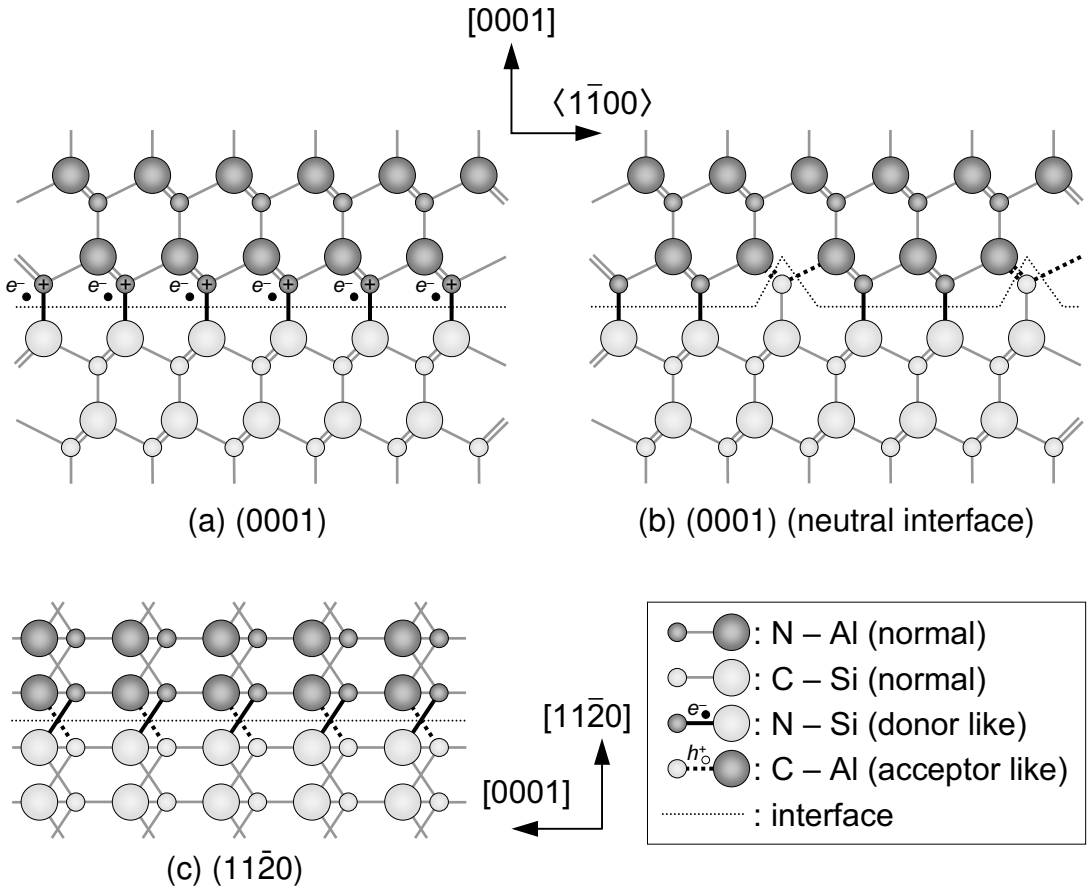

Figure 6.2: Schematics of atomic bond configurations for AlN/SiC interfaces; (a) AlN grown on a Si-terminated SiC (0001) surface, (b) AlN grown on a controlled SiC (0001) surface and (c) AlN grown on a SiC (11$\bar{2}$0) surface.

to degradation of device performance. It should be required to control the SiC surface and the initial growth of AlN for a neutral interface on (0001) which is formed by replacing one of every four N atoms with C as shown in Fig. 6.2 (b). On the other hand, the ratio of N–Si and Al–C bonds can be settled into unity at the nonpolar interface as shown in Fig. 6.2 (c).

The isopolytypic growth and the neutral interface can be achieved in the system of nonpolar 4H-AlN on 4H-SiC. Utilization of this system to MIS devices expects to improve the electric properties such as the interface state density and the channel mobility.

In this chapter, SiC MISFETs with isopolytypically grown 4H-AlN gate dielectrics are demonstrated. Due to the availability of high quality SiC epilayer [7], 4H-SiC $(11\bar{2}0)$ is used for fabrication of MISFETs although both nonpolar 4H-AlN $(11\bar{2}0)$ and $(1\bar{1}00)$ can be grown. The characteristics of MISFETs with 4H-AlN gate dielectrics are presented as well as the interface and insulating properties of MIS capacitors.

6.2 MIS Device Fabrication

6.2.1 Device structure

A schematic structure of 4H-AlN/4H-SiC n-channel MISFETs investigated in this study is shown in Fig. 6.3 (a). 4H-SiC $(11\bar{2}0)$ wafers were used as substrates. To characterize the interface state density and the insulating property of 4H-AlN layers, MIS capacitors shown in Fig. 6.3 (b) were also fabricated. As a reference, MOSFETs and MOS capacitors with N_2O-thermally-oxidized SiO_2 dielectrics were also fabricated on 4H-SiC $(11\bar{2}0)$ epilayers cleaved from the same wafer as for AlN/SiC MISFETs.

6.2.2 Growth of SiC and AlN epitaxial layers

SiC homoepitaxial growth

SiC homoepitaxial layers were grown at 1500°C by atmospheric-pressure chemical vapor deposition (CVD) using a SiH_4–C_3H_8 system with H_2 carrier gas in a horizontal cold-wall reactor (Fig. 2.5). Prior to the SiC growth, the substrates were etched with HCl/H_2 gas in a cold-wall reactor at 1300°C for 10 min as discussed in Section 2.4. The flow rates of SiH_4, C_3H_8 and H_2 for SiC growth were 0.30 sccm, 0.30 sccm and 3.0 slm, respectively, and the dopant gas was not used. The donor, most likely nitrogen, concentration N_D of epilayers was 8×10^{15} cm^{-3}. The typical growth time was 2 h where the thickness of the epilayers was $\sim$5 μm.

AlN heteroepitaxial growth

AlN heteroepitaxial layers were grown at 750°C by plasma-assisted MBE after the selective doping described in the next section. It has been concluded that the slightly Al-rich conditions are favorable for the growth of high quality 4H-AlN. However, the slightly Al-rich

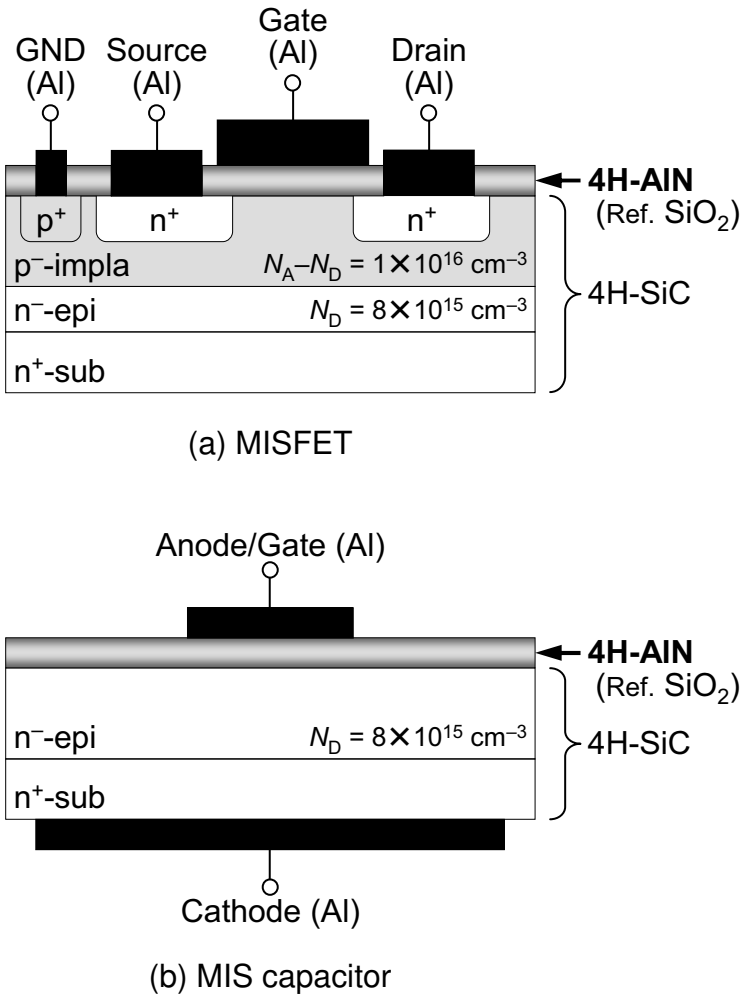

Figure 6.3: Schematics of device structure investigated in this study; (a) a MISFET and (b) a MIS capacitor.

conditions lead to formation of a number of metal droplets. If the metal droplet is formed during growth, the growth condition is locally changed under the metal droplets, resulting in the degradation of crystal quality. Since the density of droplets is high enough to contain the devices, it is expected that the formation of droplets degrade the insulating property. To avoid the formation of metal droplets, an interruption of growth was introduced during the AlN growth. In the AlN growth, Al and N* were simultaneously supplied and the set of growth for 5 sec and rest for 45 sec was repeated 144 times, where the total growth time was 2 h. The thickness of AlN layers was 120 nm for MISFETs and 69 nm for MIS capacitors, the equivalent oxide thickness (EOT) of which are 55 nm and 32 nm, respectively. There was no droplet observed on the epilayers although the growth condition was slightly Al-rich where metal droplets were formed in continuous growth.

The reflection high-energy electron diffraction (RHEED) patterns revealed that the structure of AlN was 4H and intensity oscillation was clearly observed in the initial stage of every growth periods. In x-ray diffraction (XRD) measurement, the full-width at half-maximum (FWHM) values of symmetrical $(11\bar{2}0)$ and asymmetrical $(11\bar{2}4)$ and $(30\bar{3}0)$ reflections from the 4H-AlN layers were 50, 89 and 43 arcsec, respectively, indicating that the 4H-AlN layers have comparable crystalline quality to the 4H-AlN samples discussed in Section 3.2.

6.2.3 Device process

The fabrication process of MISFETs is described as follows.

1. SiC epilayers were grown by CVD as discussed in the previous section. The donor concentration N_{D} of the eplayers was 8×10^{15} cm^{-3}.
2. *P*-well regions with a 0.70-μm-deep gradated profile were formed by Al^+ implantation at room temperature. The acceptor concentrations $N_{\mathrm{A}} - N_{\mathrm{D}}$ of the top and the bottom regions were 1×10^{16} cm^{-3} and 1×10^{18} cm^{-3}, respectively.
3. A ground (bulk) contact region was formed by selective Al^+ implantation with a deposited Al mask at the temperature of 300°C. The ground contact region has a 0.20-μm-deep box profile and an acceptor concentration of 2×10^{20} cm^{-3}.
4. Source/drain contact regions were formed by selective P^+ implantation with a deposited Al mask at the temperature of 300°C. The source/drain contact regions have a 0.12-μm-deep box profile and a donor concentration of 4×10^{20} cm^{-3}.
5. Post-implantation annealing was carried out in an Ar ambient at 1700°C for 20 min without carbon cap [8].
6. HCl gas etching was performed to remove a damaged surface layer. In order to maintain the contact regions, the etching time was limited to 5 min.
7. AlN epilayers were grown by MBE as discussed in the previous section.

8. Contact holes to ground and source/drain regions were formed by reactive ion etching (RIE) with a photo resist mask and a deposited Al spacer. Plasma of a CF_4/H_2 gas mixture was used for etching and O_2 plasma was used for cleaning.
9. Source/drain electrodes were formed by phosphoric acid (H_3PO_4) etching of deposited Al.
10. Source/drain contacts were sintered at 600°C.
11. A gate electrode was formed by H_3PO_4 etching of deposited Al.

Figure 6.4 shows a plan-view optical microscope image of a MISFET. The channel direction was parallel to [0001], and the channel length L and width W were 100 μm and 200 μm, respectively. For fabrication of MIS capacitors, the process of no. 1, 6, 7, 9, 10 and 11 was carried out.

It may be concerned that surface roughening during the annealing process for impurity activation (no. 5) affects the crystalline quality of AlN epilayer. Negoro *et al.* have reported that the surface roughening can be suppressed by using carbon cap on 4H-SiC (0001) during the high temperature annealing [9]. It has been also reported that lattice damaged by implantation is remarkably recovered on 4H-SiC (11$\bar{2}$0) and that the surface roughening is suppressed without carbon cap [8]. Figure 6.5 shows surface morphologies of the 4H-SiC (11$\bar{2}$0) substrates after the annealing at 1600°C for 15 min. Stripes of step edges were observed in this sample while no steps were observed in HCl gas etched sample shown in Fig. 2.7 (b). A number of hollows were observed in the image, which is expected to originate from extended defects such as basal plane dislocations. The detail of the step structure could not be analyzed due to the resolution limit of atomic force microscopy (AFM) measurement system. Nevertheless since the root-mean-square (RMS) roughness (1.84 Å) was comparable to the lattice spacing of 4H-SiC (11$\bar{2}$0) ($\frac{1}{2}a = 1.54$ Å), the step bunching is not so intensely advanced. Therefore it is speculated that the influence of surface roughening on the crystalline quality of AlN is negligible small.

The MOSFETs with SiO_2 gate dielectrics were also fabricated as a reference sample. Following the post-implantation annealing (process no. 5), SiO_2 gate dielectrics were formed by thermal oxidation instead of AlN growth (process no. 6) [10]. The thermal oxidation was carried out in a N_2O/N_2 gas mixture in a resistance-heated atmospheric-pressure oxidation furnace at 1300°C for 2 h. After the oxidation, contact holes to ground and source/drain regions were formed by buffered hydrogen fluoride (BHF) etching with a photo resist mask. The electrode formation process (no. 9, 10 and 11) was common to MISFETs. The oxide thickness was 64 nm for both MOSFETs and MOS capacitors.

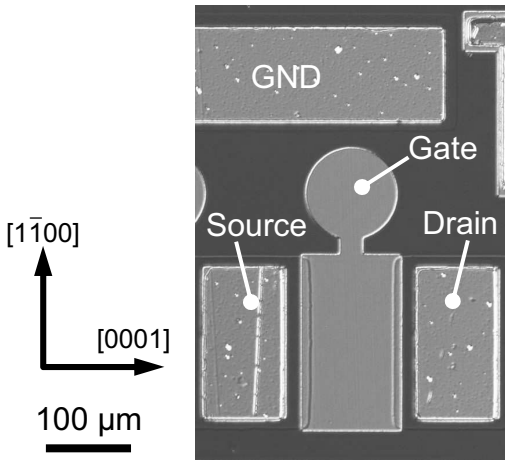

Figure 6.4: A plan-view Normarski image of an AlN/SiC MISFET.

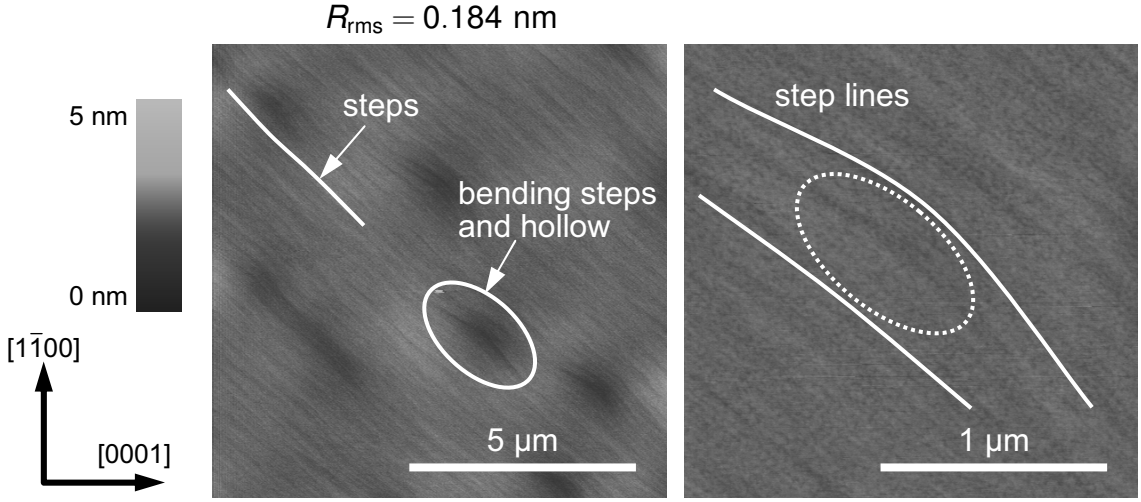

Figure 6.5: Surface morphologies of 4H-SiC (11$\bar{2}$0) after the annealing at a high temperature of 1600°C for 15 min. The solid lines show the guide of the step edge to the eye and the ellipses indicate a hollow. A hollow observed in left image is magnified to the right one.

6.3 Characteristics of 4H-AlN/4H-SiC MIS Devices

6.3.1 Characteristics of MISFETs

The SiC MISFETs with 4H-AlN gate dielectrics were characterized. Figure 6.6 (a) shows the drain current-drain voltage (I_D–V_D) characteristics of MISFETs. The I_D–V_D characteristics of MOSFETs with SiO_2 gate dielectrics is also shown in Fig. 6.6 (b).

In the measurement of MISFETs, a large current flow from drain to ground (I_{DG}) was observed, which was linearly increase with increase V_D and independent on the gate voltage (V_G). Since the I_D includes the current to ground (I_{DG}) and to source (I_{DS}), the source current (I_S) is used as the modified drain current ($I_D{}' = -I_S$) in Fig. 6.6 (a). The gate current (I_G) was negligible small ($I_G = -8.5 \times 10^{-8}$ A, -8.0×10^{-8} A at $(V_D, V_G) = (15\text{ V}, -5\text{ V}), (10\text{ V}, -10\text{ V})$, respectively) in the measurement range displayed in Fig. 6.6 (a). The I_{DG} was estimated to be $\sim 9 \times 10^{-6}$ A at $V_D = 15$ V, which was ten times as large as the $I_D{}'$ at $(V_D, V_G) = (15\text{ V}, 1\text{ V})$. Since the I_{DG} was not observed in SiO_2/SiC MOSFETs, the I_{DG} is speculated to relate the formation of AlN dielectrics but the reason is uncertain.

In the $I_D{}'$–V_D characteristics, the drain current was clearly modulated by the gate voltage and the saturation tendency of the drain current was observed as is the case for SiO_2 dielectrics. These indicate the transistor operation of MISFETs.

Figure 6.7 shows the I_D–V_G characteristics of AlN/SiC MISFETs and SiO_2/SiC MOSFETs, where the modified drain current was used for MISFETs. In the characteristics of MISFETs, the gate leakage current to source (I_{GS}) was dominant in the modified drain current ($I_D{}' = -I_S$) in the range of $E_G < -0.7$ MV/cm or $E_G > 0.08$ MV/cm where E_G is the electric field of gate dielectrics. The threshold voltage (V_{th}) of AlN/SiC MISFETs was estimated to be negative (<-10 V) although it was difficult to determine the V_{th} due to the gate leakage current, indicating normally-ON characteristics. The field-effect mobility (μ_{FE}) of AlN/SiC MISFETs was 0.49 cm^2/Vs at $E_G = 0.08$ MV/cm. On the other hand, The μ_{FE} of SiO_2/SiC MOSFETs was 67 cm^2/Vs at $E_G = 4.3$ MV/cm.

6.3.2 Interface and insulating properties of MIS capacitors

To characterize the interface properties, capacitance-voltage (C–V) measurements were carried out for the MIS (MOS) capacitors. Figure 6.8 shows the C–V characteristics of 4H-AlN/4H-SiC MIS and SiO_2/4H-SiC MOS capacitors. In the characteristics of AlN/SiC MIS capacitors, a large negative flat band shift ($\Delta V_{FB} = -10.9$ V) was observed. From the flat band shift, the effective fixed charge density Q_{eff} of the AlN/SiC MIS capacitor is estimated to be 7.5×10^{12} cm^{-2}. The interface state density (D_{it}) was calculated using Terman method [11], the results of which are shown in Fig. 6.9. The D_{it} of an AlN/SiC MIS interface is estimated to be 8×10^{12} cm^{-2}eV^{-1} at $E_c - E = 0.25$ eV, which is one order of magnitude higher than that of an SiO_2/SiC interface.

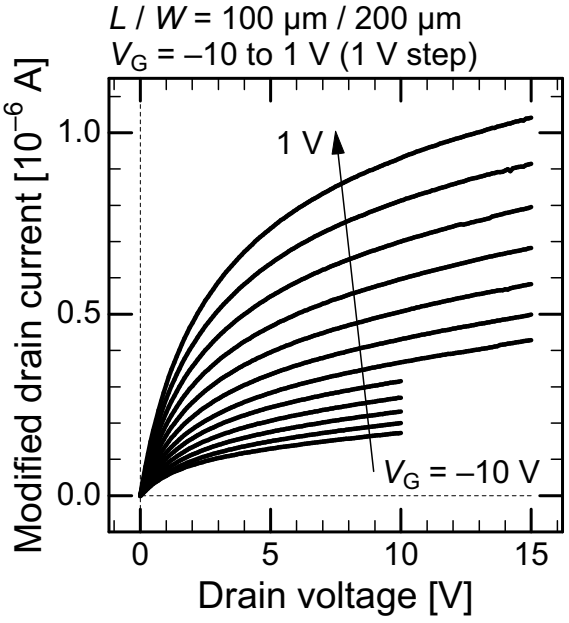

(a) AlN (thickness: 120 nm)

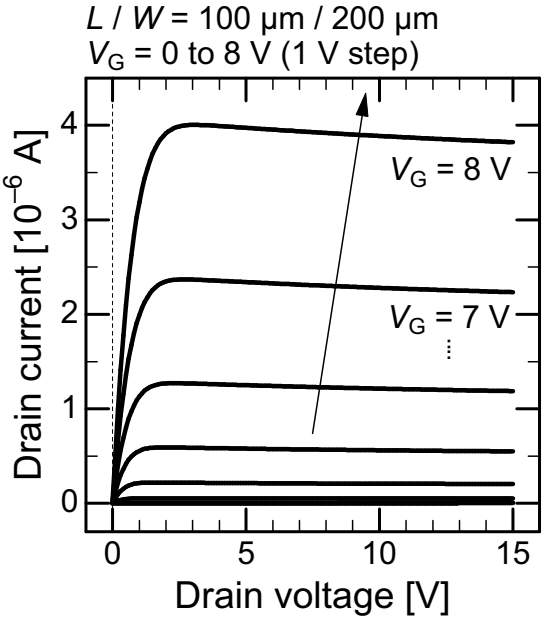

(b) SiO_2 (thickness: 64 nm)

Figure 6.6: Drain characteristics for 4H-SiC $(11\bar{2}0)$ MIS(MOS)FETs with (a) a 120-nm-thick AlN and (b) a 64-nm-thcik SiO_2 gate dielectrics. In (a), the measurement was difficult in the range of $10\ \mathrm{V} < V_\mathrm{D} < 15\ \mathrm{V}$ and $-10\ \mathrm{V} < V_\mathrm{G} < -6\ \mathrm{V}$ due to the gate leakage current.

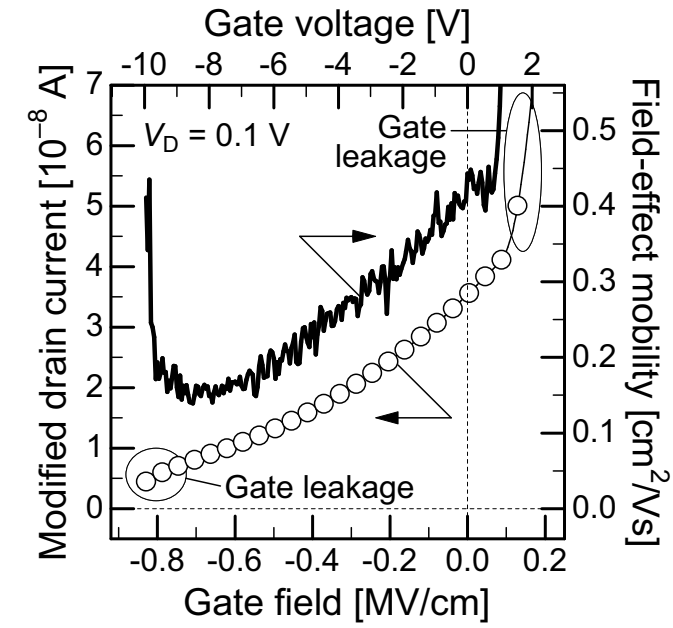

(a) AlN (thickness: 120 nm)

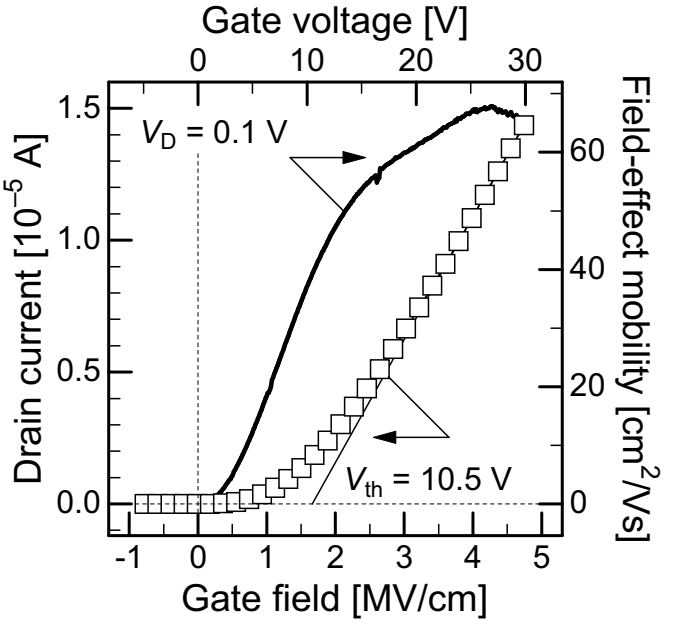

(b) SiO_2 (thickness: 64 nm)

Figure 6.7: Gate characteristics for 4H-SiC (11$\bar{2}$0) MIS(MOS)FETs with (a) a 120-nm-thick AlN and (b) a 64-nm-thick SiO_2 gate dielectrics. The drain current (thin line with symbol) and the field-effect mobility (thick line) are shown.

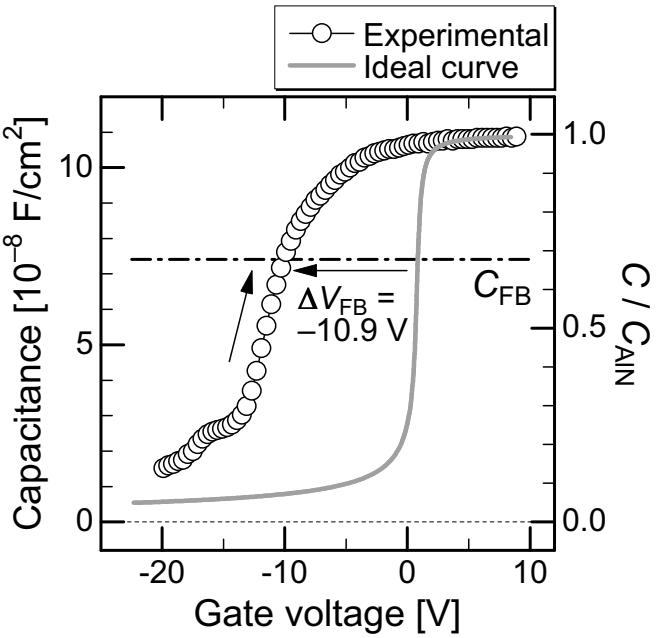

(a) AlN (thickness: 69 nm)

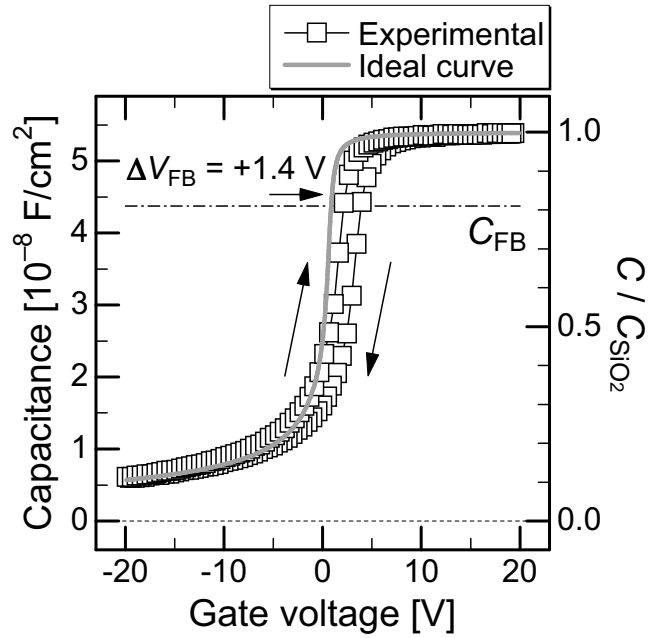

(b) SiO_2 (thickness: 64 nm)

Figure 6.8: High-frequency (1 MHz) C–V characteristics for MIS(MOS) capacitors with (a) a 69-nm-thick AlN and (b) a 64-nm-thick SiO_2 dielectrics. Experimental data (black line with symbols) and ideal curve (gray line) are shown. In (a), the experimental data was measured from the depletion state (negative voltage) to the accumulation state (positive voltage).

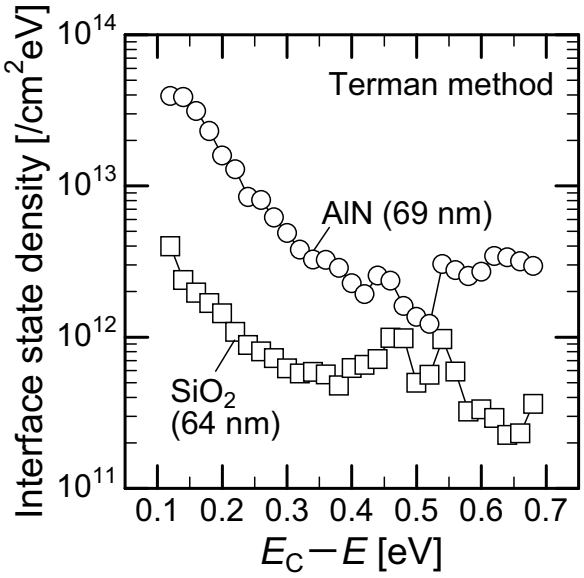

Figure 6.9: Interface state density calculated from the C–V characteristics for MIS(MOS) capacitors with a 69-nm-thick AlN (circle) and a 64-nm-thick SiO_2 (square) dielectrics by using Terman method.

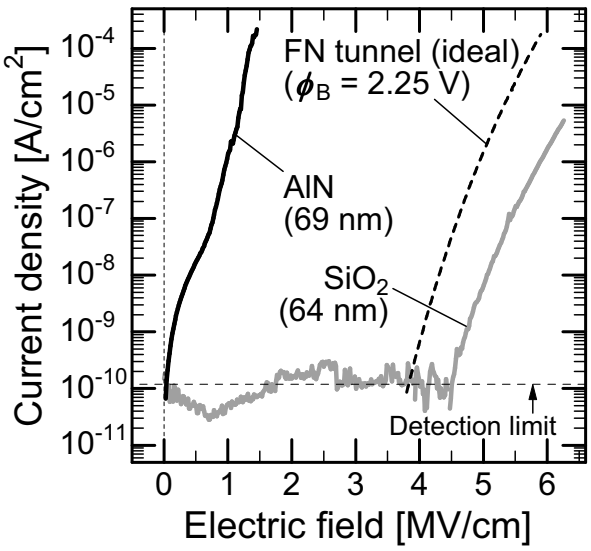

Figure 6.10: Current-voltage (I–V) characteristics for MIS(MOS) capacitors with a 69-nm-thick AlN (black line) and a 64-nm-thick SiO_2 (gray line) dielectrics. An ideal profile of the FN tunneling current is also shown by the dashed line.

The insulating property of an AlN dielectric was characterized. The leakage current profiles of MIS (MOS) capacitors are shown in Fig. 6.10. Compared with the SiO_2 dielectrics, much higher leakage current is observed. The leakage current also exceeds the ideal profile of Fowler-Nordheim (FN) tunneling current[1].

6.3.3 Discussion

In the characteristics of MISFETs with 4H-AlN gate dielectrics, the transistor operation was clearly observed. This is the first demonstration of AlN/SiC MISFETs with practical performance, which is improved from that of the previously-reported AlN MISFETs fabricated on SiC (0001) faces [4].

The AlN/SiC MISFETs indicated the normally-ON characteristics. In addition, in the C–V characteristics of AlN/SiC MIS capacitors, the negative shift of the flat band voltage was observed. These imply that carriers exist at the interface at $V_G = 0$ V. Although the origin of the carriers has not been determined yet, two possible expectations are given.

- Since the AlN/SiC interface was formed on a nonpolar $(11\bar{2}0)$ face, carriers are not emitted from interface bonds as described in Section 6.1 (Fig. 6.2 (c)). However, at the step edges of the AlN/SiC interface, the numbers of N–Si and Al–C bonds are not the same, leading to charge unbalance. Figure 6.11 shows the atomic bond configurations at the step edges. The steps are classified into two groups, that is, [0001] down steps and $[000\bar{1}]$ down steps. In each group of steps, two types of the atomic configuration are possible. If the $[000\bar{1}]$ down steps of type 1 or the [0001] down steps of type 2 exceed the other types of steps, the interface may exhibit donor-like character, that is, emits electrons.

- Oxygen impurities are unintentionally doped to MBE-grown 4H-AlN. Although oxygen in AlN can act as donors, AlN does not show n-type conductivity due to the high activation energies (∼2.0 eV) [14–17]. However, oxygen near the interface may emit electrons to SiC due to the large conduction band offset as shown in Fig. 6.12, which is so-called modulation doping.

It is believed that the dependence of off-angle and off-direction of SiC substrates will give the effect of step edges, and that the dependence of AlN layer thickness will reveal the effect of the modulation doping. Since SiC can not be alloyed with group-IV crystal (C, Si and Ge), it is difficult to form two-dimensional electron gas (2DEG) by modulation doping within

[1]The FN tunneling current J_{FN} is expressed [12]: $J_{FN} = \frac{q^2 m^* E^2}{8\pi h \phi_B m_0} \exp\left(-\frac{8\pi\sqrt{2qm^*\phi_B^3}}{3hE}\right)$ where E is the electric field, ϕ_B is the barrier height, that is, the conduction band discontinuity of 4H-AlN/4H-SiC interface, and m^* is the effective electron mass ($0.4m_0$) in AlN [13]. The barrier height was roughly estimated to be 2.25 eV from the valence band discontinuity (estimated from XPS) and the band gap energy (measured by optical reflectance).

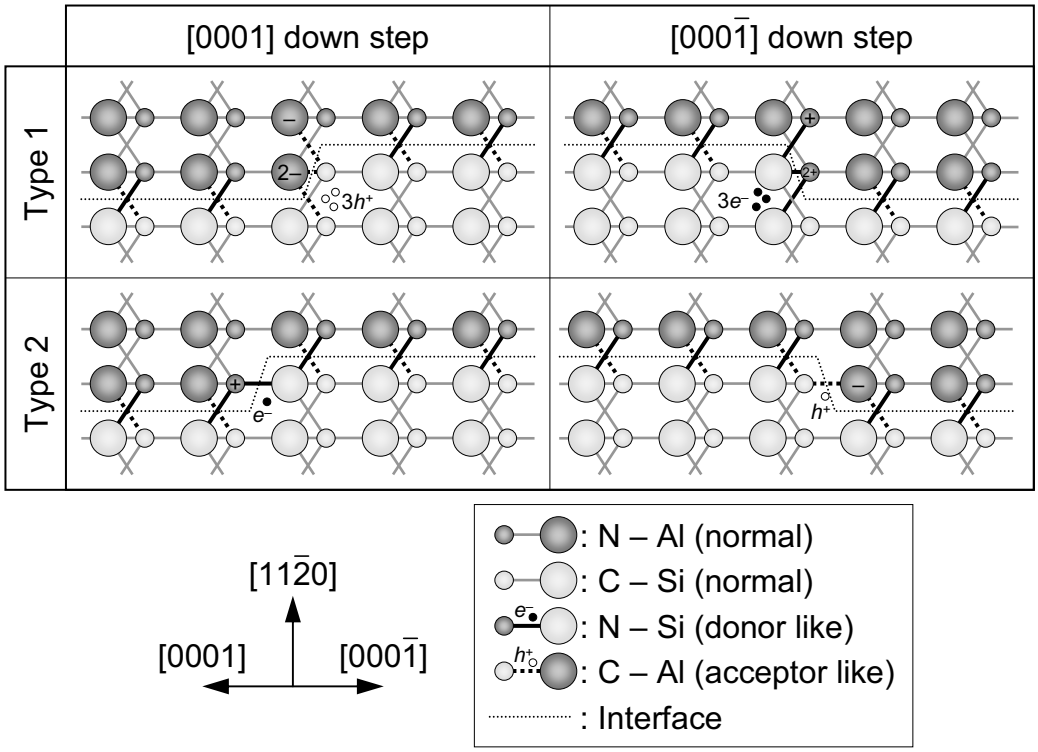

Figure 6.11: Schematics of charge unbalance at the step edges of AlN/SiC (11$\bar{2}$0) interfaces. Four types of the variation can be supposed.

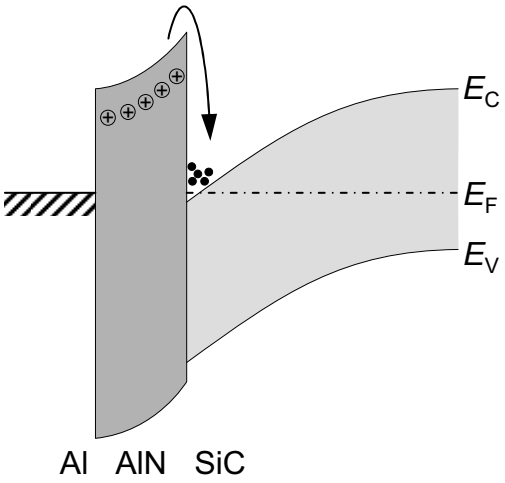

Figure 6.12: Schematics of a band structure in the Al/AlN/SiC MIS structure for the model of modulation doping from n-AlN to SiC.

group-IV heterostructure. If the modulation doping is possible in the system of AlN/SiC, it indicates the possibility for SiC high-frequency power devices.

From the viewpoint of device performance, the AlN/SiC MISFETs should be much improved. Yano *et al.* have been reported that the SiO_2/SiC MOSFETs fabricated on $(11\bar{2}0)$ exhibits very high channel mobility of 96 cm^2/Vs among SiC MOSFETs due to the low interface state density [18]. The SiO_2/SiC MOSFETs fabricated in this study was also show a high mobility of 67 cm^2/Vs, where the *p*-body of the channel region was formed by Al^+ implantation. To obtain the comparable or superior performance to the SiO_2/SiC MOSFETs, there is still room for improvement in AlN/SiC MISFETs. The maximum gate field was limited to 0.08 MV/cm due to the gate leakage current, resulting in the low channel mobility. It is believed that the suppression of the gate leakage current is effective to enhance the channel mobility, where a stacking gate of SiO_2 or Si_3N_4 on 4H-AlN is valuable for gate leakage reduction. The interface state density of AlN/SiC MISFETs was one order of magnitude higher than that of the SiO_2/SiC MOSFETs. There are three possible candidates for the origin of interface states. (1) Partial dislocations exist on the AlN/SiC interface as an end of stacking faults (SFs). The partial dislocations include a number of dangling bonds, which can form interface states. (2) N–Si and Al–C bonds at the AlN/SiC interface can form the interface states. It has been reported that N–Si and Al–C bonds form shallow states in the band gap of SiC [19]. (3) Residual oxygen or other impurity at the interface is also candidates. Several kinds of impurities exist on the SiC surface before AlN growth, which are incorporated to the interface. It is important to investigate the dependence of the growth conditions at the initial stage on the interface state density, which will give us the direction for further reduction of interface states.

6.4 Summary

SiC MISFETs with isopolytypically grown 4H-AlN as a gate dielectric have been demonstrated as a basis of electronic device applications. *N*-channel MISFETs have been fabricated by SiC $(11\bar{2}0)$ epitaxial growth followed by ion implantation for doping and 4H-AlN $(11\bar{2}0)$ heteroepitaxial growth. Although the field-effect mobility of the MISFETs and the interface state density of AlN/SiC should be improved, the MISFETs have nevertheless exhibited clear transistor operation for the first time. The MISFETs have exhibited normally-ON characteristics, implying the possibility for the modulation doping from unintentionally-doped *n*-AlN to SiC.

References

[1] C. I. Harris, M. O. Aboelfotoh, R. S. Kern, S. Tanaka, and R. F. Davis, Inst. Conf. Ser. **142**, 777 (1996).

[2] C. -M. Zetterling, M. Östling, H. Yano, T. Kimoto, H. Matsunami, K. Linthicum, and R. F. Davis, Mater. Sci. Forum **338–342**, 1315 (2000).

[3] N. Onojima, J. Kaido, J. Suda, T. Kimoto, and H. Matsunami, Mater. Sci. Forum **457–460**, 1569 (2004).

[4] N. Onojima, J. Kaido, J. Suda, and T. Kimoto, phys. stat. sol. (c) **2**, 2643 (2005).

[5] W. A. Harrison, E. A. Kraut, J. R. Waldrop, and R. W. Grant, Phys. Rev. B **18**, 4402 (1978).

[6] J. N. Stirman, F. A. Ponce, A. Pavlovska, I. S. T. Tsong, and D. J. Smith, Appl. Phys. Lett. **76**, 822 (2000).

[7] Z. Y. Chen, T. Kimoto, and H. Matsunami, Jpn. J. Appl. Phys. **38**, L1375 (1999).

[8] Y. Negoro, N. Miyamoto, T. Kimoto, and H. Matsunami, Appl. Phys. Lett. **80**, 240 (2002).

[9] Y. Negoro, K. Katsumoto, T. Kimoto, and H. Matsunami, J. Appl. Phys. **96**, 224 (2004).

[10] S. Dimitrijev, H. F. Li, H. B. Harrison, and D. Sweatman, IEEE Trans. Electron Devices **18**, 175 (1996).

[11] L. M. Terman, Solid-State Electron. **5**, 285 (1962).

[12] E. H. Snow, Sol. Stat. Commun. **5**, 813 (1967).

[13] M. E. Levinshtein, S. L. Rumyantsev, and M. S. Shur, *Properties of Advanced Semiconductor Materials* (John Wiley & Sons, Inc., New York, 2001).

[14] T. Mattila and R. M. Nieminen, Phys. Rev. B **54**, 16676 (1996).

[15] C. Stampfl and C. G. V. de, Walle, Phys. Rev. B **65**, 155212 (2002).

[16] C. Stampfl and C. G. V. de, Walle, Appl. Phys. Lett. **72**, 459 (1998).

[17] C. G. V. de, Walle, Phys. Rev. B **57**, R2033 (1997).

[18] H. Yano, T. Hirao, T. Kimoto, and H. Matsunami, Jpn. J. Appl. Phys. **39**, 2008 (2000).

[19] W. R. L. Lambrecht and B. Segall, Phys. Rev. B **43**, 7070 (1991).

Chapter 7

Conclusions

7.1 Conclusions

To demonstrate the potential of nonpolar 4H-AlN isopolytypically grown on nonpolar 4H-SiC, several aspects toward realization of high-quality growth, characterization of its properties and basic applications for electronic and optoelectronic devices have been investigated. In this study, reduction of extended defects has been achieved by realization of perfect isopolytypic growth in 4H-AlN nonpolar $(11\bar{2}0)$ and $(1\bar{1}00)$ faces. The availability of high-quality 4H-AlN enables us to characterize physical properties of 4H-AlN. Basic device structures were fabricated toward applications of 4H-AlN layers as well as 4H-AlN/4H-SiC interface. The successful growth of 4H-AlN/4H-AlGaN multiple quantum well (MQW) structure has established a basis toward high-efficient deep-ultraviolet (UV) light-emitting devices. The clear transistor operation of AlN/SiC metal-insulator-semiconductor field-effect transistors (MISFETs) has also suggested potential of the isopolytypic 4H-AlN/4H-SiC interface for electronic device applications. The main conclusions obtained in the present study are summarized as follows.

In Chapter 2, the effects of pretreatment of nonpolar SiC substrates are studied. It has been found that *ex-situ* HCl gas etching is effective to obtain an atomically flat surface of nonpolar 4H-SiC $(11\bar{2}0)$ substrates and that clear step-and-terrace structure can be obtained on 4H-SiC $(1\bar{1}00)$ substrates by HCl gas etching. *In-situ* Ga deposition and desorption is also effective in reduction of residual oxygen on the surface of nonpolar SiC substrates.

In Chapter 3, reduction of stacking faults (SFs) and threading dislocations (TDs) in 4H-AlN nonpolar $(11\bar{2}0)$ and $(1\bar{1}00)$ layers has been achieved. In 4H-AlN $(11\bar{2}0)$ growth, a flat surface of epilayers has been achieved by growth under the optimized condition of Ⅲ/V supply ratio. Transmission electron microscopy (TEM) observation has revealed that the SF density is lowered to 2×10^5 cm^{-1}, and that the partial and perfect TD densities are reduced to 7×10^7 cm^{-2} and 1×10^7 cm^{-2}, respectively, corresponding to one- or two-order-of-magnitude improvement compared with the 4H-AlN previously reported. In 4H-AlN $(1\bar{1}00)$ growth, stable layer-by-layer growth could be achieved by using SiC sub-

strates with well-formed step-and-terrace structures. The layer-by-layer growth has been confirmed by observation of anisotropic two-dimensional AlN islands on the grown surface as well as persistent oscillation of reflection high-energy electron diffraction (RHEED) intensity. Cross-sectional TEM observation has revealed that SF generation during growth is suppressed and the SF density is reduced to 1×10^6 cm^{-1}.

In Chapter 4, structure of extended defects in 4H-AlN and relationship between extended defects and the linewidth of x-ray diffraction (XRD) have been studied. TEM observation has revealed that the SFs have the stacking sequence of ABCBABABABCB which are classified in the Shockley-type double stacking fault. The Burgers vectors of the perfect TDs are determined to be $\boldsymbol{b} = [0001]$, and those of the partial TDs to be the sum of two Burgers vectors of $\boldsymbol{b} = \frac{1}{3}\langle 1\bar{1}00\rangle$ with the opposite sign ($\frac{1}{3}[1\bar{1}00] + \frac{1}{3}[\bar{1}100]$, for example) which is equivalent to $\boldsymbol{b} = \boldsymbol{0}$. The extended defect analysis also indicates that the SFs do not affect symmetrical reflections of XRD ω-scan in nonpolar 4H-AlN. In addition to extended-defect structure, the lattice constants, the band structure and the phonon mode of 4H-AlN have been investigated. High-resolution XRD (HRXRD) has revealed that the 4H-AlN is coherently grown on nonpolar 4H-SiC, implying the shift of the lattice constants toward reduction of the lattice mismatch from 2H- to 4H-AlN. From the spectra of optical reflectance (OR) and cathodoluminescence (CL) from 4H-AlN, the bandgap energy of 4H-AlN is estimated to be about 0.2 eV smaller than that of 2H-AlN. A large intensity of band edge emission from nonpolar 4H-AlN implies the direct transition type of band structure. In laser Raman scattering spectroscopy, the phonon peaks of A_1(TO), E_1(TO) and E_2^{H} are observed. These peaks have been determined to be the phonon modes of 4H-AlN, which are different from those of 2H-AlN.

In Chapter 5, growth of 4H-AlN/4H-AlGaN MQW structures has been studied to establish a basis of optoelectronic device application. To control the composition of AlGaN, Ga incorporation on AlGaN $(11\bar{2}0)$ and $(1\bar{1}00)$ has been evaluated by XRD, energy-dispersive x-ray spectroscopy and cathodoluminescence analyses. The Ga composition x of $Al_{1-x}Ga_xN$ layers grown on $(1\bar{1}00)$ is much higher than that on $(11\bar{2}0)$ under the same growth conditions. In the growth of $Al_{0.90}Ga_{0.10}N$ $(1\bar{1}00)$, it has been found that the crystal structure indicates 4H polytype and that stable layer-by-layer growth is observed, which show the same trends as in the case of 4H-AlN growth. MQW structures of 15-nm-thick 4H-AlN/4-nm-thick 4H-$Al_{0.93}Ga_{0.07}N$ $(1\bar{1}00)$ are grown on 4H-SiC $(1\bar{1}00)$. From cross-sectional TEM observation, it has been revealed that the 4H polytype is maintained in the whole of MQW structure and no extended defects are generated at the interface of AlN/AlGaN. In CL measurement, a large intensity of band edge emission of MQW has been observed at the energy of 5.35 eV, and the blue shift of the band edge emission has not been observed with increasing the excitation power density. These results demonstrate great promise of nonpolar 4H-polytype MQW structure, which is free from the internal electric field.

In Chapter 6, SiC MISFETs with a 4H-AlN as gate dielectric have been demonstrated as a basis of electronic device applications. N-channel MISFETs have been fabricated by using

4H-AlN ($11\bar{2}0$) heteroepitaxial layers grown on 4H-SiC ($11\bar{2}0$). Although further improvement of the electrical characteristics is required, the MISFETs exhibited clear transistor operation for the first time. The MISFETs have exhibited normally-ON characteristics, implying the possibility of the modulation doping from unintentionally-doped n-AlN to SiC.

7.2 Future Work

Through this work, several bases for device applications of nonpolar 4H-AlN isopolytypically grown on 4H-SiC have been established. However, there still remain several issues to be solved, and there have emerged some challenges to be accomplished in the future.

- **Further reduction of stacking faults originating from the AlN/SiC interface:** Still large number of SFs were observed, which originate from the AlN/SiC interface, especially in the 4H-AlN ($1\bar{1}00$). In the initial stage of growth, the growth kinetics is different from that during AlN growth due to the difference of surface energy between AlN and SiC. It is important to control the nucleation on a nonpolar 4H-SiC surface for realization of layer-by-layer growth from the earliest stage.

- **Growth of 4H-AlGaN ($11\bar{2}0$) with equivalent quality to the 4H-AlN ($11\bar{2}0$):** Very low Ga-incorporation has been observed in Al(Ga)N ($11\bar{2}0$) growth where the surface of Al(Ga)N layers has become rough with increasing the Al/Ga supply ratio. In 4H-AlN ($11\bar{2}0$) growth, lower densities of SFs and TDs and flatter growth surfaces have been achieved compared with the ($1\bar{1}00$) growth. If the 4H-AlGaN ($11\bar{2}0$) growth is accomplished, development of 4H-AlN/4H-AlGaN QW on ($11\bar{2}0$) with the higher quality will be possible. 4H-AlGaN ($11\bar{2}0$) layers with an equivalent quality to the 4H-AlN should be explored. Furthermore, the difference of Ga incorporation between ($11\bar{2}0$) and ($1\bar{1}00$) can be applied for fabrication of AlGaN quantum wire structures in AlN matrix.

- **Further clarification of band structure of 4H-AlN from both experimental and theoretical sides:** The experimental data in this study have indicated the direct transition type of band structures in 4H-AlN, while several theoretical calculations including this study have shown that the band structure of 4H-AlN is indirect transition type [1]. The transition type of band structures is very important for device applications, which should be studied with OR analysis at low temperature. In addition, the nonpolar 4H-AlN will exhibit the light polarization property due to the in-plane anisotropy. The polarization property is interesting for optical application, which should be examined.

- **Determination of conduction mechanism and improvement of interface properties in 4H-AlN/4H-SiC:** Although the SiC MISFETs with 4H-AlN gate

dielectrics indicated a clear transistor operation, improvement of the characteristics is needed in various respects, for example, enhancement of the channel mobility, reduction of the gate leakage current, reduction of the interface state density and the large negative threshold voltage shift. It is expected that the growth condition of the initial stage and during AlN growth affects the interface and insulating properties, respectively, and that the fabrication process of MISFETs also influences the device performance. To investigate the factors which degrade the properties will result in improvement of the device performance.

- **Control of impurity incorporation to 4H-AlN and characterization of electrical properties of impurity-doped 4H-AlN:** It is important to control the conductivity with impurity doping for both electronic and optoelectronic device applications. Difference of impurity incorporation in growth orientations will be expected as is the case for Ga incorporation in AlGaN growth. Moreover, in the 2H-AlN layers, the difficulty of conductivity control has been reported, especially in p-type conductivity, because of the large ionization energies of donors or acceptors [2]. Since the band structure of 4H-AlN is different from that of 2H-AlN, the ionization energies of donors and acceptors in 4H-AlN will be different from those in 2H-AlN, which should be investigated systematically.

Finally, we believe that further study of 4H-polytype AlN will provide not only advances in practical application but also new scientific insights into group-Ⅲ nitrides.

References

[1] K. Kobayashi and S. Komatsu, J. Phys. Soc. Jpn. **77**, 084703 (2008).

[2] Y Taniyasu, M Kasu, and T Makimoto, Appl. Phys. Lett. **89**, 182112 (2006).

List of Publications

A. Full Length Papers and Letters

1. M. Horita, J. Suda, and T. Kimoto
"Impact of Ⅲ/V Ratio on Polytype and Crystalline Quality of AlN Grown on 4H-SiC ($11\bar{2}0$) Substrate by Molecular-beam Epitaxy,"
Phys. Stat. Sol. (c) **3**, 1503 (2006).

2. M. Horita, J. Suda, and T. Kimoto
"High-quality Nonpolar 4H-AlN Grown on 4H-SiC ($11\bar{2}0$) Substrate by Molecular-beam Epitaxy,"
Appl. Phys. Lett. **89**, 112117 (2006).

3. R. Armitage, M. Horita, J. Suda, and T. Kimoto
"M-plane GaN Layers Grown by Rf-plasma Assisted Molecular Beam Epitaxy with Varying Ga/N Flux Ratios on M-plane 4H-SiC Substrates,"
J. Appl. Phys. **101**, 033534 (2007).

4. J. Suda, R. Armitage, M. Horita, and T. Kimoto
"A Comparative Study of Nonpolar A-plane and M-plane AlN Grown on 4H-SiC by Plasma-assisted Molecular-beam Epitaxy,"
J. Cryst. Growth **301–302**, 410 (2007).

5. M. Horita, J. Suda, and T. Kimoto
"Reduction of Threading Dislocations in Nonpolar 4H-AlN on 4H-SiC ($11\bar{2}0$) Grown by Molecular-beam Epitaxy with Slightly Al-rich Conditions,"
Phys. Stat. Sol. (c) **4**, 2552 (2007).

6. M. Horita, T. Kimoto, and J. Suda
"Nonpolar 4H-AlN Grown on 4H-SiC ($1\bar{1}00$) with Reduced Stacking Fault Density Realized by Persistent Layer-by-Layer Growth,"
Appl. Phys. Lett. **93**, 082106 (2008).

7. M. Horita, T. Kimoto, and J. Suda
   "Surface Morphologis of $(11\bar{2}0)$ and $(1\bar{1}00)$ Treated by High-temperature Gas Etching,"
   Jpn. J. Appl. Phys. **47**, 8388 (2008)

8. M. Horita, T. Kimoto, and J. Suda
   "Anomalous Difference of Ga Incorporation in Growth of AlGaN with Nonpolar Orientations,"
   to be submitted to Appl. Phys. Lett.

9. M. Horita, M. Noborio, T. Kimoto, and J. Suda
   "SiC Metal-insulator-semiconductor Filed-effect Transistors with 4H-AlN Gate Dielectric Isopolytypically-grown on 4H-SiC $(11\bar{2}0)$,"
   to be submitted to IEEE Electron Device Lett.

10. M. Horita, T. Kimoto, and J. Suda
    "Impact of Stacking Faults on X-ray Diffraction Line Width in Nonpolar 4H-AlN Isopolytipically Grown on 4H-SiC,"
    in preparation.

11. M. Horita, T. Kimoto, and J. Suda
    "4H-AlN/4H-AlGaN Multiple Quantum Well Structure on 4H-SiC Substrate Isopolytypically Grown by Molecular-beam Epitaxy,"
    in preparation.

B. Conferences Proceedings

1. R. Armitage, M. Horita, J. Suda, and T. Kimoto
   "Growth of Nonpolar AlN and AlGaN on 4H-SiC $(1\bar{1}00)$ by Molecular Beam Epitaxy,"
   Mater. Res. Soc. Symp. Proc. **892**, FF28–03 (2005).
   (*Mater. Res. Soc. Fall Meeting*, Boston, MA, USA, 2005.)

2. M. Horita, J. Suda, and T. Kimoto
   "High-quality Nonpolar 4H-AlN Grown on 4H-SiC by Molecular-beam Epitaxy,"
   (*Abstr. 48th Electron. Mater. Conf.*, State College, PA, USA, 2006.)

3. M. Horita, J. Suda, and T. Kimoto
   "Reduction of Stacking Fault Density in Non-polar 4H-AlN Grown on 4H-SiC $(1\bar{1}00)$ by Realization of Persistent Layer-by-layer Growth Mode,"
   (*Abstr. 7th Intern. Conf. on Nitride Semiconductor*, Las Vegas, NV, USA, 2007.)

4. M. Horita, J. Suda, and T. Kimoto
"Origin of Defects at the Nonpolar 4H-AlN (11$\bar{2}$0)/4H-SiC (11$\bar{2}$0) Interface Revealed by TEM Observations,"
(*Abstr. 9th Intern. Conf. on Atomically Controlled Surf., Interf. and Nanostruct.*, Tokyo, Japan, 2007.)

5. M. Horita, M. Noborio, J. Suda, and T. Kimoto
"First Demonstration of SiC MISFETs with 4H-AlN Gate Dielectric Heteroepitaxially-grown on 4H-SiC (11$\bar{2}$0),"
(*Abstr. 7th European Conf. on Silicon Carbide and Relat. Mater.*, Barcelona, Spain, 2008.)

C. Related Publications

1. H. Okumura, M. Horita, J. Suda, and T. Kimoto
"Impact of Surface Step Heights of 6H-SiC (0001) Vicinal Substrates in Heteroepitaxial Growth of 2H-AlN,"
Appl. Surf. Sci. **254**, 7858 (2008).
(*Proc. 9th Intern. Conf. on Atomically Controlled Surf., Interf. and Nanostruct.*, Tokyo, Japan, 2007.)

2. H. Okumura, M. Horita, J. Suda, and T. Kimoto
"Observation of Novel Defect Structure in 2H-AlN Grown on 6H-SiC (0001) Substrates by Molecular-beam Epitaxy,"
to be published in Phys. Stat. Sol.
(*Proc. Intern. Workshop on Nitride Semiconductor 2008*, Montreux, Switzerland, 2008.)

D. Books

1. J. Suda, M. Horita, N. Onojima, and T. Kimoto
"Heteroepitaxial Growth of AlN on SiC,"
Hybrid Nanostructured Materials and Their Applications
(WORDS, Tokyo, Japan, 2005) 11–22.